Simultaneous diesel and natural gas injection for dual-fuelling compression-ignition engines

Author:
White, Timothy Ross

Publication Date:
2006

DOI:
https://doi.org/10.26190/unsworks/15329

SIMULTANEOUS DIESEL AND NATURAL GAS INJECTION FOR DUAL-FUELLING COMPRESSION-IGNITION ENGINES

Timothy Ross WHITE

BE (Mech) Hons1

A thesis submitted to fulfil the
requirements of the degree of
Doctor of Philosophy

School of Mechanical and Manufacturing Engineering
The University of New South Wales
September 2006

COPYRIGHT STATEMENT

AUTHENTICITY STATEMENT

ORIGINALITY STATEMENT

‘I hereby declare that this submission is my own work and to the best of my knowledge it contains no materials previously published or written by another person, or substantial proportions of material which have been accepted for the award of any other degree or diploma at UNSW or any other educational institution, except where due acknowledgement is made in the thesis. Any contribution made to the research by others, with whom I have worked at UNSW or elsewhere, is explicitly acknowledged in the thesis. I also declare that the intellectual content of this thesis is the product of my own work, except to the extent that assistance from others in the project's design and conception or in style, presentation and linguistic expression is acknowledged.’

Signed ………………………………………………...........................

Date ………………………………………………...........................

Abstract

The introduction of alternative fuels such as natural gas is likely to occur at an increasing rate. The dual-fuel concept allows these low cetane number fuels to be used in compression-ignition (CI, diesel) type engines. Most CI engine conversions have pre-mixed the alternative fuel with air in the intake manifold while retaining diesel injection into the cylinder for ignition. The advantage is that it is simple for practical adaptation; the disadvantage is that good substitution levels are only obtained at mid-load.

A better solution is to inject both the alternative and diesel fuels directly into the cylinder. Here, the fuel in the end-zone is limited and the diesel, injected before the alternative, has only a conventional ignition delay. This improves the high-end performance. Modern, very high pressure diesel injectors have good turndown characteristics as well as better controllability. This improves low-end performance and hence offers an ideal platform for a dual-fuel system. Several systems already exist, mainly for large marine engines but also a few for smaller, truck-sized engines. For the latter, the key is to produce a combined injector to handle both fuels which has the smallest diameter possible so that installation is readily achieved. There exists the potential for much improvement.

A combined gas/diesel injection system based on small, high pressure common-rail injectors has been tested for fluid characteristics. Spray properties have been examined experimentally in a test rig and modelled using CFD. The CFD package *Fluent* was used to model the direct-injection of natural gas and diesel oil simultaneously into an engine. These models were initially calibrated using high-speed photographic visualisation of the jets. Both shadowgraph and schlieren techniques were employed to identify the gas jet itself as well as mixing regions within the flow. Different orientations and staging of the jets with respect to each other were simulated. Salient features of the two fuel jets were studied to optimise the design of a dual-fuel injector for CI engines. Analysis of the fuel-air mixture strength during the injection allowed the ignition delay to be estimated and thus the best staging of the jets to be determined.

Acknowledgements

I would like to extend my gratitude to those who have assisted me in the work that ultimately led to the assembly of this document. My supervisors, Professors Brian Milton and Masud Behnia, devised a topic that was both relevant to society's needs and able to hold my interest. Greg Heins, without whom I would not have made it through Uni in four years. J. Middelbery and Kate Ng, without whom I would not have made it through the last four. And thankyou most sincerely Mum and Dad. Your unconditional support was greatly appreciated, despite appearances often suggesting otherwise.

The heights by great men reached and kept,
Were not attained by sudden flight,
But they, while their companions slept,
Were toiling upward through the night.

Henry Wadsworth Longfellow
The Ladder of Saint Augustine, 1858.

Contents

List of Figures

List of Photographs

List of Tables

List of Equations

List of Publications

1. T.R. White, B.E. Milton and M. Behnia, *Mixing of Co-axial Natural Gas/Liquid Diesel Fuel Sprays*, "Work-in-Progress" poster presented at the 18th Annual Conference on Liquid Atomization & Spray Systems (ILASS-Europe 2002), 9-11 September 2002, Zaragoza, Spain.

2. T.R. White, *The Effect of Spark Knock on the Performance of a Modern Engine*, Young Automotive And Transport Executives Conference 2002 (YATE Conference - Formerly Young Engineers Conference): "Ensuring a Technology Friendly Transportation Industry", 29-30 October 2002, Melbourne.

3. T.R. White, B.E. Milton and M. Behnia, *Mixing of Co-axial Natural Gas/Liquid Diesel Fuel Sprays*, 4th International Colloquium Fuels, 15-16 January 2003, Technische Akademie Esslingen, Germany.

4. X.T. Tran, B.E. Milton, T.R. White and M. Tordon, *Modelling a HEUI Injector in* Matlab *and* Simulink, 2003 IEEE/ASME International Conference on Advanced Intelligent Mechatronics, 20-24 July 2003, Kobe, Japan.

5. T.R. White, B.E. Milton and M. Behnia, *Direct Injection of Natural Gas/Liquid Diesel Fuel Sprays*, Fifteenth Australasian Fluid Mechanics Conference, 13-17 December 2004, University of Sydney, Australia.

6. T.R. White, B.E. Milton and M. Behnia, *Simultaneous Injection of Natural Gas and Liquid Fuel into Diesel Engines*, 5th International Colloquium Fuels, 12-13 January 2005, Stuttgart/Ostfildern, Germany.

7. T.R. White, B.E. Milton and M. Behnia, *Visualisation of the Mixing of Intermittent Natural Gas and Liquid Diesel Fuel Sprays from High Pressure Nozzles*, The 8^{th} Asian Symposium on Visualisation, 23-27 May 2005, Chiangmai, Thailand.

8. T.R. White and B.E. Milton, *Shock Structure from Highly Under-expanded Natural Gas Jets*, 17th International Shock Interaction Symposium, 4-8 September 2006, University of Rome “La Sapienzia”, Italy.

9. T.R. White and B.E. Milton, *Visualising the Mixing of High Pressure, Intermittent Natural Gas and Liquid Diesel Fuel Sprays*, 12th International Symposium on Flow Visualisation, 10-14 September 2006, German Aerospace Center (DLR), Göttingen, Germany.

10. T.R. White, B.E. Milton and M. Behnia, *Turbulent Mixing of High Pressure, Intermittent Natural Gas and Liquid Diesel Fuel Sprays*, Turbulence, Heat and Mass Transfer 5, 25-29 September 2006, Dubrovnik, Croatia.

11. B.E. Milton, B.J. Ware, G. Milton, T.R. White, T. Gardner and M. Bevan, *Further Development of the EDS, Single-Fluid HEUI Injection System,* FISITA 2006, 22-27 October 2006, Yokohama, Japan.

Nomenclature

a	Constant in the Wave Model
A	Mass of Air or Surface Area or a constant in the Arrhenius Equation
AC	Alternating Current
AFR	Air-to-Fuel ratio (by mass)
B_0	Constant in the Wave Model
B_1	Constant in the Wave Model
BTDC	Before Top Dead Centre
c	Mass-fraction
C	Constants in the k-ε turbulence model
CCD	Charge-Coupled Device
C_d	Co-efficient of Discharge
CDF	Conventional Dual-Fuelling
cf.	Compare(d) with
CFD	Computational Fluid Dynamics
CI	Compression-Ignition
CN	Cetane Number
CNG	Compressed Natural Gas
CNK	Critical Cavitation Number
CO	Carbon Monoxide
CO_2	Carbon Dioxide
C_p	Specific Heat at Constant Pressure
D	Diameter
DC	Direct (non-alternating) Current
DDS	Diesel Delivery System
DI	Direct-Injection
DF	Dual-Fuel
E	Energy per unit mass or Enthalpy
E_A	Apparent activation energy for the ignition process
ECU	Electronic or Engine Control Unit
EGR	Exhaust Gas Recirculation
EOI	End of Injection

ETAB	Enhanced Taylor Analogy Break-up model
EUI	Electronic Unit Injector
fps	Frames per second
F	Mass of Fuel or External body force
G	Contribution to Turbulence Kinetic Energy from buoyancy
GCV	Gas Control Valve
GDS	Gas Delivery System
h	Specific enthalpy
H	Total enthalpy
HC	Hydrocarbons
HEUI	Hydraulically-actuated Electronically-controlled Unit Injector
HF	Hydraulic Flip
HPCR	High-Pressure Common-Rail
HPDI	High-Pressure Direct-Injection
I	Turbulence Intensity
ID	Ignition Delay
ICE	Internal Combustion Engine(s)
J	Diffusion Flux in continuity equations
JVB	Jet Visualisation Box
JVR	Jet Visualisation Rig
k	Eddy Viscosity or Conductivity or Turbulence kinetic energy
kfps	Thousand frames per second
K	Kelvin
K	Constant in equations for entrainment-rate
KH	Kelvin-Helmholtz
L	Litre
L	Length
LDA	Laser Doppler Anemometry
LDV	Laser Doppler Velocimetry
LES	Large-Eddy Simulation
LHV	Lower Heating Value
LPG	Liquefied Petroleum Gas
m'	Mass per unit-length

M	Mass or Mach Number
$\dot{M}$	Mass Flux
MVL	Mercury Vapour Lamp
n	Constant in the Arrhenius Equation
N	Atomic Nitrogen or Number
N_2	Molecular Nitrogen
N_c	Cavitation number
NG	Natural Gas
NO_x	Oxides of Nitrogen
OE	Original-Equipment
OEM	Original-Equipment Manufacturer
p, P	Pressure
PIV	Particle-Imaging Velocimetry
PLIF	Planar Laser-Induced Fluorescence
PM	Particulate Matter
POA	Plain-Orifice Atomiser
psi	Pounds per square-inch
q	Back-plane in Turner's Vortex-ball Model
r	Radius
RANS	Reynolds-Averaged Navier-Stokes
RCM	Rapid Compression Machine
R	The Universal Gas Constant, 8,314J/kg.K
Re	Reynolds' Number
RHS	Rectangular Hollow Section
rms	Root mean-squared
RT	Rayleigh-Taylor
R_v	Radius of the Vortex-ball in Turner's Model
School	The School of Mechanical and Manufacturing Engineering at UNSW
S	Source term in equations
SI	Spark-Ignition
SMD	Sauter Mean Diameter (sometimes SMR – Sauter Mean Radius)
SOI	Start of Injection
$\overline{S}_p$	Mean Piston Speed

SVR	Spray Visualisation Rig
TAB	Taylor Analogy Break-up model
UHC	Unburned Hydrocarbons
UI	Unit Injector
VCO	Valve-Covered Orifice
t	Elapsed time
T	Temperature
TDC	Top-Dead Centre
u, U	Axial velocity
UNSW	The University of New South Wales
$u'_{T,\,EA}$	Average turbulence intensity
V	Volume
VCO	Valve-Covered Orifice
We	Weber Number
x	*Axial location*
X	Penetration length of a Jet
Y	Mass-fraction of the jet fluid or a term in the k-ε model

Γ	Penetration constant for gas jets or Diffusion Co-efficient
γ	Ratio of Specific Heats
Δ	Difference
η	Term in the k-ε model
ε	Rate of turbulence dissipation
Λ	Wavelength of instabilities in the Wave Model
μ_t	Turbulent viscosity
ρ_a	Air density
ρ_{gi}	Buoyancy term for Prandtl Number in conservation equations
σ	Surface Tension or a constant in the k-ε model
τ	Time for droplet break-up or Stress Tensor in conservation equations
τ_{id}	Ignition Delay Time (measured in either crankshaft degrees or seconds)
ϕ	A scalar quantity
Φ	Air/Fuel Mass-Equivalence Ratio
Ω	Growth Rate of instabilities in the Wave Model or Spray Angle
∇	Gradient

1. Chapter One: Introduction

1.1 Background

1.1.1 Motivation for this Work

The introduction of alternative fuels such as compressed natural gas (CNG), liquefied petroleum gas (LPG) and alcohols for internal combustion engines is likely to occur at an increasing rate. The dual-fuel (DF) concept allows these fuels which have low cetane numbers to be used in compression-ignition (CI, diesel) engines. Most CI engine conversions have the alternative fuel pre-mixed with air in the intake manifold while retaining diesel injection into the cylinder. The main advantage of this method is simple practical adaptation, the main disadvantage is that good substitution levels are only obtained at mid-load. This is because, at low load, the diesel injectors still require a substantial fuel delivery while at high load, the extended ignition delay increases the tendency for diesel knock and the mixed fuel and air in the end-zone exacerbates gasoline-type knock. Other disadvantages are that displacement of air in the intake can reduce peak power at any given air/fuel ratio and that fuel can directly short-circuit from inlet to exhaust, thereby increasing emissions of unburned hydrocarbons (UHC).

A solution is to inject both the alternative and diesel fuels directly into the cylinder. Here, the fuel in the end-zone is limited and the diesel, injected before the alternative fuel, has only a conventional ignition delay which improves the high-end performance. In such a system, not only must the diesel be injected at high pressure but the gas as well. Such technology is often referred to as High-Pressure Direct Injection (HPDI) of the alternative fuel. Several systems exist, mainly for large marine engines but also for smaller sizes as used in trucks. For the latter, the key is to produce a combined injector to handle both fuels which is compact enough such that installation is readily achieved. Modern, very high-pressure diesel injectors are compact in size and have good turndown characteristics as well as better controllability. Hence they offer an improvement at the low end as well as having improved potential at the high end. The current work was carried-out as a first step in building a locally-developed HPDI system based upon such a modern injector for truck-sized engines.

1.1.2 Definition of "Dual Fuel"

Most people are familiar only with the term "dual-fuelling" when applied to spark-ignition (SI, gasoline) engines. In this context, the term "dual fuel" usually means that at any time the engine operates solely on either gasoline or on the gaseous fuel. Such technology has been widely used for many years and the best example of its use today is in taxi cabs which use LPG and, in recent years as the re-fuelling infrastructure has improved, CNG. The four-stroke SI engine lends itself well to operation where the gaseous fuel is introduced upstream of the throttle-body. This is often termed a "fumigated" manifold and the air/gas mixture enters the cylinder on the inlet stroke. Once warmed-up, such an engine can run entirely on the gaseous fuel with few adverse effects and little loss of operational flexibility. In more recent times, port injection of the gas has helped to improve efficiency and cold-start performance. Since 2000, Ford Australia has offered OEM systems which allow the sole use of either LPG or CNG [12, 13].

The current work deals with the dual-fuelling of CI engines only. Owing to difficulties associated with the ignition of low cetane number alternative fuels, these engines do not operate solely on the alternative fuel. The DF engine for the purposes of this study is a diesel engine that has been modified to use an alternative fuel whilst retaining diesel injection. A small amount of diesel fuel is injected to provide an ignition source for the alternative fuel which, in turn, makes up the remainder of the total energy requirement of the engine. In most cases, such DF engines can operate solely on diesel if the need arises (ie. if the alternative fuel is unavailable). For optimum economy, however, modern DF engines can operate on up to 95% (by energy) natural gas [110].

1.1.3 The Benefits of Dual-Fuelling

Dual-fuelling a diesel engine allows a proportion of the fuel used to consist of an alternative fuel. The alternative fuel of interest in this study is natural gas. The use of NG is desirable for several reasons:

- It burns more cleanly than diesel. Per unit energy, a reduction of the greenhouse gas Carbon Dioxide (CO_2) of up to 20% is achievable when using NG instead of diesel [110].
- Australia has vast reserves of (mostly yet untapped) NG. At the present rate of consumption, proven reserves will last around 90 years whereas domestic oil reserves will last less than 40 [48]. Further, conversion of the Australian vehicle fleet to locally-available NG would greatly reduce the dependence of Australia on foreign petroleum.
- As well as lower refining costs for NG when compared with diesel, NG is at this time (January 2006) exempt from federal government excise. The price of NG purchased as a retail fuel is approximately \$0.42/m^3 whereas diesel is around \$1.10/L [48]. This equates to a specific price (per unit energy) of about 1.12c/MJ for NG and 2.94c/MJ for diesel.

The dual-fuelling system allows the use of a cheaper, cleaner alternative fuel when it is available. If infrastructure at a particular geographical location is such that NG is unavailable, a well-designed system will allow the vehicle to operate solely on diesel. Diesel is available everywhere. There are, of course, many difficulties associated with the adaptation of DF technology to diesel engines. These are discussed in the next chapter.

Table 1.1. Approximate compositions and properties of selected fossil fuels and bio-fuels that are used in transport applications [26].

Fuel	Approximate average formula	Average molecular weight	Approximate C:H ratio	Energy density MJ/L	Energy density# MJ/m^3	CO_2 emissions g/MJ
Natural Gas	$\sim CH_{3.85}$	18.2	1:3.85		38.2	51.3
LNG	$\sim CH_{3.85}$	18.2	1:3.85	25.0		51.3
CNG	$\sim CH_{3.85}$	18.2	1:3.85		38.2	51.3
LPG	$\sim C_3H_{7.8}$	49	1:2.6	25.7		60.2
Petrol	$\sim C_{5.4}H_{10.7}$	80	1:2	35.2		65.8
Automotive diesel	$\sim C_{15.2}H_{22.2}$	212	1:1.9	38.6		65.8
Methanol	CH_3OH	32.04	1:4	15.8		60.8
Ethanol	CH_3CH_2OH	46.07	1:3	23.4		64.3
RME biodiesel	$\sim C_{13}H_{29}O$	201	1:2.29	33.3		85.0

1.1.4 Scope of this Work

The direct, in-cylinder injection of the alternative fuel into a DF engine (HPDI) is still in its infancy. There is presently only one organisation that has developed this technology to a stage whereby it has been applied commercially [33]. As such, there remains the potential to contribute greatly to the field of knowledge in this area of research. The work presented here is mostly concerned with the development of numerical models that were used to simulate the direct-injection of alternative fuels into CI engines. Particular emphasis was placed on the orientation of the gas nozzle and its staging with respect to the pilot (diesel) jet.

A laboratory rig was built to enable the validation of the numerical models but also to provide a qualitative insight into the simultaneous injection of diesel and natural gas. This system was based on a modern, electronically-controlled, high-pressure diesel injection system. It has done and will continue to provide a powerful design tool for the manufacture of HPDI systems of the future.

1.1.5 Thesis Outline

The first two chapters of this volume set the background for the work which was done over the duration of this project. The research encompasses many aspects of thermo-fluid engineering including the break-up of liquid jets, mixing of gas jets, ignition of fuels, numerical modelling and optical investigation techniques.

Chapter 2 provides background concerning the operation of CI engines. Fuel injection systems are described and their importance with respect to the performance of engines is established. Methods of dual-fuelling CI engines are then described and work which has been carried-out by previous researchers is reviewed. The absolute performance of a CI engine relies more heavily upon the mechanics of fuel injection than does its spark-ignition counterpart. Because of this, various ways of introducing the alternative fuel have been used with success over the past century but only in the last decade has there been achieved thermal efficiencies to match that of diesel-only operation.

Chapter 3 looks more closely at the process of liquid fuel injection, atomisation and vaporisation. The way in which gaseous fuel jets mix with air in the cylinder of an engine are then examined, compared and contrasted to liquid jets. Similarities between the structure of liquid sprays and gas jets exist which, in recent times, has led to simplifications in modelling the former.

Description of the work carried-out in this project begins in Chapter 4 which details the design and construction of the laboratory rig that was built and used. A modern, high-pressure, electronically-controlled diesel injection system was purpose-built for this study. Similarly, a system to supply and control the injection of CNG was devised and made to interface with the diesel injection system.

So that the interaction between the two fuel jets could be studied, an investigation of optical and imaging systems for photographing a transparent gas jet was performed. Chapter 5 explains how different techniques were trialled to decide upon how to maximise the usefulness of results gleaned from the rig. Following a discussion of those tests, qualitative results from the analysis of discrete injection of the two fuel jets are presented. Results from the laboratory simulation of HPDI dual-fuelling are then presented in Chapter 6. Comparison is made between DF injection using several different nozzle configurations.

The implementation of the commercial CFD code *Fluent* for modelling the DF injection is described in Chapter 7. Simulation of the discrete jets (as described by the laboratory results in Chapter 5) was carried-out and results are shown here. These results allowed the numerical models to be calibrated for the laboratory conditions.

Results from numerical simulations of the DF cases tested in the laboratory are presented in Chapter 8. Simulations were then performed for HPDI operation under conditions similar to those found in an actual engine.

A summary of the findings from this project is then presented in Chapter 9. Recommendations have been made for the design of future HPDI systems.

2. Chapter Two: The Diesel Engine

The final fundamental development in reciprocating engines came with the concept of compression-ignition by Rudolf Diesel. Diesel was trained as an engineer and was one of the first people to apply a scientific approach to the design of an engine. His initial idea was to build an engine that followed as closely as possible the cycle proposed by Sadi Carnot in 1824 [139]. In 1892, Diesel was issued a patent for an engine in which the air would be compressed to such a great extent that its temperature would exceed the ignition temperature of the fuel [94].

2.1 Development of the Compression-Ignition Engine

The modern diesel engine is a product of over a century of development in the manufacture of internal combustion engines. Whilst both two-stroke and four-stoke engines exist today, the four-stoke, owing to its higher efficiency, is more popular for most engine sizes. The four-stroke cycle was originally used for SI engines although Diesel took the concept and replaced the method of fuel delivery and ignition in an effort to improve its efficiency. The result was the CI or "diesel" engine that is known today.

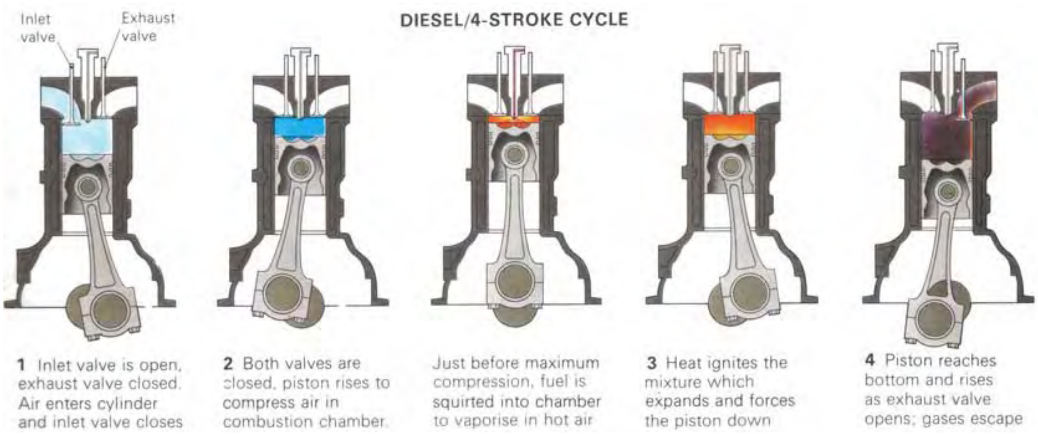

Figure 2.1. The four-stroke Diesel Cycle [119].

Late in the 19^{th} century, the Machinenfabrik Augsburg-Nürnberg (MAN) Company in Bavaria backed Rudolf Diesel financially as well as providing engineers to work with him. Their goal was to develop an engine that would burn the vast amounts of otherwise useless coal dust which, by then, had accumulated in the Ruhr valley as a by-product of industry. The first experimental engine was built in 1893 and used high-pressure air to blast the coal dust into the combustion chamber. The use of coal dust as a fuel proved too difficult to achieve, although a CI engine that used oil as fuel was successful and a number of manufacturers were licensed to build similar engines [50].

One of the major hurdles to overcome was that of how to introduce a finely-atomised spray of fuel into the cylinder's already highly-compressed air. The original oil-burning engines used very crude mechanical injection equipment so Diesel again began using air-blast methods to provide atomisation of the fuel as well as to increase the turbulence of the mixture. This proved very successful and was utilised in Diesel's third engine, built in 1895. But it required a large, complicated compressor (running at about 7 MPa) driven by the crankshaft. Because of this, CI was practical only for very large engines. l'Orange, working at Benz in 1910, developed the pre-chamber design and was able to successfully convert an "air blast" Diesel engine to run on "solid" (fuel only) injection. The dispensation of the air compressor then allowed the Diesel principle to be used on much smaller engines.

Modern diesel engines vary enormously in size and power output. Thermal efficiencies in the order of 40% are not uncommon. The one thing that these engines have in common is that fuel is introduced to the engine separately to the air and that control of the engine's speed and power output is achieved entirely by setting the fuel injection parameters. The diesel engine, unlike the SI engine, is not throttled. Its only control is the amount of fuel injected per engine cycle and the rate at which it is injected. Thus the fuel injection system itself is the most significant factor in determining how a diesel engine performs.

2.2 Operation of the Diesel Engine

2.2.1 Diesel Injection Systems

Modern diesel injectors operate at pressures above 100 MPa. This high injection pressure, coupled with the physical geometry of the injection nozzle, are the main factors in determining the rate at which fuel is delivered to the cylinder and how it subsequently burns. A detailed account of the actual physics of a diesel jet is given in the next chapter.

2.2.1.1 Conventional Systems

Since about 1930, the air-blast diesel injection system has not been widely used and has been almost entirely replaced by solid, ie. liquid-only systems [11]. For most of this time, such systems have consisted of two main components: an injection pump for the engine and a fuel “injector” for each of the engine’s cylinders. In most contemporary systems, the pump is of the “in-line” type with a piston that both pressurises the fuel to around 70 MPa and then meters the fuel for each cylinder. Fuel that is forced out of the pump is then transmitted to each cylinder’s injector through a steel line as depicted in Figure 2.2. The injector itself is an assembly that consists of a nozzle and the nozzle-holder as shown in Figure 2.3. The nozzle itself is the part of the injector that protrudes slightly into the engine’s cylinder. The nozzle-holder locates the nozzle in the cylinder head and enables connection with the line from the pump.

Modern diesel engines are usually “Direct Injection” (DI) diesels since the nozzle sprays fuel directly into the cylinder bore. In “indirect” designs, the nozzle sprays into a small “pre-ignition” chamber which connects to the bore/main chamber through a small passage. The expansion of the flame through the narrow passage helps to increase turbulence and thus mixing in the main chamber. Indirect injection is now used mostly in only very small engines or engines designed for special purposes, eg. marine auxiliaries which spend a high proportion of their time at idle. The pre-ignition chamber helps to improve mixing and thus efficiency in these applications.

2.2.1.2 Mechanical and Electronic Unit Injection (UI and EUI)

The pressures achievable by in-line pumps are sufficient to ensure atomisation of the fuel and to guarantee that no difficulty exists in forcing fuel into the combustion chamber. Higher injection pressures are, however, beneficial to the atomisation process. UIs contain their own pressure "pump" in the form of a camshaft-driven plunger and do not require transmission lines between the pump and injectors. Since there are no pressure losses through injector lines and since the strength of the lines is no longer an issue, UIs are capable of producing pressures up to 240 MPa - about double that of conventional in-line pump systems. This higher injection pressure results in higher levels of fuel atomisation and mixing within the cylinder but a major disadvantage of such systems, as shown in Figure 2.4, is the physical size of the injector.

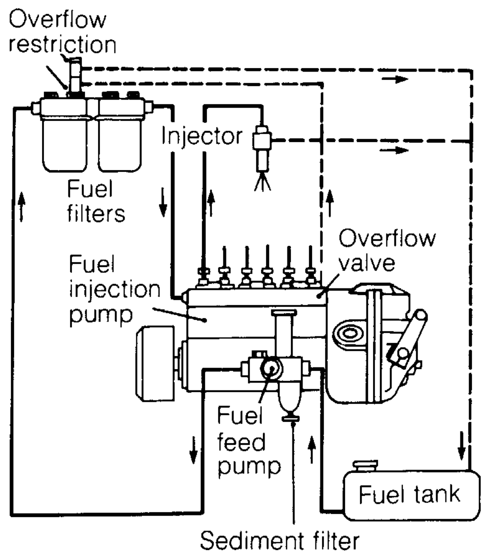

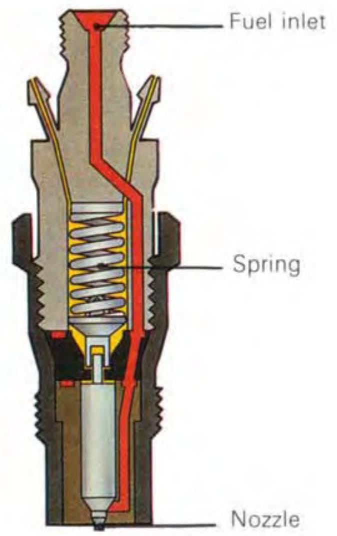

Figure 2.2 (left). **Schematic diagram of a typical in-line pump system [11].**

Figure 2.3 (right). **Cross-section of a simple nozzle and holder assembly of such a system [119].**

The EUI employs the same method of pressure generation as the mechanical unit injector but with more accurate control of the fuel delivery since the timing and duration of the injection is electronically controlled via a solenoid valve. This valve controls the amount of fuel that reaches the nozzle by opening or closing the feed or spill ports to the plunger as required.

2.2.1.3 High-Pressure Common-Rail (HPCR) Systems

As the name implies, HPCR systems have injectors that are supplied with diesel from a single accumulator/rail that holds the fuel at injection pressure using an engine-driven pump. Figure 2.5 shows how the accumulator feeds the injectors, which are in turn solenoid-controlled by a computerised engine control unit (ECU). This allows very precise control of the injection timing and quantity. The injection pressure can be 180 MPa or more, depending on the application [53]. This system was first used by Bosch in 1997 [22] and has become quite common in car-sized engines manufactured since then. Several manufacturers, including Bosch, Delphi and Denso build OEM systems for many engine manufacturers.

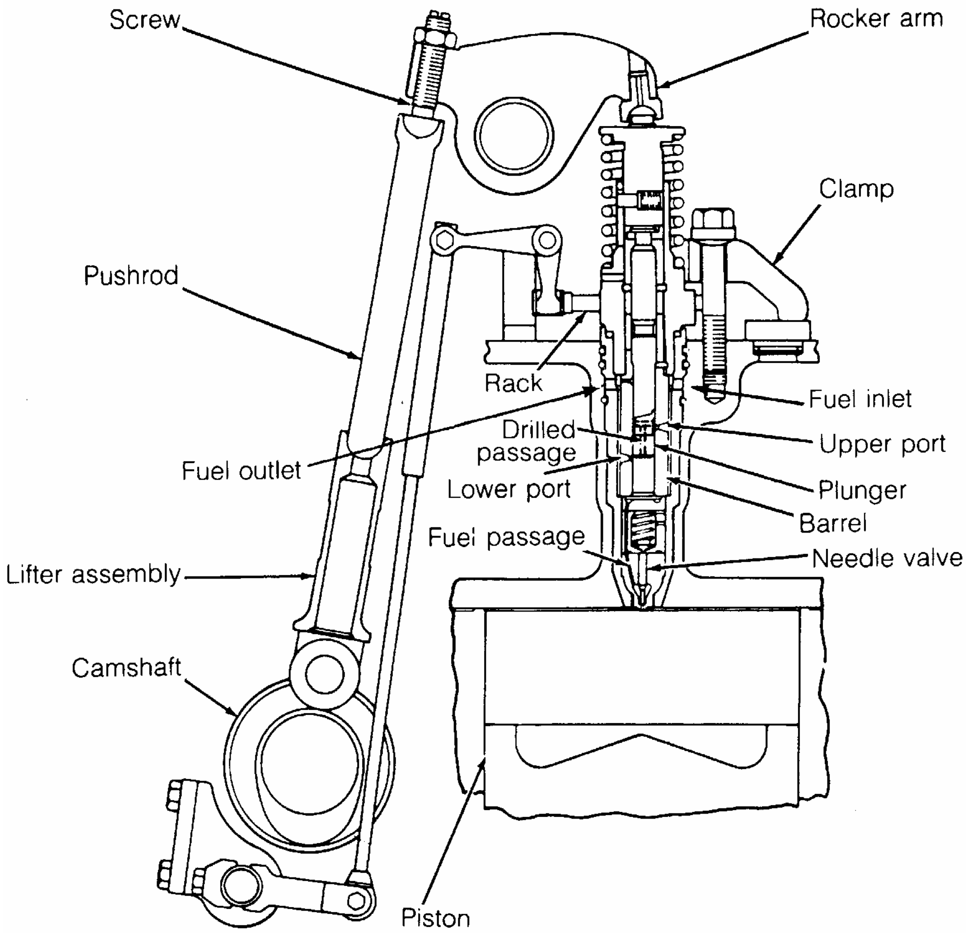

Figure 2.4. Schematic diagram of a mechanical Unit Injector [11].

2.2.1.4 Hydraulically-actuated, Electronically-controlled Unit Injection (HEUI)

The latest advance in injection technology is the HEUI system. HEUI injectors use hydraulic rather than mechanical energy to raise the pressure of the fuel to a level suitable for injection. This is achieved with a differential piston inside the unit injector. The injection timing, duration and thus quantity is solenoid-controlled as in HPCR systems. Also in common with the HPCR system, HEUI injectors are fed by a common rail. However, since the injector contains its own pressure-amplifier, the rail pressure is lower than the injection pressure. This allows the control solenoid to operate at a lower pressure than with HPCR systems. This in turn allows finer control over metering than HPCR injectors and as such has advantages for fitment to large engines where the fuel requirements and thus injection rates per cycle are high [159].

Common-rail injection system, accumulator concept
1 Fuel tank, 2 Filter, 3 Primer pump, 4 High-pressure pump, 5 Pressure-release valve, 6 Pressure sensor, 7 Fuel rail, 8 Injectors, 9 Sensors, 10 ECU.

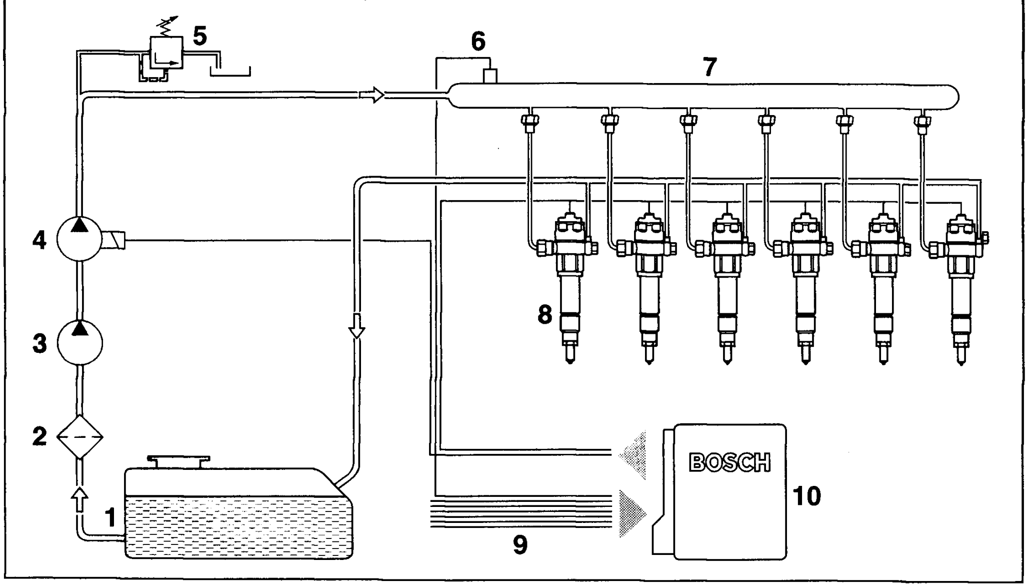

Figure 2.5. Schematic diagram of an HPCR System [21].

Caterpillar has manufactured HEUI injectors since the mid-1990s [93], these being fitted as original equipment to a number of Caterpillar and other engines such as Navistar (Ford). Pressure intensification is achieved by using the engine's lubricating oil acting on one side of a piston. The oil-side of the piston has an area ratio of 7:1

compared to the diesel-side. The pressure in the engine's oil galleries can be varied by the ECU anywhere between 500 and 3,000 psi (3.4 and 21 MPa respectively) which will create injection pressures of up to about 18,000 psi (124 MPa) [148]. A single-fluid HEUI (ie. one that uses the actual fuel for pressure intensification) is presently undergoing development in a collaborative effort between UNSW and local industry. Injection pressures beyond 250 MPa have been reached. This injector is described in Section 2.9.

2.2.2 Injector Nozzles

Irrespective of the type of injection system fitted to an engine, the injector will be fitted with a removable nozzle. The nozzle mounts to the bottom of the nozzle-holder and is the part through which fuel flows into the engine. There exists several types of nozzle but each one uses a spring-loaded needle that prevents fuel from being injected into the engine until injection pressure has been built-up in the fuel delivery/injection system. Three common types of nozzles are shown below in Figure 2.6. It is usual for different nozzles to be able to be interchanged with different nozzle-holders from the same manufacturer. This allows a common nozzle-holder to be used in several different types of engine so long as the nozzle itself is chosen correctly for flow rate and spray characteristics.

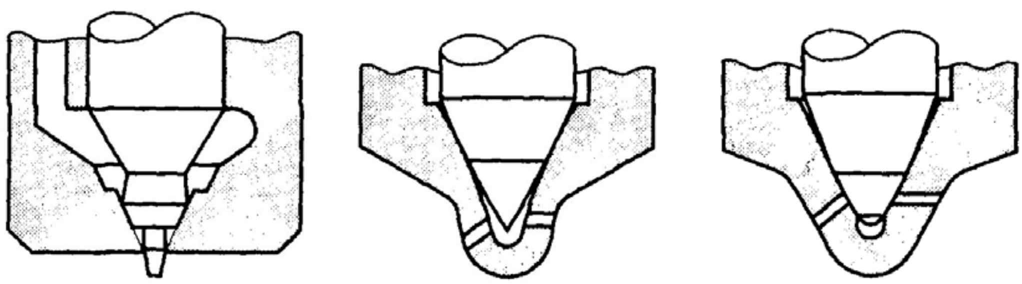

Figure 2.6. Common types of injection nozzles in use today. From the left: "pintle" type, "sac" or "mini-sac" type and Valve-Covered Orifice (VCO) type [21].

Irrespective of the type of injector, injection starts when the nozzle's needle is lifted by diesel pressure. In a conventional system, this is when the pump's piston starts its injection stroke. For a UI it is when the camshaft starts moving the plunger down. In HPCR or HEUI systems, it is when the solenoid in the injector activates and allows diesel to flow into the bottom of the injector. Typical nozzle-opening pressures are between 10 and 20 MPa. Injection continues until pressure to the needle is stopped which, in a mechanical system equates to the end of the stroke of the piston in the injection pump. In electronic systems, pressure to the needle is usually stopped by closure of a solenoid. At this point, a positive, instantaneous cut-off of the fuel occurs because the valve is snapped to its seat by the spring force. This eliminates dribbling of the fuel into the chamber and also prevents combustion gases getting back into the nozzle.

The nature of the flow across the final orifice of the diesel nozzle is the ultimate factor that dictates the effectiveness of the fuel injection system [140]. The engine's performance is directly influenced by the atomisation process in the cylinder which, for a given engine, is determined by the nozzle's spray characteristics and the flow rate. A more-finely atomised spray means that each fuel droplet has a higher surface area-to-volume ratio. Thus, the small droplet can evaporate, mix with air and burn more completely and in a shorter time than could a bigger droplet.

2.2.3 The Combustion Process

The major challenge in the design of combustion chambers for diesel engines is to achieve rapid mixing between the injected fuel and the air in the cylinder. This in turn allows complete combustion in the appropriate crank angle interval close to TDC. Since the beginning of the last century, injection pressures have gradually increased. Higher injection pressures result in a greater jet speed for a given nozzle diameter and this higher speed greatly assists with the atomisation of the spray. Similarly, higher injection pressures and velocities promote better mixing in the chamber. Achieving complete combustion in a diesel engine is perhaps more important than in a gasoline engine since incomplete combustion results not only in the emission of Carbon Monoxide (CO) but also visible soot.

Fuel is injected into the cylinder shortly before the piston reaches TDC on the compression stroke, just before the desired start of combustion. Heywood [54] defines the following four stages of combustion which are also described in Figures 2.7 from [11] and 2.8 from [54]:

1. *Ignition Delay (ab)*

This is the period between the start of fuel injection into the combustion chamber and the start of combustion. As the fuel is injected, the droplets mix with the air in the cylinder and begin to evaporate. Because the air in the cylinder is at a temperature above the fuel's ignition point, spontaneous (or "auto") ignition of some of the fuel-air mixture occurs after a delay period equating to a few crank degrees. The start of combustion can be found most easily experimentally by identifying the change in slope of the pressure/crank-angle diagram.

2. *Pre-mixed or Rapid Combustion Stage (bc)*

In this stage, combustion of the fuel which has mixed with air to within the flammability limits during the ignition delay period occurs rapidly during a few crank degrees. Since a significant amount of fuel has already been injected into the chamber, high heat-release rates are characteristic of this phase.

3. *Mixing-controlled Combustion Phase (cd)*

Once the fuel and air which pre-mixed during the ignition delay have been consumed, the burning rate (or heat-release rate) is controlled by the rate at which the mixture becomes available for burning. This is a function of the rate at which fuel is injected and then vaporises into a flammable mixture.

4. *Late Combustion Phase (de)*

Heat release continues at a lower rate well into the expansion stroke for several reasons. Firstly, a small amount of fuel may not yet have burnt. Further, of the fuel that has already burnt, a fraction of this energy may now be present in soot or other fuel-rich combustion products and can still be released. The cylinder charge is non-uniform and mixing during this period promotes more complete combustion and less-dissociated product gases. The rate of the final burn-out process becomes slower as the temperature of the cylinder gases falls during expansion.

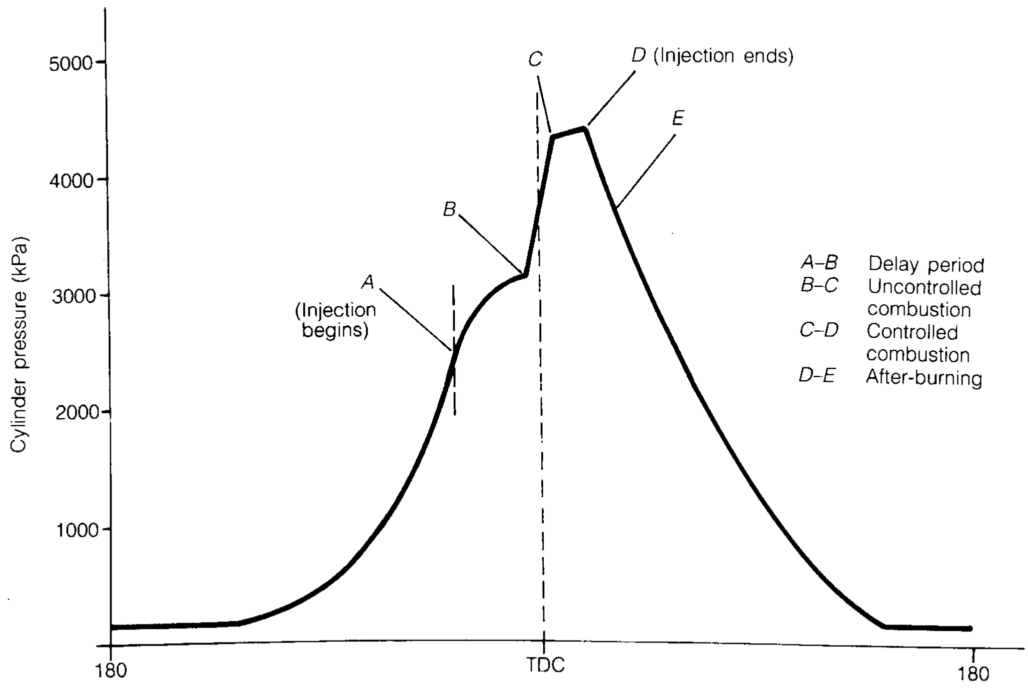

Figure 2.7. A typical pressure trace from a diesel engine showing the stages of combustion [11].

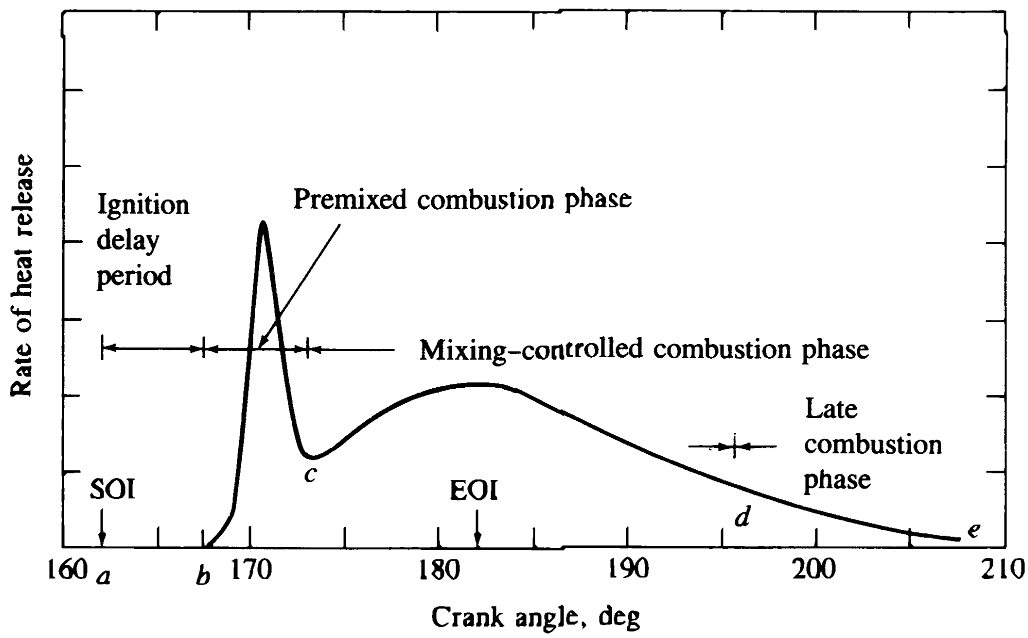

Figure 2.8. A typical heat-release rate diagram showing the stages of combustion [54].

2.3 The Ignition Process in more Detail

2.3.1 Ignition Sites

Ignition takes place after some of the injected diesel atomises, vaporises and then mixes with the hot air in the cylinder to form a combustible mixture. Studies indicate that, under normal diesel engine conditions, 70 to 95% of the injected fuel is in the vapour phase at the start of combustion [78]. However, in a typical medium-speed DI diesel engine, only 10 to 35% of the vaporised fuel has by then mixed to within flammability limits. Thus combustion is largely mixing-limited rather than evaporation-limited. Of course, under cold-starting conditions, the rate of evaporation becomes a major constraint.

Heywood [54] has described experiments in which a gaseous fuel jet was injected into swirling air flow in a rig to simulate the air-fuel mixing process in diesel engines. Plots of contours of the air/fuel ratio showed that auto-ignition occurred in a concentration band between the equivalence ratios of 1 and 1.5. Subsequent flame development occurred rapidly along mixture contours close to stoichiometric as shown in Figure 2.9. Initially, this was thought to be due to spontaneous ignition of regions close to the first ignition site. Such subsequent ignition sites would be caused by the temperature rise associated with the strong pressure wave which emanates from each ignition site due to rapid chemical energy release. But it has since been shown that spontaneous ignition at additional sites on the same spray, well separated from the original location, can occur.

2.3.2 Ignition Delay and Diesel "Knock"

The ignition delay (ID) in a diesel engine is defined as the time interval (or subtended crank angle) between the start of injection (SOI) and the start of combustion. Because the diesel engine dispenses with an externally-supplied ignition spark, the fuel must ignite spontaneously and with minimum delay when injected into the hot, compressed air in the combustion chamber [21]. If the ID is too long, most of the fuel is injected before ignition occurs. This results in very rapid burning rates once combustion starts which then causes high rates of pressure rise and high peak pressures. Under extreme conditions, when auto-ignition of most of the injected fuel occurs, this produces an audible knocking sound often referred to as “diesel knock”.

Both physical and chemical processes must take place before a significant fraction of the chemical energy of the injected liquid fuel is released. These physical processes include the atomisation of the liquid fuel jet, the vaporisation of the fuel droplets and the mixing of fuel vapour with the air. The chemical processes are the pre-combustion reactions of the air/fuel/residual gas mixture which lead to auto-ignition. These processes are affected by engine design, operating variables and fuel characteristics. For a given engine, injection system and operating point, fuel quality is then a variable factor.

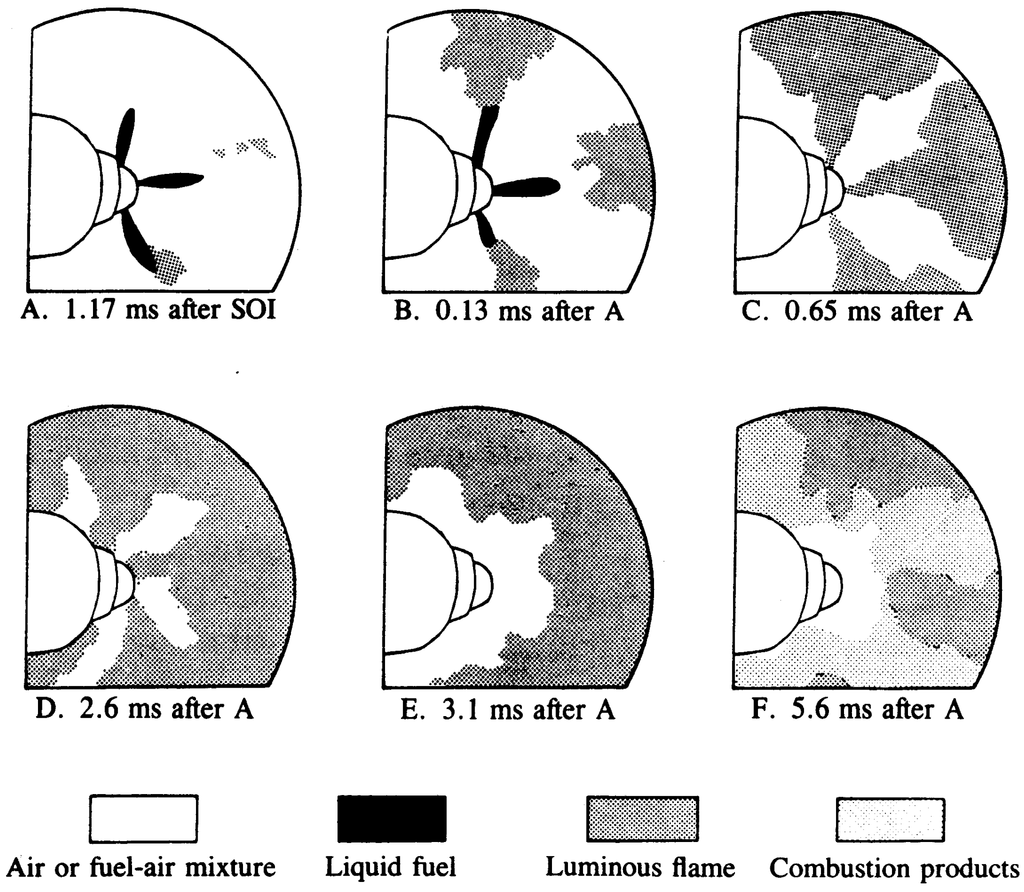

Figure 2.9. Typical flame development across the cylinder of a diesel engine [54].

Since the rate at which chemical reactions proceed affects the ignition characteristics of the fuel and thus the ignition delay, the chemical properties of the fuel are very important. They ultimately determine the engine operating characteristics such as fuel conversion efficiency, smoothness of operation, frequency of mis-fire, smoke emissions, noise and ease of starting. The ignition quality of the fuel is referred to as its "cetane number".

The cetane number (CN) expresses the fuel's ignition "quality". This may be defined as its suitability for spontaneous self-ignition, ie. the readiness with which the fuel begins to burn when injected into the cylinder of a diesel engine. The cetane number of a fuel is determined empirically using a test engine. Originally, the cetane number 100 was assigned to n-hexadecane (cetane) which ignites very easily. Slow-burning methyl-napthalene was allocated the cetane number 0. The ignition quality of the tested fuel was then given a CN relative to a mixture of these base stocks. For example, a fuel with a CN of 52 has the same ignition quality of a reference fuel made up of 52% cetane and the balance (48%) of methyl-napthalene [21]. In more recent times, owing to the difficulty of starting and operating an engine with unstable methyl-napthalene, the low-end test fuel has been replaced with the more stable heptamethyl-nonane (iso-cetane). Heptamethyl-nonane has a CN of 15 but the cetane number scale has not changed [94].

For fuels with very low cetane numbers and thus an exceptionally long ignition delay, ignition may occur sufficiently late in the expansion stroke for the burning process to be quenched. This would result in incomplete combustion, reduced power output and poor fuel conversion efficiency. For higher cetane number fuels, ignition occurs before most of the fuel is injected. The rates of heat release and pressure rise are then controlled primarily by the rate of injection and fuel-air mixing and smoother, quieter engine operation results. A cetane number in excess of 50 is desirable for smooth operation and low emissions in modern engines [21].

One of the key challenges when dual-fuelling a diesel engine is to minimise any changes to the ignition delay. This is discussed more fully later in this Chapter.

2.3.3 Correlations for Ignition Delay

2.3.3.1 Based Upon the Arrhenius Equation

In general, the length of time of the ignition delay, τ_{id}, is a function of mixture temperature, pressure, equivalence ratio and fuel properties. Many correlations have been proposed for predicting ignition delay as a function of engine and air charge variables. These are usually in the form of the Arrhenius equation and have been based on data from fundamental experiments in combustion bombs and flow reactors.

$$\tau_{id} = Ap^{-n} \exp\left(\frac{E_A}{RT}\right)$$ **Equation 2.1 [54]**

where: τ_{id} = the ignition delay

E_A = an apparent activation energy for the fuel auto-ignition process

R = The Universal Gas Constant (8,314 J/kg.K)

p = Pressure in the chamber

A and *n* are constants dependent on the fuel and, to some extent, the injection and air-flow characteristics. Representative values for the constants *A*, *n* and E_A have been found for the Arrhenius equation by various researchers using various means. Table 2.1 shows some of these values as summarised by Heywood [54].

For modern, DI diesels, the relationships developed by Hiroyasu et al, Wolfer and Stringer et al indicate ignition delay times of around 0.3, 0.4 and 0.5 ms respectively. The variation in the calculated delay times can be attributed to several factors. Most usually it is because the methods used to detect the start of combustion and hence the duration of the ID are not identical and, perhaps most significantly, the experimental apparatus and the method of air-fuel mixture preparation are different.

Table 2.1. Arrhenius Constants as Summarised by Heywood in 1988 [54].

	Conditions				Parameters		
Investigator	Apparatus	Fuel	p, atm	T, K	n	A	$E_A/\tilde{R}$, K
Spadaccini and TeVelde[43] No. 1	Steady flow	No. 2 diesel	10–30	650–900	2	2.43×10^{-9}	20,926
Spadaccini and TeVelde[43] No. 2	Steady flow	No. 2 diesel	10–30	650–900	1	4.00×10^{-10}	20,080
Stringer *et al.*[45]	Steady flow	Diesel 45–50 cetane number	30–60	770–980	0.757	0.0405	5,473
Wolfer[46]	Constant-volume bomb	Fuel with cetane number > 50	8–48	590–782	1.19	0.44	4,650
Hiroyasu *et al.*[29]	Constant-volume bomb	Kerosene	1–30	673–973	1.23	0.0276	7,280

2.3.3.2 An Empirical Relationship

An empirical formula, developed by Hardenberg and Hase [52] for predicting the duration of the ignition delay period in DI engines has been shown to give good agreement with experimental data over a wide range of engine conditions. This formula gives the ignition delay (in crank degrees) in terms of the charge temperature T (K) and pressure p (bar) during the delay (taken as TDC conditions) as:

$$\tau_{id} = \left(0.36 + 0.22\bar{S}_p\right)\exp\left\{\left[E_A\left(\frac{1}{RT} - \frac{1}{17{,}190}\right) + \left(\frac{21.2}{p - 12.4}\right)^{0.63}\right\}\right. \qquad \textbf{Equation 2.2 [115]}$$

where: $\bar{S}_p$ = Mean Piston Speed (m/s)

R = The Universal Gas Constant, 8,314 J/kg.K

E_A = (joules per mol) is the apparent activation energy $= \dfrac{618{,}840}{CN + 25}$

CN = the cetane number of the fuel.

At normal engine conditions (low to medium speed, warm engine), the minimum delay occurs when the start of injection is at about 10 to 15 degrees BTDC. The increase in delay with earlier or later injection timing occurs because the air temperature and pressure change significantly as the piston gets close to TDC. If the injection starts earlier, the initial air temperature and pressure are lower so the delay will increase. If injection starts later then the temperature and pressure are initially slightly higher but then decrease as the delay proceeds. The most favourable conditions lie in-between.

More details about ignition delay and its relevance to dual-fuelling is discussed later in this Chapter.

2.4 Optimising the Combustion Process

As emissions-reduction laws become more stringent, manufacturers must look for new ways to make the combustion process in diesel engines cleaner both from a "local emissions" point-of-view (eg. particulates and acid-rain forming gases like oxides of nitrogen, NO_x) and a "global emissions" perspective (greenhouse gases such as CO_2). Increasing injection pressures and the introduction of electronic control has meant that diesels are now almost incomparably cleaner than those of even twenty years ago but further improvements are required.

Research has shown that the formation of NO_x is dependent almost entirely on the temperature of combustion in the chamber [124]. According to the mechanisms of the oxidation of nitrogen during combustion, atoms of oxygen which dissociate at high temperatures start chain reactions of the oxidation of N_2 to NO and atomic nitrogen (N). The atomic nitrogen further combines with oxygen to produce oxides of nitrogen. Thus, if the actual rate of pressure-rise in the chamber and thus temperature can be controlled, the formation of NO_x can be greatly reduced.

For almost a century, the injection rate of in-line pump systems depended upon crankshaft position and speed and so the rate of injection and thus combustion was inflexible. With the advent of HPCR, electronic control allows the injection timing and pressure to be controlled independently of the engine's speed or position. This means that the rate of injection and hence burn can be effectively controlled using "split" or "multiple" injections. This way, the fuel is delivered into the chamber in anywhere between two and five short and discrete injections rather than in a single injection, therefore controlling the rate of mixture formation and thus burning.

Figure 2.10 shows a schematic diagram of a typical strategy for multiple-injections in a modern engine. A “pilot” injection is now usually employed to reduce the tendency for diesel knock. Combustion of the small amount of pilot diesel preceding the “main” injection means that there is little pre-mixed fuel in the chamber when ignition starts. This main injection may be then split into 2 or 3 injections so that the overall rate of heat release is controlled enough to limit the temperature in the cylinder so that NO_x is not formed. Another “post” injection is sometimes included to burn-off soot that would otherwise result in particulate emissions.

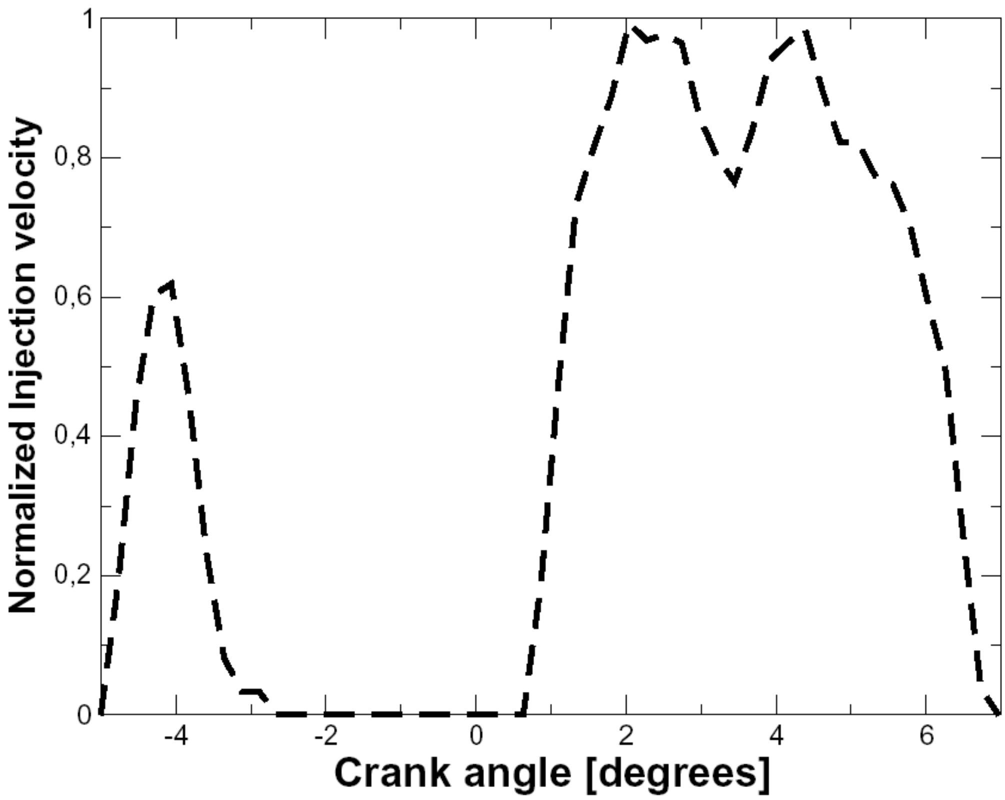

Figure 2.10. Injection-rate diagram for a pilot-injection strategy [53].

2.5 Dual-Fuelling the Diesel Engine

2.5.1 History

As described in Chapter 1, the conversion of SI engines to operate either partly or solely on LPG and more recently NG has been practiced for several decades. Yet there are several reasons why an NG engine should be based upon an existing CI engine. The most obvious is that in most large vehicles such as trucks, buses or ships, the original engine is usually a diesel. Also, since the CI engine operates at higher compression ratios than current SI engines and has no throttling, its efficiency is potentially much higher. SI engines operated on NG tend to have a short range and thus are unsuited to long-range transport, especially where NG fuelling stations are few and far between.

The operation of diesel engines on gaseous fuels is neither new nor recent. It is possible to trace its origin back to the beginning of the last century when Rudolf Diesel, as mentioned, patented a CI engine to run on coal dust and later on coal gas [1]. Subsequently, more successful commercial applications have been made, mostly for stationary applications and using the dual-fuel concept.

- The earliest operation of a dual fuel system for CI engines were experiments carried-out by Cave, Helmore and Sokes in 1929 in which Hydrogen was introduced as a secondary fuel [89]. It was stated that a 20% saving of diesel fuel was possible if Hydrogen was burned instead of diesel as the load decreased.
- By 1939, the first commercial engine fuelled with town gas or other types of gaseous fuels was produced by the National Gas and Oil Engine Co. in Great Britain. This type of engine was relatively simple in operation and was mainly employed in some areas where cheap stationary power production was required [1].
- Since the 1980s, the direct-injection of an alternative, gaseous fuel has been successfully carried-out and the efficiency of alternatively-fuelled engines has approached that of their standard, diesel-only configurations.

2.5.2 Igniting the Alternative Fuel

As described in Section 2.3, fuels manufactured for use in CI engines have a relatively high cetane number so that ignition begins shortly after the fuel enters the cylinder. For instance, diesel oil has a CN of around 50. Gaseous fuels usually have low cetane numbers and so are not suitable for CI when used alone. This is particularly true of LPG and NG which have CNs of around 10 and -10 respectively [100]. Fraser et al [41] and Naber et al [99] experimentally determined the ignition delay of methane and found that local temperatures need to be in excess of 1,200 K for ignition within 2ms. The temperature at the end of the compression stroke of even a modern, DI diesel is rarely above 1,000 K [60]. Naber et al [98] found that the effect of temperature is considerable over the temperatures most relevant to DI engine operation (900-1,300 K). The measured ignition delay in this range changes by an order of magnitude with a 20% change in charge temperature.

Since the alternative fuel cannot be ignited in the required time by CI alone, an alternative means of igniting the charge must be implemented. There presently exists three main ways in which this may be achieved:

1. Converting the engine to Spark Ignition.
2. Retaining the diesel injection system and adding the gaseous fuel to the inlet manifold (Conventional Dual Fuelling, CDF).
3. Retaining the diesel injection system and adding the gaseous fuel directly into the cylinder (High-Pressure Direct Injection, HPDI [107] or “co-injection”).

Each of these methods is discussed in more detail in the following sections.

2.6 Spark Ignition

When vehicles with existing CI engines (such as trucks or buses) are to be converted to run on NG, they are often converted to operate solely on the gaseous fuel, ie. no diesel fuel is used. This is usually achieved by substituting a spark plug for the diesel injector in the engine's cylinder head. The existing injection system is then replaced with a high-tension ignition system and the gaseous fuel is introduced through a mixer or carburettor before a throttle which is also fitted to the inlet manifold. Thus what was a diesel engine effectively becomes an SI engine. Conversion using these methods is able to be performed at relatively low cost. In more recent times, some performance improvements have been realised by the fitment of port injectors to replace the carburettor which adds a little to the cost.

There are, however, many compromises which must be accepted when converting a CI engine to SI for the consumption of NG:

- The range of the vehicle is short and it is limited to travel in regions where the infrastructure for gas refuelling exists.
- For SI to be viable, the fuel-air mixture in the cylinder must be near stoichiometric at all times to ensure that ignition occurs. This means that the engine loses one of the fundamental advantages of CI engines: the ability to operate on very lean mixtures without throttling which minimises both emissions and pumping losses.
- Typical compression ratios for SI engines operating on NG are around 12:1. Usually, a spacer must be fitted between the block and head to lower the compression ratio to prevent SI-type knock as described by White [156]. Owing to the relatively high octane number of gaseous fuels, this is sometimes not required. If it is required, it results in the loss of thermal efficiency and torque, especially at low speed, both common characteristics of CI engines.
- Studies of urban bus fleets showed that with conversion to NG operation with SI, a consumption increase of 25-30% is incurred [35]. This negates much of the improved greenhouse gas performance of engines using NG. Clearly, unless there is an abundance of cheap NG available, this consumption penalty (and thus negligible gain in emissions performance) makes SI an unattractive option for using gaseous fuels.

2.7 Conventional Dual-Fuelling (CDF)

Figure 2.11 shows a schematic layout of an engine in which NG is introduced through the inlet manifold but ignition is achieved with the injection of a small amount of diesel rather than with a spark plug. This technique, when applied to existing CI engines, is known as Conventional Dual Fuelling (CDF) [35].

2.7.1 Advantages of CDF over SI

Using the pilot diesel, local heating of the gas-air mixtures by direct contact with hot combustion products is evidently the means of gas ignition. This pilot ignition is more effective than SI since there are many individual ignition sources created, allowing for more complete and rapid combustion of the lean NG-air mixture than with a single spark plug [111]. It is also likely that much of the burning will take place within the spray zone. This minimises flame-quench problems that can occur due to excessively lean gas mixtures in the flame propagation zone when using spark ignition. Flame-quench problems with SI fumigation systems lead to high UHC and CO emissions and lowered efficiency. Minimising unburnt fuel in the end-gas also helps prevent SI-type knock that is prevalent in fumigated engines.

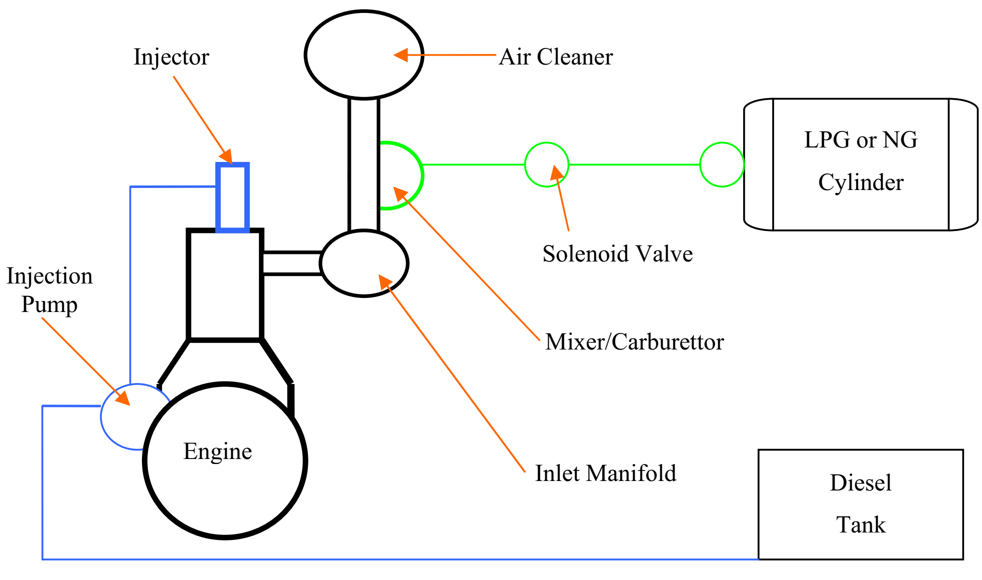

Figure 2.11. Schematic diagram of a CDF system.

Because ignition of the gas does not rely on a spark plug, near-stoichiometric mixtures at the time of ignition are not required so the engine can continue to be un-throttled. Further, CDF systems used for CI conversion allow flexible variation from NG/diesel ratios up to perhaps 90% NG through to 100% diesel operation which is important while re-fuelling infrastructure systems are being introduced.

A diesel engine is not throttled and so the mass of air per cycle is about constant, thus the mass of diesel pilot required to heat the air to auto-ignition temperature should also be constant. The optimum diesel pilot quantity is that which provides sufficient heat to the mixture for proper burning of the NG.

2.7.2 Problems Associated with CDF

The ignition delay (ID) for the diesel pilot shows a strong dependence on both the quantity and quality of pilot fuel with increasing gaseous fuel admission [51]. This increases the likelihood of diesel knock. At light load, like SI engines, CDF engines exhibit inferior fuel utilisation and power-producing efficiencies with higher UHC and CO emissions. This is again due to flame quench in the end-zone of the combustion chamber. At high loads, CDF engines exhibit an increased tendency for SI-type knock (end-gas auto-ignition) because of the higher equivalence ratio of the fuel-air mixture in the end-zone. Such limitations have tended to narrow the effective working range for CDF applications. These trends arise mainly as a result of poor flame propagation characteristics within the very lean gaseous fuel-air mixtures from the various ignition centres of the pilot.

2.7.2.1 Limited Substitution

A major disadvantage of CDF systems is that the amount of gas that can be substituted for diesel is limited by two factors:

Spark-Ignition Type Knock at High Load

Since diesel engines rely on CI, the introduction of a combustible mixture into the cylinder in a CDF conversion means that there is a high likelihood of SI-type knock occurring in the end-gas. As the proportion of gas in the inlet charge is increased, the likelihood of SI-type knock increases. Increased substitution will also usually cause an increase in the ID as described below. In extreme cases, this may lead to diesel/CI knock as described in Section 2.3.2 and it is even possible that both CI- and SI-type knock could occur during the same engine cycle.

Limitations with the Injection System at Low Load

At low load, limitations are usually encountered with the diesel injection system. Traditional in-line diesel injection systems usually have a minimum flow-rate, below which the injectors will not efficiently atomise the fuel. An injector's maximum flow rate divided by this minimum flow rate is called the "turn-down ratio" and for most in-line pump systems it is about 10 [1, 45]. Note that a typical turn-down ratio for an engine at idle is about 5 or 6, ie. the fuel used per cylinder per cycle at idle is about one-fifth that it would use at maximum power [94]. A turn-down ratio of 10 limits the minimum pilot fuel delivery to about 10% of maximum full-load delivery which, for a given power requirement from the engine, limits the amount of gas that can be utilised. Further, since these engines are not throttled, the fuel/air mixture becomes excessively lean at light loads, which leads to incomplete combustion, the loss of thermal efficiency and an increase in HC and CO emissions. To overcome this drawback, pilot fuel delivery is typically kept high which decreases total gas usage.

2.7.2.2 Ignition Delay and other Problems

Whilst the diesel pilot is retained to eliminate the ignition delay (or total lack of ignition) of the low-cetane-number gaseous fuel, the presence of the gaseous fuel almost invariably causes a delay in the ignition of the pilot itself. Ignition delay in normal diesel-only engines has been discussed in Section 2.3. In typical DI diesels, fuel is injected a few degrees before TDC into 750-1,000 K air in which it vaporises, mixes with air and auto-ignites in less than 2 ms after injection begins [96]. Many researchers have investigated the extension of ignition delay of the diesel pilot with respect to CDF engines and have attributed the following causes:

- A change in specific heat of the charge in the cylinder. Introduction of gaseous fuel into the cylinder brings about variations in the physical properties of the mixture such as the specific heat ratio and the heat transfer parameters. This can lead to significant changes in the temperature and pressure levels as TDC is approached [69]. Burn in 1977 [25] and Karim in 1980 [68] examined combustion phenomena in CDF engines fuelled with various gaseous fuels under a wide range of cold ambient temperature conditions. They found that the extent of the increase of ID was extremely sensitive to the intake temperature of the mixture.

- Dilution of the amount of oxygen in the charge. The pre-mixed air is a less favourable oxidant for the injected fuel and an extension of the diesel ignition delay may result. Nielsen et al in 1987 indicated the amount of pilot fuel and the intake temperature necessary to avoid ignition failure at part-load [1]. Later they showed that with fumigation, ignition delay of the diesel is significantly increased by the presence of NG [96]. The introduction of as little as 2% (by mass) of methane doubles the ignition delay. This was partly attributed to a change in the specific heat of the cylinder air and partly because of less oxygen being available.

- Chemical Kinetics. Karim [68] stated that none of the factors described above can alone or in combination account for the increase in ID with a relatively small addition of gas. The extension is very dependent on the type of fuel employed and is sensitive to a lowering in temperature at the end of the compression stroke. These trends suggest that chemical effects are prominent. Such effects arise from the presence of a homogeneous fuel-air mixture, albeit very lean, within and in the neighbourhood of the liquid spray. This lean mixture can undergo some chemical reactions during the relatively slow compression with the rise in temperature producing intermediate species that adversely affect the ignition reactions of the diesel. Moreover, these products can compete in the crucial regions of the pilot spray with the reactions of the diesel, bringing about a change from the trends observed in air only. The nature of these reactions is complex and uncertain.

In a study by Gunea et al in 1998 [51], it was found that the superior auto-ignition behaviour of higher cetane number diesel fuels is not inhibited by the presence of a gaseous fuel in the surrounding atmosphere within DF engines. Such fuels are not, of course, always available.

2.7.2.3 Emissions Penalties

Oxides of Nitrogen

As described in Section 2.4, the formation of NO_x has been found to be highly dependent upon combustion temperature which, in turn, shows a high dependency on the rate of burn of the charge. With CDF, the gas mixture is effectively homogeneous at the time of combustion. Thus combustion is not mixing-limited as in a diesel-only engine and the heat-release rate is higher and therefore the amount of NO_x produced is higher. The effective size of the combustion zone, which relates to the size of the pilot fuel zone, is another important factor that determines the quantity of the oxides of Nitrogen produced. On this basis and for the same total equivalence ratio, increasing the pilot fuel quantity increases the charge temperature which tends to increase the production of NO_x.

Unburned Hydrocarbons (UHC)

In fumigation, there exists the potential for some of the mixture to short-circuit directly from the inlet to the exhaust within the cylinder, allowing some UHC to escape. Reducing valve overlap would require a new camshaft and make the conversion more expensive. Also, as previously mentioned, under low-load conditions where the overall gas mixture is extremely lean, the flame may quench before reaching the end-gas. This contributes further to the emission of UHC.

With DF conversion, fumigation into the inlet manifold has been used with varying degrees of success during the past three decades although this method limits the substitution of NG due to knock, flame quench and exhaust by-pass. Better methods need to be developed.

2.8 Dual-Fuelling with High-Pressure Direct-Injection (HPDI)

Many of the disadvantages described above for fumigated engines can be overcome by injecting both the NG as well as the pilot diesel fuel into the cylinder more-or-less simultaneously. With HPDI, the NG is injected at an absolute pressure of around 20 MPa. A few degrees earlier, the diesel pilot is injected either through the same injector or another injector nearby. In this way, SI-type knock is no longer an issue and therefore compression ratios need not be limited. There is no need for throttling and the ignition delay of the diesel is not increased since the pilot is injected into air only. Beck et al [17] concluded that the direct-injection of NG with a liquid pilot has the following advantages:

- The efficiency of the diesel cycle is retained.
- SI-type knock cannot occur if the gas injection is simultaneous with the diesel.
- The engine requires no throttling.
- The cycle can operate as “lean burn” and requires no mixture ratio control.
- There will be negligible unburnt fuel in the exhaust.

With co-injection, the difficulties are in achieving the right mixing of the fuels during their limited residence time in the spray zone. Relative spray directions, nozzle locations and spray timing must be considered. The benefits are that a more uniform, mixing-controlled combustion (rather than mixing-controlled followed by flame propagation as in the fumigated systems) may be achieved. The best way to introduce both the primary and secondary fuels directly into the cylinder is through the same injector so that no complicated machining of the cylinder head needs to be performed. Such a system would then be suitable not only for new designs but also for retro-fitting to existing diesel engines.

2.8.1 Early Development of the HPDI Engine

Early work into HPDI was carried-out on very large (usually ship) engines, particularly those for LNG tankers where the boil-off gas could be used to power the ship. The reasons for this are many but likely to include the large financial savings that could be realised by using a less expensive fuel. Also, larger engines make it easier to find room to fit a gas injector as well as the original diesel injector and since cycle times are longer, controlling the injection is less logistically-difficult than on smaller, higher-speed engines.

- Einang et al in 1983 [36] used DI of methane into a 300 mm bore two-stroke single-cylinder engine. Diesel was from an unmodified injector with gas from a separate injector operating at 16 MPa. With 73% energy substitution, thermal efficiencies were slightly better than for 100% diesel operation.
- Also in 1983, the Mitsui Engineering and Ship Building Company injected gas at 25 MPa into a 420 mm bore engine. At 85% load with 5% pilot quantity, thermal efficiency matched that of full diesel operation [95].
- Wakenell et al [154] injected NG at 34 MPa into a 216 mm bore, blower-scavenged 2-stroke locomotive engine in 1987. Full rated power was achieved with 98.2% NG but a 10% economy penalty was incurred.
- Wärtsilä of Finland has since 1993 successfully implemented HPDI in larger power plants (4 MW to 30 MW). The Southwest Research Institute in the United States also tested HPDI as part of an evaluation of six alternative-fuelling techniques for locomotives during the "GasRail USA" project. HPDI was characterised as the leading solution for a low-NO_x engine that would obtain high efficiency [33].
- Nwafor and Rice [104] developed an intensifier-injector system for the HPDI fuelling of diesel engines in 1994. Using DI of the gaseous fuel in multi-cylinder installations permitted a reduction in the exhaust emissions by resorting at very light load to a reduced number of engine cylinders whilst running in the DF mode.

2.8.2 Recent Work

Only in more recent times has HPDI been realised with smaller engines. In 1992, Hodgins et al [33, 59, 60 and 107] developed an injector, based on an EUI, in which the diesel pilot and NG mix as they enter the combustion chamber through a common nozzle as shown in Figure 2.12. High-swirl mixing through a poppet valve prior to injection provided fine atomisation of the injected liquid. The injector was fitted to a single-cylinder version of the Detroit Diesel DDC-1-71 2-stroke. The bore and stroke were 108 and 127 mm respectively and the compression ratio set at 16:1. Simultaneous injection provided high efficiency at full load and matching of the 100% diesel full-load power. At part load, however, ignition delay of NG was excessive, indicating the importance of prior injection of the diesel. Flow visualisation by Ouellette and Hill [108] showed that the valve configuration needed considerable modifications to provide controllable injection and mixing. This work marked the beginning of a long relationship for the development of HPDI technology between the University of British Colombia in Vancouver and Westport Innovations Inc. Whilst several other researchers have modelled HPDI [3, 4, 45, 64, 65, 99 and 161], few have realised a working engine.

Ouellette [106] examined the diesel-pilot ignition of methane and found that an injection delay of the methane favoured the early ignition and complete combustion of both fuels. Computational results also showed that increasing the interaction between the pilot sprays and gaseous jets reduced the ID of the gaseous fuel and increased the combustion rate. From this research, the original, single-nozzle mixing injector was followed by an injector that delivered the diesel pilot and NG through different nozzles as described by Hodgins et al in 1996 [60]. With this new injector based on an EUI, the amount of pilot diesel is fixed and only when the pilot injection ends does the main (gas) injection start. A cross-sectional schematic diagram of this injector is shown in Figure 2.12.

Following the encouraging results from the 71-series engine, work began on fitment to a 6V-92TA engine. This six-cylinder engine had a bore and stroke of 123 and 127 mm respectively and displaced 9.05 L with a compression ratio of 17:1. Turbo-charging and charge-cooling yielded 224 kW at 2,100 rpm. In 1992, six-cylinder versions of the 71-

and 92-series engines powered more than 90% of the urban buses in North America [59]. The 92-series was especially popular owing to its power density but failed to meet 1991 standards for PM of 0.1 g/bhp/hr [35]. Field tests of HPDI in the 92-series engine began with one bus in 1998 at the University of California, Berkeley [33]. Independent tests of this HPDI system confirmed that diesel-cycle thermal efficiencies were retained whilst reducing emissions of NO_x by 37%, PM by 70% and CO_2 by 17% compared to diesel-only operation.

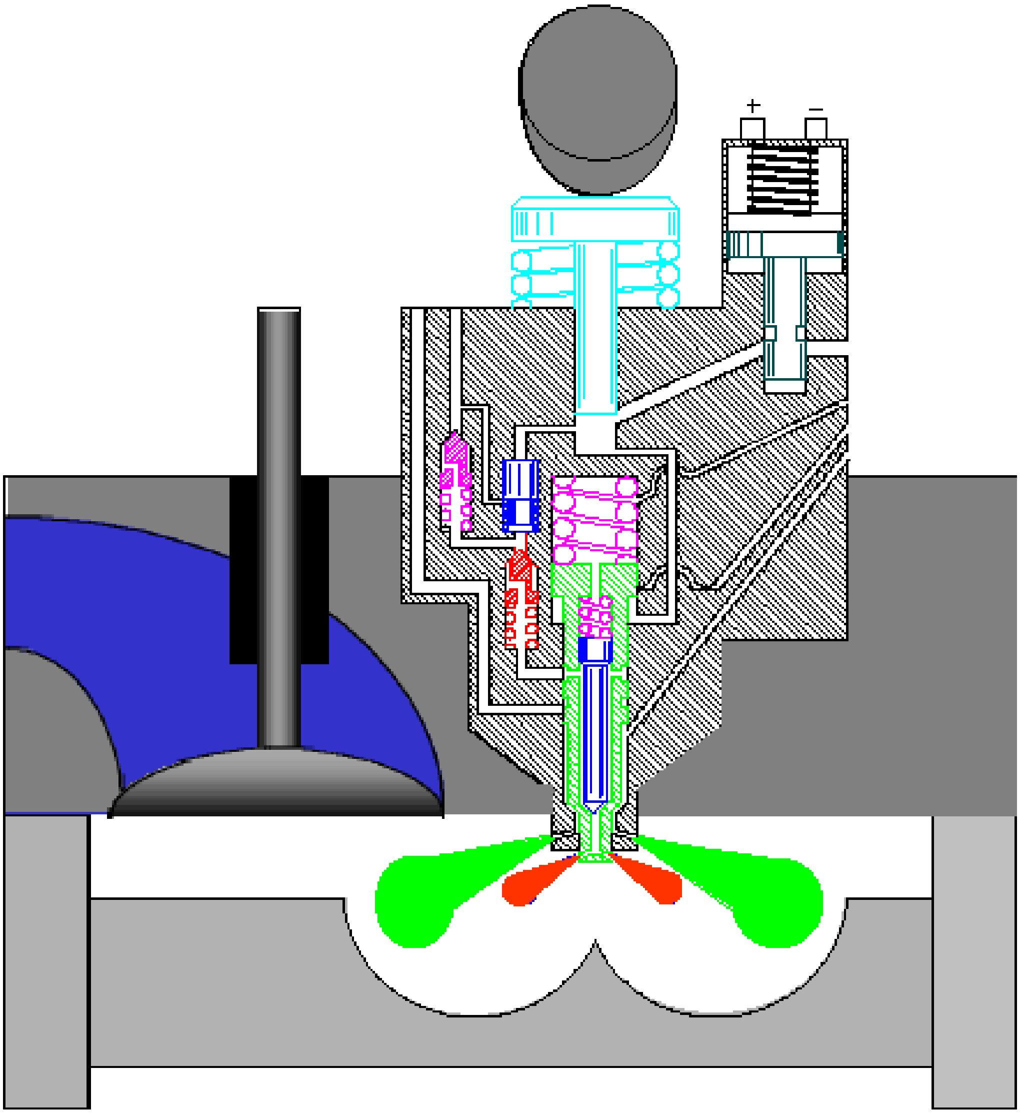

Figure 2.12. Schematic diagram of the HPDI Injector developed by Ouellette et al with Westport Innovations Inc. [107].

In September 1998, Westport announced an alliance with Cummins to incorporate HPDI using LNG into a modern 4-stroke for stationary power generation [33]. By 2002, a four-stroke, 15L Cummins ISX-400 (rated at 1,950 Nm) had been tested with the original injectors replaced with a new HPCR/HPDI system. Diesel was pumped to the rail at 25 MPa and gas was supplied to a parallel rail at the same pressure [110]. A dome-loaded regulator balanced the two pressures to minimise leakage between the fuels within the injector. Parasitic power of the LNG system was estimated to be similar to modern diesel injection systems. The performance of this engine can be summarised as follows:

- The pilot quantity remained roughly constant, independent from the load and so the percentage varied between 9 and 2.4% when the load increased from 20% to 100%.
- Torque was maintained at diesel-only levels and composite cycle efficiency was maintained within 2.3% of the diesel-only baseline.
- NO_x and PM reduced respectively to 45% and 70% of the baseline. Methane and CO emissions were low for an NG engine operating with excess air.
- CO_2 emissions were approximately 20% lower than with full-diesel operation.

Field tests were carried out using 14 trucks which were part of the 38-truck waste-transfer fleet operating in San Francisco. The trucks accumulated 837,000 km, corresponding to about 15,000 hours of operation. Only one on-road failure was reported and that was when a truck ran out of fuel. On average, each truck consumed 94% NG and 6% diesel.

More recently and in conjunction with Ford, Westport began developing an NG-fuelled CI engine for light-duty vehicles, ie. vehicles of less than 4.5 tonnes gross mass.

2.8.3 Decreased Emissions compared with Diesel-Only and CDF Operation

HPDI permits retention of the Diesel cycle, yielding high thermal efficiencies and diesel-like power and torque. With appropriate injection timing, ignition delay and combustion duration can be about the same as with 100% diesel fuelling. Fuel cannot short-circuit the valves like it can in SI and CDF engines. Fuel costs are decreased and other emissions are reduced as follows:

2.8.3.1 Reduction of Oxides of Nitrogen

A reduction of NO_x by nearly 50% at high load is achievable whilst retaining diesel-only efficiency [60]. There are several reasons for this:

- As discussed in Tao et al [145], this reduction may mostly be attributed to the flame temperature of methane being about 100 K lower than for diesel.
- Calculated heat-release rates show that the HPDI is not dominated by pre-mixed combustion to the same extent as diesel-only combustion. The peak heat release rate is lower than for pure diesel operation.
- Further reductions are realised from the enhanced mixing generated by the presence of both diesel sprays and gas jets. Such enhanced mixing has been observed in engine-based combustion visualisation of HPDI. Since NO_x forms rapidly in the high-temperature post-combustion gases, enhanced mixing brings the hot gases into contact with the cooler air earlier, reducing the time available for the NO_x to form [35].
- By controlling the delay between injections, one can effectively obtain a rate-shaped or split injection [96], the benefits of which have been described in Section 2.4.

2.8.3.2 Reduction of Particulate Matter

Studies have shown that the majority of PM is produced in the rich core of sprays [54]. Miyake et al [95] found that with HPDI, smoke was reduced by a factor of 2 or 3. NG has a lower propensity for PM partly because its carbon-to-energy ratio is about 25% lower than that of diesel. Further potential for the reduction of PM exists since NG usually contains negligible amounts of heavy hydrocarbons and sulfur. Combined reductions in soot, heavy hydrocarbons, oil and sulfates are expected to result in a 40-45% reduction in PM over diesel-only operation under the same combustion conditions.

Because it is low-sooting, NG is suitable for Exhaust Gas Recirculation (EGR) strategies and future work in this area is expected to yield significantly lower NO_x emissions [110].

2.8.4 Sensitivity to Injection Parameters

2.8.4.1 Substitution Ratio

In Hodgins et al's testing of the 71-series Detroit Diesel engine in 1992 [60], the substitution ratio was found to have a significant effect on performance. The amount of diesel required was "higher than was expected". This was attributed to the relatively low combustion temperatures in the older, naturally-aspirated test engine [59]. High-load efficiency was reduced for higher diesel ratios which was attributed to the hotter residuals causing the pilot to burn faster and thus doing more negative work on the piston (assuming the pilot is burning BTDC). With modern, turbo-charged engines with electronic timing control, such issues are not expected to affect performance.

Douville et al [35] stated that both literature and preliminary laboratory testing indicated that smooth operation of the engine can be achieved with a pilot quantity as low as 2% at high load. Gebert [45] proposed that the pilot fuel injection system should be designed to deliver the minimum possible fuel quantity. As an example, the energy contained in only one cubic millimetre of pilot fuel (about 36 J) is almost 2 orders of magnitude more than the typical electrical energy from a spark plug and more than sufficient to ignite a lean NG-air mixture.

2.8.4.2 Injection Pressure

Douville et al [35] reported that for HPDI operation, improved thermal efficiencies with increasing pilot injection pressure were found for a constant NG injection pressure. The injection pressure of the NG seems to have little effect on efficiency although load capability is enhanced at higher pressures. Higher pressures allow more fuel to enter the chamber for a fixed duration since the density of the gaseous fuel increases with pressure and the choking pressure ratio (described in Section 3.6) can be maintained until later in the cycle. Hodgins et al [59] also found that at low load, smooth engine operation was better with low injection pressures. It was postulated that small quantities injected at high pressure disperse so rapidly that the mixture is extremely lean by the end of the ignition time of the pilot fuel. This caused high cycle-to-cycle variation, large quantities of UHC and reduced efficiencies for high injection pressure/low-load conditions. To investigate the effect of ignition delay and the rate of pilot heat release, a CN = 62.2 fuel was tested. Part-load efficiencies significantly improved due to reduced ignition delay time of the pilot which resulted in increased combustion-air temperature at earlier crank angles.

2.8.4.3 Staging of the Injections

Gebert in 1996 developed a pilot diesel injection system for a CDF engine [45]. He concluded that for optimum effectiveness of the pilot ignition, the injection duration should be less than the ignition delay period so making the rate shape of the injection of little significance. Incidentally, three types of diesel injection nozzle were tested and a mini-sac nozzle was found to provide the best spray pattern. Douville et al [35] stated in 1998 that interaction between the pilot and NG plumes is a critical element in the combustion process and is well-suited to a computational study.

2.8.5 Work Conducted at UNSW

Several researchers investigated CDF technology in the 1990s with the focus turning to HPDI only recently.

- Mbarawa in 1998 [90] investigated the effect of varying the injection pressure of the diesel pilot into a cylinder containing pre-mixed CNG and air. A specially-designed combustion bomb was used to calibrate a numerical code. Laboratory work and simulation revealed that higher diesel injection pressures resulted in much more efficient combustion of the mixture.

- Miao in 2001 [91] furthered this work to include variable volume combustion such as that found in an engine. Her PhD thesis was entitled “Fundamental Studies of Combustion Phenomena in Dual-Fuel Engines”.
- With regard to HPDI, the only work so far has been Kloeckner’s Masters Thesis of 2000 [74]. Kloeckner performed an “Analysis of a Preliminary Design of a Hydraulically-Actuated Natural Gas Injector”. In this thesis, actual design parameters were suggested as a starting point in the construction of an experimental DF injector based around the HEUI (as mentioned in Section 2.2.1 and described below) that was under development within the School. Based on the required energy per cycle under diesel-only operation, the mass of gas required for a given percentage of energy substitution was calculated. More information about Kloeckner’s proposed HPDI injector is given in Appendix B.

2.9 Selecting a Diesel Injection System to be used as the Basis for an HPDI Dual-Fuel System

As described in Section 2.7, conventional diesel injectors are usually not suitable for very low flow rates and thus for use in HPDI applications owing to their low turn-down ratios. Douville, Ouellette et al [35], working with Westport Innovations Inc. in British Columbia have used UIs and EUIs with success and have recently adapted a modern HPCR injector with a high turn-down ratio as the platform for an HPDI injector [110].

For larger engines, HEUI injectors are suitable since they are capable of higher injection pressures which aid with spray penetration and mixing in large chambers. Also, since the solenoid control valve is subjected to a much lower fluid pressure than in an HPCR, fine control of the injection is possible even at the high delivery quantities required in larger engines. As described in Section 2.2, Caterpillar has manufactured HEUI injectors since the mid-1990s [93], these being fitted as original equipment to a number of Caterpillar and other engines. Yet such an injector is not suitable for use as the platform for retro-fitting HPDI since it can only be fitted to new engines that are purposely-designed to receive it.

Within the School, a new single-fluid HEUI has been undergoing development since the mid-1990s. Yudanov [159] tested this HEUI in an engine to an injection pressure of 230 MPa with only 25 MPa supplied to the accumulator. A particular benefit for DF applications is that it also exhibits a very high turn-down ratio, being able to deliver less than 1% of the maximum delivery whilst maintaining high injection pressure. Figure 2.13 describes how this HEUI uses diesel fuel as the driver for the amplification instead of an alternative oil supply. The injection and fuel systems are neither mechanically complicated nor difficult to control. Contamination of the fuel with engine oil or of the engine oil with diesel is unlikely to occur. This HEUI is also more compact in size than the Caterpillar unit which makes it potentially possible to retrofit the injector to existing engines with minimal modification.

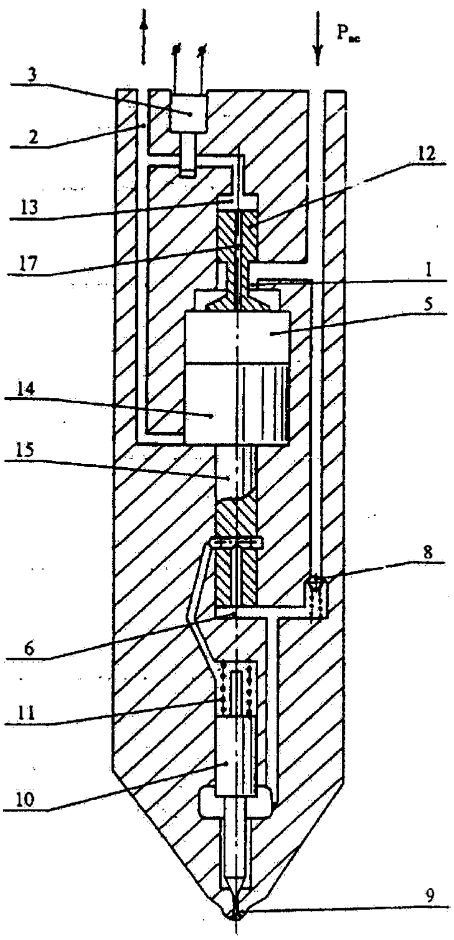

1.	Inlet port
2.	Spill port
3.	Solenoid Valve
5.	Working chamber
6.	Compression chamber
8.	Check valve
9.	Nozzle
10.	Nozzle needle
11.	Nozzle needle spring
12.	Hydraulic Differential Valve (HDV)
13.	Control chamber
14.	Piston
15.	Plunger
17.	Throttling Hole
P_{ac}	Fuel pressure from the accumulator

Figure 2.13. Schematic diagram of the HEUI developed within the School by Yudanov [159].

2.10 Beyond HPDI

Westport Innovations Inc. is now also working on NG engines which use glow-plugs for ignition rather than pilot diesel. This application is destined for engines with a swept volume of less than 5 L [110]. Such a system would have the benefit of requiring only one fuel for operation and emissions of CO_2 should be lower since no diesel is burnt.

But the ignition of several discrete jets with one or two glow plugs requires that a considerable amount of mixing takes place before combustion. This yields a longer ignition delay and a larger pre-mixed burning phase. Increased pre-mixed combustion usually yields higher NO_x and noise levels. It also limits the potential optimisation of injection timing for reducing NO_x [35]. Operation of glow plugs at temperatures in the range of 1,300 to 1,470 K has been required to achieve short ignition delays and, at these temperatures, reliability of the plugs is an issue with early tests showing an average life of only 100 hours. It has been observed that ignition delay can be controlled to between 0.7 and 1.7 ms depending on engine load, air/fuel ratio and EGR level. Special shields around the glow plug are employed to limit cooling due to the intake air and CNG jet flow fields.

Much work still needs to be done before this glow-plug technology can be commercialised. In the near future, HPDI remains the most effective way to operate CI engines with natural gas.

3. Chapter Three: Fuel Jets

In this project, the interaction of two different fuel jets was studied immediately after injection into the cylinder of an engine. Whilst the gas jet undergoes no phase change during injection, the behaviour of the diesel spray is complex. During and after injection of the fuel from the injector nozzle, the jet of liquid atomises into droplets and then vaporises.

3.1 Liquid Fuel Jets

Liquid jets have been the focus of many researchers now for more than a century. The development of diesel and gas-turbine engines has meant that fuel jets have received much of this attention. Whilst a diesel injector creates a particular kind of jet, the understanding of such jets builds upon fundamental studies of liquid jets in general.

- Plateau, in 1873 [113], proposed that to achieve a state of minimum surface energy, a round jet of diameter D must break into equal segments whose length must be about 4.5D.
- Rayleigh, in 1878 [118], carried out a temporal, inviscid stability analysis of a liquid cylinder flowing with a uniform velocity. He demonstrated that break-up results from a hydrodynamic instability caused by surface tension and occurs at a relatively low jet Reynolds Number, *Re* [81]. Rayleigh's results hold for liquid jets at low velocity where capillary effects and the effects of the external air stream can be neglected. At higher velocities, such as those found in atomising sprays, the coupling of the jet with the surrounding air must be considered [46].
- The first step in this direction was taken by Weber in 1931 [155], who extended Rayleigh's analysis and showed that the liquid viscosity has a stabilising effect that lowers the break-up rate and increases the size of the observed droplets [81].

3.2 Diesel Fuel Jets

3.2.1 Flow through a Diesel Injection Nozzle

Since the time of Weber and as particular applications for liquid jets have become more specialised (eg. diesel injection), work has tended to focus more on particular types of jets. The current work deals with "hole"-type nozzles as discussed in Section 2.2.2. Such nozzles, including those of the sac and VCO types, have been the industry-standard for some time [140]. In each case, the actual orifice consists of a plain hole with a diameter of less than 1 mm and a length/diameter ratio of about 4 [116, 130, 131 and 132].

Under appropriate conditions, the spray from the circular orifice into initially stagnant gas contains droplets of a size much smaller than the nozzle exit diameter. Divergence of the jet begins at the nozzle exit and this type of break-up is called "atomisation". Atomisation is influenced by factors including nozzle and cylinder geometry, thermodynamic properties of the fuel, behaviour of injection system and, most importantly, the aerodynamic liquid-gas interaction [43]. Theories about the controlling processes for low-speed jets have been well developed. In contrast and in spite of the importance of atomisation in its applications, it is still not well understood. Research of note includes the following:

- DeJuhasz in 1931 [31] proposed that the jet break-up process occurs within the nozzle itself and that liquid turbulence may play an important part.
- Castleman in 1932 [27] postulated that atomisation is due to aerodynamic effects between the liquid and gas leading to unstable wave growth on the liquid jet's surface. Other mechanisms based on liquid turbulence were proposed by Holroyd in 1933 and Sitkei in 1959 (both reported in [121]).
- Liquid supply-pressure oscillations were noted by Giffen and Muraszew in 1953 [49] to have an effect on the outcome of the atomisation process. Since these oscillations are commonly found in injection systems, it was suggested that they play an essential role in the atomisation mechanism itself.

- Ranz in 1958 [117] suggested that changes in nozzle design could supply different initial disturbance levels to the flow which could be one of the important mechanisms of atomisation.
- In the following year, Bergwerk [19] tested diesel injection nozzles. He observed the nozzle hole to be filled with liquid except for a separation cavity that appeared the upstream corner. Increasing the pressure caused the cavities to extend throughout the hole, increasing the ruffles of the spray and ultimately causing a sudden transition in the appearance of the jet from ruffled to smooth and glass-like. This also corresponded with a change in the co-efficient of discharge of the nozzle. He concluded that liquid cavitation phenomena inside the nozzle could create large-amplitude pressure disturbances which then lead to atomisation in the flow. In separate work, also in 1959, Sadek [128] hypothesised that cavitation bubbles may influence the jet break-up process.
- Shkadov in 1970 investigated the effect of changes in the interface tangential stresses in a boundary layer stability analysis and confirmed the existence of unstable short-wavelength surface waves [121].
- Various mechanisms of atomisation were proposed by Reitz and Bracco in 1980 but they concluded that none of these taken alone could explain their experimental results [116].
- More recently, techniques have become available to see the flow inside the nozzle, ie. the “flow regime”. This has led to new insights into what causes the initial break-up of the spray. It has been shown that the nozzle geometry has a strong effect on the characteristics of the exit flow and the subsequent spray behaviour [8].
- It is now generally accepted that break-up of the jet is mainly caused by a combination of nozzle and aerodynamic effects as described in Section 3.4.

3.2.2 Flow Regimes

3.2.2.1 Single-Phase Flow

Figure 3.1 shows a schematic diagram of the cross-section of a hole-type diesel nozzle, with diesel flowing through as a single, liquid phase. Single-phase flow through a nozzle exists at low injection pressures and flow rates.

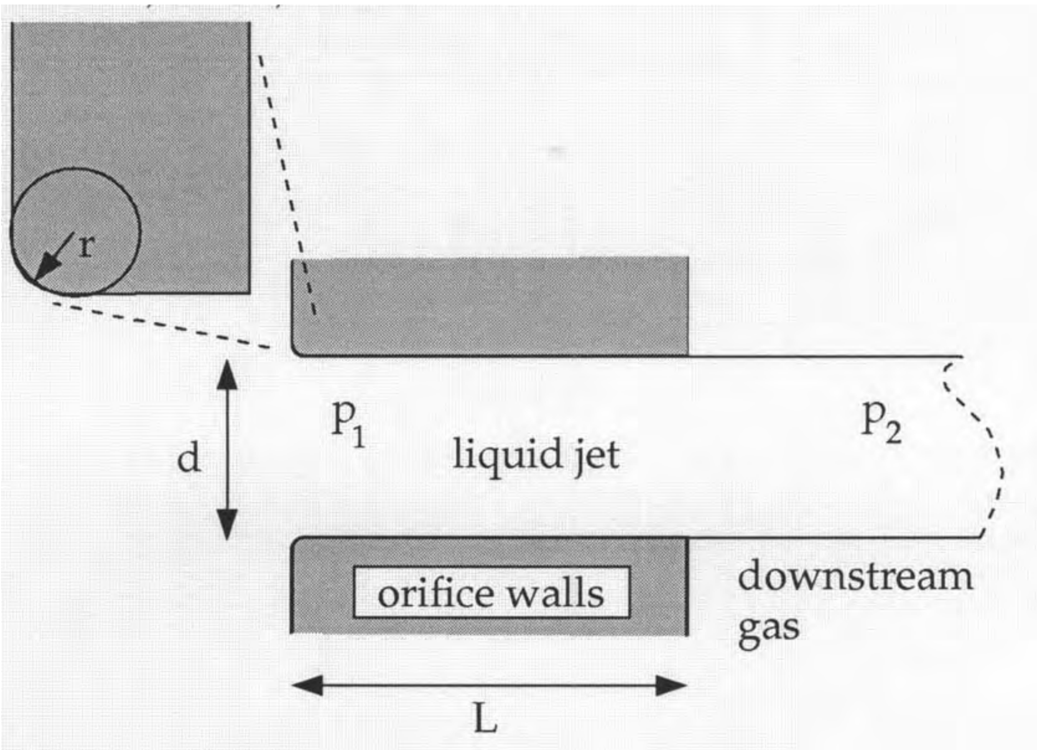

Figure 3.1. Schematic diagram of the cross-section of a hole in the nozzle from a diesel injector [39].

3.2.2.2 The Onset of Cavitation

As the flow rate increases, the diesel is forced around the corners of the inlet to the nozzle hole at increasing speed. Cavitation bubbles form because of the very low static pressure that occurs in high-speed nozzle flow near a sharp inlet corner [132]. The low static pressure is predicted by incompressible potential flow theory, which indicates that flow around a sharp corner (eg. a corner with a zero radius of curvature) will have infinite negative pressure. This physically impossible result is a direct consequence of the restriction of constant density. In real nozzles, the density decreases with decreasing pressure, most likely leading to a change in phase. The sharper the corner and the higher the velocity, the more likely cavitation is to occur. The cavity formation has been found to be a function of the cavitation number, N_c:

$$N_c = \frac{(P_1 - P_2)}{P_2}$$ **Equation 3.1 [140]**

P_1 and P_2 are the pressures at the nozzle entrance and exit respectively. The intensity of cavitation increases with cavitation number. It can be seen that even with high flow rates and therefore large pressure drops, cavitation can be suppressed if the downstream pressure is significantly high. One use of cavitation number is to determine when cavitation occurs for a given orifice geometry and size. During normal operation of a diesel injector, cavitation number can be expected to be between 0.5 and 5.0. The co-efficient of discharge, C_d, of an injection nozzle varies with the level of cavitation and is independent of *Re*. The curve in Figure 3.2 is typical for an orifice. The whole curve will shift left, right, up or down for different geometry or size but the trend remains the same. At low values of cavitation number, the C_d is mostly constant. As the cavitation number increases to a value in the region of 0.5 to 5, the C_d begins to decrease.

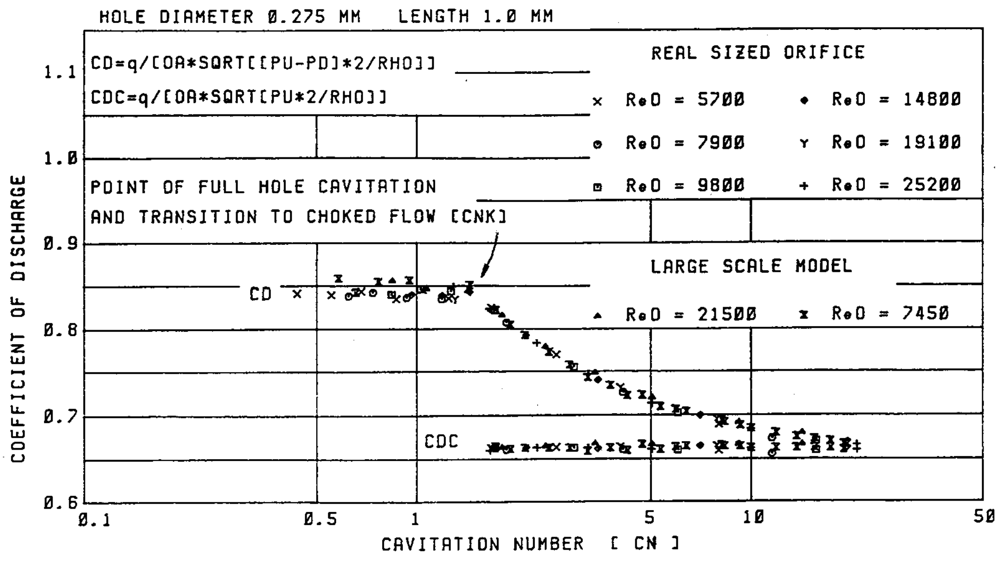

Figure 3.2. Effect of cavitation on co-efficient of discharge for a typical nozzle [140].

3.2.2.3 Development of Cavitation and the Onset of Hydraulic Flip

Once cavitation begins, there is a small divergence of the jet at the exit of the orifice and the spray takes on a slightly more bushy appearance. A further slight increase in cavitation number sees the main cavitating region spreading down the length of the hole. As this cavitation approaches the end of the hole as depicted in Figure 3.3, there is a significant increase in spray angle, the spray is bushy and is still atomising at the exit from the hole. If pressure increases further still, the cavitation disappears and the flow emerges as a smooth column of liquid fuel of smaller diameter than the orifice as represented in Figure 3.4. Clearly, atomisation is impaired. This phenomenon was described by Bergwerk in 1959 [19] and constricted jets have since been noted by a number of other researchers into diesel and other sprays. The phenomenon has also been observed in rocket injectors where it has been referred to as "hydraulic flip", HF [140].

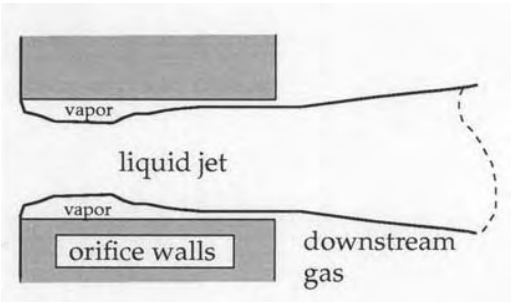

Figure 3.3. Schematic diagram of a cavitating nozzle [39].

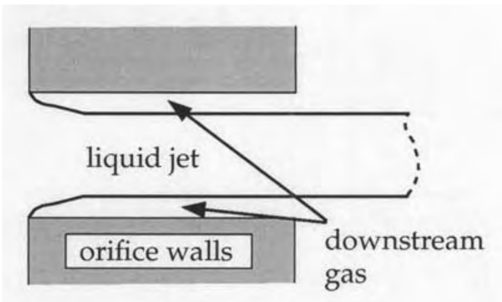

Figure 3.4. Schematic diagram of a nozzle that has proceeded to Hydraulic Flip [39].

3.3 Cavitation

Cavitation with respect to the flow inside an injection nozzle occurs under the same circumstances as cavitation in general engineering flows. When the local ambient pressure at a point in the liquid falls below the liquid's vapour pressure at the local ambient temperature, the liquid can undergo a phase change, creating empty voids termed cavitation bubbles. As previously mentioned, Bergwerk [19] was the first to publish work on cavitation in diesel nozzles. Following the publication, however, there was some confusion regarding cavitation and hydraulic flip. In some instances, cavitation and HF were regarded as the same thing and hence it was recommended that cavitation be avoided. Since that time, much work has been done with regard to studying this phenomenon. Researchers have used a combination of real size and large scale models of nozzles and orifices in order to study cavitation and its effects. Cavitation has been identified as a major contributing factor to the atomisation of a diesel jet and the main reason for primary break-up [14]. Notable work on cavitation includes:

- Nurick in 1976 [103] provided a model of cavitating nozzle mass flow and validated it with measurements in relatively large, low-speed flows.
- Reitz et al in 1982 [121] proposed that among other factors such as turbulence, surface instability, etc. which contribute to the aerodynamic break-up, cavitation phenomena are a dominant factor which complement the aerodynamic effects.
- Hiroyasu et al in 1991 observed that jet break-up length was shortened due to cavitation which was fixed at the nozzle entrance. When the vapour cavity at the hole walls was too strong to be disrupted at the nozzle (ie. when HF was occurring), the break-up length increased which resulted in a non-atomising, smooth jet [43 and 56]. They took photos of low-speed, cavitating nozzle flow and observed a very significant connection between the nozzle flow and the downstream spray.
- Soteriou et al in 1999 [141] studied flow structure in scaled-up nozzles using a laser light sheet. They showed that cavitating nozzles could be scaled for mass flow rate measurements so long as the cavitation parameter was controlled. They then studied the effects of cavitation and hydraulic flip on atomisation and concluded that cavitation was the predominant mechanism causing atomisation [72].
- Arcoumanis and Gavaises in 1999 [8] used a transparent, six-hole, large nozzle by matching *Re* and cavitation number to real nozzles. Their investigation revealed two types of cavitation: that originating in the entrance to the hole and cavitation strings developing in the sac volume. The strings linked adjacent holes and interacted with the pre-existing cavitation to result in chaotic discharge variations. An extension of this work with real nozzles was reported in 2000.

The work of Soteriou et al in the last decade [140, 141 and 142] has provided much of the information leading to the fundamental understanding of cavitation. Their work shows that cavitation in the nozzle hole causes atomisation of the jet immediately upon exit and is entirely beneficial. This cavitation process produces homogeneous foam rather than large voids as shown in Figure 3.5. Their work also demonstrates, however, that HF must be avoided. They believe that HF occurs because once the foam-filled, separated boundary layer reaches the end of the orifice, gas from the downstream chamber is drawn up the sides of the orifice into the region of recirculation. The cavitation disappears and the jet consists entirely of liquid fuel and is laminar in appearance. As a result, the break-up length is dramatically increased and atomisation inhibited. Once HF has occurred, a further increase in cavitation number does not produce any change in the appearance of the jet.

Testing was performed with scaled-up models consisting of two types of nozzles. Firstly, model nozzles with simple holes and a large reservoir on the upstream side were evaluated. Then, model mini-sac nozzles with the presence of a needle in the upstream area were compared to the first nozzles. Whilst cavitation proceeded to HF in the simple nozzles, the sac-type models did not. This difference was attributed to the effect of the upstream flow path geometry on the nature of the boundary layer within the holes and on the levels of turbulence in the flow. Hence the turbulence inside the hole was greater when the diesel had to flow around the needle to get to the holes compared with the simple-geometry nozzle. This encouraged re-attachment of the boundary layer before the exit from the hole.

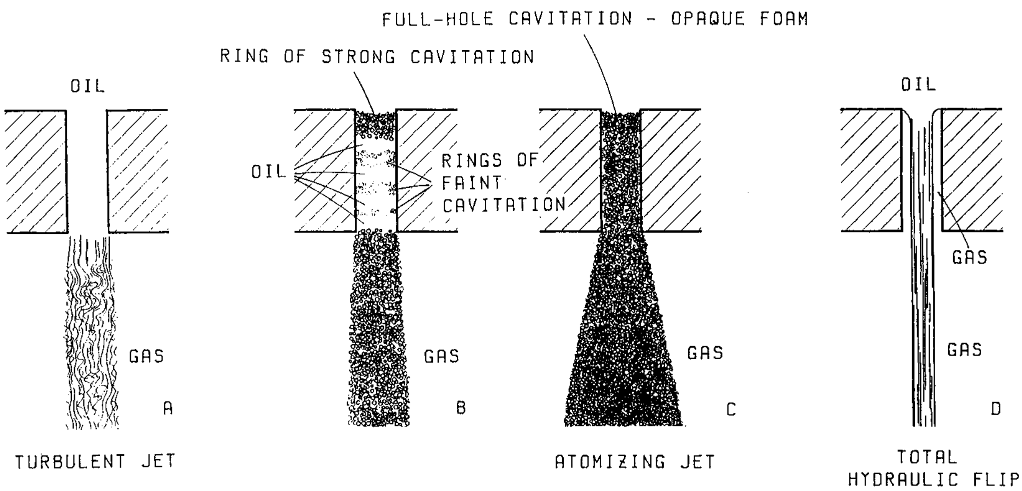

Figure 3.5. Representation of the three different flow regimes as tested by Soteriou et al [140].

3.4 Modelling Liquid Jet Break-up

Since the realisation that effects inside the nozzle as well as aerodynamic effects play a large part in the atomisation of the jet, the spray formation process has been divided into primary and secondary break-up.

- The primary break-up is the first disintegration of the coherent liquid into ligaments and drops [84]. In a diesel injector, primary break-up is now acknowledged to be mostly a result of cavitation.
- The secondary break-up is the disintegration of already existing droplets into smaller ones because of aerodynamic forces that are induced by the relative velocity between droplets and the surrounding gas. The aerodynamic forces make surface waves grow which are then split off to generate smaller droplets.

3.4.1 Modelling Primary Break-up

Serious work began on the numerical simulation of jet break-up in the 1980s. Before cavitation was realised to be such a significant contributing factor, the break-up of a jet issuing from a nozzle was believed to be primarily a result of the interaction between the high-speed liquid jet and the relatively stagnant air in the cylinder. Indeed, such an analysis still holds for a jet issuing from a nozzle that is not cavitating.

3.4.1.1 The "Blob" Model

Reitz and Diwakar in 1987 [120] developed a model for use with full-cone diesel sprays and its use in the ensuing years became wide-spread. Their method was based on the assumption that drop break-up and atomisation within the dense spray near the nozzle exit are indistinguishable processes. Thus their detailed simulation can be replaced by the injection of spherical droplets or "blobs" with uniform size which are then subject to secondary, aerodynamic break-up as in Figure 3.6. The diameter of these drops equals the nozzle-hole diameter, *D*. Whilst the fuel is not really injected as blobs, this modelling approach has proven to be very successful in distributing the spray and achieving the correct ignition and combustion characteristics. The blobs also provide a foundation for the aerodynamic growth of surface waves which characterises secondary break-up. In those days of relatively low computational power, the blob model was convenient since it avoided the need to resolve the dense spray/liquid interface at the injector nozzle exit.

Until very recent times, this model remained popular as a basis upon which other work has been built. In a study in 1995, [124] Reitz and Rutland used the Blob model for primary break-up in conjunction with the “Wave” model (as described below) for secondary break-up. The Blob model was then reviewed and used in the work of Dan in 1997 [30], Hong et al in 2000 [61] and as recently as Lettmann in 2004 [84].

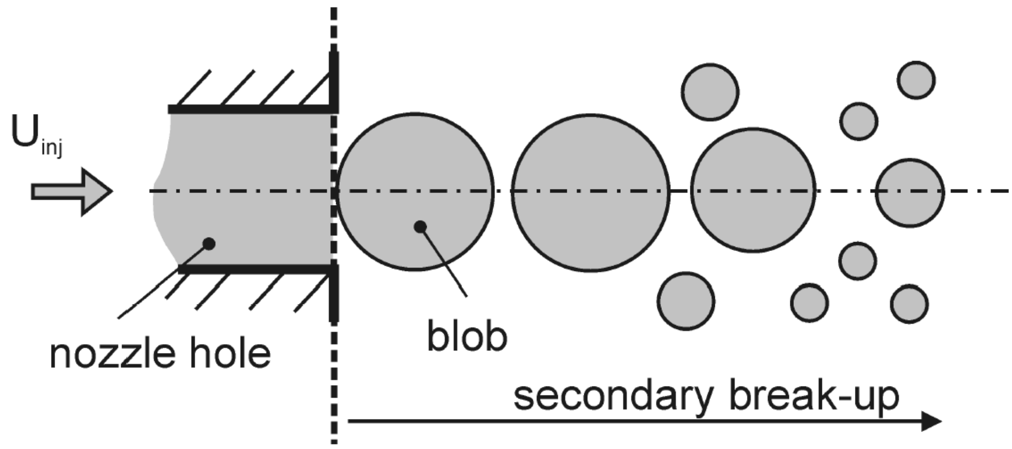

Figure 3.6. Diagrammatic representation of the “Blob Model” [84].

3.4.1.2 Models that consider Nozzle-geometry Effects in Estimating the Intensity of Cavitation

Since the inception of the Blob model, the realisation that nozzle effects (ie. cavitation) play such a large role in the break-up process has led to models that place a greater emphasis on this. Such models have been referred to as “nozzle flow” models [75]. These models assume that break-up is controlled by a characteristic turbulence timescale (usually obtained from the k-ε model as described in Appendix H) applied to the nozzle flow. Initial drop sizes are then related to the turbulent length scales.

Huh et al in 1991 [62] and Arcoumanis et al in 1997 [9] developed models that ascribe liquid break-up to nozzle flow turbulence [75]. Arcoumanis and Gavaises in 1998 [8] introduced a comprehensive hybrid break-up model that accounts for cavitation-induced break-up based upon cavitation collapse time in the liquid jet. They used a separate model for secondary break-up.

Sarre, Kong and Reitz in 1999 proposed a model capable of determining the spray initial conditions such as C_d, velocity, initial droplet diameter and cone angle by taking account of the nozzle inlet conditions, cavitation, injection flow rate and chamber conditions. The model was classified in two regimes, ie. turbulent flow and cavitation [75]. Indeed, the work of Reitz et al at the Engine Research Center, University of Wisconsin, Madison has been pivotal in the advancement of the modelling of primary break-up since their first model in 1987.

Nishimura et al in 2000 [102] developed a cavitation model to be used with the CFD package *KIVA-3* [6]. This model tracks bubble dynamics inside the nozzle and transfers the bubble-collapse energy to turbulent kinetic energy. Upon leaving the nozzle hole, bubble dynamics are tracked within the liquid core where the cavitation bubble-collapse energy is used to induce additional break-up force. The Taylor-Analogy Break-up (TAB) model, as described later, was used for secondary break-up.

The application of both primary and secondary break-up models to the numerical work that was carried-out as part of the present project is detailed in Section 7.3.1.

3.4.2 Modelling Secondary (Droplet) Break-up

3.4.2.1 Instability Analysis

Interaction between the jet and air leads to instabilities on the surface of the jet. The culmination of about a century of work into the analysis of liquid jets has led to the identification of two main types of such perturbation of the jet. These instabilities are usually the result of either Rayleigh-Taylor (RT) or Kelvin-Helmholtz (KH) perturbation.

The Rayleigh-Taylor (RT) Instability is a type of fluid instability that occurs any time a dense, heavy fluid is being accelerated relatively by light fluid. Any perturbation along the interface between the two fluids will grow and the growth rate of the instability and the rate of mixing between the two fluids depends on their relative kinematic viscosity [39]. A consequence is that for a liquid droplet decelerated by drag forces in a gas phase, instabilities may grow at the trailing edge of the droplet as in Figure 3.7 [84]. This is particularly relevant to a jet of small diameter and low *Re* (about 100) discharging into a stagnant gas [81]. The phenomenon was first discovered by Lord Rayleigh in the 1880s. It was later applied to all accelerated fluids by Sir Geoffrey Taylor in 1950 who investigated the stability of the interface between two fluids of different densities in cases of an acceleration (or deceleration) normal to this interface [84].

The Kelvin-Helmholtz (KH) Instability occurs when velocity shear is present within a continuous fluid or when there is sufficient velocity difference across the interface between two fluids. This instability is characterised by waves that appear between two superimposed fluids of differing densities and velocities. A familiar example is the ripples that form when wind flows over a pool of water: tiny dimples in the smooth surface will quickly be amplified to small waves and ultimately white-caps. It is named after Helmholtz who, in 1868, studied the dynamics of two fluids of different densities when a small disturbance such as a wave is introduced at the boundary connecting the fluids. Lord Kelvin furthered the studies in 1871 [84].

3.4.2.2 Jet Break-up Regimes

An investigation of the effect of surface tension and viscosity on the RT instability was conducted by Bellman and Pennington in 1954 (reported in [143]). Then, study of the KH instability of a stationary, round liquid jet injected into an "incompressible gas" (*sic*) by Reitz and Bracco in 1992 [121] has led to a unified approach to the classification of the jet break-up process with respect to the relative liquid/gas velocity. This analysis of the KH instability led to a general dispersion relation between the wavelength of the disturbance and its frequency, from which different jet break-up regimes were deduced. Note that the specific effects of cavitation were not considered at this time. The classification is with respect to increasing relative liquid-gas velocities where the different jet break-up regimes are characterised by the appropriate dominating break-up forces. Four regimes were identified: Rayleigh break-up, first wind-induced break-up, second wind-induced break-up and the atomisation regime.

The last two are the ones relevant in diesels and the aerodynamic disintegration forces are thought to arise from the growth of unstable, short-length surface waves on the jet. In these jet break-up regimes where the jet disintegrates more-or-less immediately upon leaving the nozzle, there can be then considered break-up regimes for the individual droplets.

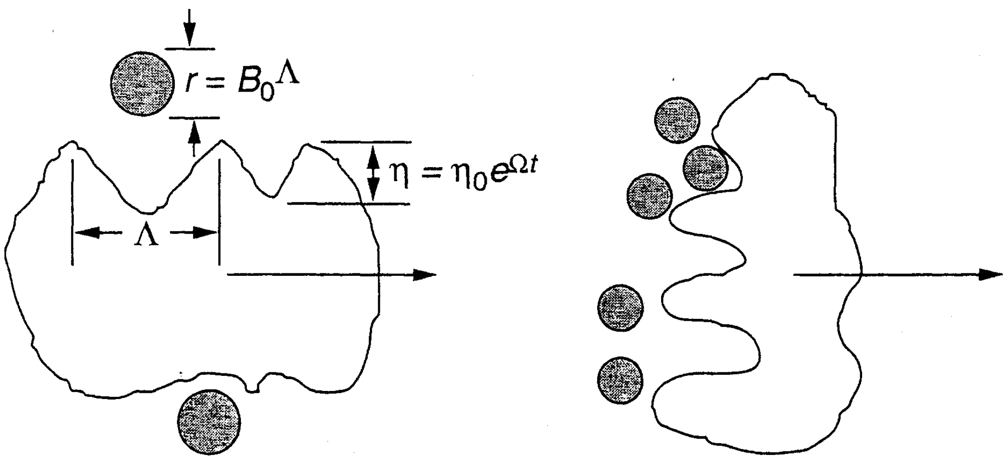

Figure 3.7. Schematic representations of perturbation of droplets as a result of Kelvin-Helmholtz (left) and Rayleigh-Taylor (right) instabilities [84]. The symbols shown here are defined in Section 3.4.3.2.

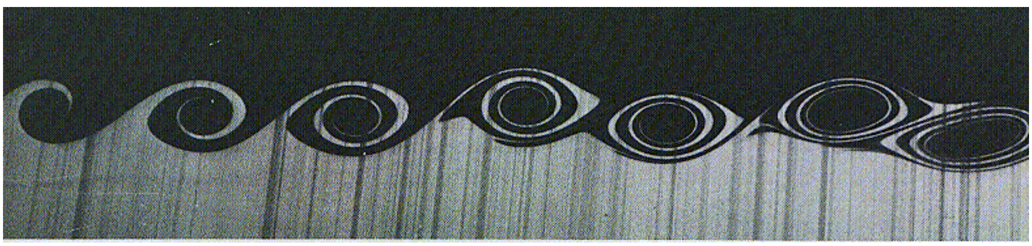

Photo 3.1. The most familiar example of the consequence of the KH Instability is when waves form as a breeze blows over water. Here, the upper stream is moving to the right faster than the lower one which contains fluorescent dye. The upper stream is also being perturbed at the most unstable frequency [152].

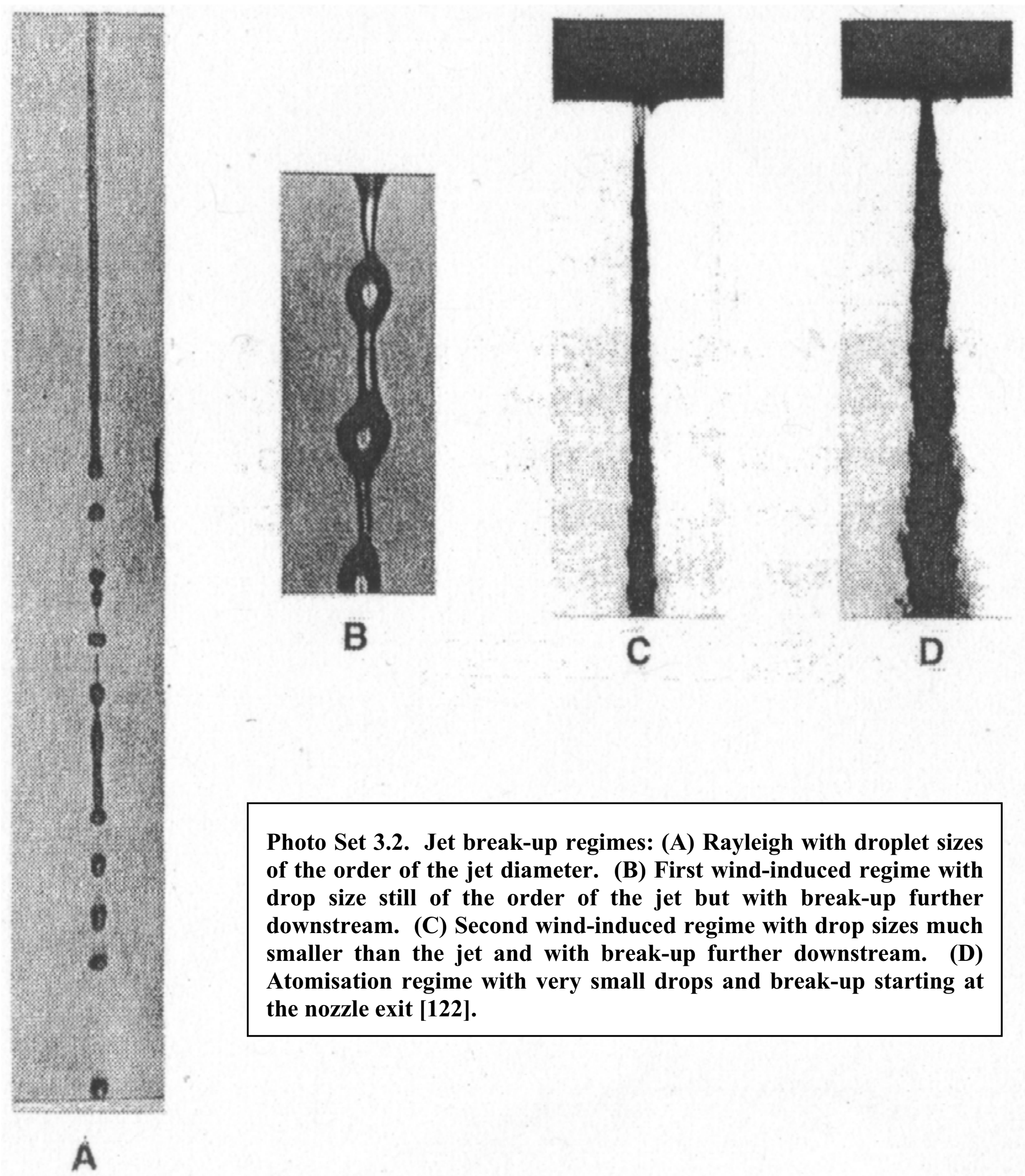

Photo Set 3.2. Jet break-up regimes: (A) Rayleigh with droplet sizes of the order of the jet diameter. (B) First wind-induced regime with drop size still of the order of the jet but with break-up further downstream. (C) Second wind-induced regime with drop sizes much smaller than the jet and with break-up further downstream. (D) Atomisation regime with very small drops and break-up starting at the nozzle exit [122].

3.4.2.3 Droplet Break-up Regimes

Reitz and others [82 and 143] have studied the break-up of single drops in transverse, high-velocity air jets. They found that as the relative velocity increases, three basic types of droplet break-up are encountered which depend on the Weber Number, *We*, of the flow.

Weber number is defined as the ratio of inertia forces to surface tension forces acting on a fluid as shown in Equation 3.2. The characteristic length scale *D* can be taken to be the Sauter Mean Diameter, SMD, of a droplet. SMD is defined as the diameter of a drop having the same volume/surface-area ratio as that of the entire spray. Experiments [61 and 75] have shown that SMDs upon injection from in-line pump systems are in the order of about 50 μm and less for higher-pressure systems.

The three break-up regimes have been referred to as the "bag" break-up regime, the "shear" or "boundary layer stripping" regime and the "catastrophic" break-up regime [143]. These are described below and illustrated in Figure 3.8 as summarised by Lee and Reitz [82]. In diesel sprays the droplets span a large range of velocities and hence Weber Numbers, thus it is expected that all three mechanisms are relevant. The bag regime begins at We = 12. Transition to the so-called shear type begins at about We = 80. Multi-mode (combined bag and shear) occurs between this range.

$$We = \frac{\rho_a U^2 D}{\sigma} \qquad \textbf{Equation 3.2}$$

Bag Break-up

When drops are introduced into a low-velocity air stream, the drop becomes flattened and a thin, hollow bag is blown downstream which is attached to a more massive toroidal liquid rim. The bag eventually busts, forming a large number of small fragments. The rim then disintegrates forming a small number of large fragments.

Shear Break-up or Boundary Layer Stripping

As the relative velocity is increased, break-up now originates from the equator of the drop. Viscous boundary layers develop in the drop and in the surrounding gas. The accelerated liquid is thought to be stripped from the drop at its equator.

Catastrophic Break-up

At sufficiently high air velocities the drop experiences an even larger dynamic pressure change on its surface. Once again, the drop is flattened into a sheet and the accelerating sheet breaks into large-scale fragments by means of the RT instability. Much shorter

KH waves originate at the edges of the fragments and these waves are stretched to produce ligaments which then break up into very small droplets.

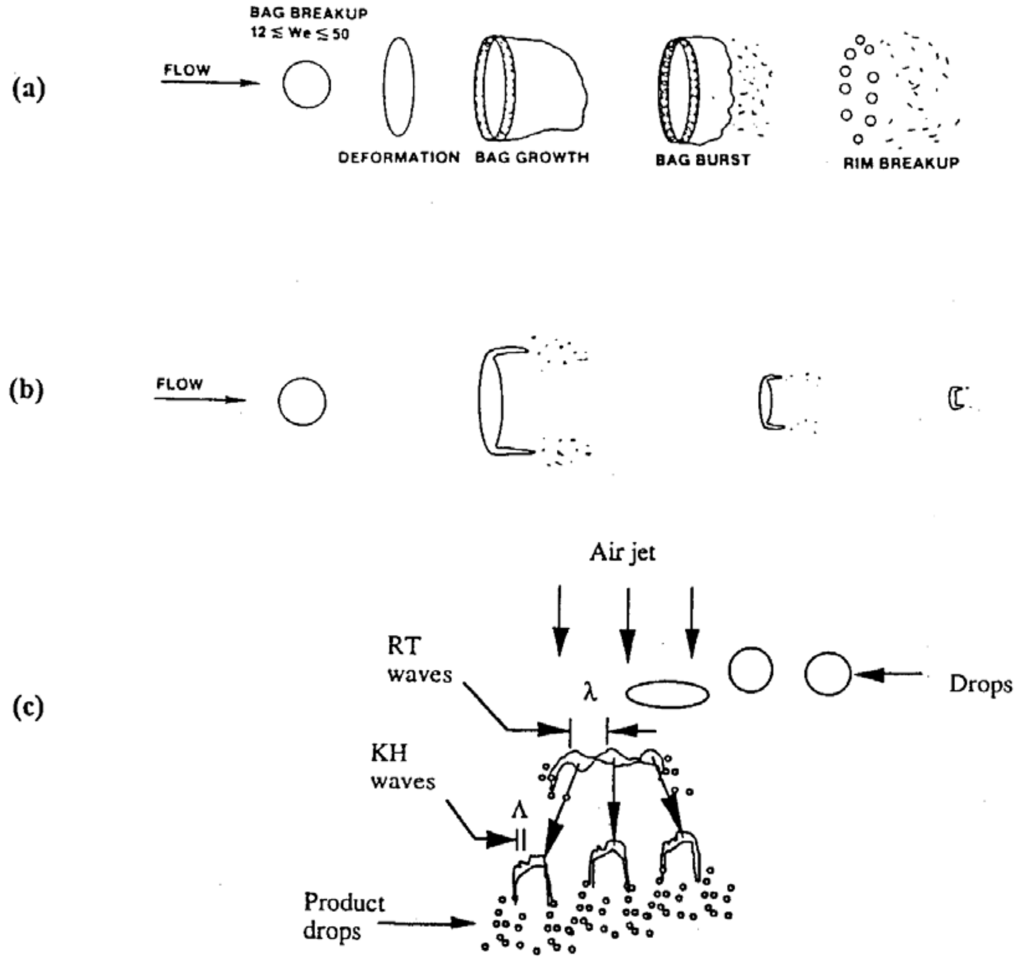

Figure 3.8. Droplet break-up regimes: (a) bag, (b) boundary layer stretching and stripping and (c) catastrophic break-up [82].

3.4.3 Secondary Break-up Models

The early work on instability analysis has steadily evolved in the last thirty years. As discussed, with the advent of modern computing power, the simulation of spray break-up has in the last decade received much attention. Of models that deal with jet break-up by the interaction between the liquid jet and relatively stagnant air, the "TAB" and "Wave" models are ubiquitous in modern numerical codes.

3.4.3.1 The TAB Models

The Taylor-Analogy Break-up (TAB) model is a classic method for calculating droplet break-up. This method is based upon Taylor's analogy between an oscillating and distorting droplet and a spring-mass system as shown in Table 3.1.

The standard TAB model was introduced by O'Rourke and Amsden [105] into the context of diesel sprays in 1987. It has been used to predict both primary and secondary break-up for both diesel and gasoline sprays [75]. The radii of the product droplets are determined by an energy balance equation which has since been found to generally lead to an under-prediction of the drop sizes in diesel engine environments [143]. Schmidt and Corrandi used the *KIVA* code with the TAB model in 1997 and found that it can produce excessive droplet break-up which is not in agreement with experiments [102].

Table 3.1. Taylor's analogy between the forces on a droplet and on a spring-mass system [39].

Spring-Mass System	**Distorting and Oscillating Droplet**
Restoring force of Spring	Surface Tension Forces
External Force	Droplet Drag Force
Damping Force	Droplet Viscosity Forces

The Enhanced TAB (ETAB) model as proposed by Tanner in 1997 [143] utilises the break-up condition of the standard TAB model but handles the droplet break-up differently: the rate of product droplet creation is assumed proportional to the number of product droplets with the proportionality constant dependent on the break-up regime. Tanner compared the ETAB model to the standard TAB method using *KIVA* and with the experimental data of Hiroyasu and Kadota [58] and Schneider [133]. Results using the ETAB model were found to compare much more favourably to the experimental results than did those found using the standard TAB model.

3.4.3.2 The Wave model

The so-called Wave break-up model is suitable for very-high-speed injection where the KH instability is believed to dominate the spray break-up, ie. where $We > 100$ [39].

This model considers the break-up of the injected liquid to be due to the growth of KH instabilities inducing the shearing-off of droplets from the liquid surface. The rate-of-change of the drop radius and the resulting child droplet size are related to the growth rate of the instabilities, Ω, and wavelength, Λ, of the fastest growing surface wave [120].

$$\Omega = \frac{0.34 + 0.38 We_g^{\ 1.5}}{\left(1 + \sqrt{\frac{We}{\mathrm{Re}}}\right)\left(1 + 1.4T^{0.6}\right)} \sqrt{\frac{\sigma}{\rho_l r_0^{\ 3}}}$$

Equation 3.3 [120]

$$\Lambda = \frac{9.02a\left(1 + 0.45\left(\frac{We}{\mathrm{Re}}\right)^{1/4}\left(1 + 0.4T^{0.7}\right)\right)}{\left(1 + 0.865 We_g^{\ 1.67}\right)^{0.6}}$$

Equation 3.4 [120]

with subscripts l and g referring to the liquid and gas phases respectively. The droplet radius, r, and time for break-up, τ are then given by:

$$r = B_0 \Lambda$$

Equation 3.5 [120]

$$\tau = \frac{3.726 B_1 a}{\Lambda \Omega}$$

Equation 3.6 [120]

Here, B_0 and B_1 are constants and are discussed further in Chapter 8. This model has become popular for use in high-speed fuel injection applications [61 and 75] and so is the model chosen for the numerical simulations in the current project. Tanner [143], in his study mentioned above, also compared the Wave model to the ETAB model. Good agreement was found between each of the ETAB and Wave models and the experimental data. Recent improvements account for RT instabilities resulting from deceleration of the drops [112]. The application of these models to numerical work is discussed further in Section 7.3.1.

3.5 Gaseous Fuel Jets

Owing to their single-phase but compressible nature, gas jets provide different challenges to study when compared with liquid sprays. Modern investigation techniques have allowed them to be quite well understood. Since this study deals with fuel jets for a reciprocating engine, the fuel jet is of a transient nature. Whilst many studies have concentrated on steady jets, relatively few have been made on the transient gas jet [149].

A qualitative model of the structure of a gaseous jet was developed by Turner and first published in 1963 [151]. The "Vortex Ball model", shown in Figure 3.9, depicts the jet as consisting of two distinct regions. The initial region is called the "quasi-steady region" and is described by existing steady-state relationships for velocity and concentration decay. Most of the mixing with the surrounding fluid occurs here. This initial region feeds a transient vortex region (the ball) which forms the head of the jet. As the jet progresses, the radius of the vortex ball, R_v, increases due to the quasi-steady jet feeding it through a region called the back plane, q.

It is assumed that the entrainment into the vortex ball of the surroundings is negligible. Momentum flux from the quasi-steady jet transfers to the vortex ball at all points along the back plane where the quasi-steady velocity is greater than the back plane velocity. The motion of the vortex ball and hence the position of the leading edge of the jet is governed by equations for the conservation of momentum.

Batchelor in 1967 carried-out flow visualisation of the early stages of a jet which revealed the formation of a vortex "mushroom" or "ball", suggesting that a model similar to the one used by Turner could be utilised for transient jets [108]. Abramovich and Solan in 1973 [5] modelled a starting, laminar round jet as a quasi-steady state jet feeding a vortex structure. Witze [157 and 158] applied the same model to a turbulent round free jet in the early 1980s. In more recent times, Rubas [127] and Hill and Ouellette [56] used Turner's model as the foundation of their studies into transient jets.

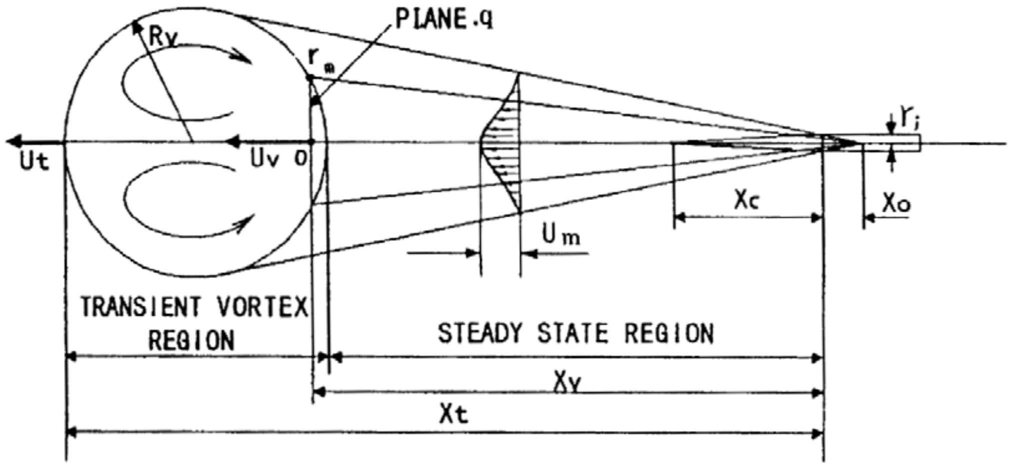

Figure 3.9. Turner's "Vortex Ball Model" [23].

Owing to the high speed of the fluctuations, it is very difficult to observe the growing process of large-scale vortices in a transient gas jet. The vortices have a great effect on the mechanism of mixture formation between the jet itself and the surroundings. Hyun et al in 1996 [63] attribute the rolling-up of vortices in the mixing flow region to KH instabilities in the shear layer having a large velocity gradient.

3.6 Under-expanded Jets

With High-Pressure Direct-Injection (HPDI) of NG, the ratio of gas injection pressure to cylinder pressure is usually well above the choking limit which, for methane, is 1.86 [86]. At these higher pressure ratios, the exit Mach number at the nozzle remains equal to one but the exit static pressure is greater than the ambient or cylinder pressure. Substantial gas expansion from the exit pressure to the cylinder pressure is required downstream from the nozzle and this is why such gas flow is called "under-expanded".

Under-expansion is a complex adjustment process involving expansion and compression waves which form a barrel-shaped shock pattern [56] as shown in Figure 3.10. An expansion "fan" originating from the corners of the orifice is generated. The velocity of the gas increases to supersonic speed as it passes through the expansion fan with a corresponding decrease in the static pressure and density. Then, as the gas passes through the compression and shock structures, its velocity decreases and the static pressure and density increase. As shown in Figure 3.11, the expansion waves are reflected at the flow boundary as compression waves and the jet boundary pressure remains equal to the cylinder pressure. At the high injection pressure ratios found in HPDI, the intercepting shocks can no longer reflect at the axis and are instead connected by a normal shock or "Mach disc".

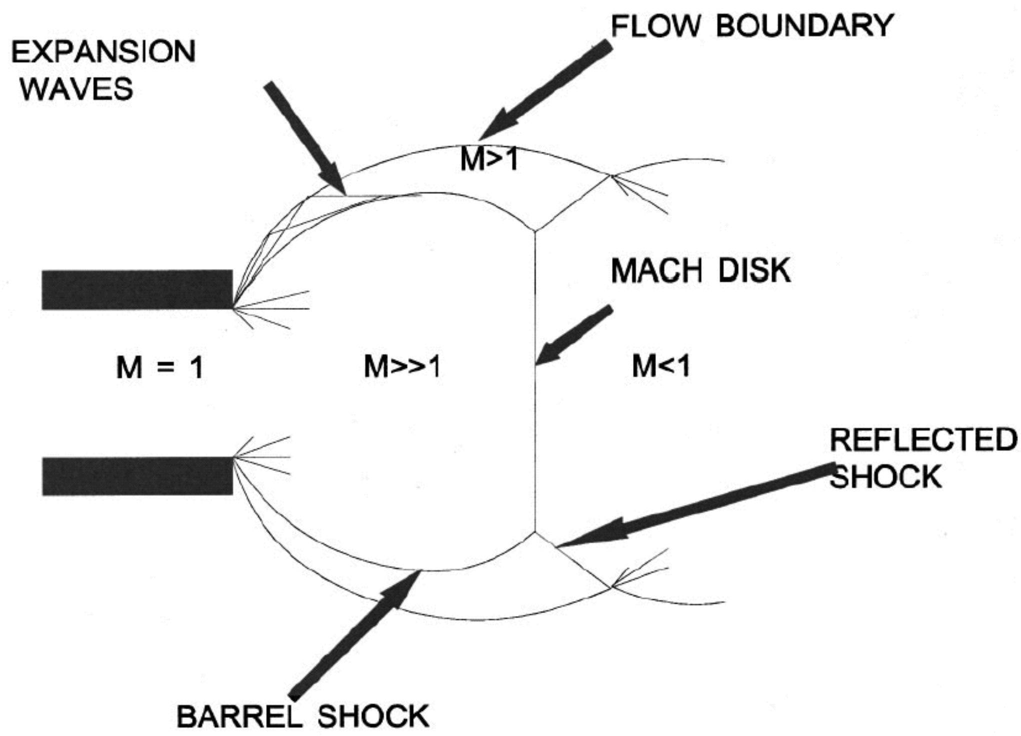

Figure 3.10. Schematic diagram of a Mach disc resulting from under-expanded flow [56].

3.7 Penetration of a Transient Gas Jet

3.7.1 Self-Similarity

How far a gas jet actually penetrates into the cylinder is a key area of study in the current work. Steady jets have long been recognised as having a "self-similar" profile. This means that the penetration/spread ratio of the jet is essentially linear, ie. the jet angle remains relatively constant as supported by Turner's model. Rizk in 1958 [126] measured the penetration rate of incompressible jets. His photographs showed that the jets became self-similar as flow progressed:

$$\Gamma = \frac{X_t}{\left(\dot{M}_i / \rho_a\right)^{1/4} t^{1/2}}$$ **Equation 3.7 [56]**

where X_t is the penetration length of the jet, $\dot{M}_i$ is the momentum injection rate at the nozzle, ρ_a is the density of air in the chamber, t is the time from SOI and Γ is a constant whose value is 3 ± 0.1 for turbulent jets issued from round nozzles. Measurements by Witze in 1980 [157] and 1983 [158], Kuo and Bracco in 1982 [77], Miyake et al in 1983 [95] and Chepakovich in 1993 (reported by [56]) have confirmed this analysis to be pertinent to transient jets.

Kouros, in 1993 [76], found that transient jets continued to display self-similar behaviour even when perturbed by harmonic oscillations. Birch's results from 1978 [20] indicate that even highly under-expanded jets conform downstream to self-similar behaviour and a universal law of penetration can be obtained by scaling the data with the square-root of the nozzle-to-chamber density ratio.

3.7.2 Actual Penetration

Kleinstein in 1964 [73] proposed a now widely-accepted axial velocity and concentration (mass fraction) decay formula for axially symmetric, turbulent, compressible free jets based on linearisation of the momentum equations developed by Turner in 1962 [151].

$$\frac{u_{centreline}}{u_0}, \frac{Y}{Y_0} = 1 - \exp\left[\frac{-1}{k\frac{2x}{d_0}\left(\frac{\rho_{ambient}}{\rho_0}\right)^{0.5} - 0.7}\right]$$ **Equation 3.8 [73]**

Where $conditions_0$ are at the jet's origin (ie. the nozzle orifice), u is the speed of the jet and Y is the mass-fraction of the jet fluid. Kleinstein determined separate values for the eddy viscosity k for velocity decay and for concentration decay based on fits with previously published experimental data.

Rubas et al in 1998 [127] modified a single-cylinder version of a Caterpillar 3516 engine to operate on the direct-injection of NG using glow-plug ignition. A spacer-plate between the block and head was modified to allow optical access. Planar Laser-Induced Fluorescence (PLIF) of the NG was used to visualise the gas jets inside the cylinder. Figure 3.11 shows dimensionless jet penetration versus dimensionless time measured from the PLIF data during motoring and with a stationary piston. Also shown is the predicted distance using Kleinstein's model, here referred to as the "Vortex Ball" model. Calculated penetration distances agreed with measured data. Thus the model may be useful in doing preliminary screening of the effects of injector design parameters such as orifice size, fuel pressure and also engine operating conditions. Unfortunately though the model can be used only to predict average characteristics in the jet and isn't capable of predicting the large-scale structures seen with the PLIF.

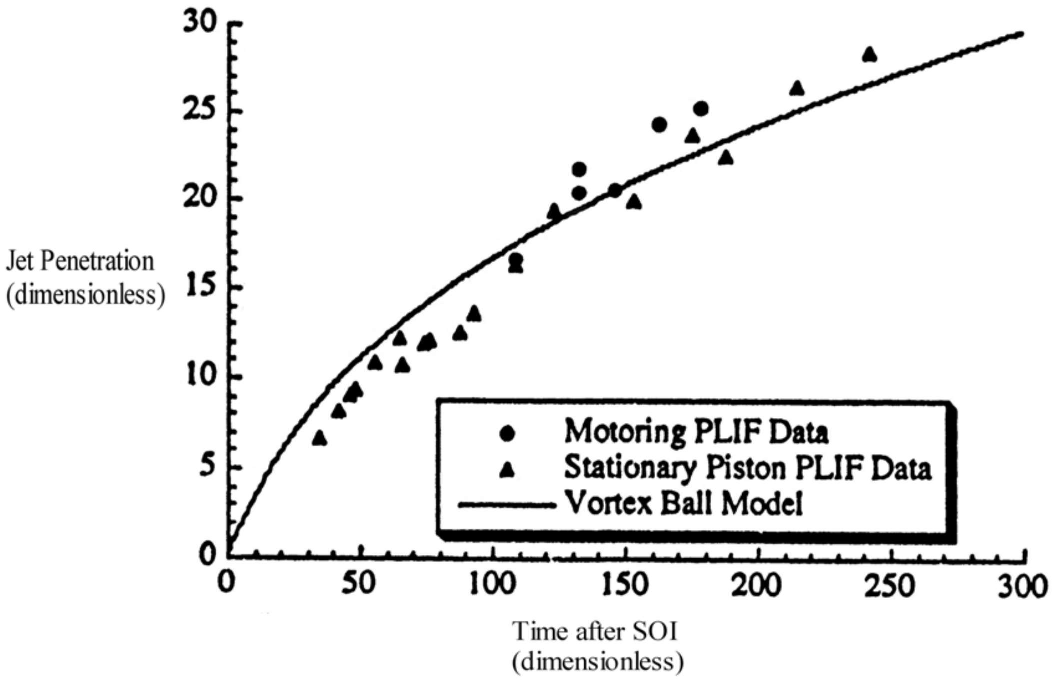

Figure 3.11. Jet penetration found in experiments by Rubas et al compared to that predicted by Kleinstein's model [127].

More recently in 1999, Hill and Ouellette [55] furthered work into self-similarity and the determination of a penetration constant with respect to under-expanded jets for HPDI (Figure 3.12). They found that scaling based on the nozzle exit momentum flux-to-density ratio applies for a wide range of conditions if the opening transient is short compared to the duration of injection. From studying their own experiments and from the photographic work of Rizk in 1958 [126], they observed that the transient gas jet seemed to approach a self-similar configuration with an asymptotic jet width/length ratio (D/X_t) of 0.25 ± 0.05. The transition length was about 10-15 hole diameters. For D/X_t between 0.2 and 0.3 respectively, the jet penetration constant, Γ, had a value between 2.89 and 3.04. Thus, once a jet has travelled 10-15 nozzle diameters, a value of $\Gamma = 3 \pm 0.1$ is suitable for use under most conditions for compressible flows. This holds true even when there is substantial thermal and species diffusion and even with transient jets from highly under-expanded nozzles. Hill and Ouellette suggested that the jet, once injected, may be considered to have "forgotten" its original configuration so that $\dot{M}_i$ is the only significant characteristic of the nozzle flow. Also, the only significant characteristic of the chamber fluid is its density.

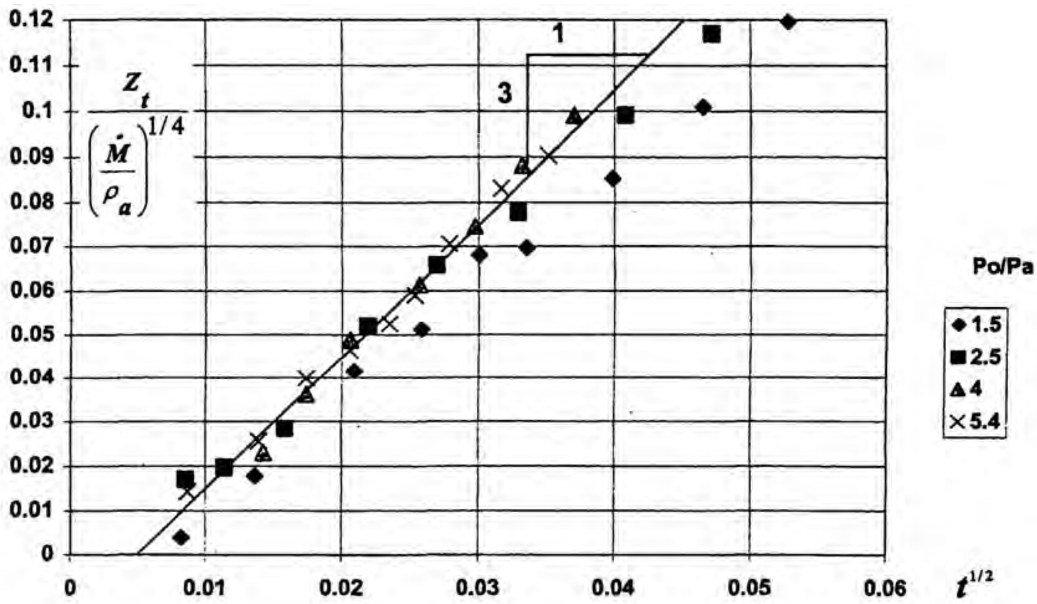

Figure 3.12. Jet penetration data from Hill and Ouellette [55].

3.8 Entrainment and Mixing

3.8.1 Qualitative Considerations

Telford, in 1966 [146], attributed the rate of entrainment into a jet as a function of the turbulence level, thus relating entrainment to Reynolds stress in the flow. In fluid dynamics, the Reynolds stress (or the Reynolds stress tensor) is the stress tensor in a fluid owing to the random turbulent fluctuations in fluid momentum. The stress is obtained from an average taken (typically in a loosely-defined fashion) over these fluctuations [39]. As described above, the present understanding is that ambient gas is mostly entrained into the sides of the “quasi-steady region” (Turner) [151] or the “mixing flow region” (Hyun et al) [63]. Early work into studying this entrainment was carried out by Abramovich and Solan in 1973 [5] and Witze in 1980 [157]. Further, Kato et al in 1987 [70] postulated that the entrainment velocity is a function of not just a local velocity scale such as the centreline jet velocity but also its time derivative. This hypothesis was cited as an extension of the original Taylor entrainment hypothesis which stated that the “mean inflow velocity across the edge of a turbulent flow is assumed to be proportional to a characteristic velocity or the mean flow velocity over the cross-section at the level of the inflow”.

Tomita et al in 1996 [149] used Laser Doppler Velocimetry (LDV) to investigate the effectiveness of a transient gas jet in entraining air in the cylinder into which it is injected. In this study, air was injected at 500 kPa through a nozzle of diameter 0.82 mm into a vessel containing ambient, quiescent air at atmospheric conditions. Micro-balloon particles of diameter 40 μm were seeded in the quiescent air and were illuminated by a laser sheet. A CCD (Charge-Coupled Device, ie. digital) camera was used to photograph the injection at several different time steps. LDV was also used by Cossali et al in 2001 [29], focussed on near-field behaviour in the early stages of injection where the velocity profiles were not self-similar, ie. unlike those far downstream. In these early stages of jet development, in the near-field the jet volume becomes larger than that injected which suggests entrainment of the surrounding gas into the jet head. This finding differed significantly from the mechanism responsible for entrainment in the quasi-steady part of the jet. It follows that the frequently-used model which assumes the head vortex growing due to mass entrainment from the steady-state jet cone should be modified when dealing with the initial part of the jet injection. In cases such as fuel jets for an engine, however, where *X*/*D* for a jet is usually large owing to ignition delay, this is not so relevant.

Also of limited relevance but of interest (since fuel jets for reciprocating engines must be pulsed) is that several researchers have stated that fully-pulsed jets offer an improvement in mixing/entrainment over steady jets. Amongst this research is that of Bremhorst and Hollis in 1990 [24] who carried-out Laser Doppler Anemometer (LDA) measurements in a fully-pulsed, subsonic air jet. They found that the mean centreline velocity decay was linearly related to the inverse of the effective distance from the exit for some 50 diameters but centreline velocity decay was much slower than for steady jets. This was attributed to domination by the periodic component and its associated pressure field which affected the jet momentum.

3.8.2 Quantitative Measurements

Birch et al in 1977 [20] used Raman Spectroscopy to measure the turbulent concentration parameters in a round free jet up to 70 diameters downstream from the source. Note that this is about the same as the region of interest in the present study into HPDI of NG. They studied an isothermal jet of NG, consisting of approximately 95% methane and issuing from a diameter 12.65 mm tube with X/D = 50 and with *Re* = 16,000. It was shown that the intensity of concentration fluctuations has an asymptotic value of 28.5% in the far field region of the jet. Results from this work are shown in Figures 3.13 and 3.14.

Abraham in 1996 [2] found that there were few studies that examined the entrainment rate in transient, turbulent, gaseous jets and none regarding the total mass entrained in the jet as a function of its penetration. Abraham employed quasi-steady assumptions to obtain an equation for the total mass entrained as a function of time for a gas injector of the type used for HPDI. Also assumed was that the pressure was constant in the chamber into which the fluid is being injected and thus the flux of momentum in the axial direction is constant. The axial profile was taken to be self-similar.

$$\frac{\dot{M}_e}{\dot{M}_i} = K\frac{x}{d}\left(\frac{\rho_a}{\rho_i}\right)^{0.5} \qquad \textbf{Equation 3.9 [2]}$$

$\dot{M}_e$ is the rate of mass entrainment into the jet whilst $\dot{M}_i$ is the mass rate of injection. K is a constant whose value is discussed below. Equation 3.9 can be manipulated by substituting terms for the nozzle diameter, jet velocity and by incorporating the definition of Witze in 1980 [157] that the arrival of the jet tip should be taken as the instant when the average velocity reaches 70% of the final steady-state value. Then, by integrating, the total mass entrained by the jet may be defined for the instantaneous position of the tip of the jet, X_t, as:

$$M_e = \frac{1}{0.7}\left(\frac{8\pi}{3}\right)^2\left(\frac{K}{4\pi^{3/2}}\right)^2 \rho_a X_t^{\,3} \qquad \textbf{Equation 3.10 [2]}$$

The entrainment rate was thus found to scale linearly with axial penetration and the total mass entrained is shown to have a cubic dependence on axial penetration of the jet. The actual value depends on the constant K whose value has been obtained from measurements by various researchers. Abraham summarises the work of nine previous researchers who sought the value of K for steady jets. For short, convergent nozzles K ranges from 0.26 to 0.32. The value is lower for long tubes with values as low as 0.2 quoted for K in the fully developed region. The value of K is not a constant in the developing region and appears to increase to a steady value in the developed region.

Recognising the need for a more precise value of K and especially for transient jets, Abraham performed computations for transient gas jets in a quiescent ambient environment with pressure ratios of 0.5, 1 and 2. It was found that a value of K between about 0.21 and 0.23 mostly fitted the results for a jet issuing from an injector suitable for HPDI.

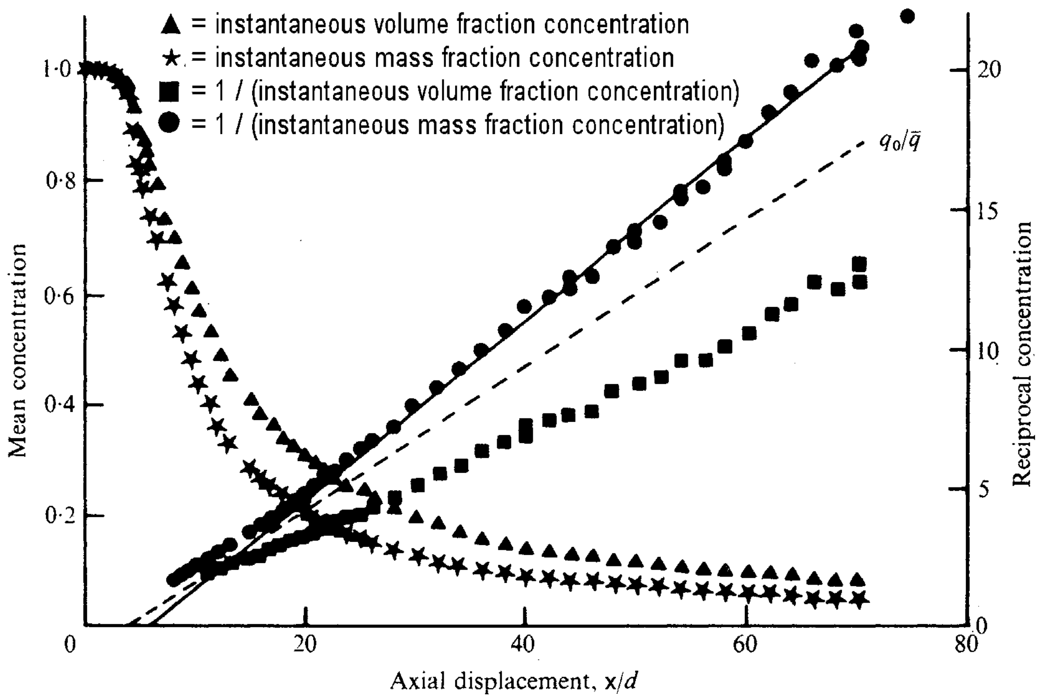

Figure 3.13. Axial Decay of Mean Parameters in a Turbulent Methane Jet [20].

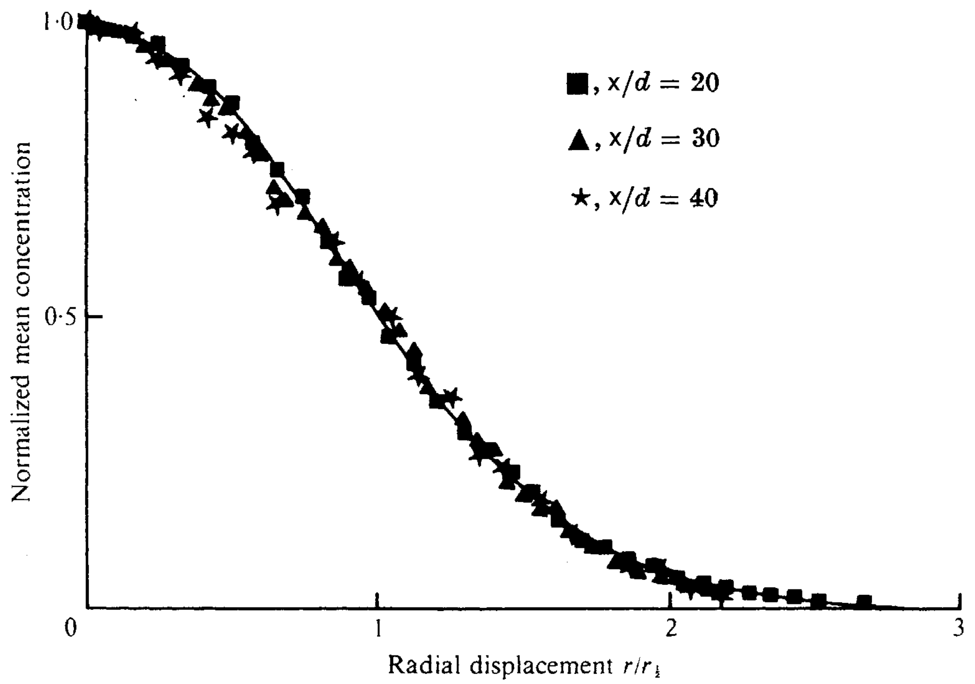

Figure 3.14. Radial Decay of Mean Parameters in a Turbulent Methane Jet [20].

3.9 Analogy between a Transient Gas Jet and a Diesel Spray

So as to simplify the algorithms used in numerical simulations, Sato et al in 1984 [129] investigated the feasibility of approximating a diesel spray as a gaseous jet. Figure 3.15 shows the structure of a diesel spray and a transient gas jet respectively and parallels between them may be drawn as follows. The "penetration" part in the spray corresponds to the "steady" part in the jet. Similarly, the "stagnation" part in the spray corresponds to the "unsteady" part in the jet. In the penetration/steady part, the static pressure is lower than that of the surroundings and consequently the surroundings are entrained into these parts. The distribution of concentration in the spray is similar to that in the steady jet. On the contrary, in the stagnation/unsteady part, the static pressure is higher than the pressure of the surroundings and there is a radial velocity. As a consequence, the surroundings are at first pushed away as a wave but then entrained as the spray/jet head passes.

Abraham, Bracco et al in 1995 [3, 4] studied the mixing rate of diesel sprays compared with gas jets in the context of an HPDI engine. They found that in the absence of combustion, the mixing rate of fuel and air was initially faster in sprays than in gas jets since sprays transferred their momentum more readily into ambient air. In the presence of combustion, the initial burning rate of the spray was found to be faster than that of the gas jet, consistent with the faster mixing rate. However, the results were somewhat inconclusive since it was also found that the geometry of the combustion chamber had a noticeable influence on the mixing of the ambient air and the injected fuel.

Hill and Ouellette [56] also conducted numerical simulations to compare the mixing rate of diesel sprays and gas jets. As shown in Figure 3.16, evaporating diesel sprays with small droplet sizes mix at much the same rate as gaseous jets when both are injected with an equivalent momentum injection rate. The evaporation rate of the diesel is, of course, highly dependent on the droplet size. Note that for the data presented in Figure 3.16, the droplets have a Sauter Mean Radius (SMR) of only 5 μm which is very small.

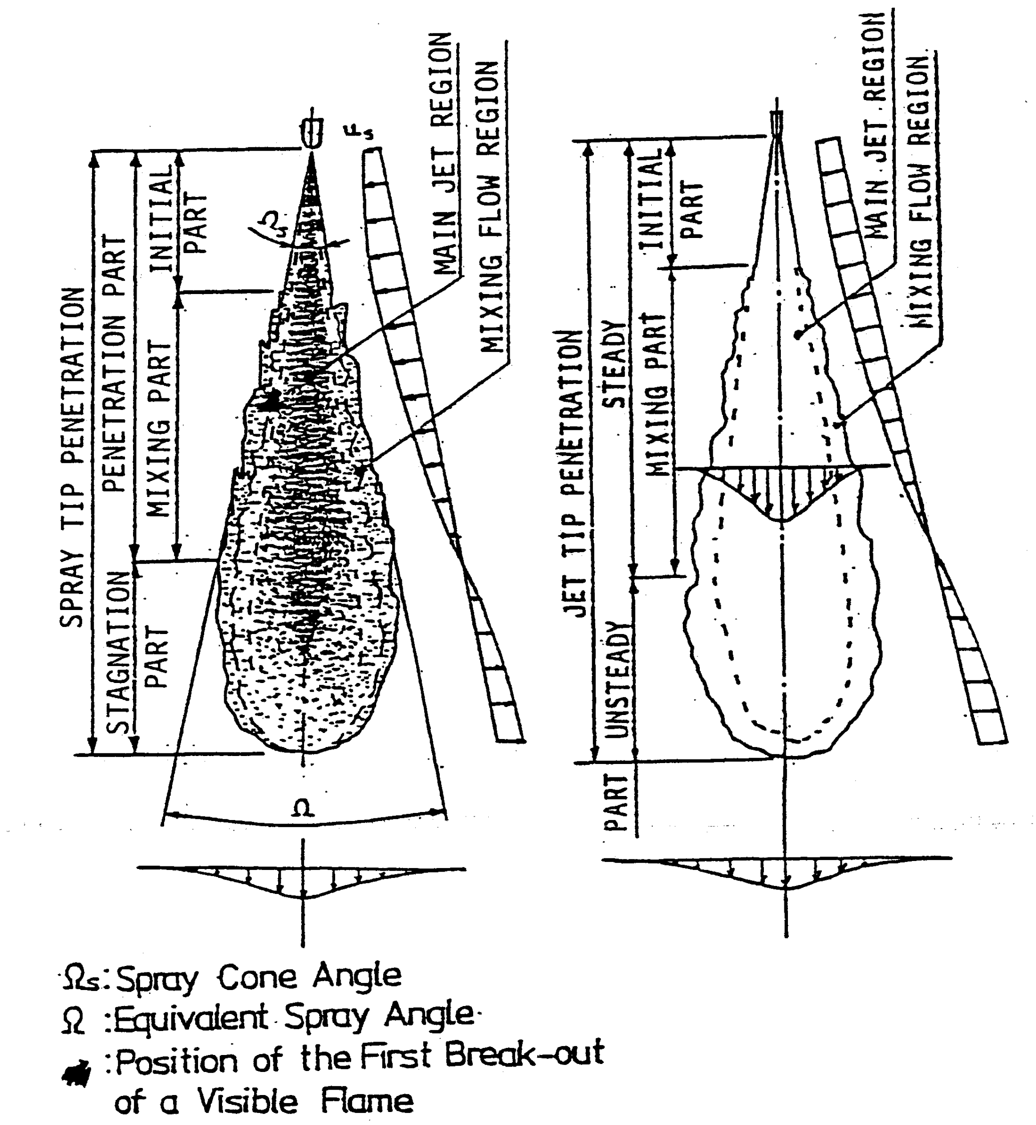

Figure 3.15. Analogy between a diesel spray (left) and a gas jet (right) by Sato et al (1984) [129].

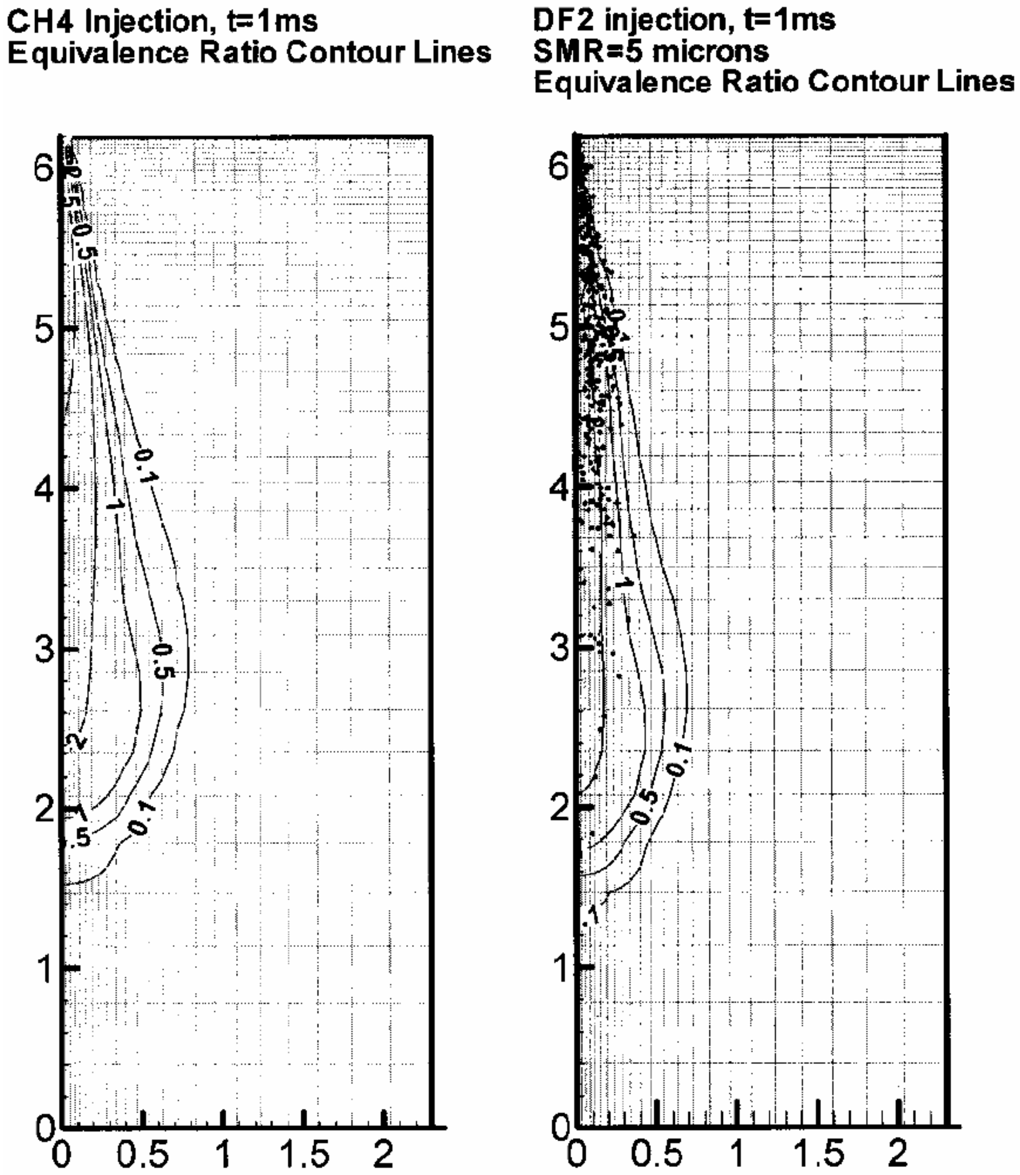

Figure 3.16. Hill and Ouellette's simulations of penetration and mixing of diesel sprays compared with that of gas jets [55].

3.10 The Interaction between the Gas Jet and the Diesel Spray

The study of how fuel jets of different species interact has been studied in depth with relation to co-axial jets. Such research has received increasing attention in recent years owing to its relevance in liquid-propellant rocket motors and injectors for scramjets. Of some interest to the current work is that Favre-Marinet et al in 1999 [37] who studied the interaction of co-axial jets with large density differences. Lasheras and Hopfinger in 2000 [81] studied the instability and atomisation of a liquid jet in a co-axial gas stream although Weber Numbers were lower and the subsequent droplet size larger than in the present study.

Yet the conditions under which HPDI have been achieved so far are not with co-axial fuel jets. Whilst in the future the development of a co-axial injector for HPDI may be desirable, thus far only discrete, plain orifices are the state-of-the-art.

As described in Section 2.8, few organisations have focussed on HPDI. Of those that have modelled the DF injection such as Ouellette and Abraham, the focus has usually been on how the discrete jets interact with the air in the cylinder rather than how the two jets form to combine a combustible mixture. As such, there exists the potential to contribute to the understanding of how the fuel jets mix with each other. The present work aims to quantify the conditions under which a DF injector should operate to achieve optimum performance from the engine.

4. Chapter Four: Laboratory Rig Design and Construction

4.1 Scope of the Laboratory Work

A laboratory rig was designed, built and operated to visualise both a diesel spray and a gas jet being injected into a chamber. This rig consisted of injection systems for both diesel and NG, a combined (DF) injector for the two fluids and photographic equipment to capture images of the jets when injected discretely as well as when both were injected simultaneously. The rig as a whole has been named the Jet Visualisation Rig (JVR)

The main purpose for constructing the JVR was to provide a tool to calibrate numerical models, which form the other main component of the current work and are described in later chapters. Analysis of photographs taken using the JVR also allowed a qualitative study of the discrete and mixing jets for an HPDI application. Other useful information regarding properties of the injection systems was also obtained, such as the turn-down ratio of the diesel injector and the maximum flow-rate of the gas injector.

The commissioning of the JVR and the development of the DF injector has also provided a solid foundation for combustion testing of the HPDI concept at UNSW. Such testing will be carried out in future in the School's Rapid Compression Machine (RCM) as described by Mbarawara [90] and Miao [91] in 1998 and 2001 respectively.

4.2 Major Equipment Used

A photograph of the main components of the completed test rig is shown in Photo 4.1. The JVR consists of several sub-assemblies, including:

- The Jet Visualisation Box (JVB) into which the dual-fuel injection occurs and through the walls of which the injection can be seen. The "test section" through which the photographic beams pass and are captured exists inside this box.

- The Diesel Delivery System (DDS) which provides high-pressure diesel to the dual-fuel injector.
- The Natural Gas Delivery System (GDS) which provides medium-pressure NG to the dual-fuel injector.
- Photographic systems which consist of both still and video imaging equipment for three photographic techniques: standard "back-lit" photography, shadowgraph and "schlieren" imaging.

The way in which these systems were made and fit together is detailed in the next section.

4.3 Construction of the Test Rig

Design and construction of the test rig was undertaken solely by the author. Since the rig was built "from scratch", this work involved a considerable amount of machine work and welding. Drawings of the parts that were made for the rig are included in Appendix C.

4.3.1 Jet Visualisation Box (JVB)

A container into which the fuel jets could be injected was required and several options were considered. A glass fish tank was a logical first choice. Glass would be resistant to both diesel and NG and would be fairly scratch resistant. However, since most such aquariums are constructed from glass panes held together with silicone sealant, it was suspected that it would be only a matter of time before the diesel caused the silicone to come away from the glass. A plastic material was then investigated. Of the two commonly-available engineering plastics, acrylic (Perspex) was chosen over polycarbonate (Lexan) owing to its higher optical quality. Whilst it would perhaps be less chemically-resistant than polycarbonate, the acrylic would be easier to work with and would be less prone to warpage under heat from high-intensity light sources.

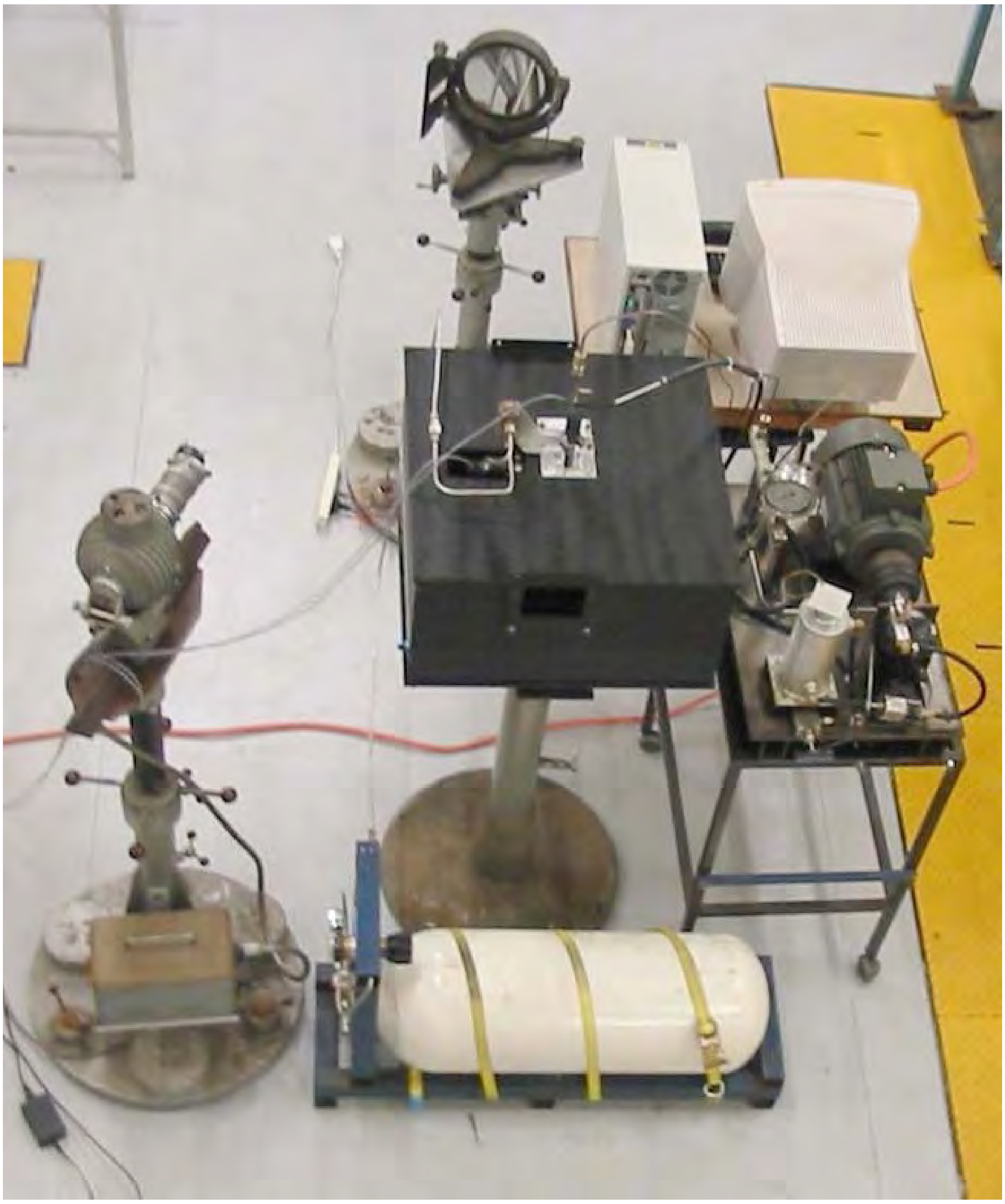

Photo 4.1 Main components of the test rig. The JVB is mounted centrally on a stand with the DDS on the trolley to the right. The gas bottle and regulator is on the floor in front of the JVB. The light source and collimating mirror (described later) are to the left and top of the photo respectively.

4.3.1.1 Basic Box

The box consisted of four walls and a base. The dimensions of the box were determined by estimating the expected penetration of the diesel jet. The walls were spaced far-enough apart such that the spray would not impinge upon the area of the clear walls where the photographic equipment would potentially be placed. As a result of this, the box was built to have a base that was nominally 600 mm square and a wall height of 400 mm. The thickness of the wall panels was 6 mm whilst the base was 8 mm. To provide a better seal against the contents of the spray box leaking, the box was constructed using milled housing joints to connect the walls to the floor. *Acrifix* adhesive was used to both permanently secure the four walls to each other and to the floor and to seal all of the joints.

Photo 4.2. Photo of the JVB during construction, showing how the walls were held in place by housing joints milled into the base. *Acrifix* adhesive was used to seal the box.

4.3.1.2 Mounting the Injectors

A lid for the box was made to both mount the dual-fuel injector assembly and to help contain the injected fuels. The lid started as a square of acrylic the same size as the base of the box. Also in common with the base, a groove that formed a housing joint for the box sides was milled into the lid. Since the lid was to be removable from the box, these joints were not glued and so both the location of the lid as well as sealing relied upon the accurate machining of the groove.

The lid of the box also had to be machined to make provision for mounting the dual-fuel injector assembly. Whilst acrylic is quite strong, it is also flexible and so an aluminium "head" was made to mount the injector assembly upon (Photo 4.3). The first DF injector assembly was designed to be compatible with the RCM as well as the JVR. Because of this, the injector assembly was to sit on top of the aluminium head as it would on the head of the RCM, with only the nozzles projecting through into the chamber as shown in Photo 4.4.

Photo 4.3: The Aluminium insert for mounting injectors on the JVB lid *in situ*.

Photo 4.4: The original "RCM-compatible" DF injector assembly mounted on the lid of the JVB.

4.3.1.3 Attitude Adjustment

To provide a rigid mount for the acrylic box and to enable fitment to a stand, a square "shoe" was made from 50 mm square RHS. Nuts were welded into the bottom of the shoe so that bolts could be screwed in to secure the box to a stand. The shoe was then bonded to the base of the JVB using silicone sealant. For the experiments being carried out in the current project, the box was mounted on a stand taken from an old drawing board which had a height-adjustable base. Shims were used between the rails that adapted the stand to the box to enable alignment of the test section within the box to the various light sources used.

4.3.1.4 Light Exclusion

Excluding ambient light from the test section was critical when using Polaroid film to capture shadowgraph images of the jet as discussed in Section 4.4.1. This was because the Polaroid film was mounted directly to the side of the JVB rather than being held in a conventional camera with a shutter. Thus any light entering the box before or after the shadowgraph was activated would expose the film and either distort or destroy the results. Excluding light from the test section was also beneficial even when using the CCD (Charge-Coupled Device, ie. digital) cameras with either the shadowgraph or schlieren techniques. Both of these techniques rely on collimated light beams subsequently bending to form an image on a photographic plate or CCD element, the result of which is interpreted in terms of the intensity of the captured illuminated bands or shadows. Extraneous light entering the box would not be collimated and thus would over-expose areas of the image which should otherwise be shadowed.

To exclude extra light, the base and lid of the box was painted flat black. Opaque, black self-adhesive book covering was used to cover the walls of the box. This excluded light as well as the paint did but was also easily removable in the event that the areas to be covered and uncovered needed to be changed regularly. Finally, a large piece of black velvet was placed over the JVB during testing to provide extra insurance against light entering. With the lights in the laboratory dimmed, the velvet in place and the box itself blacked-out, the shadowgraph pictures had the best chance of turning out properly.

4.3.2 Diesel Delivery System

Originally it was planned to build the DDS around the HEUI injector built within the School as described by Yudanov in 1996 [159] and in Section 2.9 in this volume. However, shortly before construction of the JVR commenced, it was found that the only HEUI available in the School had been seriously damaged with a long lead-time on repair. Thus it was decided to base the system around a commercially-available, high-pressure injector.

An HPCR injector from a Bosch system was subsequently used. This injector was purchased in 2001 for the Masters Thesis of Chew [28] in which the feasibility of fitting a modern diesel injection system to the RCM was studied. The injector, Bosch part number 0-445-110-011, was originally fitted to the engine of a Mercedes-Benz “Vito” van. This engine was a four-cylinder, turbo-charged and, with a swept volume of 2.2 L, rated at 90 kW. The nozzle on this injector was of the mini-sac type, typical of those found in modern, medium-sized HPCR engines which use Bosch injection equipment that have a swept volume of between 2 and 5 L [32]. Such nozzles have been described in Section 2.2.2 and in Figure 2.6. This name "mini-sac" is derived from the fact that the nozzles typically have between four and six discrete nozzle orifices fed by a small chamber in the nozzle body, ie. the sac.

The DDS was constructed using a combination of original-equipment (OE) diesel injection parts, other purchased items and a number of parts being made by the author to fit all of these components together. Most of the OE parts were taken from a pair of Iveco engines which were donated to the School in 2003. These engines were similar to that as described for the Mercedes van. A schematic diagram of the DDS is shown in Figure 4.1 and a photograph of the completed system is shown in Photo 4.5. The entire rig was mounted on a 10 mm-thick steel plate measuring 700 x 450 mm. This plate allowed the rig to be transported easily without the motor and pump suffering misalignment. The key components of the DDS (as listed in the schematic diagram) were as follows:

4.3.2.1 Pump

The heart of the DDS was a 3-bank plunger pump which was sourced from one of the Iveco engines. This pump, the Bosch CP-1, is a first-generation HPCR design and has been fitted on engines with an output of up to 95 kW [135]. The nominal output of the pump per revolution is 60 mm^3 at a design pressure of 135 MPa [150]. The pump required several brackets to mount it to the rig's base plate as detailed in the drawings in Appendix C.

4.3.2.2 Tank

Fuel for the pump was drawn via an in-line filter from an aluminium tank purpose-built by the author. An inlet manifold was made for the pump since its OE manifold had not been purchased with the pump.

4.3.2.3 Motor

The pump was driven by a 3-phase electric motor purchased especially for this application. It was connected to the pump using a purchased flexible coupling and several adaptors manufactured by the author (Photos 4.6 and 4.7). The motor's speed was controlled by an inverter already present in the laboratory.

4.3.2.4 Fuel Rail

Diesel from the pump was delivered to a fuel rail. The fuel rail, like the pump, was an OE item sourced from the Iveco engines. Since the source engine was a 4-cylinder, there were four ports on the fuel rail which would normally be used to feed the four injectors. Here, one port was used for the injector, one for a pressure-gauge, one as a return-line to the tank via a regulator and the fourth was blanked-off.

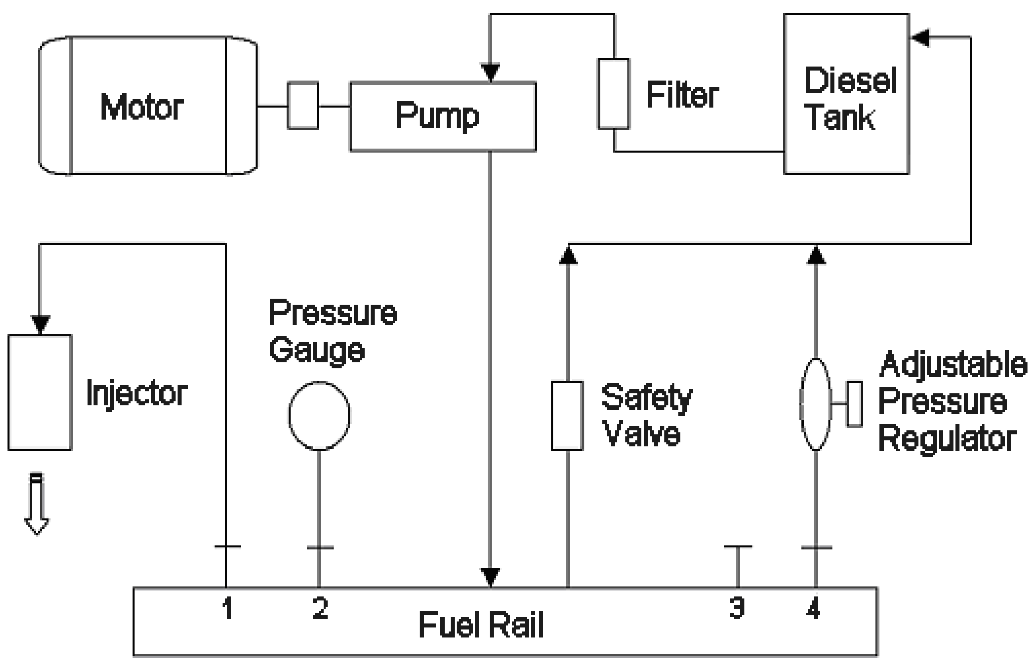

Figure 4.1. Schematic diagram of the Diesel Delivery System.

4.3.2.5 Pressure Regulator and Gauge

Pressure regulation of the rail and thus the system was achieved by placing a needle-valve in-line with the return line from the rail to the tank. The needle-valve was sourced through Tecpro in Sydney and was capable of handling pressures up to 30,000 psi (200 MPa), making it suitable for this application. The pressure gauge also came from Tecpro. An over-pressure valve was standard on the Iveco's fuel rail. This valve was modified so that it could be adjusted between approximately 50 MPa and the standard 180 MPa to aid with regulation of the pressure during testing.

Photo 4.5. The completed Diesel Delivery System.

4.3.2.6 Plumbing

The HPCR injector was supplied with diesel at around 135 MPa from the fuel rail via a length of high-pressure diesel pipe. This pipe (and all of the other pressure-side plumbing) consisted of 6 mm steel tube with a wall thickness of 2 mm. Such tube is normally used to make aftermarket injector lines and was sourced from West End Diesel Service in Sydney. The pipe-ends were of a compression fitting/ferrule type. The standard fittings for this line suit Bosch diesel injection equipment and thus had metric (JIS) threads. Hydraulic unions were purchased from Pirtek to adapt the imperial (UNF) ports on the needle-valve to the metric thread of the gland nuts.

4.3.2.7 The Injector

The HPCR injector from the Mercedes van and used by Chew was severely damaged by the time the rig neared completion. Thus it was substituted with a very similar injector, sourced from the Iveco engines. Owing to the donation of the Iveco engines, the Internal Combustion Engines (ICE) laboratory within the School was in possession of eight (8) such injectors at the time of writing.

Photo 4.6. The motor-to-pump adaptor shown with the pump.

Photo 4.7. Components of the motor-to-pump adaptor.

The nozzle of the Iveco's injector, however, was replaced with the still-serviceable nozzle from the Mercedes injector: Bosch part number DSLA-136-P-736. According to Bosch literature [21], the DSLA-P series are small, mini-sac nozzles with a needle diameter of 4 mm. This injector was designed to be mounted centrally and vertically in the 4-valve head of its source engine and as such its nozzle had six equi-spaced holes, each with a diameter of 0.2 mm, lying on a plane normal to the axis of the injector. Each hole created a jet whose axis was between 12 and 13 degrees downwards from horizontal. The use of the axi-symmetric Mercedes nozzle meant that the spray from each hole should be very similar and thus more suitable for using in preliminary studies of DF injection than the Iveco's nozzle. The Iveco's nozzle contained only five holes, all injecting at slightly different angles since this injector sat at an angle in the 2-valve head of the Iveco engine. The spray from the Iveco nozzle's hole would probably be somewhat different to each other since each hole was provided with pressurised diesel from a different azimuthal location within the sac chamber.

Special brackets were made to attach the diesel injector to both the lid of the JVB and later to the RCM. Also, one of the Iveco engine's fuel rail-to-injector lines was modified to allow the injector to be fitted to either the JVB or the RCM in any rotational orientation without having to modify the delivery line from the pump rig. The Diesel rig was tested for leaks up to 180 MPa before commissioning and worked as well as was planned.

4.3.3 Natural Gas Delivery System

The challenges presented by construction of the GDS were different to that for the diesel system. Whilst the gas system needed only to operate at pressures up to 20 MPa, the compressible and dry nature of the gas posed specific problems. Similar to the DDS, the GDS consisted of a combination of purchased and manufactured parts. A schematic diagram of the system is shown in Figure 4.2 and the main components are described below.

4.3.3.1 Gas Storage

A 55 L, automotive-style CNG cylinder was sourced from MED in Villawood. Such cylinders are able to store up to 20 MPa of CNG. Since the cylinder was round and thus difficult to mount securely, the author fabricated a frame from welded RHS as shown in Photo 4.1. The cylinder was filled at Agility NGV (a subsidiary of AGL) in Alexandria. Mr Hendra Satyo, Agility NGV's Project Engineer, kindly provided this service until such time as a conventional account for re-filling could be set up with AGL.

4.3.3.2 Pressure Regulator and Plumbing

A *Tescom* pressure regulator was purchased from Victoria Fittings and Valves in Melbourne. This regulator allowed the gas delivery pressure to be set anywhere between ambient and the pressure in the gas cylinder. Owing to the geometry of the standard tap and port assembly on top of the gas cylinder, the regulator could not be fitted directly to the cylinder but rather had to be mounted remotely on the frame. Swagelok ¼" stainless-steel tubing and fittings were used to connect the cylinder to the regulator and the regulator to the injection control valve. The tube used compression-style fittings similar to the diesel lines.

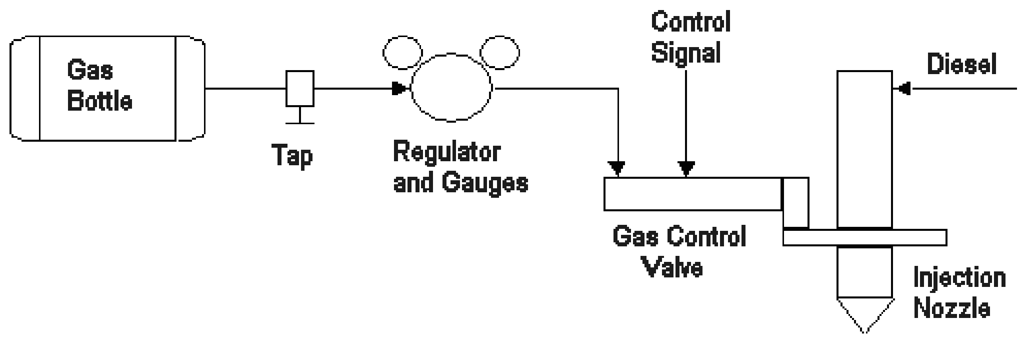

Figure 4.2. Schematic diagram of the Gas Delivery System.

4.3.3.3 Injection Control

A modified Bosch HPCR injector from an Iveco engine was used to control the injection. Details of how this solution was reached are detailed in the following sections.

4.3.3.4 Injection Nozzles

Several different nozzles were made by the author to test different geometries of dual-fuel injection. The manufacture of these nozzles is also detailed in the following sections.

4.3.4 Design and Manufacture of the Gas Injector

The biggest issue with construction and operation of the NG injection system lay with how to control the gas flow, ie. how to switch the injection on and off. Conventional solenoid valves were investigated but none were available with the required combination of pressure capability and switching time. As an example, a valve which could handle up to 9 MPa was found but the minimum shuttle time for the valve was 5 ms. Since the entire injection may need to take place in 3 or 4 ms (and at upwards of 15 MPa), such a valve was clearly not suitable.

4.3.4.1 Controlling the Gas Flow

Recent publications on the state-of-the-art revealed that the latest generation of HPCR injectors are now using piezo-electric elements rather than the solenoid actuators which have been used until now [34, 47, 79 and 84]. Figures 4.3 and 4.4 show such an element and a schematic diagram of an injector fitted with this type of element respectively. Whilst the piezo-electric stack would be useful for creating a gas control valve (GCV) from scratch, such technology was both expensive and untried within the School. Thus it was decided to first investigate whether an HPCR diesel injector could do the job. When using the diesel injector to control gas, problems were likely to occur in several areas:

- The lack of lubrication provided by the gas when compared with diesel which could result in seizure of the internal working parts of the injector.
- The much lower mass and density of the gas when compared with diesel which could result in the gas not being able to overcome mass and spring forces within the injector.
- The much lower viscosity of the gas when compared with diesel which could result in excessive leakage within the injector.

To perform a fundamental test to see whether the idea of using an HPCR injector to control gas had any merit whatsoever, one of the School's spare Iveco injectors was plumbed to a cylinder of Argon at 10 MPa. A test report is included in Appendix D. It was found that only a minor modification to the needle spring was required for the injector to work satisfactorily with gas.

Whilst the injector was able to switch the gas flow consistently, calculations found that the flow-rate of the gas through the HPCR injector's nozzle-holes was marginal. This nozzle had five holes, each with a diameter of approximately 0.2 mm. The GCV was required to flow enough gas to choke a nozzle of diameter 0.4 mm and so it was decided to increase the potential flow of the HPCR injector's nozzle.

Figure 4.3. A piezo-electric stack like that being investigated for use in next-generation HPCR injectors [79].

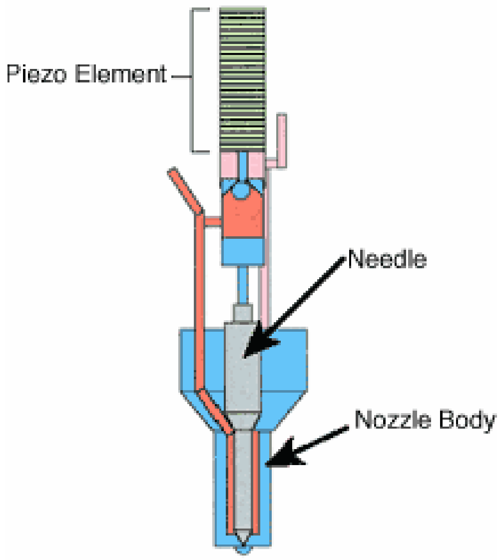

Figure 4.4. Schematic diagram of a next-generation HPCR injector which uses a piezo-electric stack rather than a solenoid [79].

The injection nozzle was removed from the nozzle holder (injector body) and a hole drilled through the tip of the nozzle body into the nozzle's sac chamber (Figure 4.5 and Photo 4.8). The effect was like creating one extra nozzle hole but of a much larger diameter than the existing ones. The diameter of the hole was set to 0.8 mm which was deemed the largest size that could be made without interfering with the needle's seal with the sac chamber. The original five holes were not modified. With control of the gas flow now established, a way of delivering the gas to the model "cylinder" (the JVB) had to be achieved.

4.3.4.2 Design and Construction of the Gas Injection Nozzle

The ultimate goal of this research was to assist in the creation of a dual-fuel injector that can be retro-fitted to existing engines. As such, dimensions of the "prototype" nozzle built for the laboratory testing resembled the production-intent nozzle as closely as possible with respect to the physical geometry.

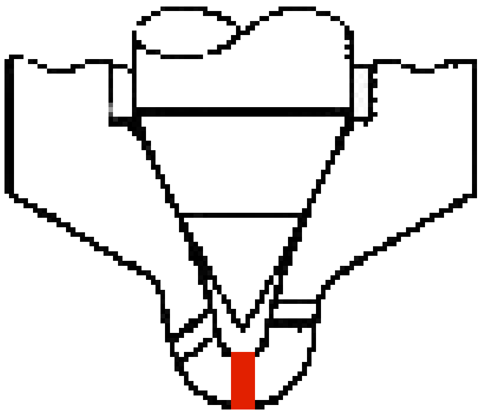

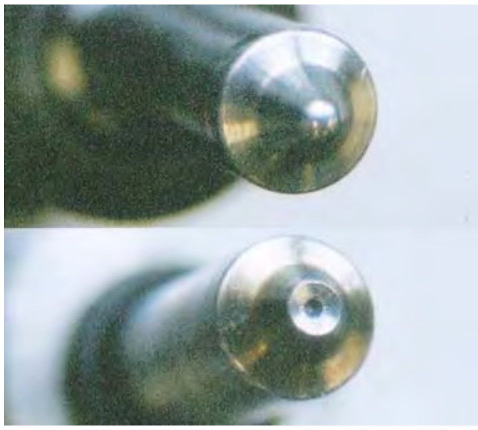

Figure 4.5. (left) Cross-sectional view of the modified nozzle for the GCV. The red line shows where the 0.8mm hole was drilled to increase the flow.

Photo 4.8. (right) Photo of the end of the standard nozzle (top) and the modified nozzle (bottom) for the GCV.

In the case of a diesel injector, the control valve for determining the start and end of injection may be considered to be the spring-loaded needle within the nozzle. Ideally, the gas injector would operate similarly to a diesel injector in that the control valve would be very close to the nozzle orifices. Thus there would be little "dead" volume within the nozzle, ie. volume that would result in a delay of the start and end of the injection as the gas expanded and contracted within the nozzle. Such an idealised design would look something like that proposed by Kloeckner in 2002 [74] and shown in Appendix B. Any dead volume between the GCV and the nozzle orifice/chamber is highly undesirable when an injector is fitted to an engine. This volume will, upon the end of injection, still contain fuel. This fuel, upon exposure to the hot combustion products in the chamber, can burn. Such a rich mixture would result, in the case of a diesel injector, with emissions of soot and UHC. With a gas injector, emissions of CO and UHC would be a concern but, more importantly, the nozzle orifices would tend to become clogged over time with deposits of combustion products.

First Gas Nozzle

Owing to the limited manufacturing capability within the school, it was decided that manufacturing a nozzle similar to that which could be subsequently fitted to an engine as part of a DF injector was not feasible. Instead, a nozzle body was designed and made by the author that would be used only for testing in the JVR and later in the RCM. This would allow testing of the timing, orientation and mixing of the gas with the diesel although it would not be in a compact form suitable for production. This nozzle body interfaced with the GCV to deliver the gas from it through a nozzle orifice into the chamber. The nozzle body was in the form of a sleeve that would mount over the Mercedes' HPCR injector nozzle for the diesel. Since this first nozzle sleeve was designed to be able to be fitted to the RCM as well as to the JVR, compromises had to be made with the internal workings of the nozzle because the GCV had to clear the head of the RCM. A cross-section of this first sleeve is shown in Figure 4.6. Photo 4.9 shows how the sleeve forms the basis of a DF injector.

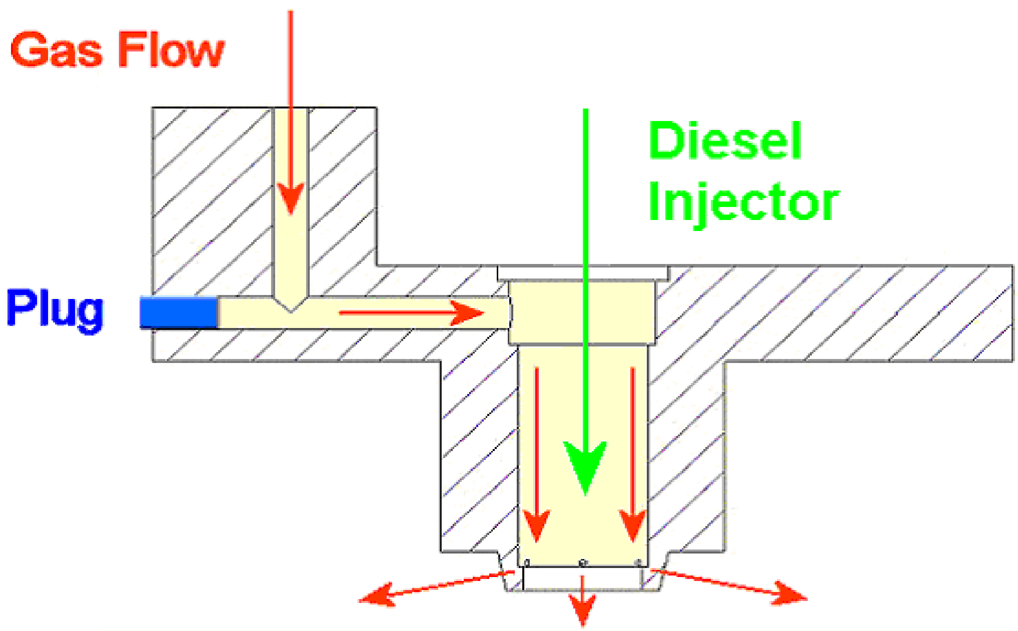

Figure 4.6. Cross-section of the nozzle sleeve made for the first DF injector assembly.

The central bore through the axis of the sleeve fitted over the nozzle of the HPCR diesel injector. The sleeve sealed to the nozzle by a press-fit on the bottom and an o-ring on the top. Upon the GCV opening, gas entered the sleeve through the vertical gallery on the left-hand side of the sleeve as shown in the figure. The horizontal gallery was plugged with a grub-screw at the circumference after it had been drilled through to the central bore and so gas flowed into the annular space between the bore of the sleeve and the nozzle of the diesel injector. The gas exited this sleeve through nozzle orifices at the bottom of the sleeve, the axes of which were drilled parallel with the axes of the orifices in the nozzle of the diesel injector, ie. 12.5° down from horizontal.

Testing of this first nozzle with a gas supply pressure of 16 MPa to the GCV resulted in only a very low-speed jet issuing from the nozzle hole. Subsequent Fanno flow analysis of the galleries in the sleeve (described in Appendix E) confirmed that the path the gas had to travel between the GCV and the nozzle was tortuous enough to cause a large restriction in the flow.

Photo 4.9. The first DF injector assembly. *Main Image:* The diesel injector (left) fits axially inside the gas nozzle sleeve. NG from the GCV (right) enters the sleeve through an adaptor that is welded to the sleeve and that fits over the GCV's modified nozzle. *Insets:* Close-ups showing how the diesel nozzle just protrudes from the gas nozzle sleeve. The gas nozzle holes may just be seen.

Second Gas Nozzle

A second nozzle sleeve was designed, this time specifically for the JVR and with the GCV placed much closer to the sleeve's nozzle hole. Also, only one nozzle hole was drilled into the bottom of the sleeve since the JVR would be used to take pictures of only one pair of diesel/NG jets at a time. Whilst the build-up in pressure inside the nozzle sleeve still took some time, a choked gas jet was able to be seen issuing from the nozzle hole. A cross-section of the second gas sleeve and a photograph of the DF injector assembly built around it are shown in Figure 4.7 and Photo 4.10 respectively.

As with the first gas sleeve, the axis of the orifice in the second one was parallel to the axis of the diesel orifice. When the gas nozzle sleeve was assembled over the diesel nozzle, the tip of the diesel nozzle just protruded from the sleeve. This resulted in a parallel separation of the axes of the two nozzles of 3 mm, as shown in Figure 4.8.

This second nozzle sleeve was found to provide a satisfactory jet. It was decided to build a total of three different nozzle sleeves, gas "injectors", each with a different angle of axis of the orifice. This would allow testing to gauge their relative mixing performance.

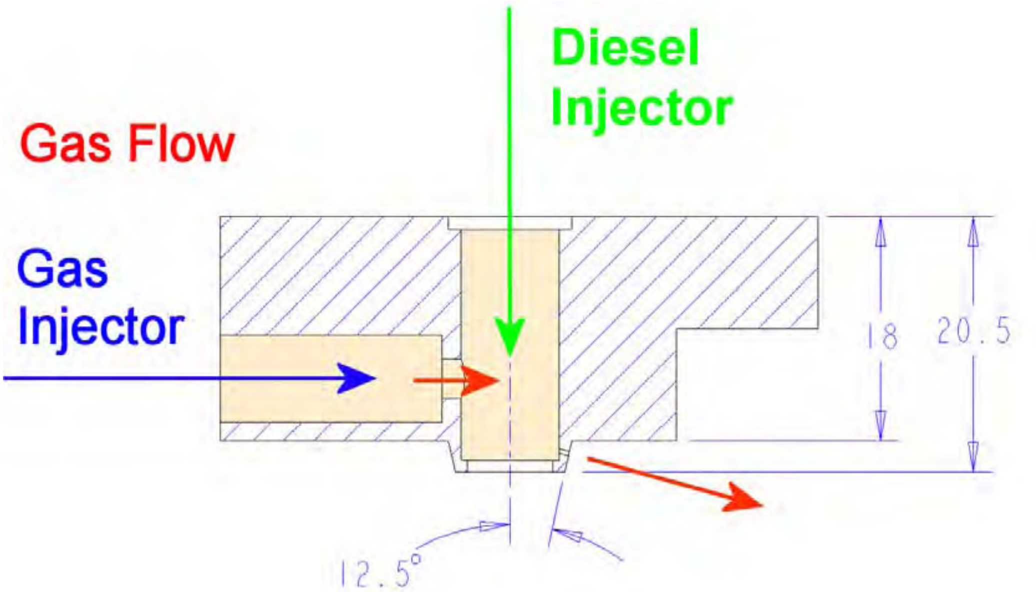

Figure 4.7. Cross-sectional drawing of the second gas nozzle sleeve. The nozzle of the GCV fits into the bore on the left-hand side of the sleeve.

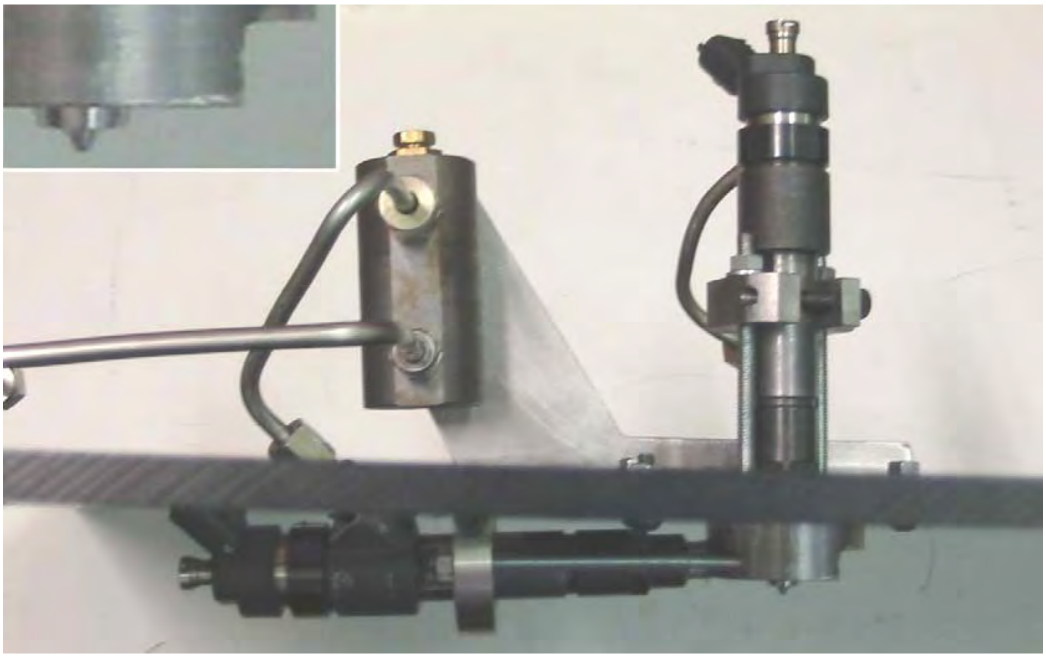

Photo 4.10. The second DF injector assembly. ***Main Image:*** **The injector assembly fitted to the lid of the JVB. The gas nozzle sleeve is in the same orientation as in Figure 4.7. The steel cylinder to the left of the diesel injector is a small accumulator which supplies gas to the GCV.** ***Inset:*** **Close-up showing how the diesel nozzle just protrudes from the gas nozzle sleeve, as per the first DF injector assembly shown in Photo 4.9.**

Figure 4.8 shows cross-sections of each of the three injectors' experimental test sections which were also their respective computational domains in the numerical study. The axis of the diesel injection orifice is shown as a blue dashed line whilst the axis of the gas injection orifice is shown as the green dashed line. For each of the DF injector assemblies, the axis of the diesel nozzle was 12.5° down from a horizontal plane. The difference between the injectors lies in the angle of the gas nozzle. In each case, the initial spacing of the centres of the two nozzle holes is 3 mm.

- The "parallel" injector's gas nozzle orifice was angled down at 12.5° and so the axes of the gas and diesel nozzles run parallel in the combustion chamber.
- The "converging" injector's gas nozzle orifice was angled down at 25.0° and so the axes of the gas and diesel nozzles intersect in the combustion chamber.
- The "diverging" injector's gas nozzle orifice ran horizontal and so the axes of the diesel and gas jets spread apart as the injection progresses.

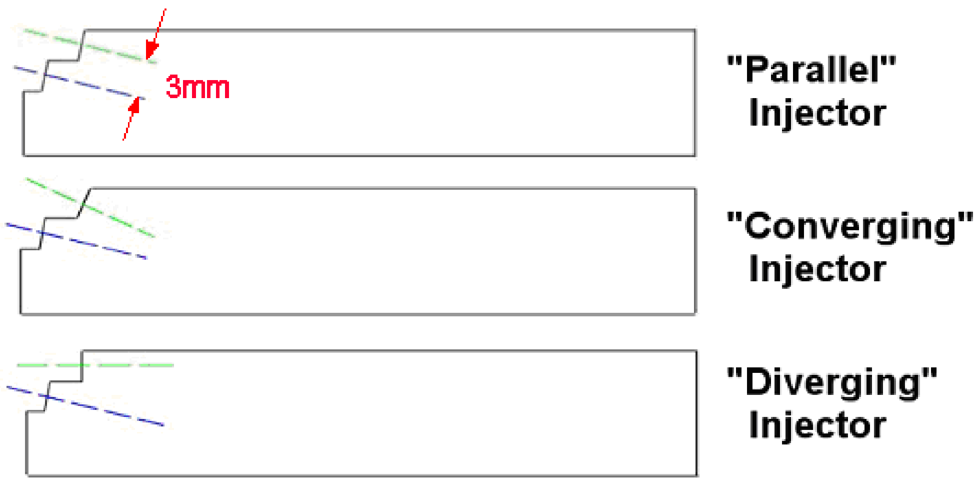

Figure 4.8. Comparison of injection axes for the different injectors.

4.3.4.3 Diesel Blocker

The diesel nozzle used for this study had, as previously described, six equi-spaced holes of diameter 0.2 mm. The six holes were all located on a conical face such that the spray angle was approximately 12.5° down from horizontal. To allow analysis of the mixing of a single diesel spray and a single gas jet, five of these holes had to be either blocked-off or their jets re-directed so that that a single jet could be photographed without the image being confused by the presence of the other jets.

Owing to the high injection pressure (up to 180 MPa), plugging-off the holes was not feasible. Thus a small "blocker" was made from aluminium channel to deflect the five "unused" jets away from the photographed test section. The profile of the gas and diesel nozzle orifice lands was filed into the channel so that it could sit closely to the surface of the lands but still let the gas jet and a single diesel jet through unmolested, as shown below in Photo 4.11. The blocker was initially glued to the underside of the gas sleeve although in time and after many tests the plate would break free. When repeatedly gluing the blocking plate back on became tiresome, the bottom face of the gas sleeve was drilled and tapped so that the blocker could be bolted-on to the nozzle sleeve as shown below.

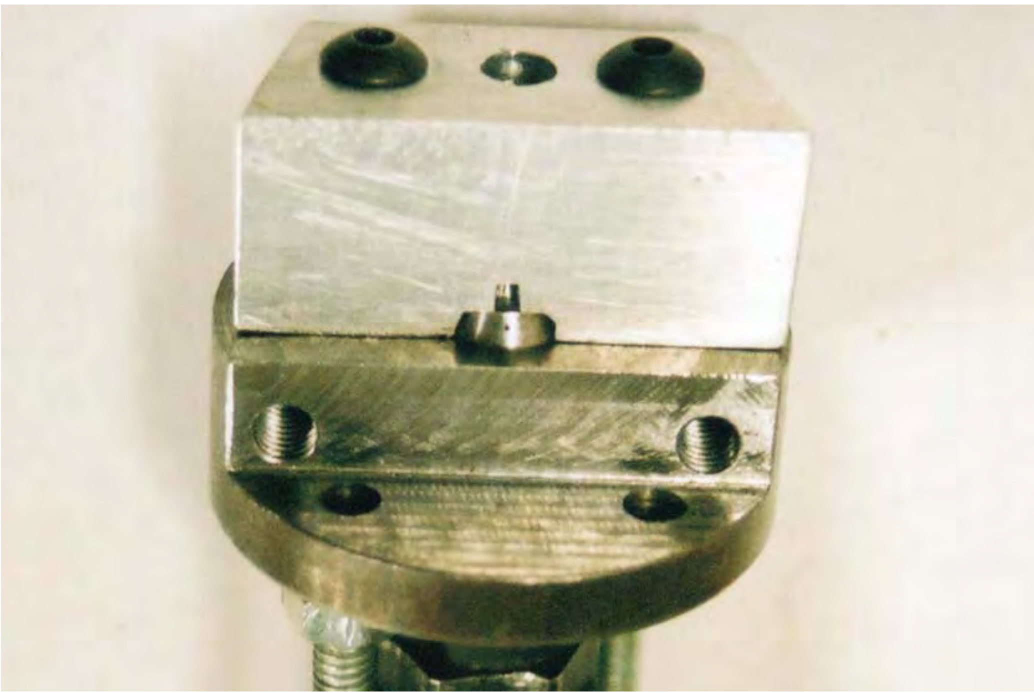

Photo 4.11. The diesel blocker shown *in situ*.

4.3.5 Digital Control Unit

Both fuel injectors were solenoid-controlled. The timing and duration of the injection was a direct function of the timing and pulse-width of the power supplied to the injectors' respective solenoids. Thus an electronic controller was required that would be able to provide an electrical pulse of a set timing and duration independently to each of the two injectors. Further, a third channel was required to send a step-type pulse to the camera equipment so that a photograph could be captured at the correct time during the injection.

Mr Ben Ware, an employee of the School, purpose-built for this project a digital control unit. A photograph of this unit is shown in Photo 4.12. It is built around a CMOS FLASH-based 8-bit microcontroller, manufactured by Microchip Technology Inc. The unit had three output channels, each capable of providing a pulse of up to 24 V. The delay for each of the three independent channels (two injectors and one camera) could be set between 0 and 6 seconds in increments of 100 μs. Similarly, the duration of the injection and camera pulses are able to be set between 0 and 6 s in increments of 100 µs. Leads to the DF injector and camera equipment were connected to the control unit by BNC plugs. Dual-fuel injection and photography (ie. timing of the three channels) could be started by either pressing a button on the control unit itself or by a signal received by a BNC-connector on the box.

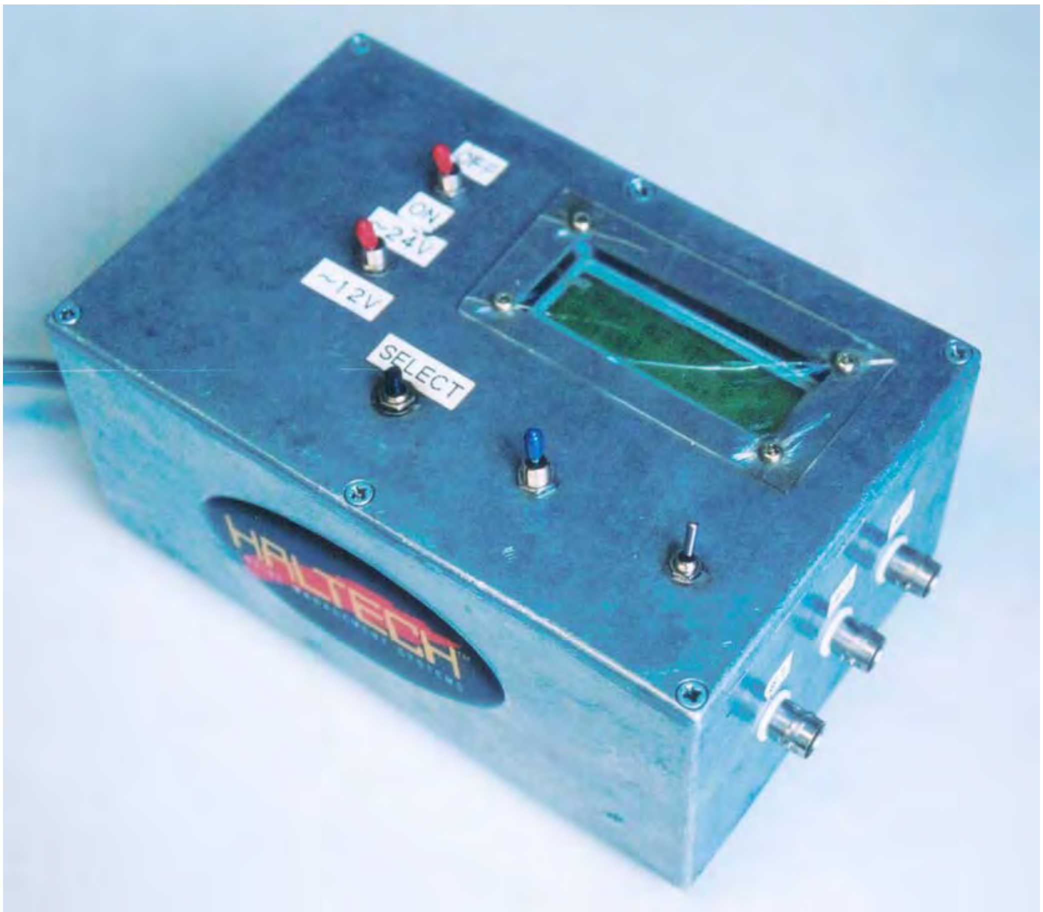

Photo 4.12. The three-channel digital control unit.

4.4 Photography Equipment and Set-up

With a method established for supplying fuel jets to the test chamber, techniques to enable photography of the behaviour of the jets were required. Since the liquid and gas jets both had a nozzle speed in the transonic regime, any method had to operate at very high speed. Several options existed for capturing images of the dual-fuel jets, including conventional flash-photography using an SLR camera, using Polaroid film and photography using a digital camera. The use of a digital camera was highly desirable for several reasons, mostly since it would allow many photos to be taken in a short time without having to wait for development of the film. Further, once set-up, the digital camera would cost nothing to run.

In the case of the mostly-opaque diesel jet, conventional photographic techniques could be employed. Visualisation of the transparent natural gas jet, however, was a more difficult task. The fact that the gas jet was clear and invisible in normal lighting conditions made photography quite complicated. It was decided that the shadowgraph technique was a good choice to start with. As the work progressed and the limitations of the shadowgraph system became apparent, a schlieren system was subsequently developed. Also, at about this time, the School purchased a high-speed digital video camera. It was this camera when used with the schlieren system that has provided the bulk of the useful results from this study.

4.4.1 Imaging Systems

4.4.1.1 Backlighting

The simplest method and that which was used to capture images of the discrete diesel jet was "backlighting". In this method, high-intensity halogen bulbs were used to illuminate the test section. A diffuser (in the form of a translucent plastic sheet) was placed between the lights and the test section so that even illumination was obtained. The camera (first a still CCD and later the high-speed video camera as described later) was then used to capture a silhouette of the diesel jet as it passed through the test section between the light source and the camera as shown in Photo 4.13.

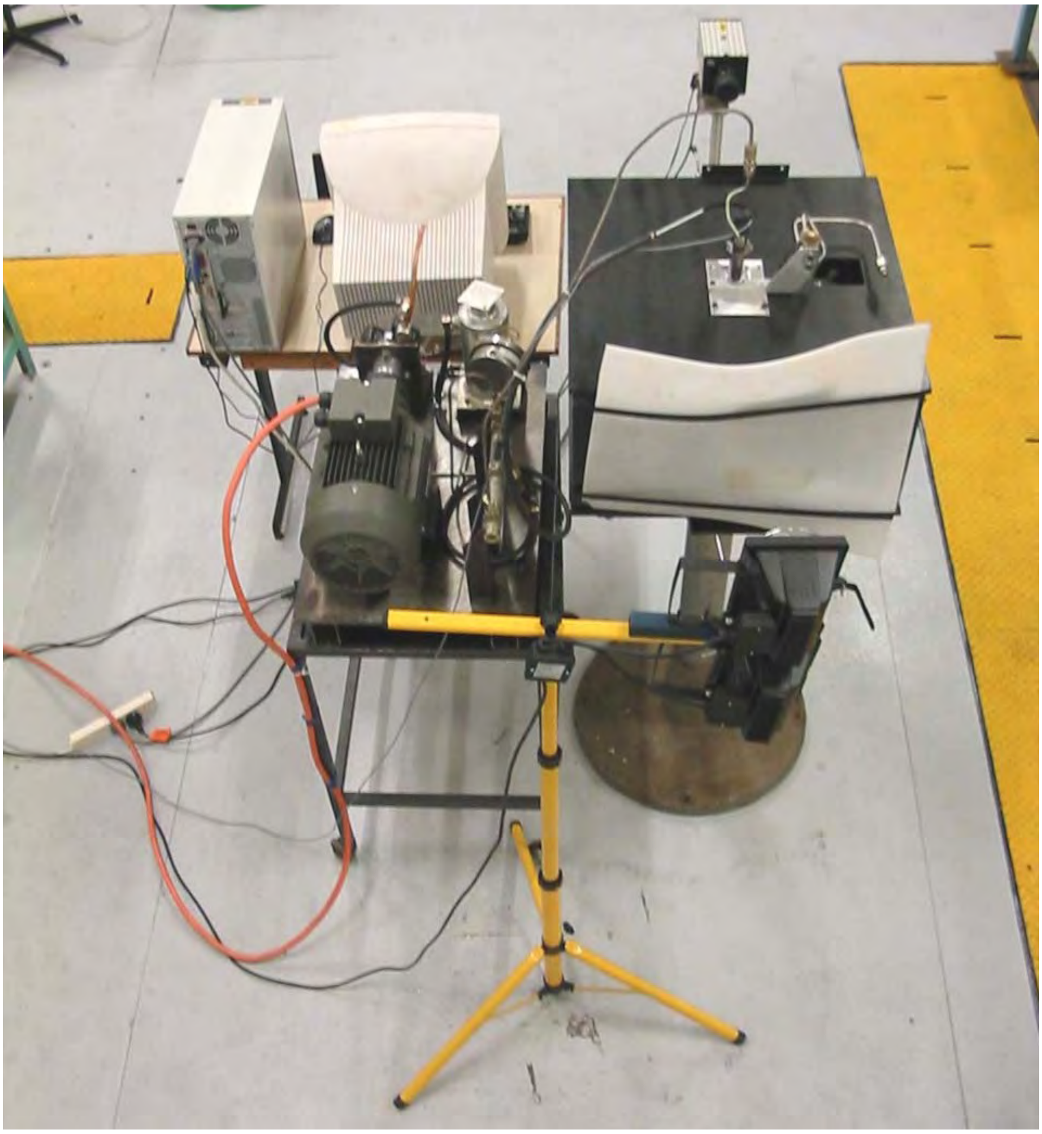

Photo 4.13. Back-lighting set-up for the JVB.

4.4.1.2 Shadowgraph Imaging

The shadowgraph is a relatively simple technique that enables otherwise invisible features in a gas to be made visible. In this application, it was used to capture images of both the diesel and gas jets alone as well as some images of the mixing jets. Vapour regions in the diesel jet which would, using backlighting, be invisible to the camera were also able to be detected using the shadowgraph. Similarly, the boundaries of the gas jet were able to be determined.

The shadowgraph system in its simplest form consists of a small, bright light source, a collimating lens or concave mirror and a viewing screen or photographic plate as shown in Figure 4.9. If the air in the test section is stagnant then the intensity of illumination on the screen or plate is uniform. When flow is established in the test section (assumed here for simplicity to be two-dimensional with each light ray passing through a path of constant-density air), any light ray passing through the region in which there is a density gradient normal to the light direction will be deflected (refracted) as though it had passed through a prism [134].

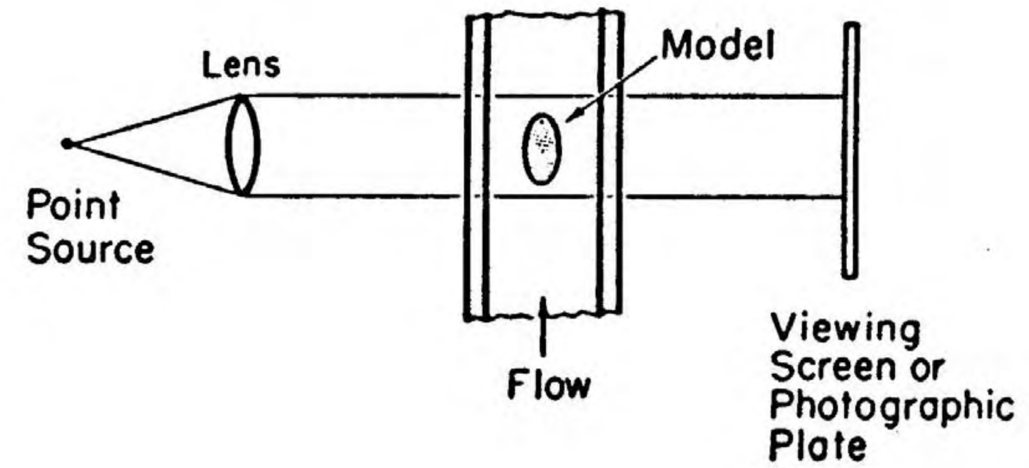

Figure 4.9. A simple shadowgraph system [134].

This refraction then causes the collimated beams to either converge or diverge, thus creating areas of either relative illumination or darkness to form onto whatever medium the image is being projected. Usually the image is projected onto a photographic plate although a camera can, with careful placement, be situated directly in the beam as described in Section 5.1.3. A limitation of the shadowgraph system for flow visualisation is that if the density gradient in the flow is constant, every light ray will be deflected by the same amount and thus there will be no change in illumination on the photographic plate. Therefore, only if there is a gradient in the density gradient will there be cause for the light rays to either diverge or converge. For this reason, the shadowgraph is suited mostly to flows with rapidly-varying density gradients and is insensitive to flows with gently-varying gradients. It is an easy way of making shock waves visible.

The Aerodynamics Laboratory within the School possessed a shadowgraph system which included a slit light source (in the form of a spark generator) and collimating optics (two mirrors). These components were all housed in a large box as shown below in Photo 4.14.

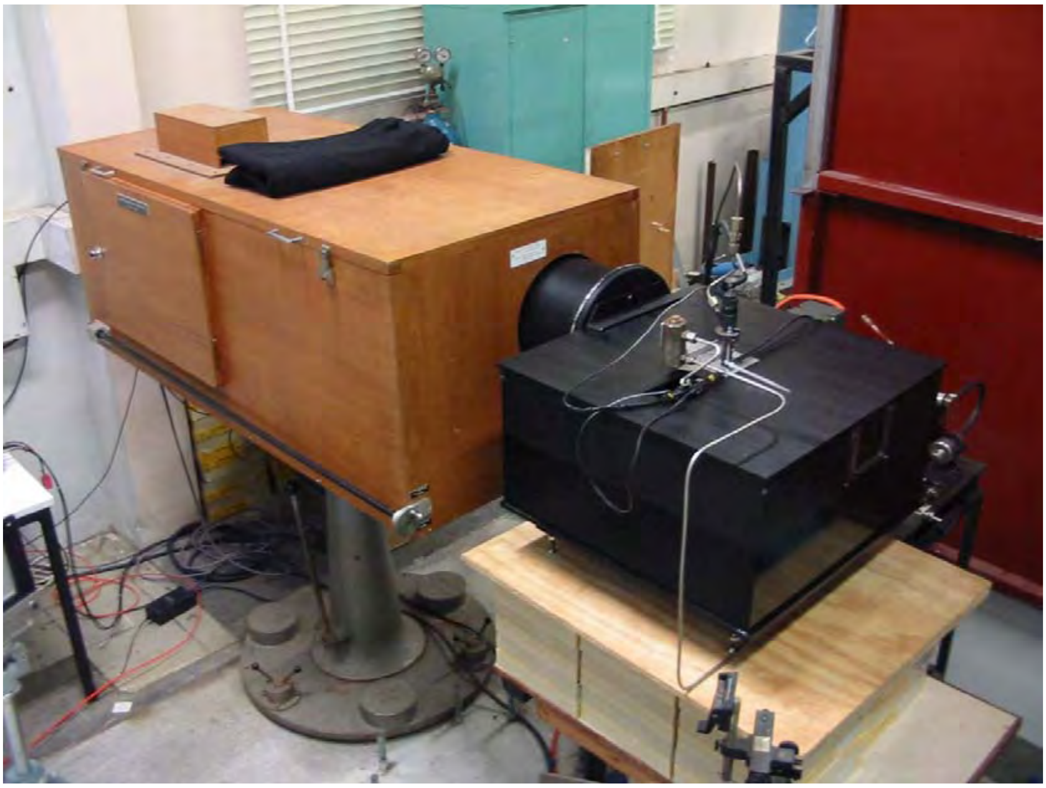

Photo 4.14. The School's shadowgraph system shown mated to the JVB.

4.4.1.3 Schlieren Imaging

A development of the shadowgraph system is the schlieren system. The word *schlieren* is German for "shadows". Figure 4.10 shows a schematic layout of a schlieren system. Part of the system consists of the same equipment as a shadowgraph set-up: light from a uniformly-illuminated slit/line source of small but finite width is collimated by a lens or concave mirror before passing through the test section. In a schlieren system, after the light has passed through the test section, it is brought into focus by a second lens or mirror before being projected on a plate or screen. At the focal point, where there exists an image of the source, there is introduced a knife-edge which cuts off part of the light.

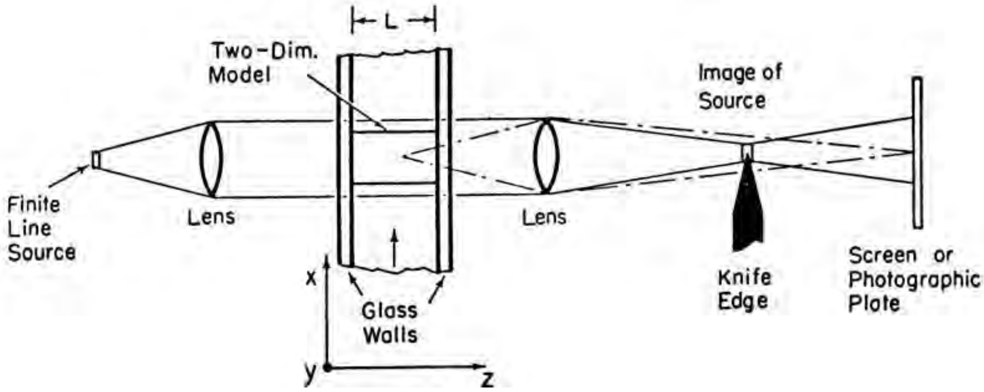

Figure 4.10. Schematic diagram of a schlieren imaging system [134].

With no flow in the test section the knife-edge is usually adjusted so as to intercept about half the light. The screen is uniformly illuminated by the portion of the light escaping the knife-edge. Like the shadowgraph, when the flow is established in the test section, any light ray passing through the region in which there is a density gradient normal to the light direction will be refracted. But in the schlieren system, depending on the orientation of the knife-edge with respect to the density gradient and upon the sign of the density gradient, more or less of the light passing through each part of the test section will be intercepted by the knife-edge. Only the light that escapes the knife-edge will illuminate the screen. Thus the schlieren system makes the actual density gradients visible in terms of intensity and illumination rather than the gradient of the gradient upon which the shadowgraph relies.

The Aerodynamics Laboratory within the School also had equipment that could be used to set-up a schlieren system. The light source consisted of a Mercury-vapour lamp with an adjustable aperture. Collimating and focussing was achieved with two mirrors, each with a focal length of 60 inches. A clamp fitted to a height-adjustable stand was used to hold a knife-edge which, in this work, consisted of a safety razor-blade. A schlieren set-up for the current work is shown in Photo 4.15.

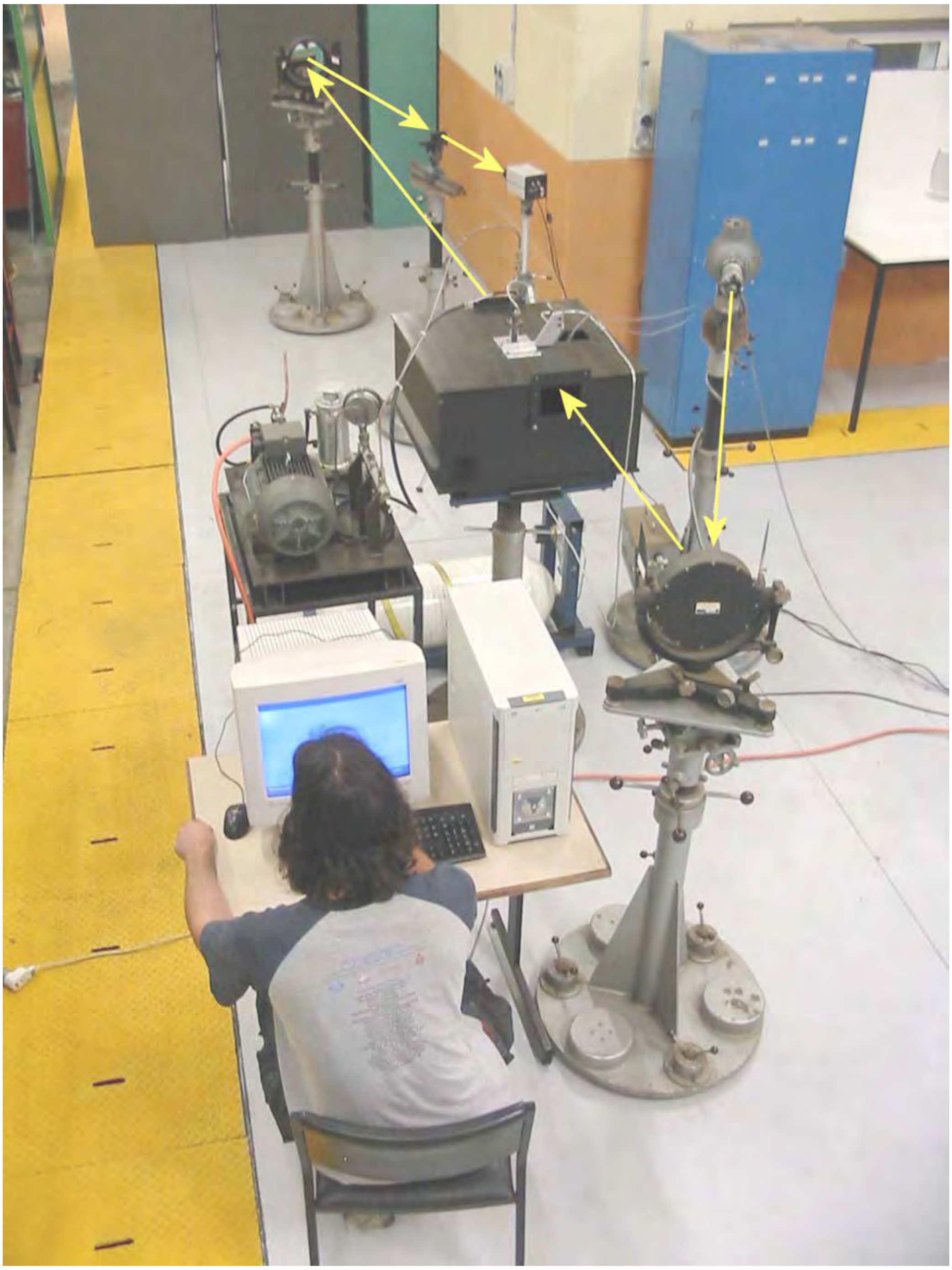

Photo 4.15. The School's schlieren imaging system, modified and installed as part of the current work. In this particular set-up, light from the slit-source is collimated by the first mirror before passing through the test section. Then, the light is focussed by the second mirror and intercepted by the knife-edge before being captured by the camera. Analysis may then be performed as it is here by J.M. Middelberg.

4.4.2 Camera Equipment

4.4.2.1 Polaroid Film

The first method used to capture images was Polaroid film. Such film, in a 5” x 4” format, had been used in the Aerodynamics Laboratory in conjunction with the shadowgraph system for many years. That film had since been superseded by 4¼” x 3¼” film and so a new film holder was purchased for the work here. A photograph of the new film-holder assembly (assembled to the JVB) is shown in Photo 4.16.

Photo 4.16. The School’s shadowgraph system shown mated to the JVB. The new Polaroid film holder is in the foreground.

4.4.2.2 CCD Still Camera

The digital camera used here was the SensiCam *Fast Shutter* made by the PCO company of Bavaria. It was purchased by the School as part of a PIV (Particle Imaging Velocimetry) system in 1999. The camera is black-and-white only but provides pictures with 1280 by 1024 pixel resolution. It was originally fitted with a conventional lens which had both variable aperture and focus but fixed zoom. In the current work, the camera was connected to a PC card with a fibre-optic link. Software on the PC controlled both the delay and exposure time of the camera and allowed up to 74 frames from the camera to be stored at a time. External triggering of the camera was achieved by connecting the external trigger source to the camera's PC card using a standard BNC cable.

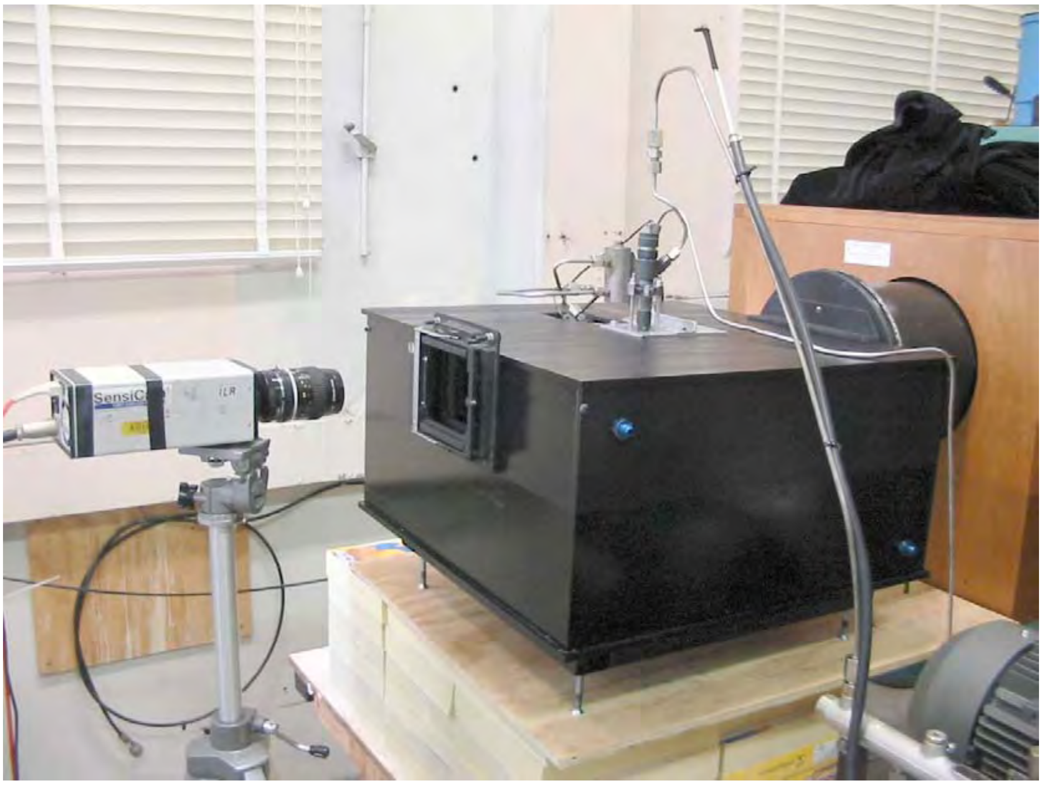

Photo 4.17. The PCO "SensiCam" camera in use with the shadowgraph.

Whilst visualising high-speed jets was not its intended application, the camera proved suitable owing to its extremely high electronic "shutter" speed. An effective exposure time of 2 μs was used for the current work. Unfortunately, the camera can only take pictures at a rate of 8 frames per second and owing to the short duration of the DF injection, the camera when used in this work could capture only one frame per injection.

4.4.2.3 High-Speed Video Camera

At around the time that the JVR became fully operational, the School purchased a high-speed video camera. The *X-Stream XS-4*, manufactured by IDT of Florida, is capable of taking 5,000 frames per second at a resolution of 512 x 512 pixels. In its configuration for the current work it was used to take a frame measuring 512 pixels wide by 128 pixels high at a rate of 20,000 frames per second (fps). The physical size and appearance of this camera is similar to the still camera shown in Photo 4.17.

5. Chapter Five: Commissioning the Test Rig

5.1 Evaluation of the Photographic Techniques

Setting-up the dual-fuel visualisation rig and taking results from it was an evolutionary process. A timeline of the progress through the different methods of testing is shown in Figure 5.1. Detailed below are the relative merits of each of the combinations of photographic techniques and the equipment used.

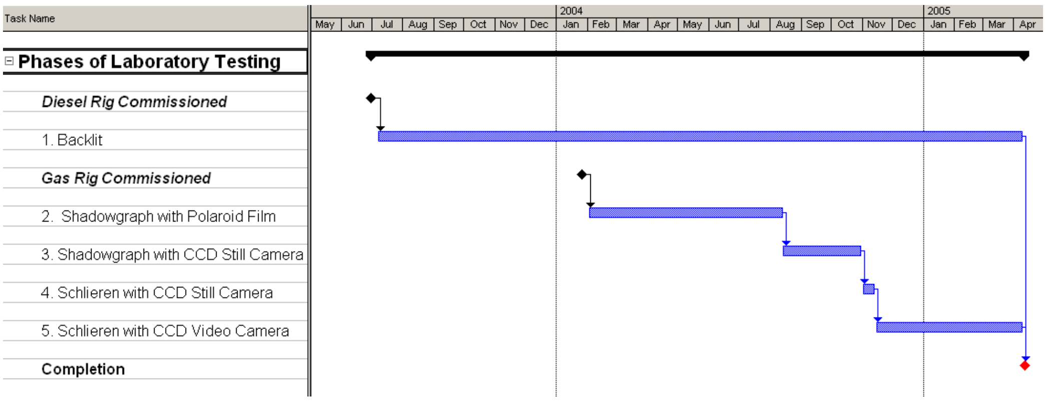

Figure 5.1. Timeline of set-up and testing

5.1.1 Backlit Photography with the Digital Still Camera (Diesel Spray Only)

The Diesel Delivery System (DDS) was the first part of the rig to be completed. Some investigative photos of the diesel spray were recorded using backlighting and the CCD still camera. This simple photography provided useful information about the shape and penetration rate of the diesel jet. Early photography work concentrated upon learning about the properties of this HPCR system.

The diesel jet proved to be highly repeatable – subsequent photographs taken at the same injection and photographic timing showed that the actual start of injection (SOI) for the HPCR injector varied by only 10 μs. Thus, for a set delay between injection and photography, the variation of the penetration of the spray was only a few millimetres between subsequent photos. This meant that a penetration history of the diesel jet could be satisfactorily built-up using the still camera. To this end, series of photos were taken with the delay between SOI and triggering of the camera being gradually increased. Backlit photographs from the still camera were similar to those taken later with the video camera as shown in Section 5.2.

About six months later, after completion of the DDS, the gas injection system was ready to try and this facilitated the employment of shadowgraph optics so as to be able to see the gas jet. The School's shadowgraph system was set-up initially with Polaroid film.

5.1.2 Shadowgraph Imaging with Polaroid Film (Diesel Spray and Gas Jet)

Many issues presented themselves with the thirty year-old shadowgraph system. Repeated failures of small components such as plastic (insulating) fasteners and other electrical connectors caused many delays in gathering results.

For any type of photography, there exists two ways of controlling the amount of exposure of either the film in a conventional camera or the CCD element in a digital camera. One method is to control the intensity and duration of the light-source. The alternative is to control the duration of the opening of the shutter or, in a CCD camera, the charging-time of the elements. Since the Polaroid film was not fitted in a camera with a shutter, exposure of the film was set by controlling the duration and intensity of the light source. The light source in the shadowgraph equipment consisted of a spark generator (Photo 5.1) and so the duration was essentially fixed to about 20 μs of spark time. The intensity of the spark could be controlled with an aperture (Photo 5.2).

Since there was no shutter and so as not to expose the film before or after a test was run (ie. a photograph taken), the Polaroid film had to be loaded and unloaded in complete darkness. Light was excluded from the test section using the techniques described in

Section 4.3.1. As further insurance, all testing with the Polaroid film was carried-out at night. A few minutes were required for the film to develop after each frame was captured. All the photos were scanned into a digital format so that they could be compared in an efficient manner.

Photo 5.1 The spark generator inside the shadowgraph box.

Photo 5.2 The adjustable aperture on the spark generator.

After the first photos were taken, it was realised that the optical quality of the acrylic walls of the JVB was not as good as was required. Acrylic is not a very hard plastic and as a result the walls of the box were susceptible to damage. Despite all reasonable precautions being taken during construction of the box, the wall surfaces through which light from the shadowgraph passes through to the camera or film contained many scratches and blemishes which showed-up on the film as solid, dark lines as witnessed in Photo 5.3. To overcome this problem, the acrylic walls adjacent the region of the test section were removed and replaced with glass inserts which could be easily replaced if the need arose.

Images taken with the Polaroid film enabled an idea of how well the gas injector was working. They allowed the identification of the non-choked flow from the first gas nozzle as described in Section 4.3.4 which prompted modification of the nozzle to be started in parallel with the setting-up of the CCD still camera. Yet the cost of the film and the time it took to digitise the results proved prohibitive. The Polaroid film was thus replaced with the CCD still camera.

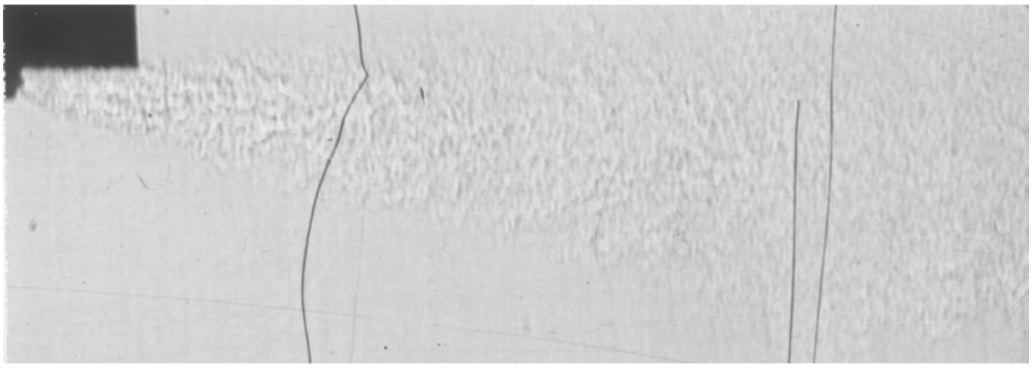

Photo 5.3. An early result using the Polaroid film. Three large scratches on the acrylic wall can be seen as near-vertical lines.

5.1.3 Shadowgraph Imaging with the CCD Still Camera

The spark-generator and collimating optics of the shadowgraph were retained whilst using the CCD camera for shadowgraph imaging. Despite now having more flexibility with a proper camera and electronic control, a lot of effort was required to actually form the shadowgraph image for capture. The first tests were carried-out with the camera placed directly in-line with the test section such that the collimated light would enter the lens directly. The result was that an image of only part of the test section was obtained.

The effectiveness of both the shadowgraph and schlieren systems rely on refraction of collimated light. Even after the light passes through the test section, it remains mostly collimated. Early runs with the CCD camera in the shadowgraph beam revealed that the normal camera lens, designed for operating in conditions of dispersed light, was not suitable for operation in the collimated light beams. The light appeared to exit the back of the lens still collimated. When using the large-format Polaroid film this clearly is not an issue since an actual-size image is formed on the film. When using a conventional lens for the CCD camera in this work, however, it resulted in an image being captured that was the size of the camera's aperture, ie. a diameter of about 15 mm. Since the work here was involved with simulating the conditions in an engine with a cylinder bore of at least 100 mm, this meant that the small pictures were not very useful. Two alternatives were found to enable large-image capture with the shadowgraph: the use of a photographic plate and the use of a "telecentric" lens.

5.1.3.1 Using a Photographic Plate to form an Image

The first way to increase the effective field-of-view was the employment of a photographic plate or screen as mentioned previously in Section 4.4.1. Such a device was ubiquitous in the early days of photography and is still common in large-format photography to set the focal length of bellows-type cameras. Bellows cameras, as shown in Photo 5.4, were in widespread use before the advent of variable focal-length lenses. They consist essentially of two parallel boards which are connected by bellows. The lens is fitted into the front board whilst the back board includes the film-holder. The focal length between the lens and the film is set by changing the distance between the lens-board and the film-holder or by moving the lens independently. The bellows allows for this adjustment whilst still isolating the film from ambient light.

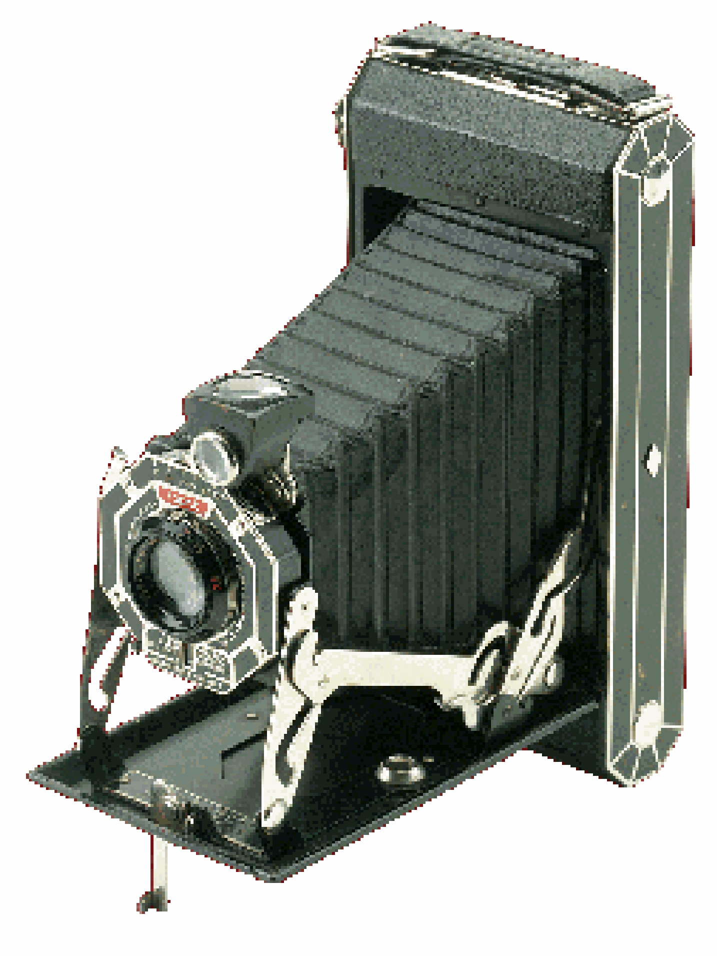

Photo 5.4. A bellows camera with the lens-board at the front and the film-holder in the board at the back [80].

To test whether the image to be projected on the film would be in focus, the photographer would first fit in place of the film a sheet of ground or "frosted" glass. The light would be diffused on the rough surface of the glass and so an image could be seen upon it. Once the focal distance was determined for the particular lens in use, the ground-glass was removed and the film was installed so that a picture could be taken.

In the work here, a high-quality ground-glass screen was ordered from *BosScreen* in The Netherlands. This "photographic plate" was used to momentarily show the shadowgraph image so that it could be captured by the CCD camera. In this way, instead of the CCD camera directly photographing the test section and receiving its collimated light, it captured the image projected onto the plate. The light coming from the plate was no longer collimated and thus a normally-sized photo was taken. Use of the photographic plate allowed an image to be captured of the entire region-of-interest of the jet. This region extended to a jet penetration length of about 50 mm which is about the radius of the bore in a modern, mid-sized diesel engine. Yet owing to the etching on the plate, resolution of the photo of the glass screen was not, of course, as good as the photo taken directly of the test section. Further, when using low "shutter speeds", it was found that too much light was diffused by the plate and the image proved to be too dark.

Photos 5.5 and 5.6 show sample photographs taken using the photographic plate and normal zoom lens respectively. Neither of these methods of photography proved adequate and so an alternative solution to viewing the entire region-of-interest was sought.

5.1.3.2 Using a Telecentric Lens

Telecentric lenses are normally used in machine-vision applications to create an image that is free of perspective distortion. As shown in Figure 5.2, the aperture of the telecentric lens is positioned directly at its focal point and so only parallel (or almost parallel) rays are able to pass through this aperture. Therefore, as the reflecting object seems to be infinitely remote, there can be no perspective distortion [147]. Owing to the special optics inside the lens, it was found that the image captured by the CCD camera was now equivalent in size to the diameter of the objective (front) lens. This was about 40 mm which was deemed adequate for this study. Further, it provided a much clearer image than the photographic plate and allowed faster exposure times since no intensity was lost through the ground-glass.

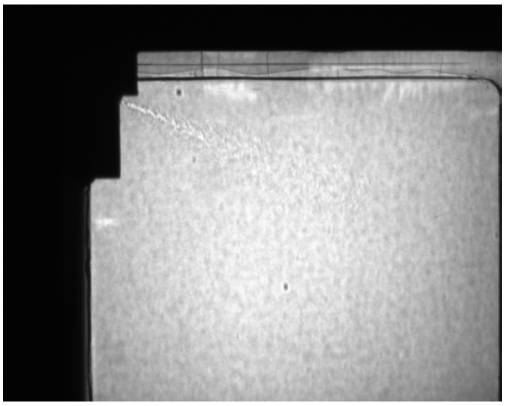

Photo 5.5. Large-field but low resolution image using the ground-glass screen.

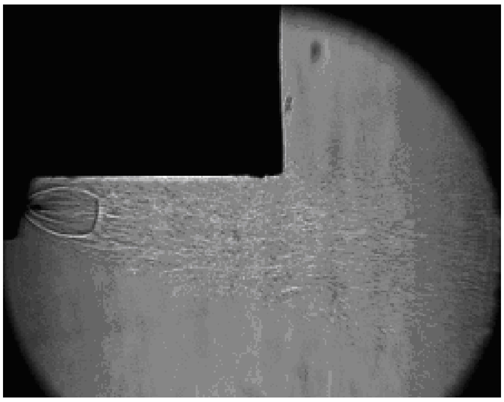

Photo 5.6. High resolution but small-field image using a normal lens with no screen.

The CCD still camera provided a quick and easy way to obtain pictures. Photos of quality as good as that in Photo 5.6 were obtained but this time for a field-of-view with a diameter of about 40 mm rather than the 15 mm as with the normal zoom lens. Still, the boundaries of the gas jet were not defined as well as had been hoped and so it was decided to try a schlieren system.

5.1.4 Schlieren Imaging with the CCD Still Camera

Setting-up the schlieren optics was carried-out in between test sessions of the shadowgraph system with the CCD camera. Again, the spark-source and collimating optics of the shadowgraph box were retained. A focussing mirror and knife-edge holder were added to the system. As with using the CCD camera in conjunction with the shadowgraph-only optics, the ground-glass screen was found to reduce the intensity of the image too much. Thus the telecentric lens was again placed directly in the beam, ie. where the photographic plate is shown in Figure 4.10. Use of the telecentric lens with the schlieren optics created further challenges. Since in the schlieren system the beams come to a focal point (unlike with the relatively simple shadowgraph), focussing the camera lens is required. Note here that focus of the actual *schliere* was not the issue but rather focussing the boundaries of the test section, ie. the injector etc. so that useful measurements could subsequently be taken from the photographs.

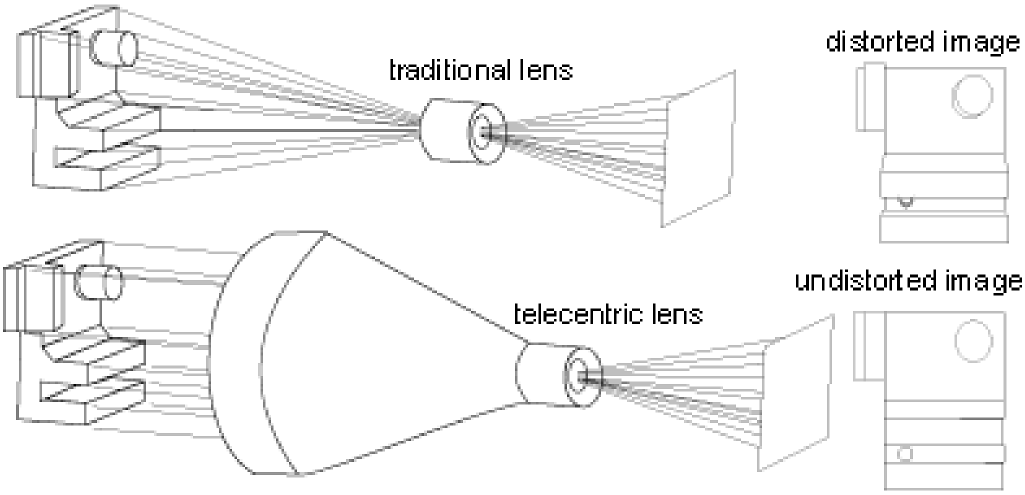

Figure 5.2 The mapping of three-dimensional objects onto a two-dimensional plane with a telecentric lens is based on a parallel projection. The resulting image appears like an orthographic projection [147].

The correct positioning of the focussing mirror and camera within the beam also proved critical to achieving an image that was focussed. This was because the “conjugate distances” of the optical system needed to be considered as shown in Figure 5.3. The camera/telecentric lens assembly needed to be placed in the beam and the focus of the lens set so that an image of the appropriate size would fall onto the CCD element. A good set-up was found when the following distances were used as shown in Figure 5.4:

Test Section/Focussing Mirror:	6,000 mm
Focussing Mirror/Knife Edge:	1,524 mm (60”, the focal length of the mirror)
Knife-Edge/Front of Camera Lens:	710 mm
Focal Length of Camera Lens:	160 mm

Therefore the focal point of the image was (710-160) = 550 mm, about one-third of a focal-length from the knife-edge. This meant that the actual image size being caught by the camera had a diameter of about 22 mm since the conjugate distance/object distance = 550/1,524 mm and the original image size had a diameter of about 60 mm.

$$Size = \frac{550}{1{,}524} \times 60 \approx 22mm$$

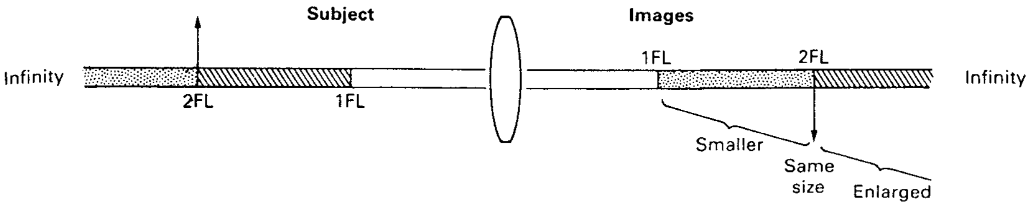

Figure 5.3. Determining conjugate distances [80].

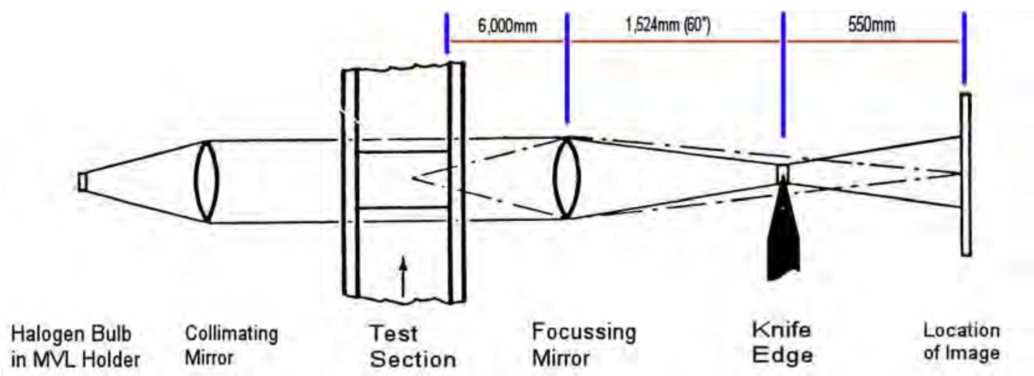

Figure 5.4. Conjugate distances used with the schlieren system.

With the adaptation of the schlieren system it was found that imperfections in the new glass windows on the JVB resulted in shadows that were affecting the results. Photo 5.8 shows a sample schlieren image where the effect of the glass pane over the viewing ports can be seen. In the test from which this image was captured, one of the two glass panes was removed completely and the top part of the second pane was broken off. In the sample image, the top part is where there was no glass located in the beam. The boundary of the jet in this top part of the image can be seen with relative clarity. The darker, lower section of the photograph is where the glass remained and the boundary of the jet can be seen here to be lost in the shadows which have occurred by distortion of the collimated beams as they passed through the glass. As a result of this finding, the glass windows were removed completely and the viewing ports in the box were left as open holes.

Photo 5.7. Extra equipment required to turn a shadowgraph system into a schlieren system. From left: focussing mirror, knife-edge holder and the Mercury-Vapour Lamp that would later be used as a light source for the video camera.

Replacing the shadowgraph optics with a schlieren set-up yielded excellent images of the gas and dual-fuel jets but where the gas jet alone was concerned, the pictures were not very useful. As mentioned previously, the diesel jet was highly consistent in its timing between injections. This meant that a penetration history of the jet could be reliably constructed from a series of still photos taken at sequential time intervals. This was not the case, however, for the gas jet. Owing to the GCV being built from a modified HPCR diesel injector, the actual SOI of the gas varied by up to 1.0 ms between injections. For this reason, the only way to reliably study the penetration history of the gas jet was with a video camera.

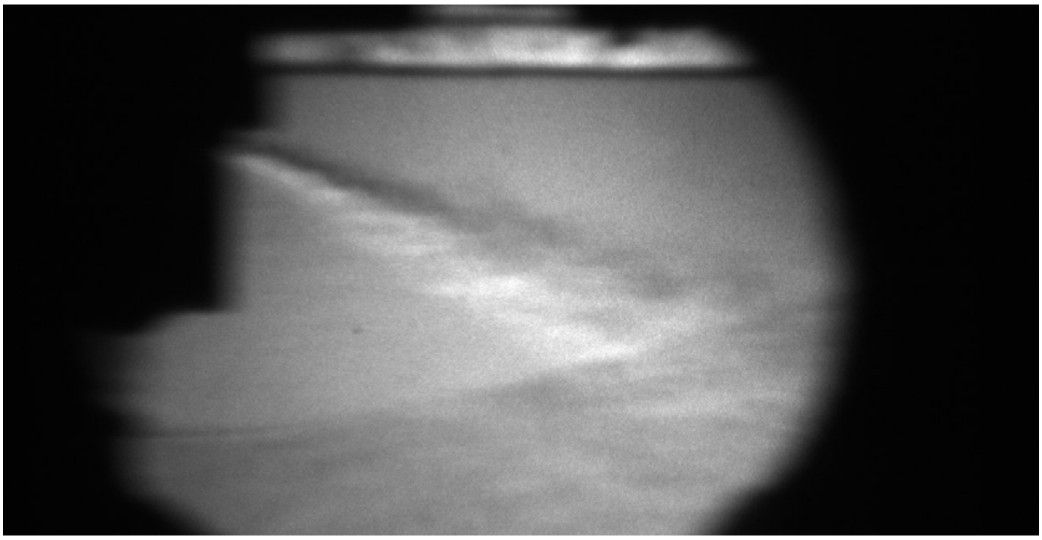

Photo 5.8. Sample schlieren image showing the effect of the glass windows

5.1.5 Schlieren Imaging with the CCD Video Camera

The high-speed CCD video camera was delivered to the School in November 2004. Whilst expensive, it proved to be the item of equipment that at last allowed useful results to be gleaned from the JVR.

The video camera was fitted with the telecentric lens and placed directly in the beam as described above for the still camera. Since a series of photographs were now to be taken, a constant light-source had to be found to replace the spark-source from the shadowgraph equipment that had been used until this time. At first, the Mercury-Vapour Lamp (MVL) assembly as used by the Aerodynamics laboratory for taking still schlieren photos was used. This assembly consisted of a Mercury-vapour discharge globe mounted in a housing (Photo 5.9) which was then mounted on a height-adjustable stand. The housing was complete with a variable aperture (Photo 5.10) that would later prove indispensable for adjusting the amount of light through the system. Since the shadowgraph box had been done-away with, the collimating optics also needed to be replaced. Another of the Aerodynamics Laboratory's 60" focal-length concave mirrors was used to achieve collimation of the light.

Photo 5.9. The MVL's bulb-holder and aperture assembly.

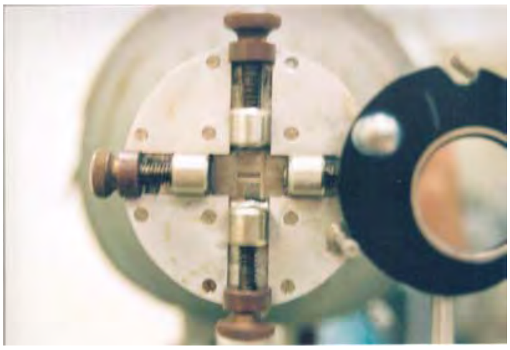

Photo 5.10. The MVL's adjustable aperture.

Whilst very bright, because the MVL's bulb used AC power and was a vapour-discharge light source rather than having a filament, the intensity of the light source was found to pulse at 50 Hz - the frequency of the mains power. To overcome this, an adaptor was made so that a conventional 12-volt DC bulb as used in an automotive driving-light could be placed in the holder. This 100 W halogen bulb was subsequently powered by a 12 V truck battery and provided ample intensity for the schlieren system. Pictures of the original and modified light sources are shown in Photos 5.11 and 5.12.

As described previously, the only way to effectively study the gas jet using the injector built for this study was to use video rather than still footage. Careful set-up of the schlieren optics allowed the full field of interest to be studied and provided a very well-defined outline of the gas jet as shown in Photo 5.13. Not only was a better outline of the gas jet able to be seen but turbulent structures within the jet were shown in detail. A photographic technique and camera combination had at last been found that would provide satisfactory results for this study.

Photo 5.11. The standard vapour-discharge bulb assembly (right) on its mount and the new halogen bulb and its holder (left).

Photo 5.12. The new halogen bulb and its holder assembled to the bulb mount.

Backlighting with CCD Video Camera

Whilst an acceptable penetration history of the diesel jet could be achieved with staged still photos, clearly there were advantages with using a video camera. Using video meant that not only would the growth of the jet be able to be more accurately measured but the development of instabilities within a jet could also be monitored and the break-up process more fully understood. Thus the use of the high-speed video camera provided a significant benefit for photographing the diesel injection as well as the gas.

Photo 5.13. Sample frame taken from the high-speed schlieren video.

5.2 Characteristics of the Diesel Spray

To gain an understanding of the operating characteristics of the diesel injector around which the Jet Visualisation Rig had been built, photographs of the diesel spray alone were taken using both backlighting and shadowgraph techniques in conjunction with the high-speed CCD video camera. For backlighting work, two 500 W floodlights were placed behind a translucent plastic sheet as described previously and shown in Photo 4.13. The diffuse light beams were able to penetrate the diesel vapour and so the boundary of the diesel liquid/gas phase was able to be viewed. Then, using the shadowgraph equipment whereby the parallel light beams would be refracted by the diesel vapour, a better indication of the boundary between the vapour phase and the ambient air was established.

5.2.1 Optimum Operating Pressure

As discussed in Section 3.2, modern injectors are designed to operate at a pressure and flow-rate set to maximise atomisation of the fuel. Injectors designed this way usually operate with nozzle flow in the cavitation regime [140] so it was reasonable to expect that the nozzle here would show signs of cavitating flow.

Photo Sets 5.14 through 5.19 show series of photographs of diesel injections at pressures between 60 MPa and 160 MPa. In each case, the electrical pulse sent to the injector was of 0.3 ms duration. This resulted in an actual (hydraulic) injection time of about 0.5 ms at the lowest pressure of 60 MPa, increasing to a duration of about 0.8 ms at 160 MPa. The delay between the start of the injection signal and the hydraulic SOI varied between 0.3 and 0.4 ms, the delay decreasing as the pressure increased. Each frame shows a scale in the top-right corner where each line on the scale corresponds to one millimetre of distance. The time scale in the bottom-left corner is the time after the start of the electrical injection pulse, ie. the time after “electrical” SOI.

It can be seen that the diesel spray has quite different characteristics at different injection pressures. At the lowest and highest pressures, the jet is relatively narrow, while at intermediate pressures such as 120 MPa it is more dispersed. This is a function of the nozzle design. For injection pressures lower than 120 MPa, cavitation on the nozzle is probably not as vigorous. For pressures above 120 MPa, cavitation perhaps gives way to (at least partial) hydraulic flip as described in Section 3.2.2. The dispersed spray is more desirable since in an engine it creates a wider burning region immediately after ignition, which desirably should occur in a CI engine between about 0.5 and 1.0 ms after SOI [94].

A review of literature revealed the operating pressure of first-generation Bosch HPCR systems such as the one used here to be 135 MPa [44, 47, 97 and 135]. The pressure in the cylinder of a modern, turbo-charged DI engine could be expected to be around 5 MPa at the end of the compression stroke with pressures rising to perhaps as high as 15 MPa during combustion. When considering this offset to the atmospheric conditions under which the tests here are being carried-out as well as subtle differences in the plumbing of the test rig, 120 MPa in the laboratory could be expected to provide similar diesel flow conditions and injection qualities as 135 MPa in an engine. Considering this and from these experiments, the 120 MPa spray was selected for the DF work.

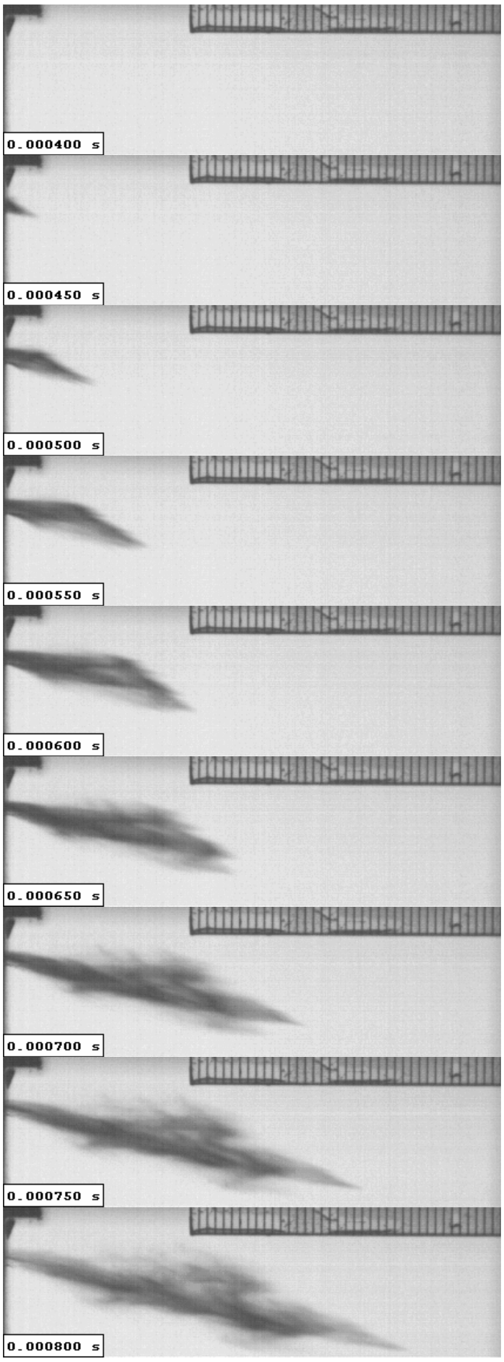

Photo Set 5.14. Jet development with an injection pressure of 60 MPa.

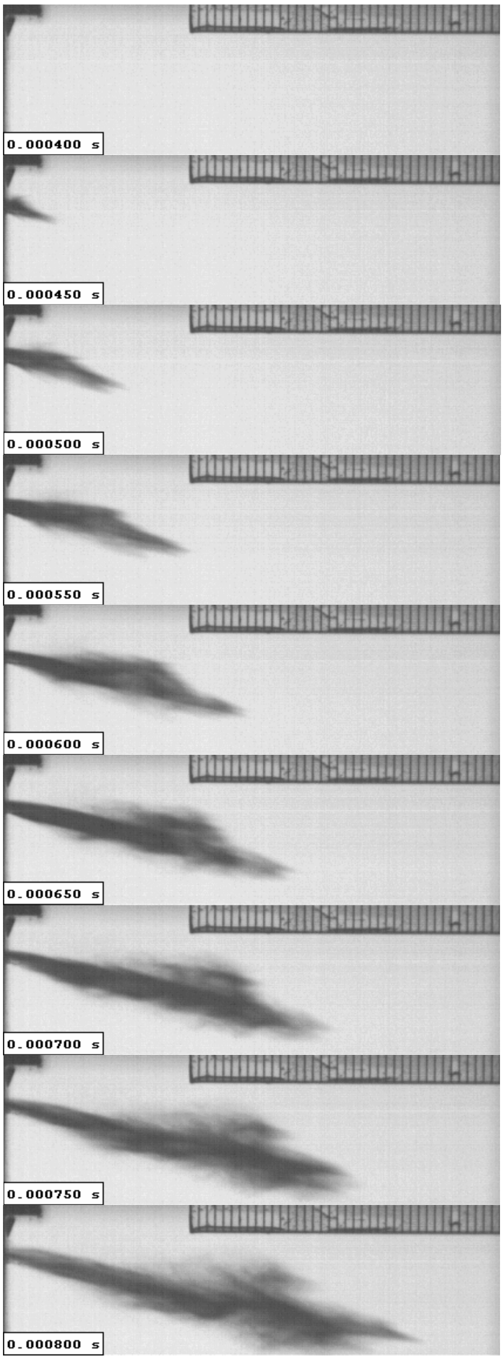

Photo Set 5.15. Jet development with an injection pressure of 80 MPa.

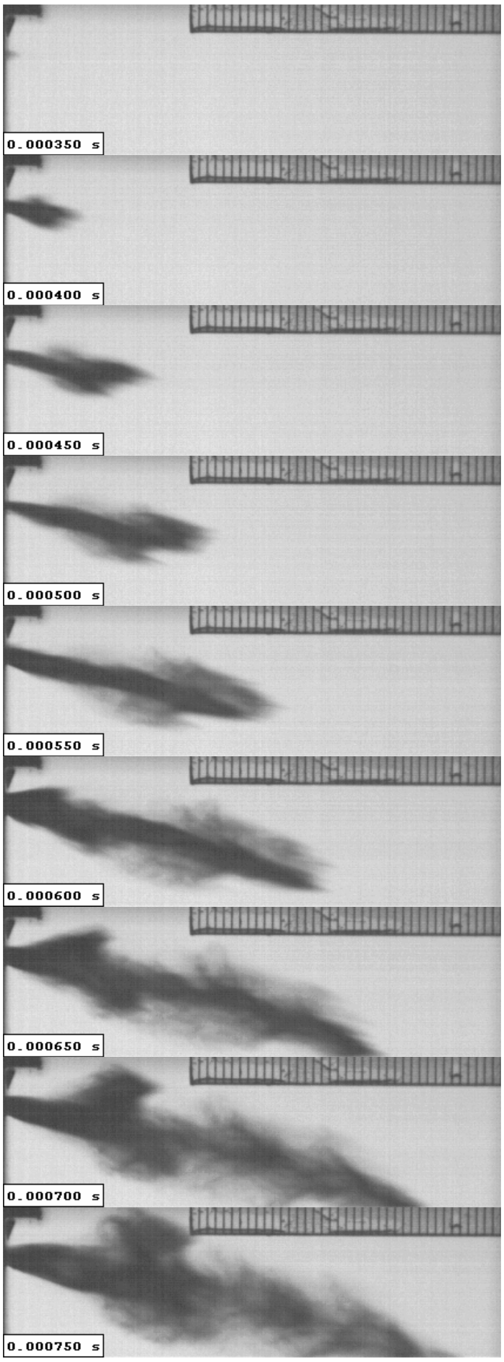

Photo Set 5.16. Jet development with an injection pressure of 100 MPa .

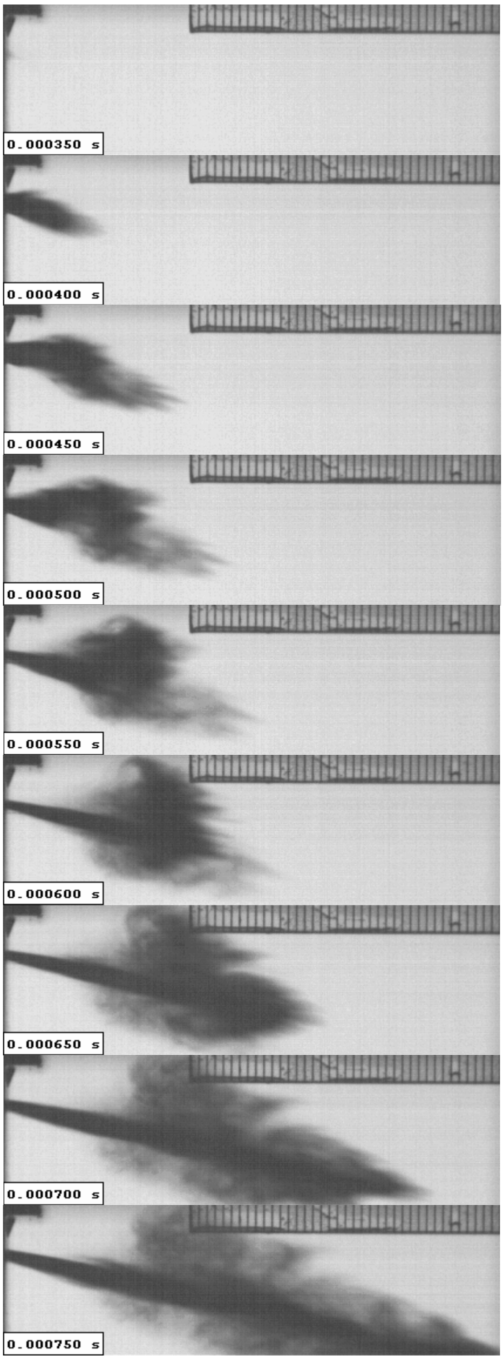

Photo Set 5.17. Jet development with an injection pressure of 120 MPa.

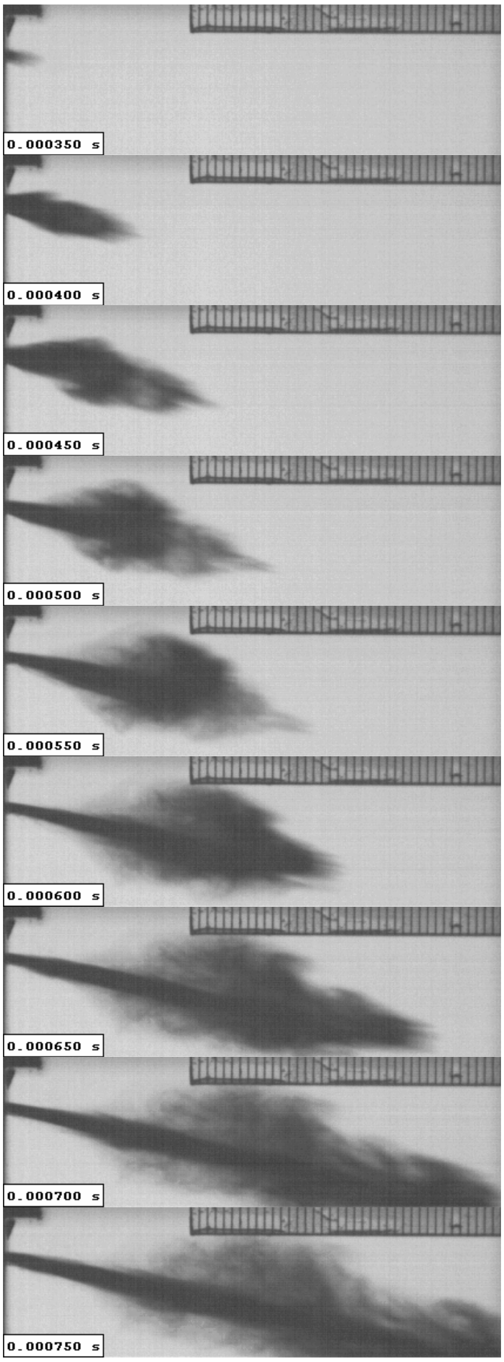

Photo Set 5.18. Jet development with an injection pressure of 140 MPa.

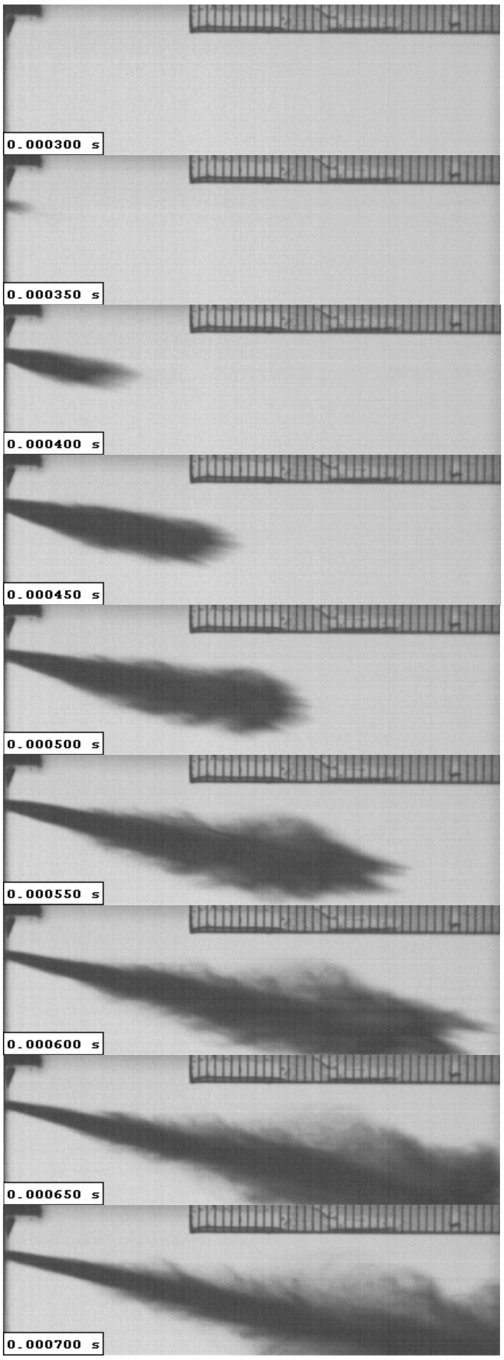

Photo Set 5.19. Jet development with an injection pressure of 160 MPa.

5.2.2 Quantity of Fuel Delivered from the Injector

5.2.2.1 Delivery per Pulse

Results from tests to calibrate the amount of fuel delivered (for each of the six nozzle holes) as a function of injection pressure and injection time are shown in Figure 5.5. Note that the injection time is the electronic pulse time delivered to the HPCR injector from the ECU, not the actual flow time.

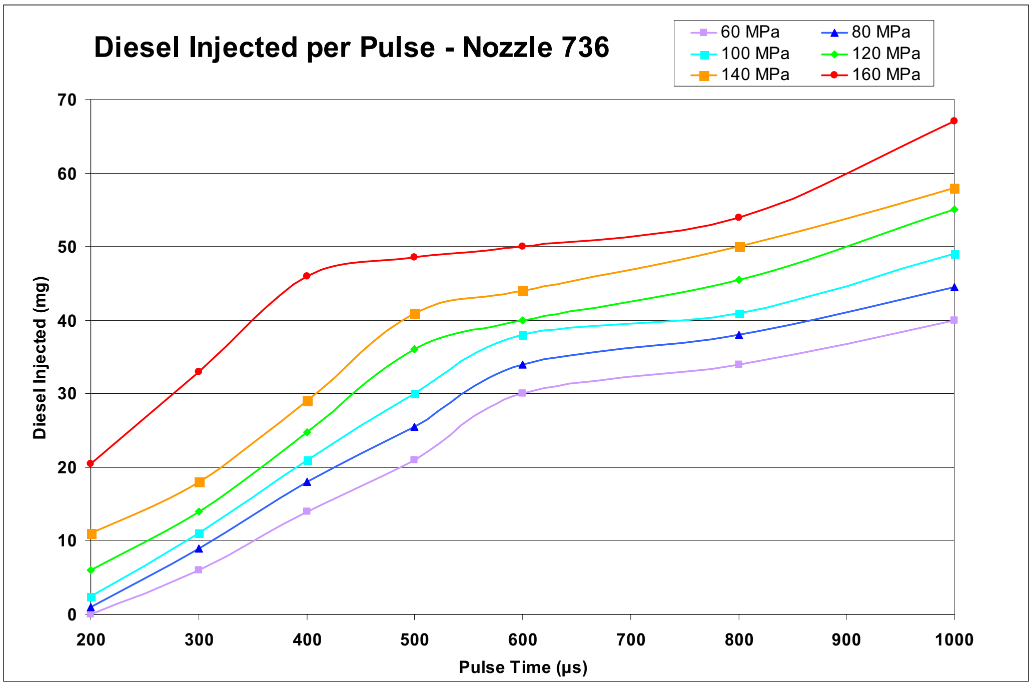

Figure 5.5. Diesel delivery from the HPCR injector used in the current work.

5.2.2.2 Fuel Flow-Rate from the Injector

Whilst the total fuel delivery from the injector is important, equally-so from a performance and emissions point-of-view (as described in Section 2.4) is the actual injection rate. As just described, a complication lies in calculating the injection rate owing to the duration of the electrical signal to the injectors not necessarily being the same as the length of time that diesel actually issues from the nozzle. These delays are caused by hydraulic and other mechanical forces and inertias acting within the injector.

Also, because of the time it takes for the nozzle's needle to fully open and close, the flow from a nozzle is not uniform for the entire duration of injection. The flow rate will gradually increase until such time as the needle reaches full lift. There will then be a period of reasonably steady flow until such time as the needle begins to close. The flow rate will then gradually decrease until the nozzle is fully-seated and the flow stops.

Table 5.1 shows hydraulic injection times for the corresponding electrical pulse times for the HPCR injector operating at 120 MPa which was the pressure chosen for the reasons described in Section 5.2.1.

Table 5.1. Diesel Delivery characteristics of the HPCR injector at 120 MPa.

Electronic Injection Duration (ms)	Hydraulic Injection Duration (μs)	Fuel Delivered (mg)	Flow Rate per hole based on Hydraulic Duration (g/s)
0.1	0	0	0
0.2	133	6	*
0.3	550	14	43
0.4	950	24.75	45
0.5	1,150	36	50

***An unrealistically high rate was calculated for this injection**

Figure 5.6 shows graphically the effective flow rate from each of the six nozzle holes. The flow rate per hole is important in this study since the CFD modelling considers only one hole of each of the diesel and gas injectors.

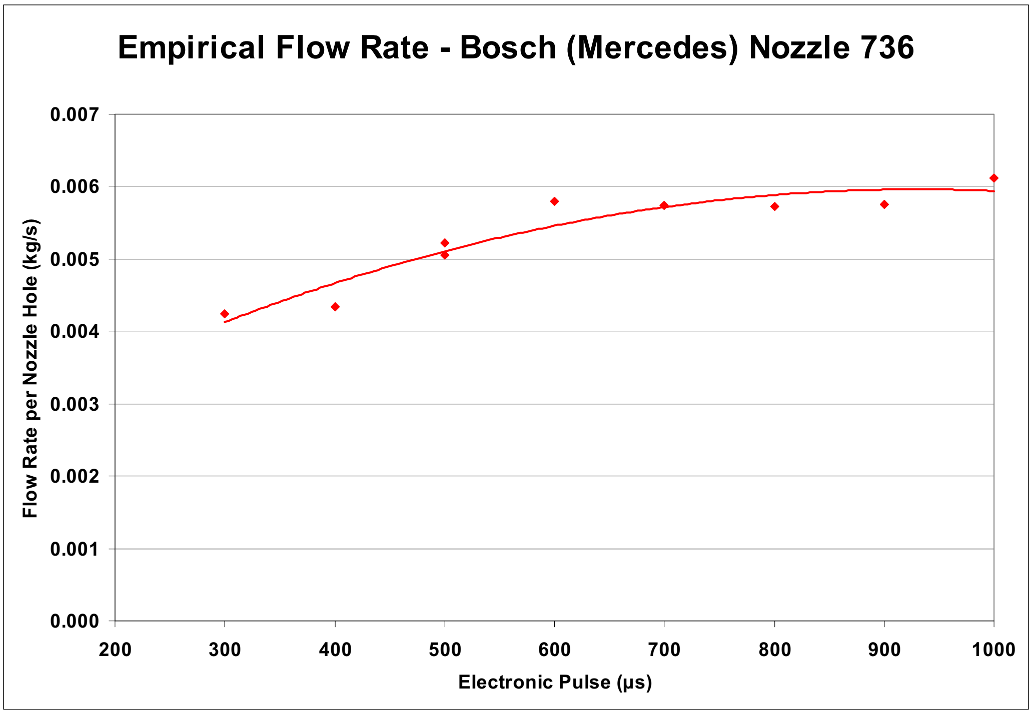

Figure 5.6. Average flow rate per nozzle hole at 120 MPa.

5.2.3 Penetration of the Diesel Spray

To add confidence to the choice of 120 MPa as the injection pressure for the subsequent DF tests, Photo Sets 5.20 through 5.23 compare the penetration of jets at three different pressures. It can be seen that the advance of the jet through the chamber is roughly linear for most of the sprays. The general trend of increasing penetration for higher pressures (for a given time after SOI) can be seen, consistent with the fact that at higher injection pressures the jet will have a higher initial speed. Results from this test have been summarised in the graph, Figure 5.7. An interesting result that may be seen from this summary is the deviation from the general trend of the 120 MPa injection.

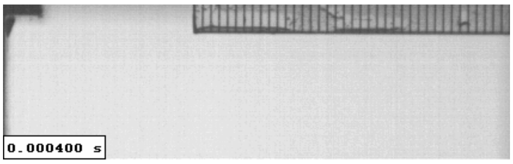

60 MPa

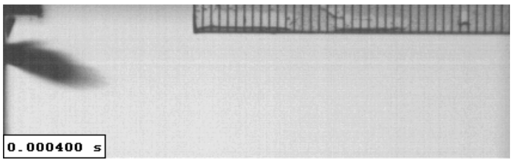

120 MPa

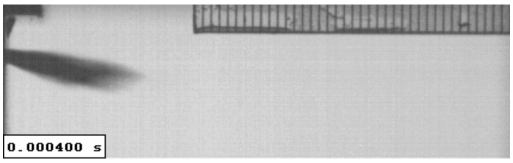

160 MPa

Photo Set 5.20. Relative jet penetration 0.4 ms after the electrical SOI.

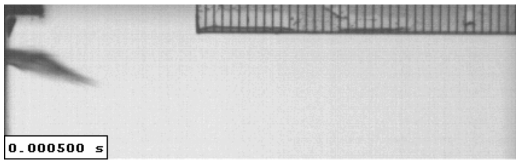

60 MPa

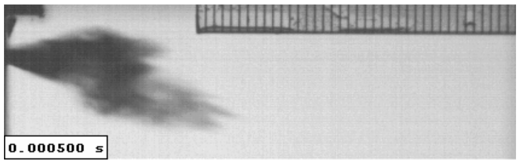

120 MPa

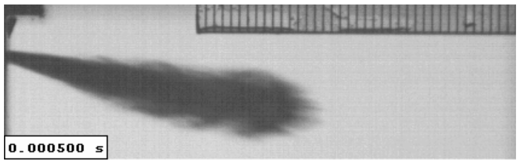

160 MPa

Photo Set 5.21. Relative jet penetration 0.5 ms after the electrical SOI.

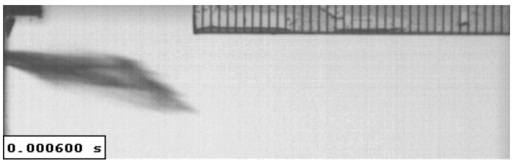

60 MPa

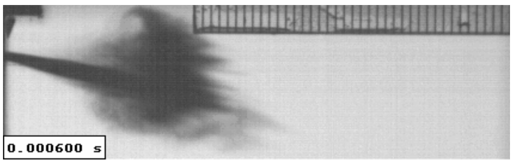

120 MPa

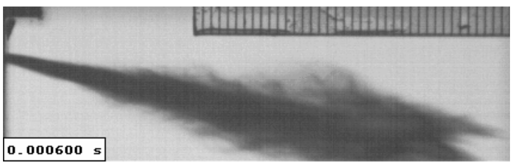

160 MPa

Photo Set 5.22. Relative jet penetration 0.6 ms after the electrical SOI.

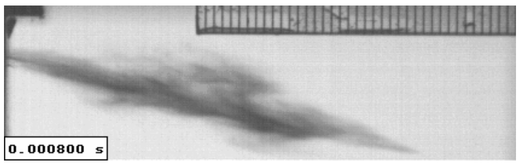

60 MPa

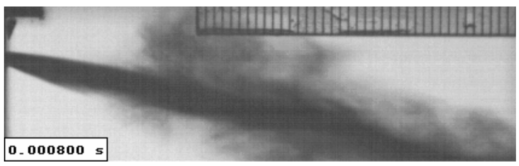

120 MPa

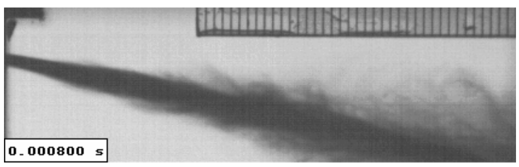

160 MPa

Photo Set 5.23. Relative jet penetration 0.8 ms after the electrical SOI.

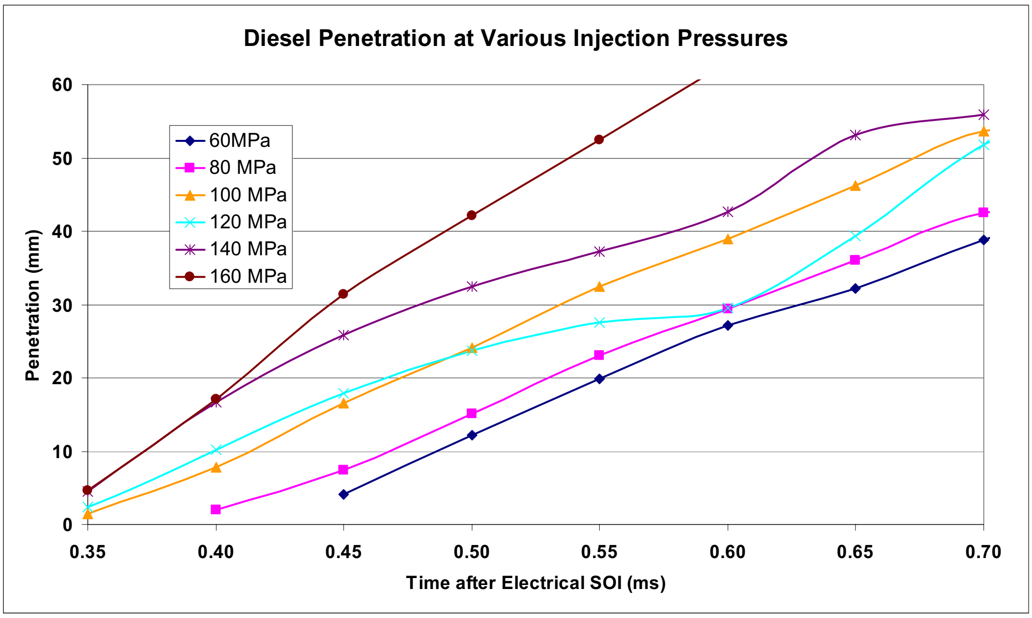

Figure 5.7. Diesel spray penetration as a function of Injection Pressure.

Again it is apparent that the jet at 120 MPa is more dispersed than the others. This is indicative of a higher amount of jet break-up than the other sprays which indicates a higher amount of atomisation. As described in Section 5.2.1, the HPCR system has been designed for an injection pressure similar to this and so the most effective break-up of the spray should be achieved at this pressure. At about 0.2 ms after hydraulic SOI, the rate of penetration of this jet decays compared to the others. This higher rate of atomisation of this jet means that the mean diameter of the droplets of fuel is smaller. These smaller drops have less momentum than larger drops and so their speed decays more quickly because of aerodynamic drag than do the larger drops.

The rate of penetration of the 120 MPa jet then picks-up shortly afterwards which is likely to be a consequence of the still-intact liquid core overtaking the initial parts of the spray which have since atomised and vaporised. In a real combustion chamber, of course, the temperature is much higher than the ambient conditions in the laboratory and the rate of vaporisation of the is fuel much higher. In such a situation this penetration length of the liquid core is unlikely to be seen.

5.2.4 Shadowgraph Analysis of the Diesel Spray

When photographing the diesel jet under conditions of backlighting with a strong lamp, only the liquid regions of the jet can be clearly seen. This is because vapour regions are permeated by the diffuse light and thus are not able to be seen on the photograph. When using the shadowgraph or schlieren techniques, however, the collimated light beams will be distorted as they pass through the vapour regions and so these regions should show as a shadow in the photographs. Shadowgraph was used by Badock et al in 1999 [14] whilst studying cavitation phenomena in the nozzles of HPCR injectors. They also used laser light sheeting to help identify the intact liquid-core in cavitating nozzles as shown in Photo Set 5.24.

Photo Sets 5.25 and 5.26 show backlit photographs of a diesel jet at 120 MPa and of 0.3 ms (electrical) duration compared to shadowgraph images of another jet under the same conditions. The time record shown on the backlit photographs is the time after the electrical SOI. The shadowgraph technique was used here rather than schlieren imaging since the contrast of the images could be more easily controlled and images of better resolution could be obtained this way. In the early photographs the jets appear to be similar. As the jet progresses the results are somewhat counter-intuitive in that the backlit photos seem to show more dark areas than the shadowgraphs. In the late stages, however, from about t = 0.7 ms onwards, the benefit of the shadowgraph becomes clear. In the images following this point in time and especially after the injector's needle has closed, voids begin to appear in the jet in the backlit photographs. The corresponding shadowgraphs, however, show that these apparent voids are actually regions in which the diesel has vaporised and through which backlighting passes uninhibited.

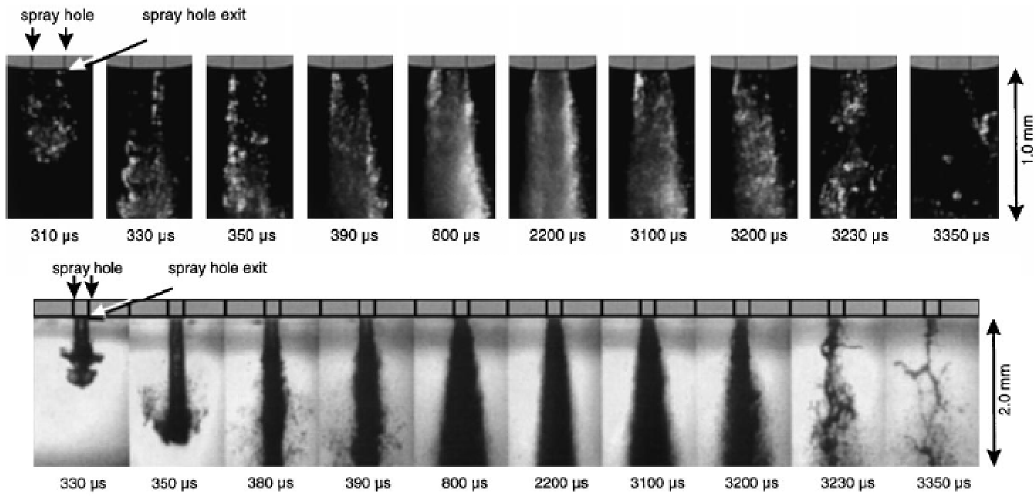

Phot Set 5.24. Badock et al's comparison of laser light sheeting (top) and shadowgraph (bottom) for the diesel spray from an HPCR injector. Rail pressure was 25 MPa, chamber pressure 1.5 MPa, nozzle diameter and length 0.2 mm and 1.0 mm respectively with a pulse duration of 2.0 ms [14].

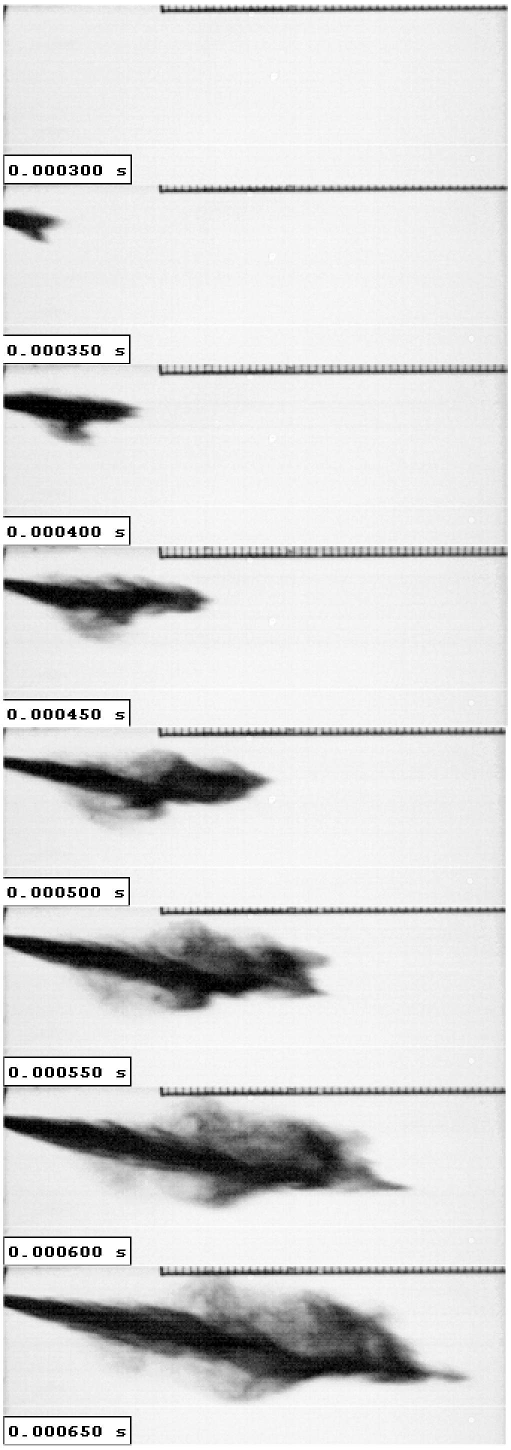

Photo Set 5.25. Backlit images of the diesel spray with a rail pressure of 120 MPa and pulse duration of 0.3 ms.

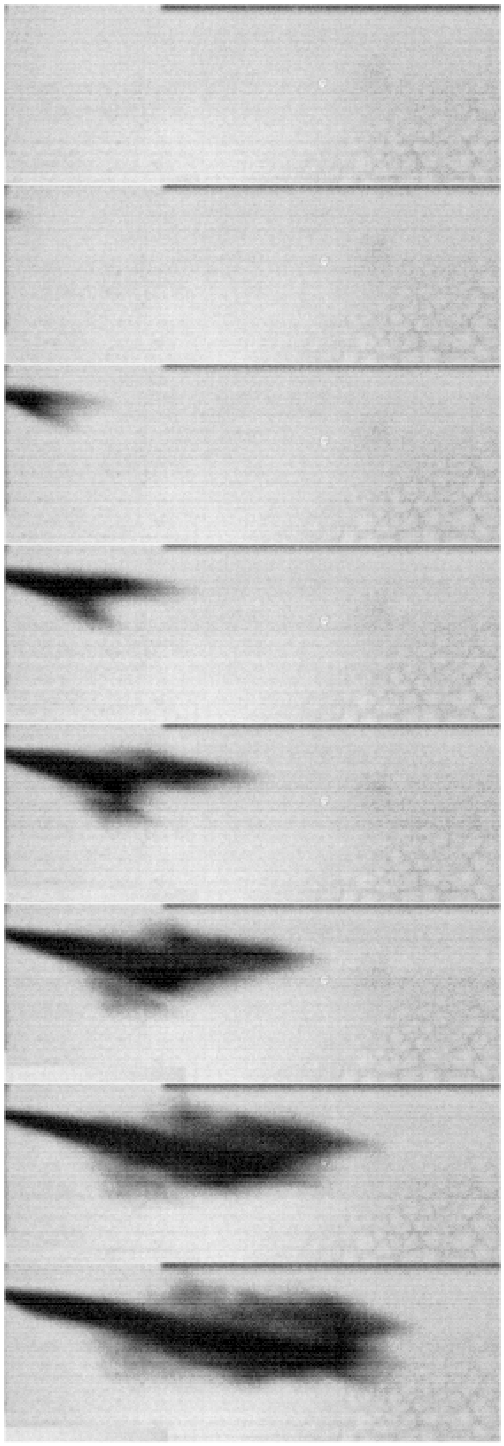

Photo Set 5.26. Shadowgraph images of the diesel spray with a rail pressure of 120 MPa and pulse duration of 0.3 ms.

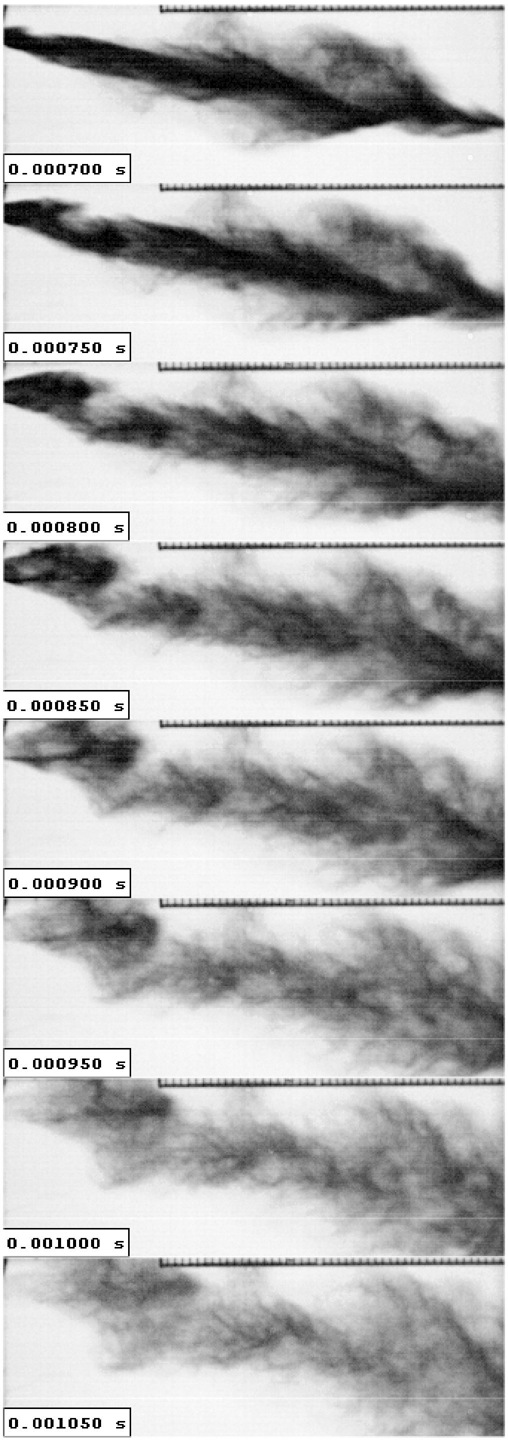

(Continuation of Photo Set 5.25)

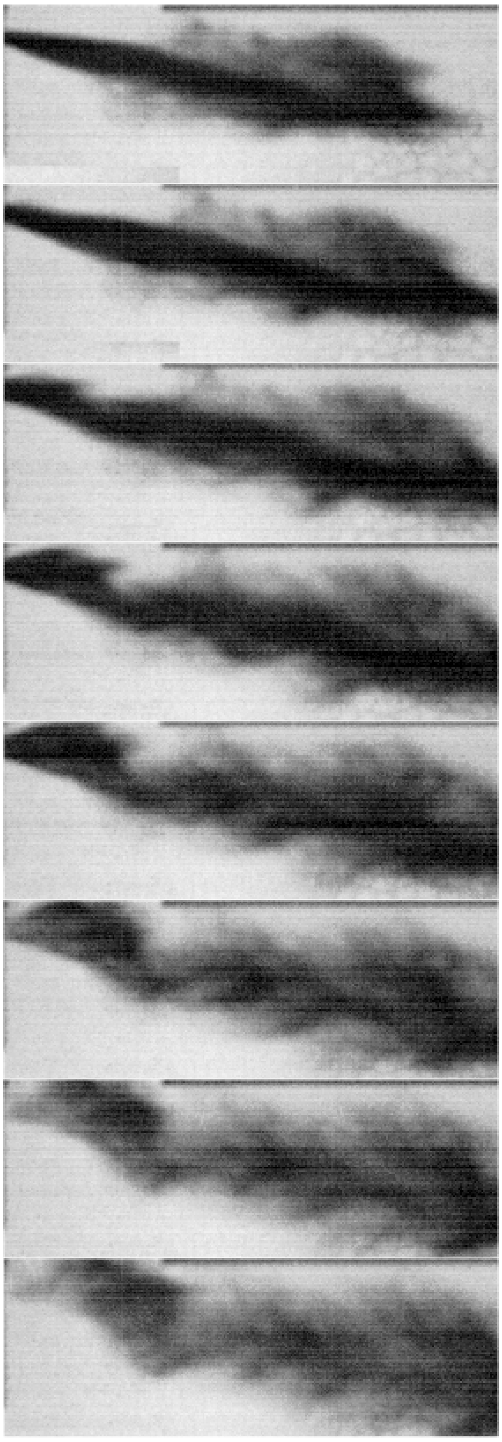

(Continuation of Photo Set 5.26)

5.3 Characteristics of the Gas Jet

As for the diesel spray, a baseline for the performance of the gas injector was determined by studying the gas being injected into the chamber by itself. Most of the analysis was performed using the schlieren technique since it provided more detail of the periphery of the jet. Schlieren video of the jet was taken as it travelled across the test section so that the rate of penetration could be measured. The shadowgraph proved useful, however, for identifying the location of the shock wave in the under-expanded flow. An estimate of the actual injection pressure was made from analysis of shadowgraph results of the near-field of the injection nozzle.

5.3.1 Development of the Gas Jet

Photo Set 5.27 shows a series of images taken from high-speed schlieren video analysis over a period of 2 ms. The jet can be seen to emerge from the nozzle at about 2.2 ms after SOI. Initial progress of the jet across the chamber is relatively slow, owing to the GCV being manufactured from a modified HPCR diesel injector as described in Section 4.3.4. This meant that the response time of the valve opening (when using gas at 16 MPa rather than liquid at 135 MPa) was somewhat delayed. Also, since the gas was compressible and the volume in the nozzle body between the GCV and the injection orifice significant, injection at full pressure was not achieved instantaneously. Instead, the injection rate built up over a period of time.

5.3.2 Injection Pressure

Natural gas, which has a ratio of specific heats, γ, equal to approximately 1.3, when flowing through a nozzle chokes at a pressure ratio of 1.86 [86]. Therefore, a minimum injection pressure of about 190 kPa should be used if injecting into atmospheric conditions. Hence, the upstream pressure of 16 MPa used in the work here means that the jet is substantially under-expanded at the nozzle outlet. The locally-sonic exit velocity, assuming the expansion to have occurred isentropically, can then be estimated as approximately 420 m/s.

As described in Section 3.6, under-expanded jets will, at high pressure ratios, form a normal, standing shock wave known as a Mach disc. Photo Set 5.28 shows typical images taken using the shadowgraph method. The high-velocity streams from the edge of the nozzle are visible feeding into a normal shock downstream with a barrel shock surrounding them on the outside. The area ratio of the normal shock to that of the nozzle exit is about 4.7, which indicates that the flow into the normal shock has a velocity of around 870 m/s at a Mach number of about 2.9. Downstream of the normal shock, the velocity can then be estimated as 200 m/s (Mach number 0.46).

Visualisation indicates that the initial jet takes a few milliseconds to build to sonic after the flow commences. To some extent, this delay will depend on the design of the nozzle, particularly the distance from the control valve to the exit. Shadowgraph images of the gas jet are shown in the following photographs.

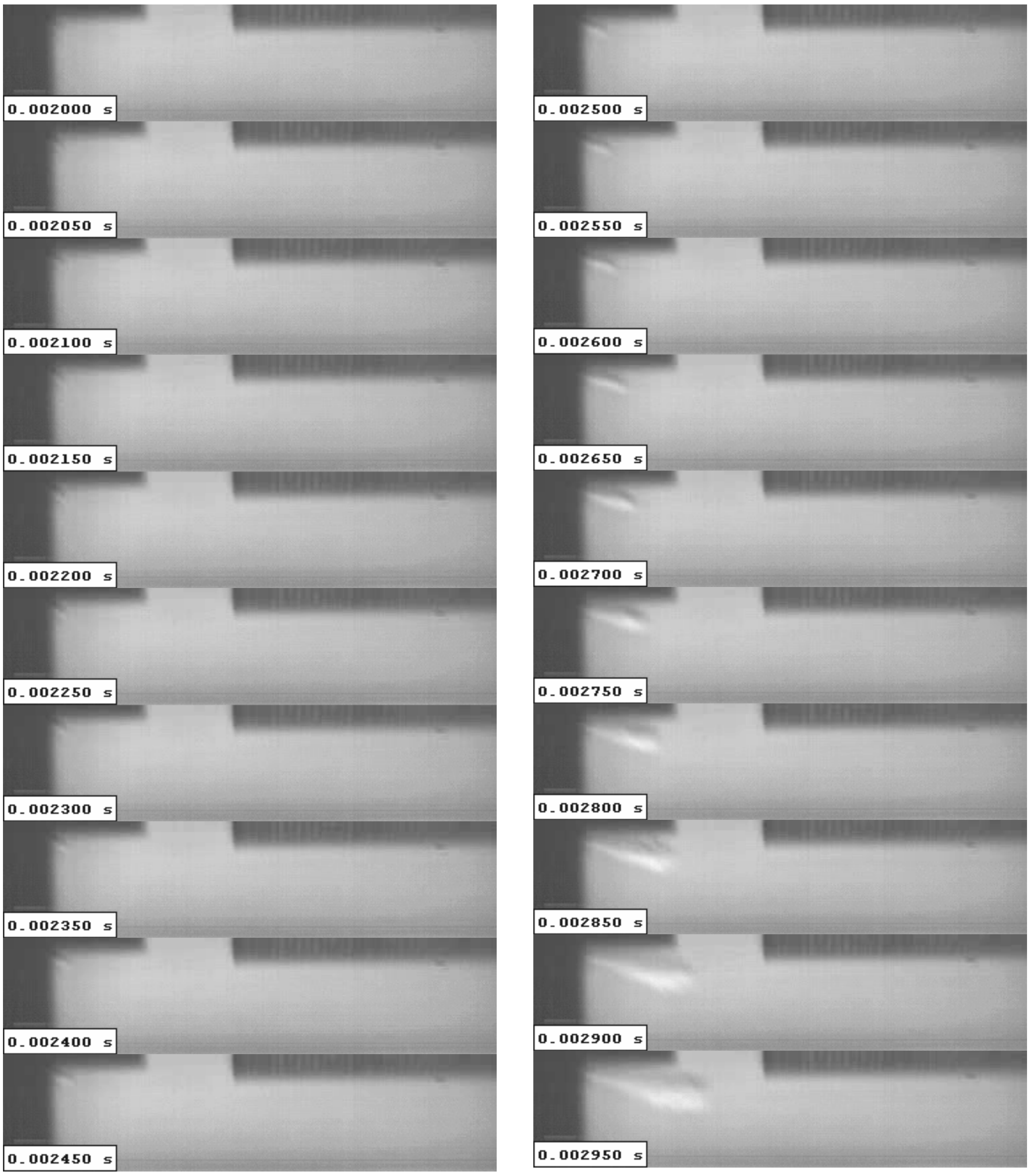

Photo Set 5.27. Schlieren images of the development of the gas jet. The time is that elapsed after the start of electrical SOI. The gas jet starts at around 2.2 ms after SOI. Significant growth starts 2.6 ms after SOI.

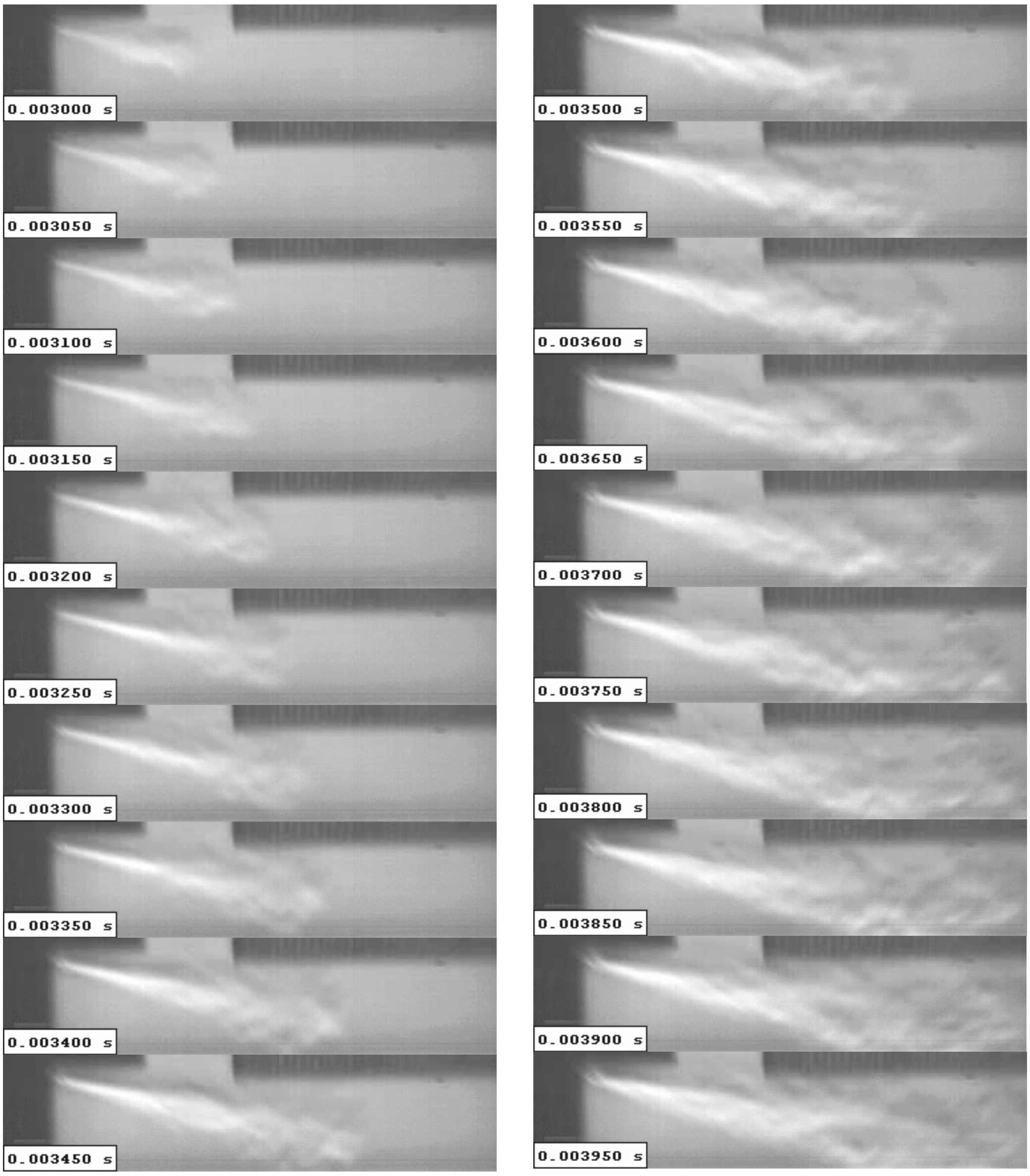

(Continuation of Photo Set 5.27.)

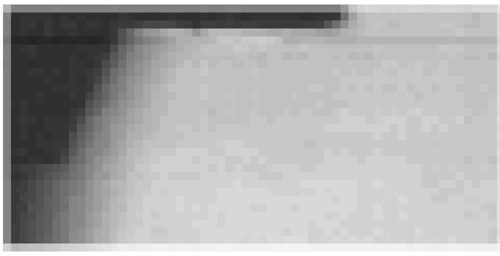
SOI

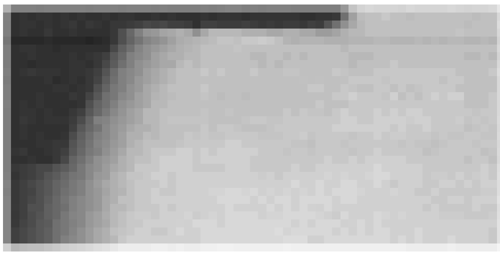
0.5 ms

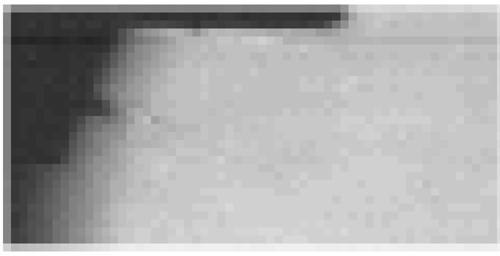
1.0 ms

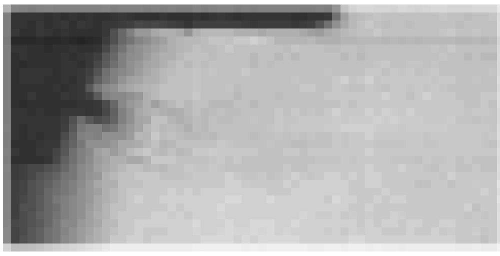
1.5 ms

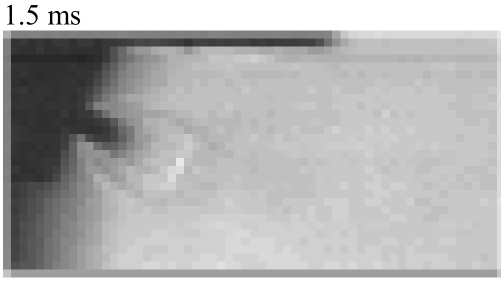
2.0 ms

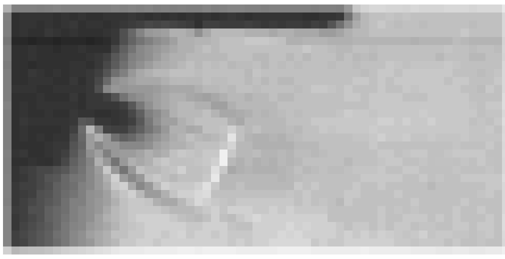
2.5 ms

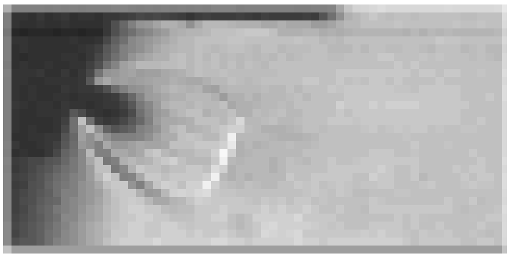
3.0 ms

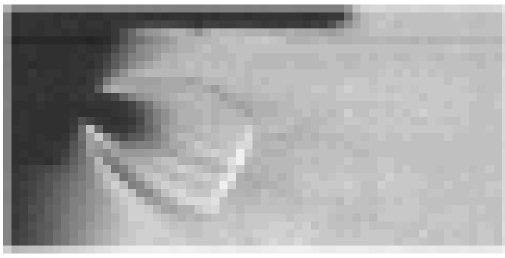
3.5 ms

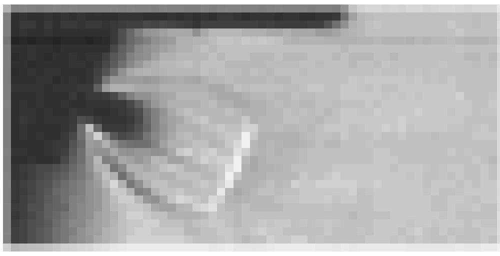
4.0 ms

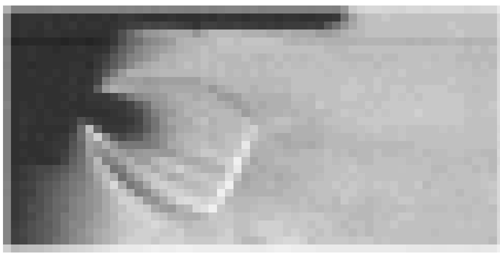
5.0 ms

Photo Set 5.28. Shadowgraph images of the near-field of the gas nozzle. The time is that elapsed after the start of actual SOI for this particular test.

Ashkenaz and Sherman in 1966 [10] theoretically determined the axial position of the Mach disc downstream of an ideally-uniform nozzle exit-flow of gas (injected into the same substance) as a function of the injection pressure:

$$\frac{x_{disc}}{D_{jet}} = 0.67\sqrt{\frac{P_0}{P_a}}$$ **Equation 5.1 [10]**

Such an analysis was carried out by Hill and Ouellette [55] during their study of gas jets for HPDI as shown in Figure 5.8. This study was repeated in the current work. Results from analysis of the "parallel" gas nozzle (in which the axis of the orifice was drilled to be parallel to the axis of the orifice of the diesel nozzle) are shown in Figure 5.9.

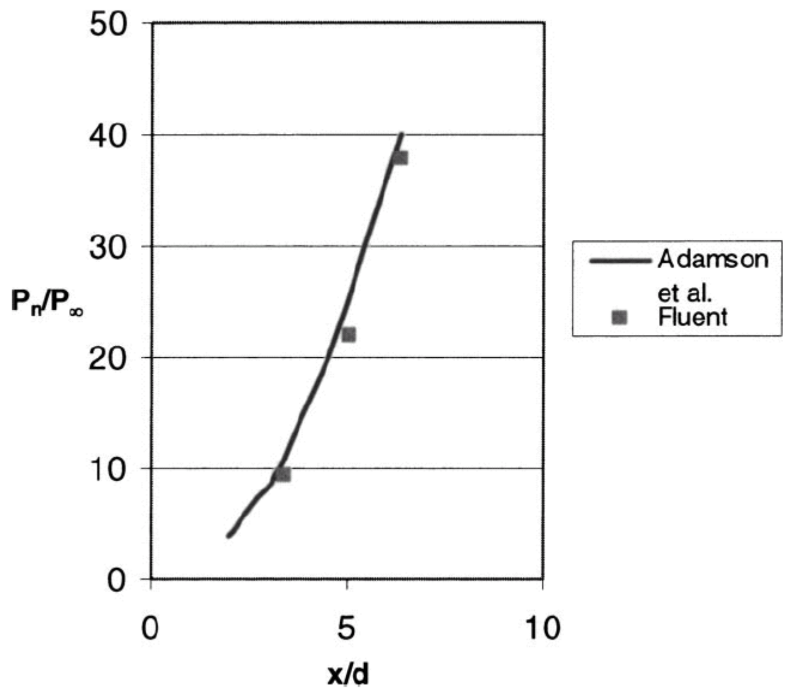

Figure 5.8. Location of the Mach disc for a given injection pressure ratio as tested by Hill and Ouellette (diagram from [86]).

In the current work, the injection reaches a quasi-steady state at about 4 ms after SOI where the injection pressure was calculated to be about 13.5 MPa. This represents a loss of about 2.5 MPa through the gas injector. This compares well with the work of

Rubas et al in 1998 [127] where for a reservoir pressure of 18 MPa, an injection pressure of 14.4 MPa was realised. Considering this pressure drop, for a modern, turbo-charged engine the gas delivery pressure to the injector should perhaps be increased from the 16 MPa used here to around 20 MPa to ensure that about 16 MPa is available at the injection nozzle in accordance with the recommendations of Kloeckner [74].

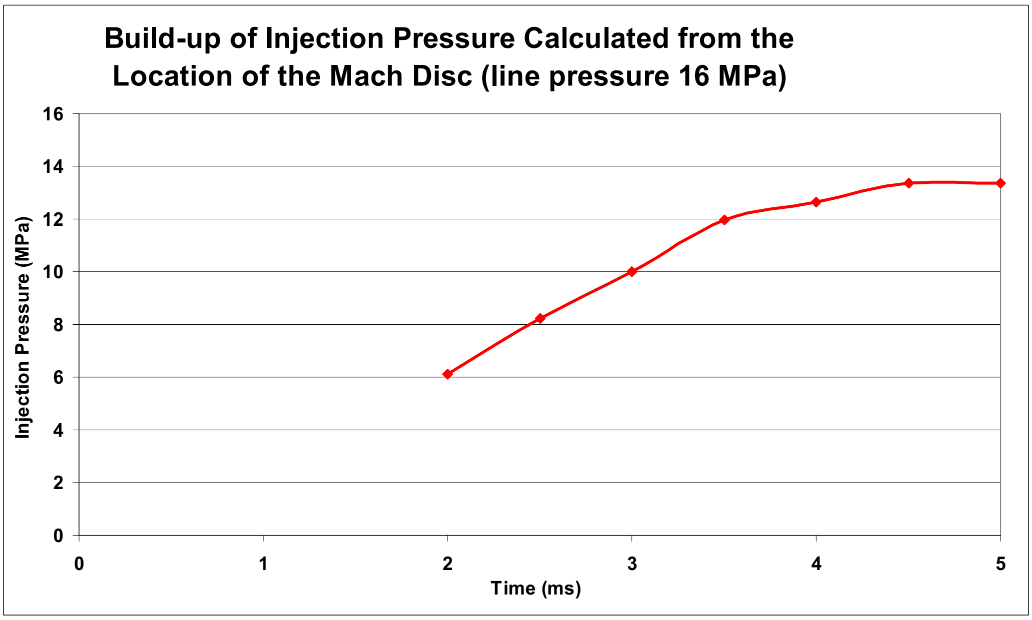

Figure 5.9. Increase of Injection Pressure over time calculated for the parallel nozzle. Calculations were based upon the relation of Askenaz and Sherman [10].

5.3.3 Penetration Rate of the Jet

Ideally, the growth of a gas jet will yield a curve as discussed in Section 3.7 and in Figure 3.12. Owing to the compromises made during the design of the gas nozzle (discussed in Section 4.3), achieving the ideal penetration profile proved impossible. Schlieren video images allowed a plot of the velocity of the leading edge of the gas jet to be developed. The velocity attenuates rapidly from the barrel shock as the jet expands. From Photo Set 5.27 it can be seen that the amount of gas entering the chamber in the first 2 ms after SOI is negligible. Jet growth was slow in the next 1.0 ms until the pressure difference across the injection orifice has exceeded the choking pressure.

Testing of the gas injector revealed that despite the time of SOI being variable within a period of about 1.0 ms, once injection started the rate of jet growth was consistent. Figure 5.10 shows the development of a typical gas injection through the parallel nozzle with a reservoir pressure of 16 MPa. Results were similar for the converging and diverging nozzles. The time-scale has been offset from that which was referenced from the electrical SOI (as used in the photo set) so that time = 0 is now the time when a significant amount of gas starts to issue from the nozzle.

In the early stages of jet development (until around 1.5 ms after actual SOI), the jet was found to approximately fit the curve $X = e^{0.002t}$ where X is the axial penetration of the jet in millimetres and t is the time after SOI in seconds. After this time, the injection pressure stabilises and the jet growth takes on the classical growth rate where penetration is proportional to the square root of time for a jet that starts at full pressure. The injection profile achieved by the GDS in the JVR was deemed satisfactory for the purposes of study in this project.

5.3.4 Summary

The NG jet emerges with little turbulence and accelerates over a short time period of about 1.0 ms before establishing itself as a fully under-expanded jet with a normal and barrel shock structure. This time period is due to several factors, probably the most significant being the relatively slow temperature drop in the metal of the nozzle passages. That is, the initial expansion may be nearer isothermal than isentropic. Other factors are the friction and pressure wave motion between the control valve and nozzle.

The shock structure grows for the next 1.0 ms and the turbulence scale becomes larger and more intense. This seems to be associated with the size of the normal shock. Once the shock system is established, the jet downstream of it becomes highly turbulent and changes very little until the flow slows as the valve closes. This should provide the system for interaction with the diesel jet. Initially, just after the shock, the gas has a velocity of about 200 m/s but the attenuation is rapid due to the low inertia and the rapid growth in cross-section of the front. Typical instantaneous measured tip velocities in this downstream region are about 40 m/s.

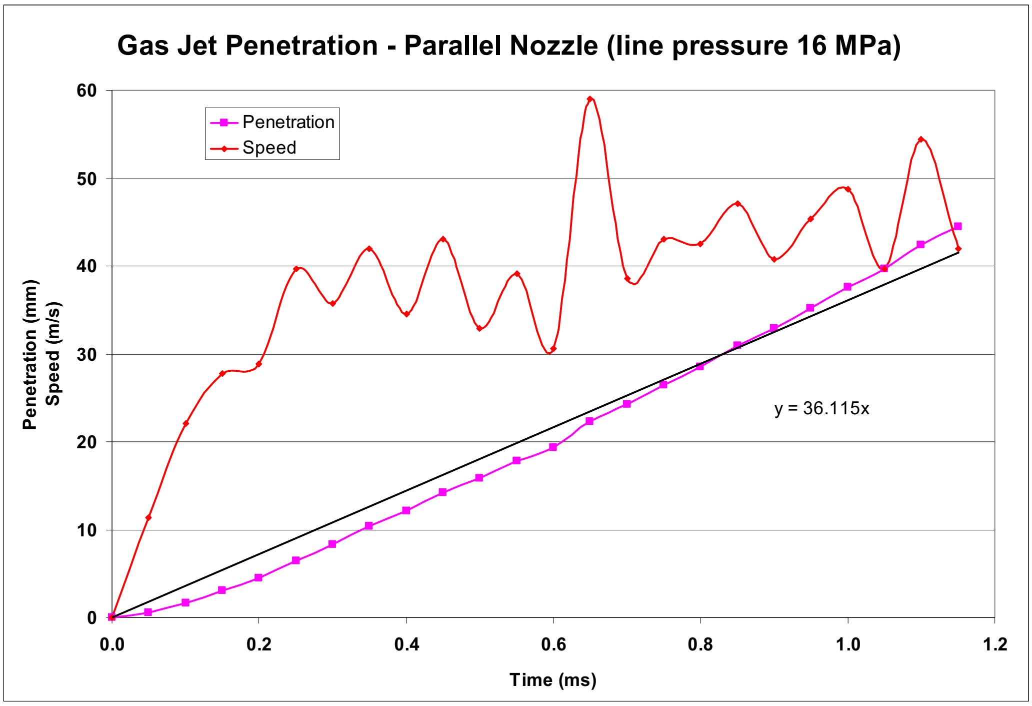

Figure 5.10. Jet penetration found from the gas injector built for this study.

5.4 Experimental Design

Before simulating actual dual-fuelling scenarios, the operating conditions of the engine were decided upon. The cylinder of the Rapid Compression Machine (RCM) [91] has a bore of 108 mm and an effective stroke of 157 mm which equates to a swept volume of 1.44 L. With a clearance height of 10.5 mm, the compression ratio is 16:1. An engine consisting of six such cylinders and turbocharged would be typical of that fitted to a modern prime-mover and could be expected to produce power in the order of 300 kW.

5.4.1 Determining the Parameters to Test

5.4.1.1 Defining Engine "Load"

"Load" for a diesel engine is often defined by the air/fuel mass-equivalence ratio at which an engine is operating. Equivalence ratio, Φ, is defined as:

$$\Phi = \frac{(A/F)_{stoichiometric}}{(A/F)_{actual}}$$ **Equation 5.2**

For typical diesel engines, the stoichiometric air/fuel ratio (AFR) is approximately 15:1. For the purposes of this project, "full load" has been defined as an equivalence ratio of 0.75 which is about the limit of richness at which a modern diesel may run without producing an excess of soot. For $\Phi = 0.75$, the actual AFR is about 20:1.

5.4.1.2 Fuel Requirements of the "Test Engine"

Full-load (ie. $\Phi=0.75$) for the RCM-sized cylinder requires 88 mg or about 100 mm^3 of diesel per cycle. Taking the lower heating value (LHV) of diesel to be around 43 MJ/kg [90], this equates to an energy input of about 3.78 kJ.

5.4.1.3 Gas Substitution

The relative amount of gas that could be substituted at different load points of the engine had to be established. In this project, the level of substitution always refers to the percentage of the total energy content (not mass) of the fuel charge represented by the alternative fuel.

One consideration in determining the fuel ratio was how much substitution an engine could tolerate without experiencing ignition or efficiency problems. Under normal operating conditions, eg. for a truck on the highway, it is desirable to operate the engine with as high a gas substitution ratio as possible. Wakenell et al [154] achieved a 98.2% substitution although this was in a large, mostly steady-state ship engine. Ouellette et al [109] report a more realistic condition in a 15 L four-stroke truck engine where the pilot amount varies between 2.4 and 9% when load is varied respectively between 20 and 100%.

The other consideration was what the laboratory rig would be capable of simulating. The digital control unit was described in Section 4.3.5. The minimum increment of injection time available was 0.1 ms. This placed some limitation on the number of different simulations that could be explored with the laboratory rig. As described earlier in this chapter, it was revealed that the minimum quantities available from the HPCR injector at the set operating pressure of 120 MPa were 6 mg for a 0.2 ms pulse and 14 mg for a 0.3 ms pulse. For an RCM-sized cylinder, Table 5.2 shows possible DF operational scenarios using these minimum diesel delivery quantities.

5.4.1.4 Injection Geometry

As described in Section 4.3.4, it was decided to compare three different dual-fuel injector geometries (“injectors”) to gauge their relative mixing performance.

5.4.2 Cases to Test

It was decided to test cases for each of the three nozzle geometries with the following variables:

- The two minimum diesel delivery quantities (6 mg and 14 mg).
- Then, for each of these two pilot quantities, a case where SOI for the two jets was simultaneous and then a case each where the gas jet started 0.25 ms, 0.50 ms and then 0.75 ms after the diesel jet.

In each case, the total fuel delivery (and thus load case for the theoretical engine) was being determined by the duration of the gas injection. Thus the gas was left flowing for long enough so that cases 2 through 9 described in Table 5.2 could be simulated.

Table 5.2. DF scenarios possible with the HPCR diesel injector used in the current work.

Case	Engine Load (%)	Diesel Pulse Width (ms), mass (mg) and energy delivered (kJ)	Energy-based Gas Substitution (%)
1	100	2.0*, 88, 3.784	NIL
2	100	0.2, 6, 0.257	93.2
3	100	0.3, 14, 0.602	84.1
4	75	0.2, 6, 0.257	90.9
5	75	0.3, 14, 0.602	78.8
6	50	0.2, 6, 0.257	86.4
7	50	0.3, 14, 0.602	68.1
8	25	0.2, 6, 0.257	72.7
9	25	0.3, 14, 0.602	36.4

***Extrapolated from the test results shown in Figure 5.5.**

5.4.3 Photographic Technique

The three different imaging techniques available and tested (backlighting, shadowgraph and schlieren) were described in Sections 4.4 and 5.1.

Backlighting was used for the initial analysis of the diesel spray whilst further information about the amount of atomised liquid that was vaporising was revealed using the shadowgraph. Shadowgraph analysis was also used to study the near-field of the gas nozzle where the standing shock wave formed. The schlieren technique was found to provide the most information in the majority of cases where the gas jet was to be studied. The bulk of the results analysed here were taken using the schlieren technique in conjunction with the high-speed CCD video camera.

Image clarity of the pictures captured using the schlieren technique was limited by the available light source and by resolution of the digital video camera. As reported by Langford [80], the light intensity from a source is inversely proportional to the area onto which the image falls. A minimum photographic rate of 20,000 frames per second (20 kfps) was found to be required to study the fuel jets with any confidence and a rate of 40 kfps was used to determine the jet speed. At these high frame rates the camera's exposure time for each frame was 47 and 22 μs respectively and so the intensity of the light source became a limiting factor in how fast the camera could be run.

6. Chapter Six: Laboratory Results - Dual Fuel Injection

The properties of the diesel spray and NG jet when injected discretely were discussed in the previous chapter. Now, the simultaneous injection of the two jets is studied. In pilot-ignited dual-fuelling as studied here, the entrainment of the air in the cylinder by both the diesel spray and gas jet dictates the nature of the combustion. The entrainment characteristics of the gas jet, however, have a greater effect on the efficiency of the combustion since the gas jet is being injected into an environment where the diesel has already mixed with the air. Thus the gas jet will entrain not only the air in the cylinder but also diesel vapour and, ideally, some already-ignited diesel so as to trigger its own ignition. Finding the appropriate nozzle geometry and "staging" time of the gas jet with respect to the diesel spray is important so that the ignition delay of the fuel mixture can be minimised. Only qualitative properties are investigated in this chapter. Quantitative analysis is discussed with reference to the numerical work which is detailed in the following chapters.

6.1 Comparison of Gas Nozzle Geometries

Photo Sets 6.1 through 6.3 show pictures taken with the high-speed schlieren video for the diverging, parallel and converging injectors respectively. In an actual engine there will exist, as discussed in Section 2.8.2, an optimum period of delay between the injection of the diesel and the gas so that the diesel has time to ignite before the gas enters the combustion chamber. But here, where an appropriate value for the angle of intersection of the axes of the two injection nozzles must first be established, it was useful to analyse the mixing of the jets when their SOI was simultaneous. Since both jets were still flowing under pressure during the mixing process, their interaction was more obvious than that which would occur if there was a delay between the two injections. In the photos sets that follow, SOI for the gas jet was set to be within 0.1 ms of SOI for the diesel spray. The electronic duration of the diesel spray was 0.3 ms in each case which resulted in the actual injection duration being about 0.6 ms. This duration provided enough time for the gas to be entrained into the diesel spray.

Diverging Injector

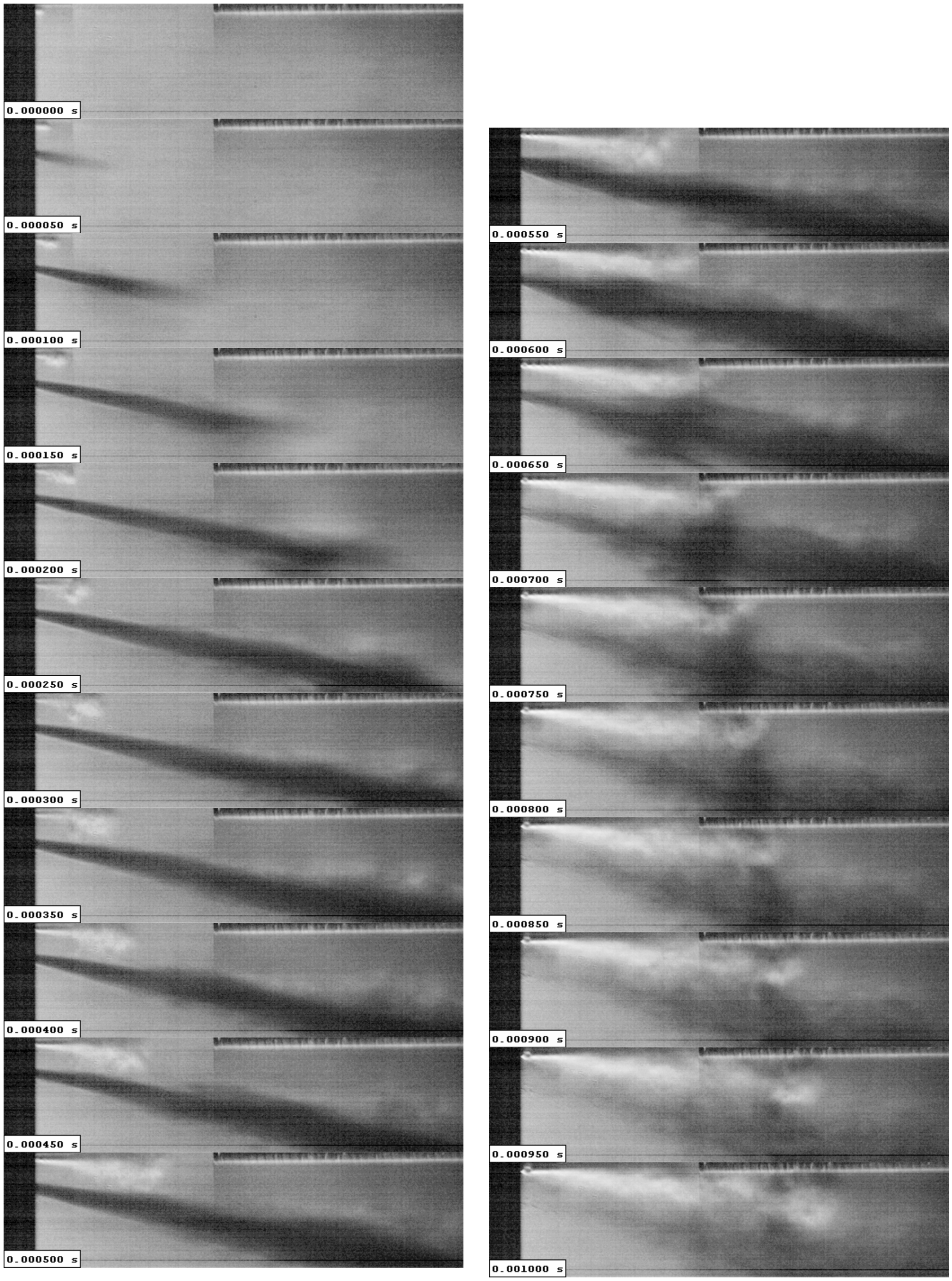

Photo Set 6.1. High-speed schlieren video of the diverging DF injector. The time scale is from the simultaneous SOI of both jets.

Diverging Injector

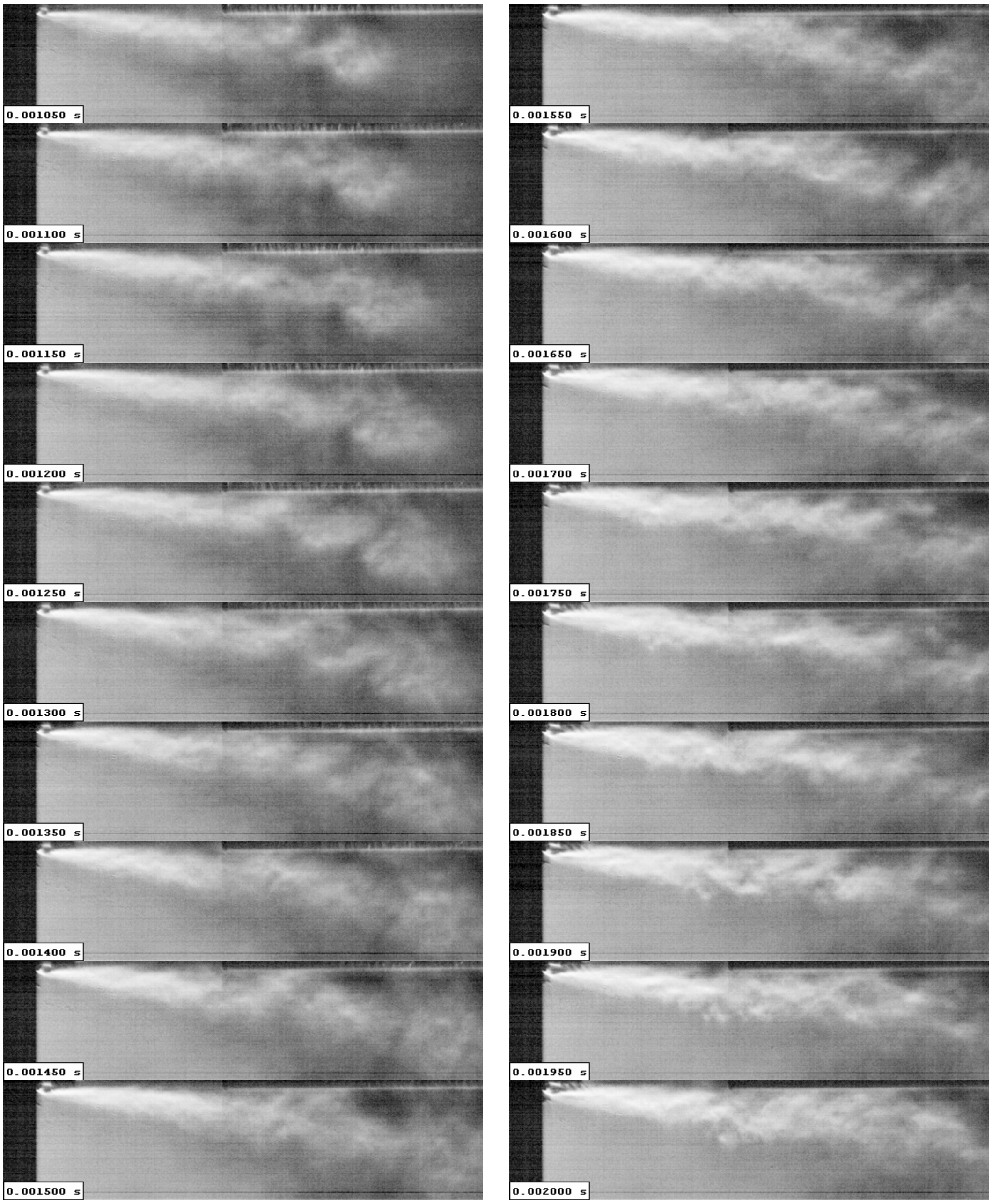

(Continuation of Photo Set 6.1.)

Parallel Injector

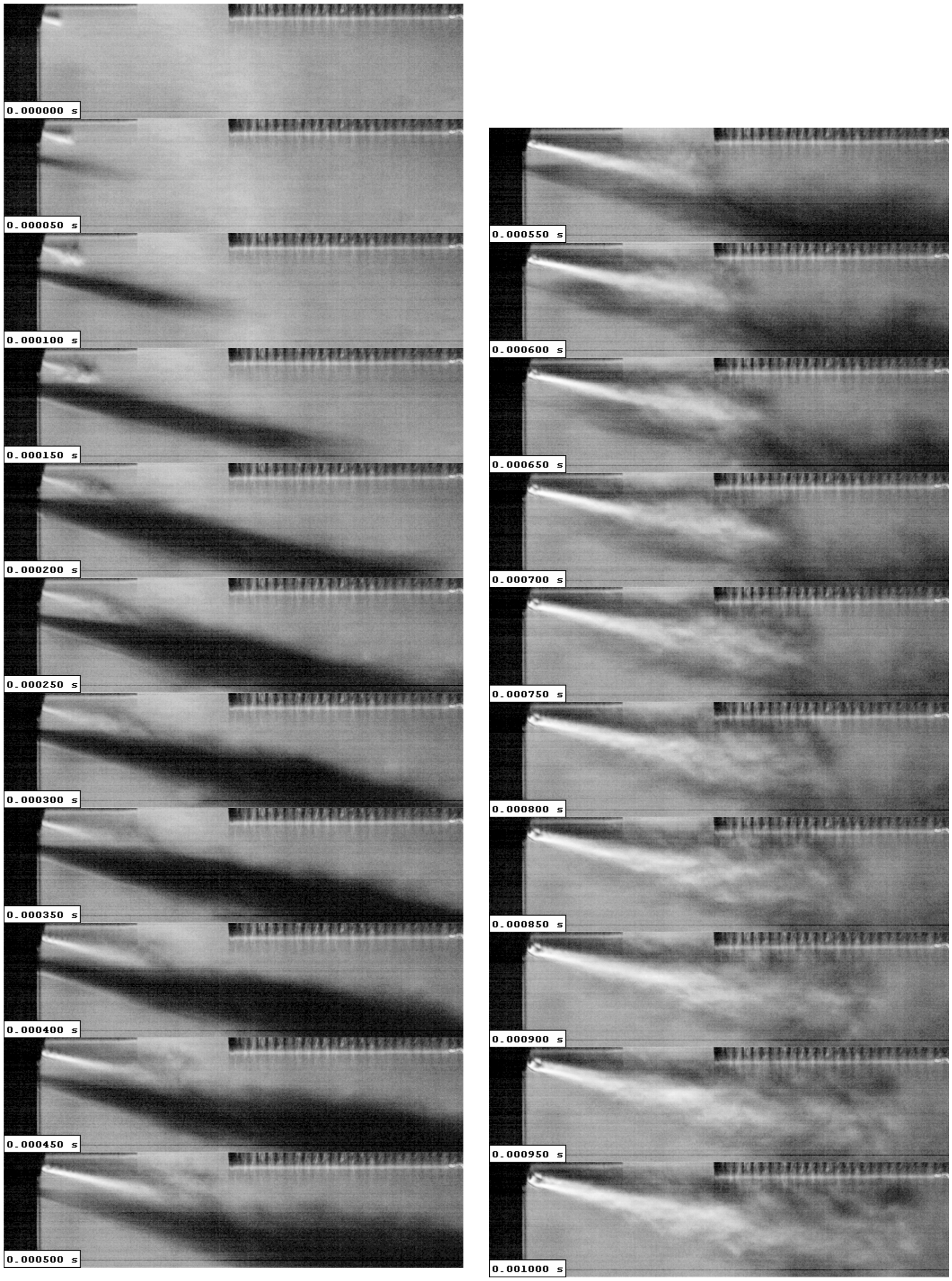

Photo Set 6.2. High-speed schlieren video of the parallel DF injector. The time scale is from the simultaneous SOI of both jets.

Parallel Injector

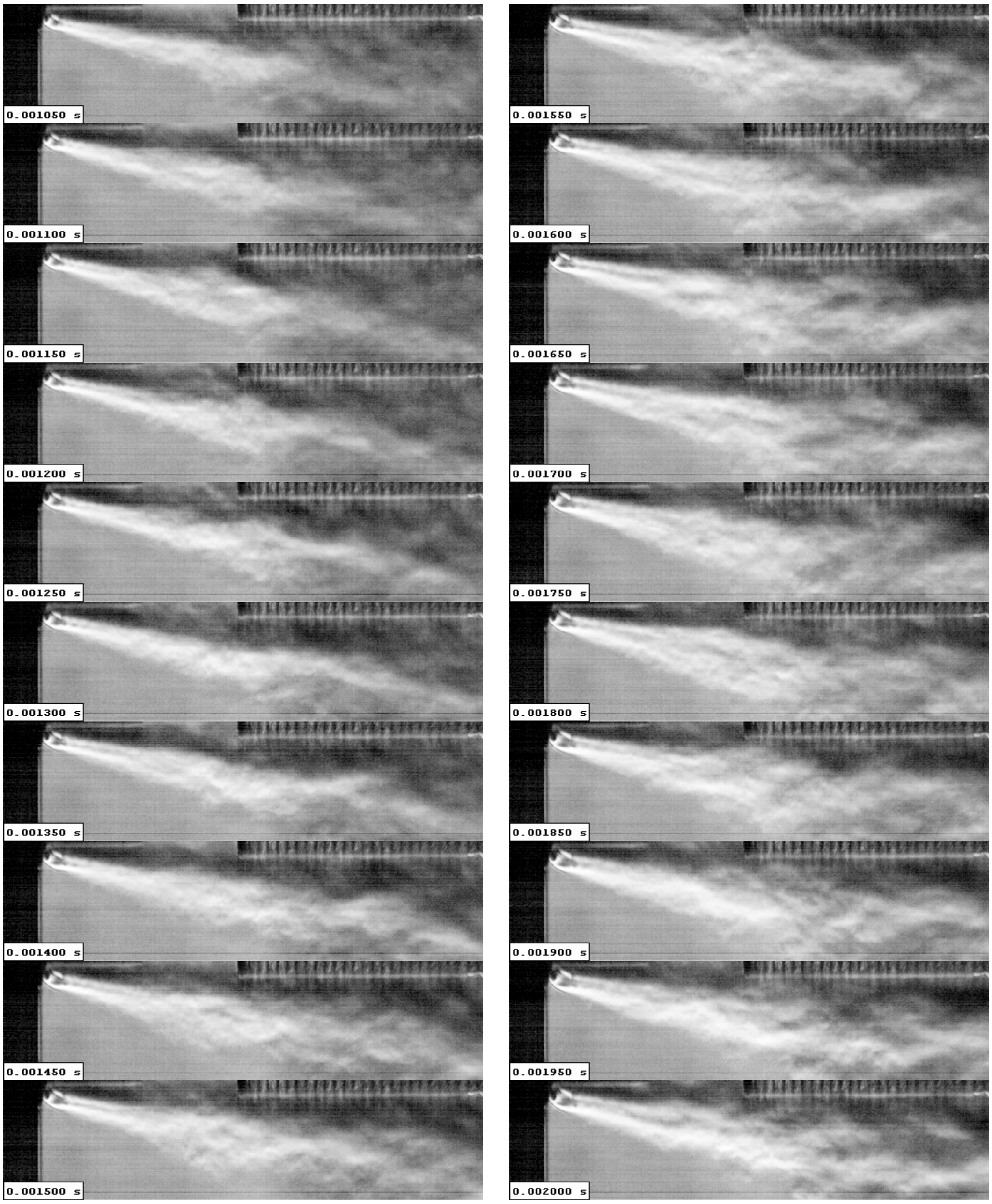

(Continuation of Photo Set 6.2.)

Converging Injector

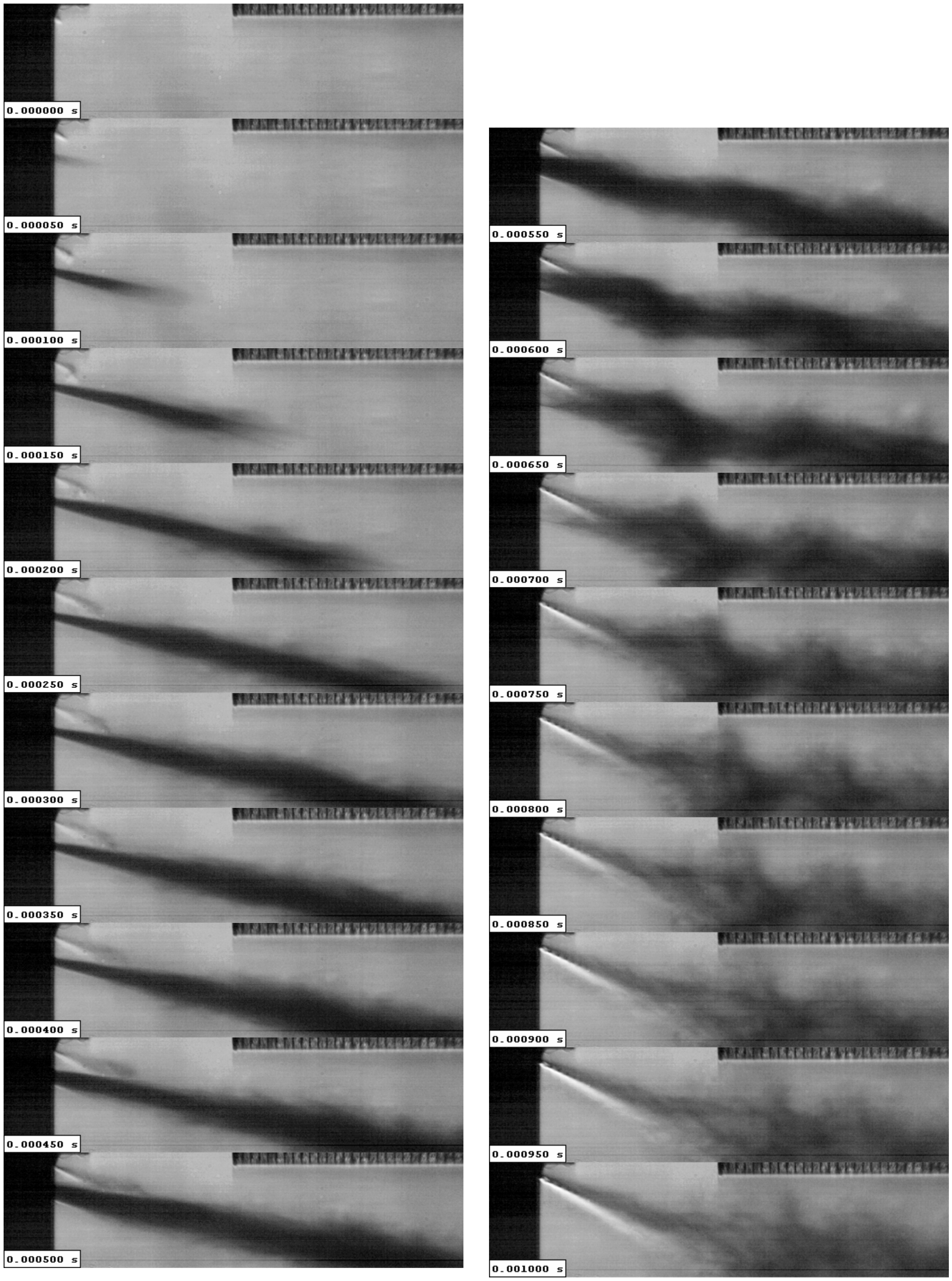

Photo Set 6.3. High-speed schlieren video of the converging DF injector. The time scale is from the simultaneous SOI of both jets.

Converging Injector

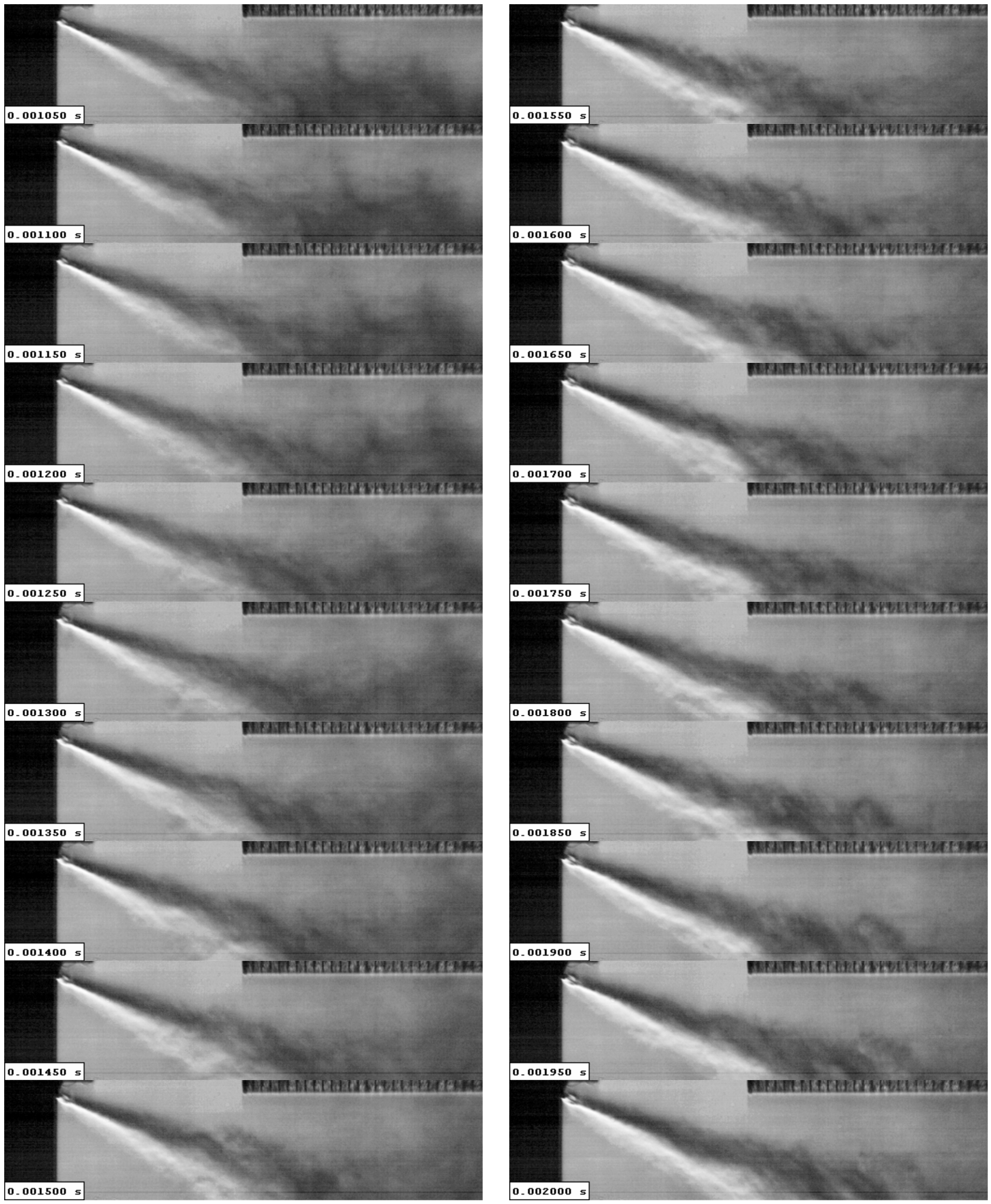

(Continuation of Photo Set 6.3.)

6.1.1 Diverging Nozzle

Photo 6.4 below shows an enlargement of a frame from Photo Set 6.1 in which the development of the jets from the diverging injector was recorded. This frame is taken 1.0 ms after simultaneous SOI of the jets. It can be seen that the gas and diesel are not mixing very well, with only a small amount of superposition of the darker diesel over the relatively unaffected, lighter gas.

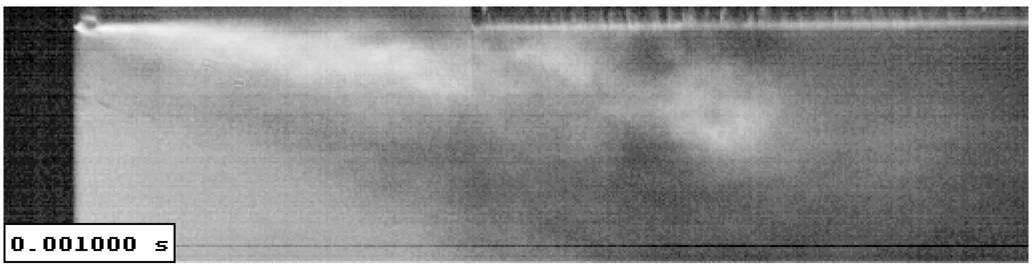

Photo 6.4. DF injection with the diverging injector 1.0 ms after simultaneous SOI.

6.1.2 Parallel Nozzle

Photo 6.5 shows an enlargement of the frame taken 0.6 ms after simultaneous SOI from the parallel injector. Mixing is perhaps a little better than for the diverging case insofar as the jets start-off travelling in the same direction. It seems, however, that the boundary layer of the gas jet is running along the top of the diesel spray. The reduction in the relative speed between the diesel spray's top boundary layer and the gas/air mixture in the cylinder means that Kelvin-Helmholtz instabilities are likely to be less intense. Mixing of the vaporised diesel with the ambient air in the chamber as well as with the NG is thus likely to be inhibited.

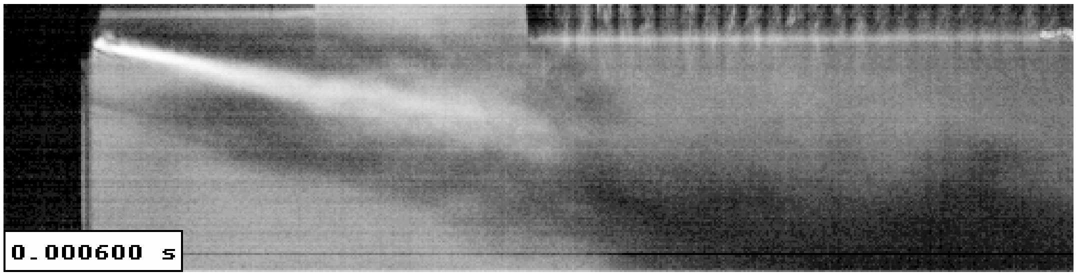

Photo 6.5. DF injection with the parallel injector 0.6 ms after simultaneous SOI.

6.1.3 Converging Nozzle

In Photo Set 6.3, the axis of the gas jet intersects the axis of the diesel spray at an included angle of 12.5°. Photo Set 6.6 shows enlargements of the frames from this set of results from the converging injector between 0.6 and 1.4 ms after simultaneous SOI of the jets. Initial entrainment of the gas jet into the diesel is excellent but after cessation of the diesel injection, inertia carries the gas jet down at the angle of the nozzle hole's axis. Thus the latter stages of the injected gas will not necessarily follow the diesel and so whilst ignition is assured, it will not necessarily occur as rapidly as if the gas was to follow the diesel right across the chamber.

6.1.4 Development of the "Optimised" Nozzle

In the case of the jets from the parallel injector, if there is no staging delay for the gas, the jets are separated in the very early period of the injection. However, due to the cross-sectional expansion of both the head of the gas jet and the stripped liquid, the interaction is quite good by 0.7 ms. The gas starts to interact with the liquid diesel particles by about 0.4 ms. By 0.7 ms, the gas jet front is colliding with a major liquid mass. This is due to the slow movement of the stripped liquid particles. For the jets from the converging injector, the interaction begins almost instantly in the case where there is no delay. However, the gas jet tends to pass below the bulk of the stripped liquid as the process proceeds. This is more noticeable when the gas jet is delayed. The tests indicate that a convergence angle of only a few degrees is required for the best interaction. With these observations as a guide, a fourth gas nozzle-sleeve was made.

This nozzle was made with the axis of the orifice at 17.5° below horizontal, ie. about half-way between the parallel and converging nozzles. Frames from high-speed schlieren video for this optimised injector are shown in Photo Set 6.7.

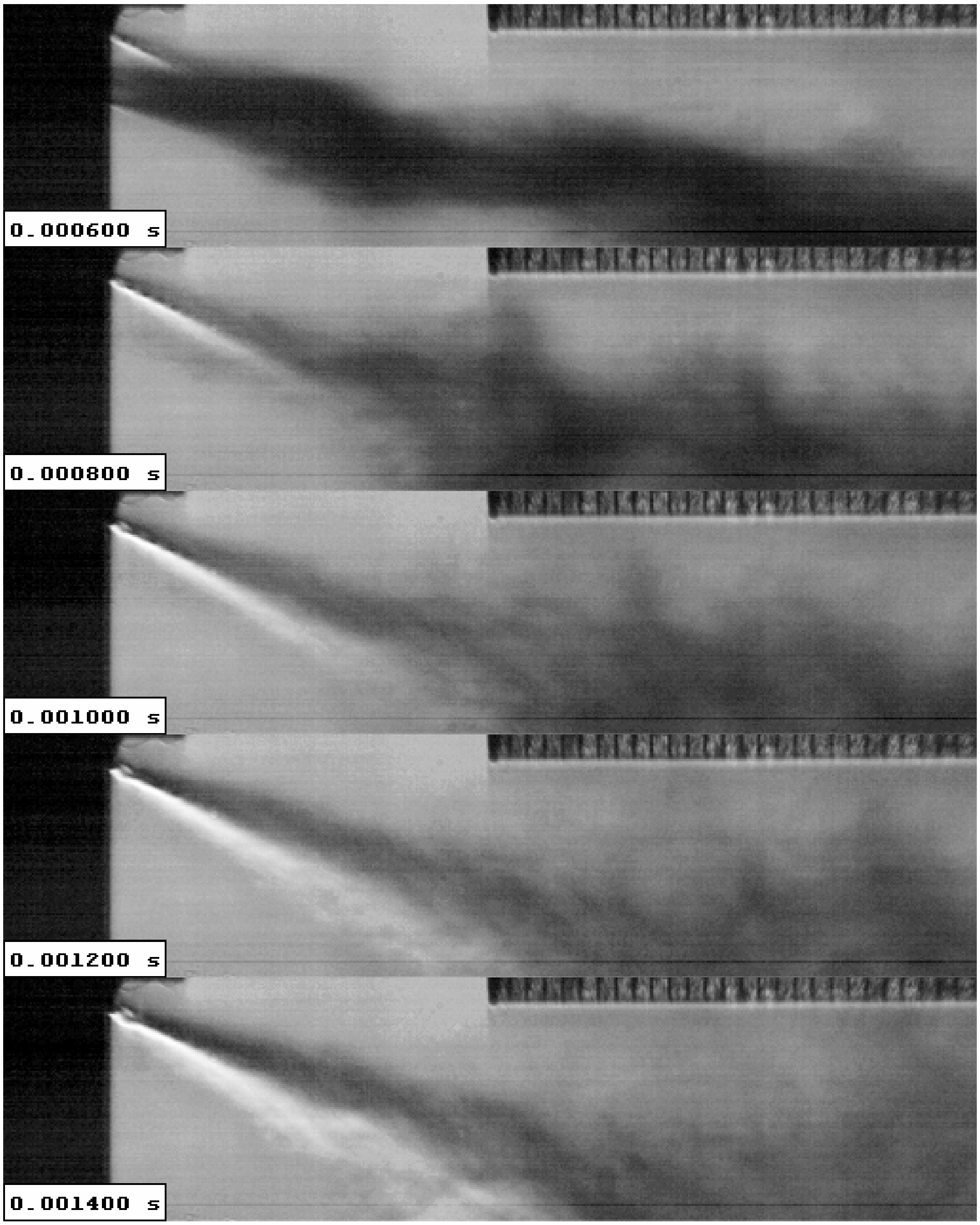

Photo Set 6.6. Enlargement of some frames from Photo Set 6.3 showing how, for the converging nozzle, initial mixing is excellent though latter stages of the gas injection do not follow the diesel.

The results shown in Photo Set 6.7 are very promising. The jets' axes and the actual sprays intersect at about one-third of the way across the chamber. Whilst some gas continues across the chamber above the diesel spray, the bulk appears to be entrained into the diesel and even after cessation of diesel injection, the residual momentum of the mixture in the chamber draws the ensuing gas into the already-injected diesel vapour cloud. A negligible amount of gas passes below the path of the diesel spray.

6.2 Staging

Staging of the gas jet after the diesel spray is critical to ensure that both jets experience the shortest ignition delay possible. In this study, "staging" is a term used to refer to the time delay between the SOI of the diesel and the SOI of the gas. The gas should not be injected so soon as to affect the ignition of the diesel. Similarly, the gas should enter into the chamber when there is already an ignition source, ie. a flame.

On the other hand, the amount of diesel that is being injected is very small and so will not burn for very long. Thus the delay of the gas jet should not be so long that the jet enters the chamber after the diesel has extinguished. Combustion of the gas should be mixing-controlled as described for diesel engines in Section 2.2.3. Rapid, pre-mixed burning creates high energy-release rates which lowers efficiency, increases the undesirable formation of oxides of nitrogen and will, over time, damage the engine.

A further benefit of optimising the staging between the injections is to have the effect of split or multiple injections as described in Section 2.4. Such strategies have been developed in recent years to assist with controlling emissions. Splitting the diesel injection has proved to be a useful tool for controlling the effective energy-release rate. With HPDI, the injection of the NG is analogous to a second diesel injection.

Photo sets 6.8 through 6.11 show high-speed schlieren video results from the optimised nozzle. In these photo sets, various delays of SOI for the gas injection with respect to the diesel injection have been investigated.

Optimised Injector

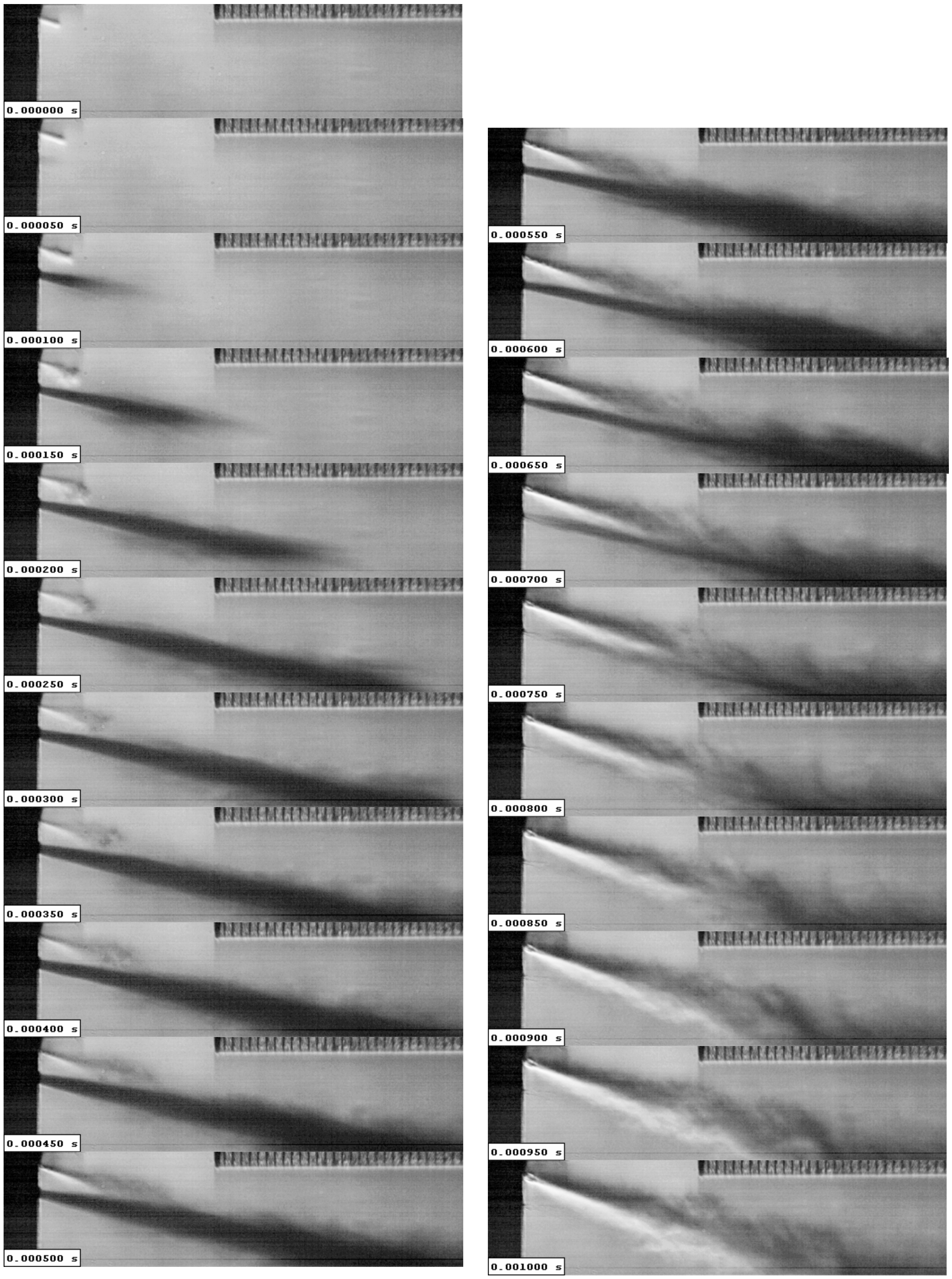

Photo Set 6.7. High-speed schlieren video of the optimised DF injector. The time scale is from the simultaneous SOI of both jets.

Optimised Injector

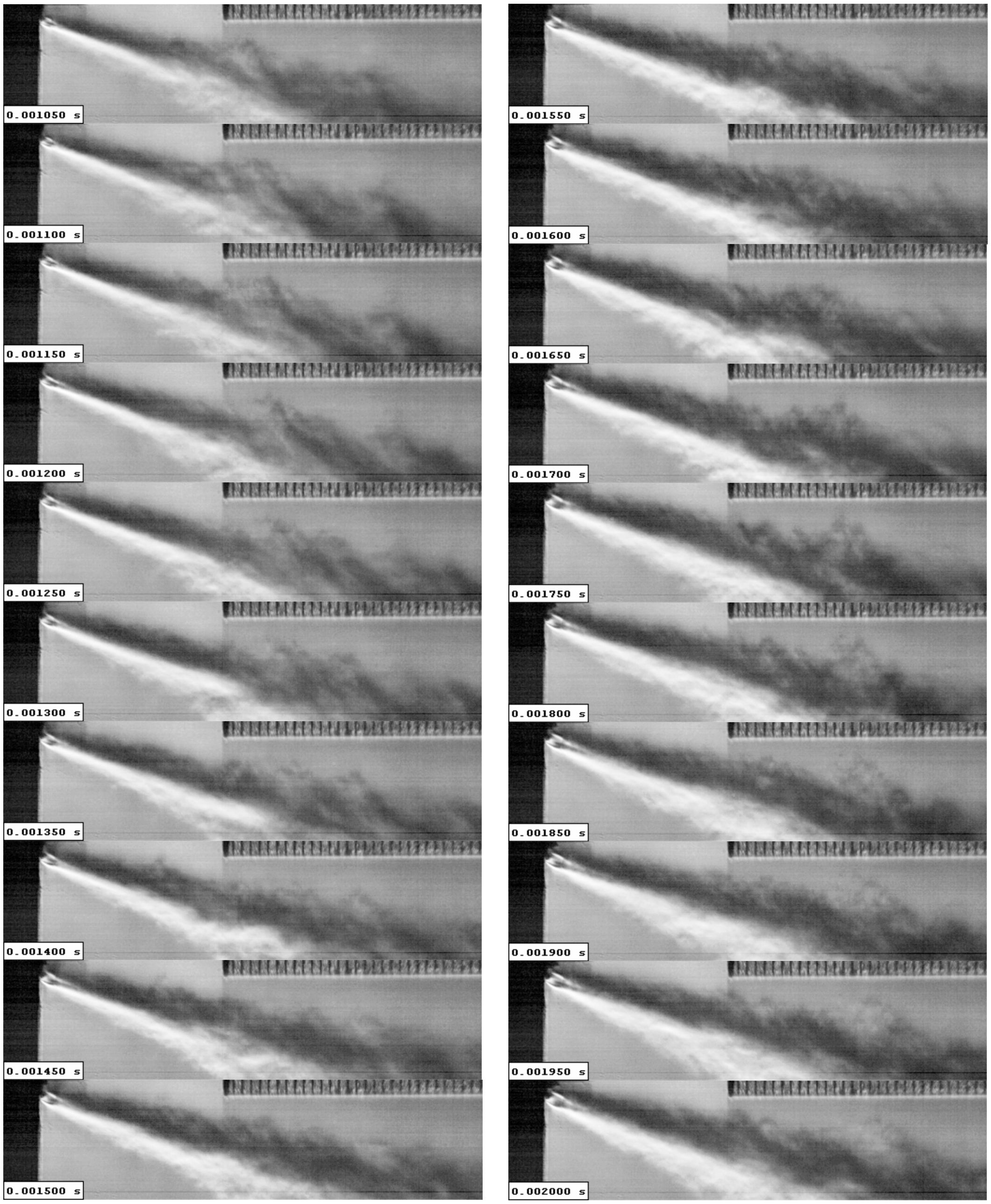

(Continuation of Photo Set 6.7.)

Gas Injection delayed by 0.25 ms

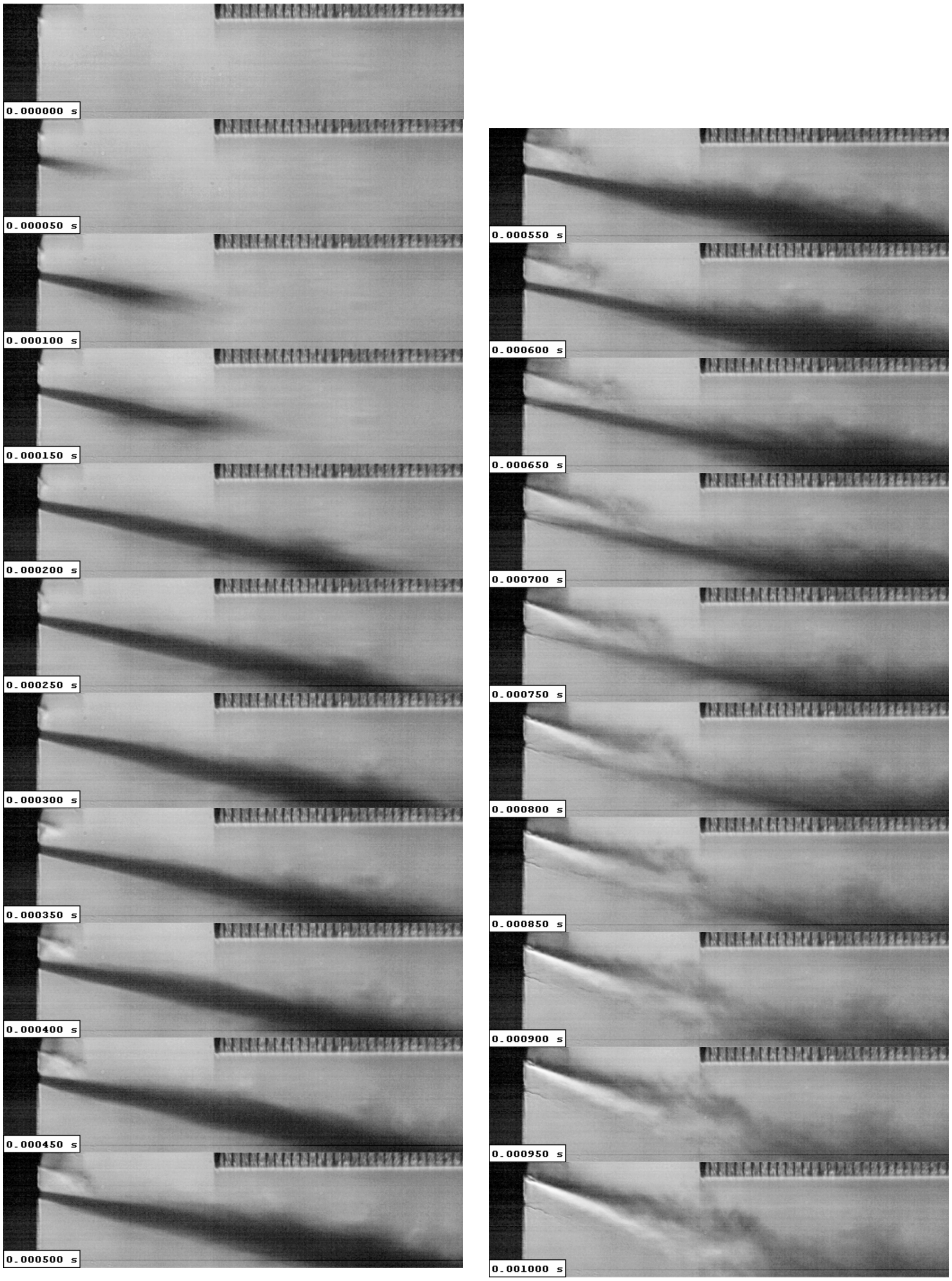

Photo Set 6.8. High-speed schlieren video of the optimised DF injector – gas injection starts 0.25 ms after diesel.

Gas Injection delayed by 0.5 ms

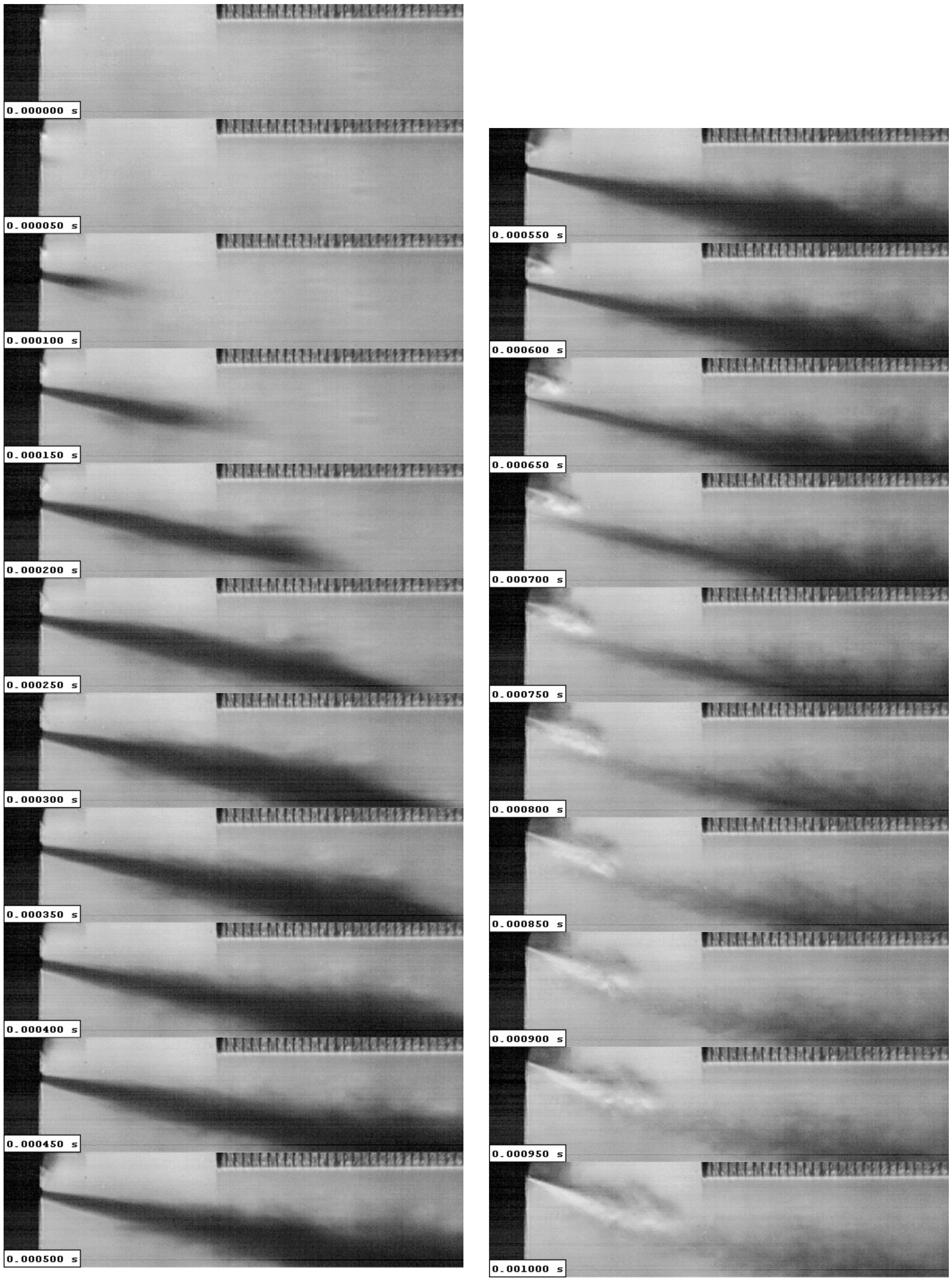

Photo Set 6.9. High-speed schlieren video of the optimised DF injector – gas injection starts 0.5 ms after diesel.

Gas Injection delayed by 0.75 ms

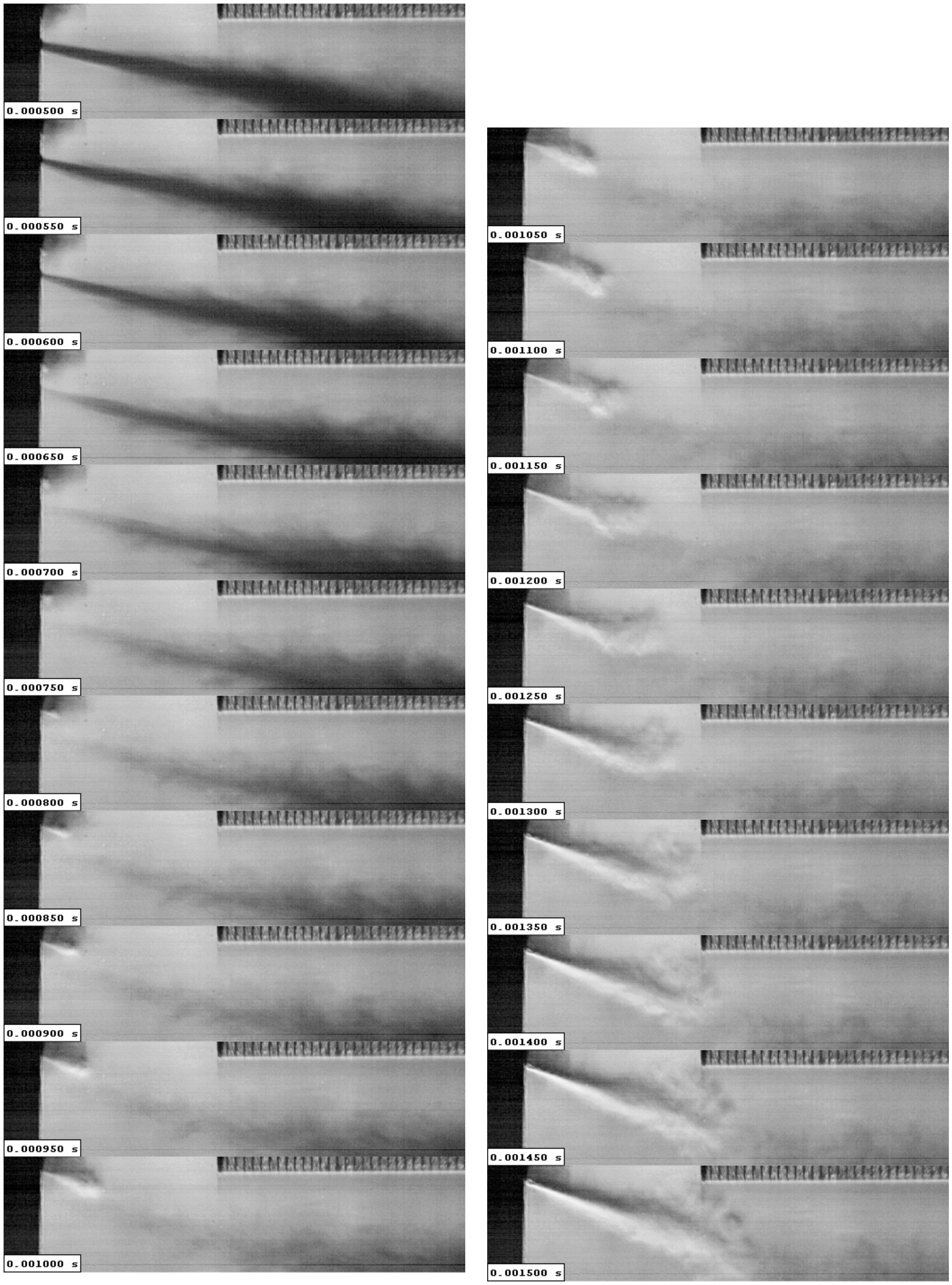

Photo Set 6.10. High-speed schlieren video of the optimised DF injector – gas injection starts 0.75 ms after diesel.

Gas Injection delayed by 1.0 ms

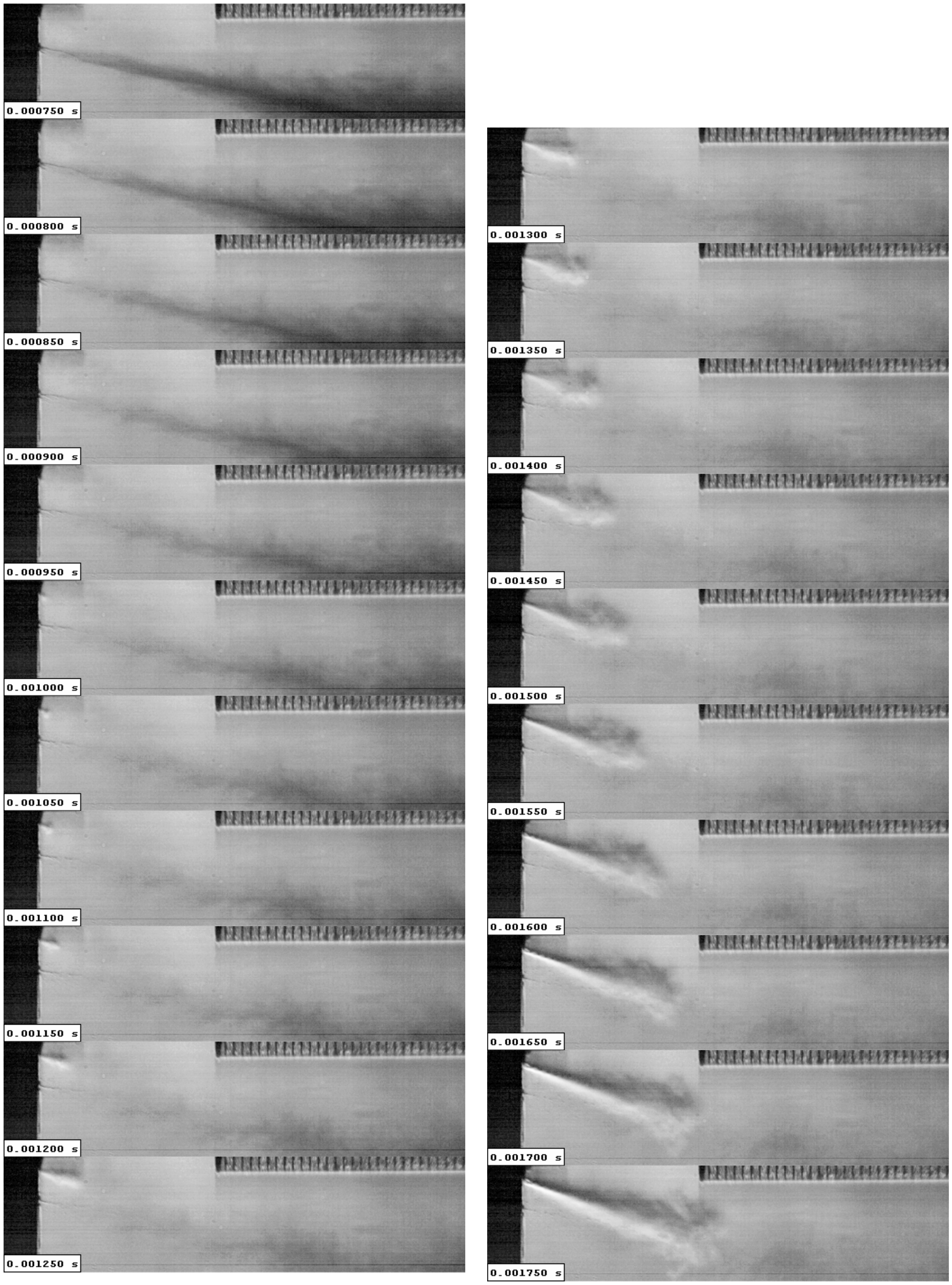

Photo Set 6.11. High-speed schlieren video of the optimised DF injector – gas injection starts 1.0 ms after diesel.

As discussed in the previous chapter, the rate of injection of the gas is initially very slow. The decision as to which is the best delay for the gas jet is primarily based upon which delay allows enough time for the diesel to ignite so that the ignition delay of the gas is effectively nil; ie. so that the temperature in the chamber has risen from, say, about 900 K to between 1,300 and 1,400 K by the time the gas is entering the chamber. This delay, however, must of course be balanced with the requirement that, so as to maintain high fuel-conversion efficiency, the entire duration of combustion should not exceed about 40 to 50 crank degrees [54]. Correlations for the ignition delay of diesel were presented in Section 2.3.2. From these correlations, the delay in a modern, high-compression (or turbo-charged) engine ranges between about 0.3 ms (Hiroyasu) and 0.5 ms (Stringer et al). Considering the likely ignition delay for the diesel, for the cases presented above with the diesel injection pulse duration of 0.3 ms, the 0.5 ms delay is perhaps ideal.

Perhaps as important though is how the head of the gas jet and subsequently the steady/mixing part (as described in Section 3.9) approaches the end of the diesel injection. In the 0.7 through to the 1.0 ms frames in Photo Set 6.9 above, the gas jet can be seen to be following the trail of the diesel closely. Thus the gas is in an excellent position to be ignited by the diesel which, by the 1.0 ms frame should in this area certainly have ignited. Also at this stage, only a relatively small amount of gas has entered the chamber and so the majority of the injected gas (indeed all that follows from this time) will experience mixing-controlled combustion.

6.2 Conclusion – Laboratory Results

Flow visualisation tests on the mixing of a gas fuel jet and a diesel fuel spray indicate that a small convergence angle of only a few degrees will give optimum mixing. While their simultaneous start gives good mixing, it occurs early and is likely to affect the ignition of the diesel fuel.

Depending upon the injection pressure of the diesel, the spray is likely to enter at a higher initial velocity than the gas jet. The instantaneous tip velocities of the diesel injections shown in the previous chapter reach a maximum at about 0.4 to 0.45 ms after the jet appears. They then oscillate with a second peak appearing at about 0.6 ms. At the pressures of 60, 120 and 160 MPa, the maximum measured values are respectively 160, 240 and 280 m/s with minimums (except during the very first time increment) of around 60 m/s in each case.

Given these values, it could be expected that the gas jet in the dual fuel configuration would not overtake the liquid. However, this is not the case. While the liquid tip velocities are high, stripped or highly-atomised liquid is left well behind and the gas front easily penetrates into these potential ignition sources. A 1.0 ms delay is too great as the diesel jet has moved too far from the nozzle and a delay of 0.5 ms provides a reasonable compromise. These values are compared with CFD results in the following chapters.

7. Chapter Seven: Numerical Work – Set-up

Diesel engines are widely used as a means of generating power for society. Improvements in efficiency and reductions in emissions are constantly sought owing to increasing prices for fossil-fuels and increasingly-stringent emissions laws. For these reasons, the numerical simulation of injection and combustion processes has been an area of considerable interest in the last two decades. Rapidly-improving computational resources have allowed detailed modelling that was not possible even a decade ago. The description of the break-up mechanisms due to aerodynamic liquid-gas interactions constitutes a real challenge, requiring the three-dimensional mathematical formulation of instabilities occurring on the phase-dividing surface of a two-phase flow [143].

Some researchers write their own numerical code whilst others use commercial codes such as *KIVA* [6], *STAR-CD* [15], *Fire* [38], and *Fluent* [39]. Much work has focussed on modelling the injection and combustion processes in an engine. In the work here, spray atomisation and break-up forms an important part of the modelling since the amount of atomisation of the spray directly affects how the liquid diesel mixes not only with the air in the combustion chamber but also with the NG jet.

The code being used here is *Fluent* version 6.1.18. This code has been used within the School since the late 1990s and has been applied to a wide variety of flow problems. With respect to the current work, the capabilities of *Fluent* include the modelling of cavitation in the nozzle of a diesel injector and the subsequent jet break-up caused by surface instabilities. Evaporating sprays are able to be simulated as well as chemical species mixing and reaction which is applicable to the multi-species, multi-phase problem studied here. Various models are available for considering turbulence in flows. Homogeneous and heterogeneous combustion models are available although these were not used here. Previous researchers have used *Fluent* for simulating gas injection [66, 85] although its use in spray applications does not appear to be widespread.

7.1 The Domain

The domain used for the CFD work was based on the School's "Rapid Compression Machine" (RCM) as mentioned in Section 5.4 and described by Miao [91]. Whilst most of the validation of this numerical work was carried-out using high-speed photography, combustion testing of the DF injection will eventually be carried out in the RCM and so its cylinder was decided upon as the choice for the computational domain.

The RCM is a constant-volume combustion apparatus and is, in effect, a single-stroke engine simulator [90]. It consists of a cylinder with a swept volume of 1.4L which is about the size of a cylinder in a typical truck engine. Compressed air is used to drive the piston from BDC to TDC at high speed. When the piston reaches TDC it is captured and held, the injector fires and constant-volume combustion occurs. The combustion chamber's pressure and temperature history immediately following the injection is logged for later analysis of the combustion. Further information about the RCM is provided in Appendix G.

The three-dimensional numerical domain constructed for the current work has the same dimensions as the RCM when the piston is at TDC. The boundaries of the domain include the cylinder wall, the piston crown (bottom), the cylinder head (top) and the outer faces of the fuel injector. The diesel injector used in the laboratory experiments in the current work had a nozzle that was of the mini-sac design with six equi-spaced holes. The RCM's cylinder is itself axi-symmetric and so, in the situation where the diesel and gas nozzles were oriented so that the holes were (vertically) co-planar, it was computationally-efficient to model the combustion chamber as a segment of one-sixth of the cylinder.

The boundaries of this domain are shown in Figure 7.1 in which the gas injection inlet to the computational domain is shown as the green point and the diesel inlet as the blue point. As described in the previous chapters, three different dual-fuel injector geometries ("injectors") were to be simulated using CFD. Laboratory testing resulted in the manufacture of a fourth injector and this was found to provide the best mixing as described in Section 6.1.4. Figure 7.2 shows a cross-section of the numerical domain for the parallel injector. The only change between this domain and that of the other three injectors was the angle of the axis of the gas nozzle hole with respect to the diesel nozzle.

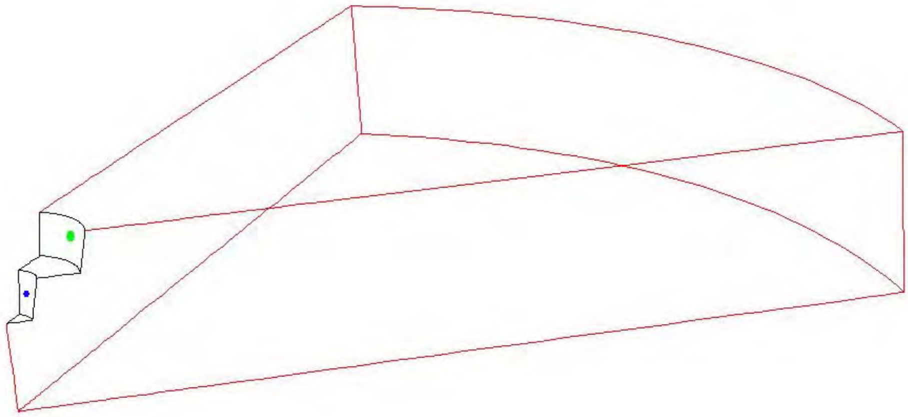

Figure 7.1. Outline of the computational domain which consists of one-sixth of the combustion chamber of the RCM.

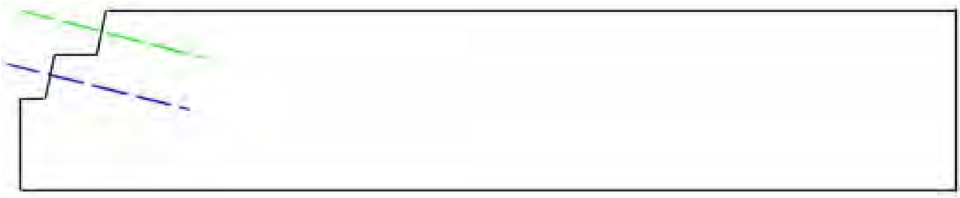

Figure 7.2. Vertical cross-section through the computational domain. The green axis is that of the gas injection nozzle, the blue that of the diesel injection nozzle.

7.2 The Code

7.2.1 The Governing Equations

The Navier-Stokes equations are the fundamental partial-differential equations that describe the flow of fluids. They are based on the three universal conservation laws: conservation of mass, conservation of momentum (Newton's Second Law) and conservation of energy. For all flows, *Fluent* solves conservation equations for mass and momentum. For flows involving heat transfer or compressibility, an additional equation for energy conservation is solved. For flows involving species mixing or reactions, a species conservation equation is also solved. Additional transport equations are solved when the flow is turbulent. The actual Navier-Stokes equations are given in Appendix H.

7.2.2 The Solver

Fluent provides three different solver formulations for the equations: segregated, coupled implicit and coupled explicit. All three solver formulations will provide accurate results for a broad range of flows [39], but in some cases one formulation may perform better (ie. yield a solution more quickly) than the others. The segregated and coupled approaches differ in the way that the continuity, momentum, and (where appropriate) energy and species equations are solved. The segregated solver solves these equations sequentially (ie. segregated from one another), while the coupled solver solves them simultaneously (ie. coupled together). Both formulations solve the equations for additional scalars (eg. turbulence or radiation quantities) sequentially.

The segregated solver traditionally has been used for incompressible and mildly compressible flows. The coupled approach, on the other hand, was originally designed for high-speed compressible flows. Both approaches are now applicable to a broad range of flows (from incompressible to highly compressible) but the origins of the coupled formulation may give it a performance advantage over the segregated solver for high-speed compressible flows such as that used in the current work. Owing to advantages that it could offer with identifying the Mach disc in the results, a coupled solver with explicit time-stepping was tried first. Computational resources proved to be insufficient to solve any cases in a realistic time-frame and so a segregated solver was used for all the results presented here.

7.2.3 Discretisation

Fluent uses a control-volume based technique to convert the governing equations to algebraic equations that can be solved numerically. This control-volume technique consists of integrating the governing equations about each control-volume, yielding discrete equations that conserve each quantity on a control-volume basis. The process that *Fluent* uses to discretise the Navier-Stokes equations is detailed in Appendix H.

7.3 Sub-Models in the Code

The use of sub-models in the numerical scheme allows complicated physical processes within the flow to be solved using empirical estimations. By resolving physical processes in this way, however, approximations are necessarily introduced into computations [124]. Today, even with the relatively high-power of even desktop computers, such models are required to allow resolution of some physical processes within a sensible time-frame. Modern, multi-dimensional models are especially promising since they are capable of reproducing most of the details of the flow-field in an engine [7]. These sub-models are typically those for turbulence, wall boundary layers, processes in the fuel spray and chemical reactions that can be used to simulate combustion and pollutant formation.

7.3.1 Diesel Injection Models

The simulation of spray formation begins with drops at the position of the nozzle holes that subsequently penetrate the combustion chamber. The starting conditions of these drops, such as the initial radius and velocity components are not known and must be assumed or calculated. Because the droplets near the nozzle are a product of the primary break-up, their properties are mainly determined by the flow conditions at the end of the nozzle hole. Note that the primary break-up is considered here to be the first disintegration of the coherent liquid into ligaments and drops, described in detail in Section 3.4.1.

The secondary break-up is the disintegration of already existing droplets into smaller ones as described in Section 3.4.2. This is caused by the aerodynamic forces that are induced because of the relative velocity between the droplets and surrounding gas.

These forces make surface waves grow in the form of Kelvin-Helmholtz and Rayleigh-Taylor instabilities. Parts of the waves split off and generate smaller droplets.

7.3.1.1 Primary Jet Break-up Model

Fluent offers several models for simulating different types of engineering spray equipment. For this study of a diesel injector, the "Plain-Orifice Atomizer" (POA) model is suitable. In such an atomiser, the liquid is accelerated through a nozzle, forms a jet and then forms droplets. This model can be used to simulate the nozzle geometry of a diesel injector which is essentially a long, thin orifice that connects a high-pressure reservoir of diesel fuel within the injector to the compressed air in the combustion chamber. Using the POA model in *Fluent* enables the injection and subsequent atomisation of the diesel jet to be modelled without the need to create complicated mesh geometry around the nozzle. The location of the actual orifice and the direction it faces are specified from menus and then parameters particular to the nozzle are entered numerically. The main parameters used in the cases modelled in the current work and as depicted in Figure 7.3 were as follows:

Nozzle diameter:	0.2 mm
Nozzle length:	0.8 mm
Chamber temperature:	293 K (ambient conditions)
Mass-flow rate:	5.00 g/s
Injection duration:	0.5 ms

The injector used in the laboratory work, from an HPCR system, had a multi-hole, mini-sac nozzle and the injection pressure could be set up to 180 MPa. As described in Section 3.2.2, the plain orifice may operate in any of three different flow regimes: single-phase, cavitating and flipped. The regime in which the nozzle operates depends upon the upstream and downstream conditions of the fluid and the geometry of the nozzle. The transition between regimes is abrupt and produces radically different sprays. As put forward by Soteriou et al [140], modern, multi-hole, mini-sac nozzles operate almost always in the cavitating regime and so the CFD model in this work was set to simulate cavitating flow. In *Fluent's* POA model, the onset of cavitation was found to be able to be controlled by carefully setting the parameter for the inlet radius, *r*. Setting *r* to 15 μm caused cavitation and resulted in the jet taking on a similar appearance to that studied in the laboratory.

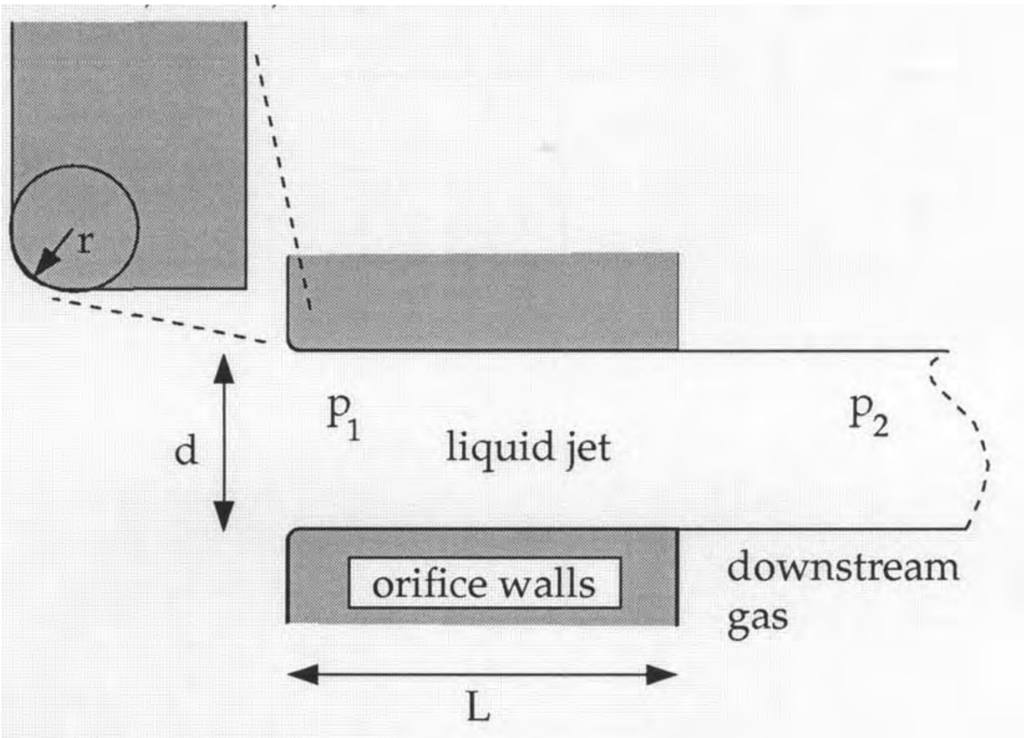

Figure 7.3. Illustration of the parameters used in *Fluent*'s Plain-Orifice Atomiser model [39].

7.3.1.2 Secondary Jet Break-up

Droplet break-up

Fluent offers two industry-standard spray break-up models as described in Section 3.4.3: The Taylor Analogy Break-up (TAB) model and the Wave model. The *Fluent* manual [39] recommends the use of the TAB model for low-Weber Number injections, in particular low-speed sprays into a standard atmosphere. The Wave model on the other hand is popularly used in high-speed fuel injection applications (where the Weber number is higher than 100) and so is the model used in the current work.

The Wave model of Reitz [120] was detailed in Section 3.4.3. It considers the break-up of an injected liquid to be induced by the relative velocity between the liquid and gas phases. It assumes that the time required for the spray to break-up and the size of the droplets that result is related to the fastest-growing Kelvin-Helmholtz instability. The wavelength and growth rate of this instability are used to predict the details of the forming droplets.

Droplet Drag

Fluent provides a method to determine the co-efficient of drag for the droplets by taking into account variations in the shape of the droplets. The dynamic drag model is applicable in almost any conditions and is compatible with both the TAB and Wave break-up models. Conventional droplet drag models assume that the droplet remains spherical throughout the domain. In practice, the shape of an initially-spherical droplet becomes distorted as it moves through a gas, particularly when the Weber Number is large. In extreme cases, the droplet's shape will approach that of a disc, which has significantly higher drag than a sphere. Thus the conventional drag models, which assume that the droplet remains spherical, are unsatisfactory. *Fluent's* model accounts for the effects of droplet distortion by linearly varying the drag between that of a sphere and that of a disc.

Droplet Collision

When drops collide, the following things can happen [39]:

- They can experience coalescence.
- They can maintain their sizes and temperatures but undergo velocity changes – a "grazing collision".
- They can undergo a "shattering collision". Shattering occurs at high *We* when coalesced drops form a stretched liquid ligament that breaks into droplets due to wave instabilities.

In *Fluent*, the collision frequency and the probability of coalescence between drops in two parcels controls the outcome of collision interactions.

7.3.2 Gas Injection

As described in Section 3.6, under-expansion occurs when the pressure ratio is higher than 1.86 for ideal gas behaviour at the nozzle. With under-expanded conditions, the flow chokes at the exit of the nozzle. Since the expansion process involves some shocks, it is unlikely that the flow field near the nozzle will be very accurate unless a very fine grid is used.

As described in Section 3.7.2, Hill and Ouellette in 1999 and 2000 [55, 56] modelled transient gas injections for HPDI engines using the *KIVA-2* code. They described how, as put forward by previous researchers, that a gas jet, once injected, may be considered to have "forgotten" its original configuration so that the mass flux, $\dot{M}_i$, is the only significant characteristic of the nozzle flow. This is illustrated by Equation 3.7 in the current work. Hill and Ouellette used this finding to create a model for the gas injection whereby the exact features of the nozzle could be approximated. The "Virtual Nozzle" model meant that the exact features of the gas nozzle (such as its very small diameter when compared with the bore of the chamber being modelled) did not need to be resolved. This was an approach analogous to the POA model used in *Fluent* to simulate the effects of the diesel nozzle.

Equation 3.7 states that penetration will be the same so long as the rate of mass injection is duplicated for a given chamber density. Derivations from Equation 3.7 lead to Equation 7.1 which describes conditions for a virtual nozzle that will provide a correctly-expanded nozzle with the equivalent momentum-injection rate.

$$\frac{D_c}{D_n} = \sqrt{\frac{0.546}{M_c^{\ 2}}\frac{P_0}{P_a}}$$

Equation 7.1 [56]

Subscript *c* refers to the virtual nozzle which provides a correctly-expanded jet and subscript *n* refers to the real nozzle. P_0 and P_a are the pressures in the gas reservoir and the chamber respectively whilst *M* is the Mach number and *D* is the diameter of the nozzle.

Hill and Ouellette found that the corrected case predicted penetration about 5% higher than the uncorrected case despite the identical momentum injection rate. This was attributed to the fact that the uncorrected cases were run using a grid that was not fine enough to properly resolve the required pressure adjustments.

In the current work it was decided to directly model the actual nozzle orifice rather than use models. Advances in computational power even during the last five years mean that much finer computational meshes are able to be used for a given computational time. Zakrzewski in 2002 [160] showed that *Fluent* was capable of capturing shock waves, albeit with a coupled solver. Since the NG does not change its phase during or after the injection, its introduction into the computational domain was through a simple "mass-flow" inlet which had a diameter of 0.4 mm. In *Fluent*, parameters for such inlets need to be specified so that the compressible gas entering the chamber does so at the correct density. To this end, the fluid's stagnation temperature was set to 336 K for ambient conditions of 293 K. This effectively simulated a choked nozzle for the final mass-flow rate of 3.5 g/s for the NG.

7.3.3 Turbulence Model

The injection of both the diesel and natural gas occurred under high pressure. For resulting velocities of the diesel and NG both exceeding 400 m/s, the Reynolds' Numbers of the two nozzles were in the order of $1x10^6$ and $20x10^3$ respectively. These injections can safely be taken to be predominantly turbulent.

Turbulent flows are characterised by fluctuating velocity fields. These fluctuations mix the transported quantities such as momentum, energy and species concentration which causes those quantities to fluctuate as well. These fluctuations can be on a very small scale and happen with a high frequency and so direct simulation would be (computationally) prohibitively expensive. To overcome the computational expense whilst still providing an acceptable level of accuracy, *Fluent* manipulates the instantaneous (exact) governing equations to remove the small fluctuations. This results in a modified set of equations that are computationally more economical to solve.

These modified equations do, however, contain new variables and so turbulence models are needed to determine these variables in terms of know quantities. There exists two alternative ways in which the small-scale turbulent fluctuations can be transformed into equations that are computationally inexpensive: Reynolds Averaging and "filtering". Both methods introduce extra terms into the governing equations that need to be modelled to obtain a solution.

- Reynolds-Averaged Navier-Stokes (RANS) equations represent transport equations for the mean flow quantities only. If the mean flow is steady, the governing equations will not contain time derivatives and so a steady-state solution is economical to calculate. Advantages also exist in unsteady flows such as those in the current work since the time-step for the calculation will be determined by the global unsteadiness rather than by small-scale fluctuations caused by the turbulence. More details about how *Fluent* deals with Reynolds Averaging are given in Appendix H.

- The alternative approach is to create a set of "filtered" equations. This approach, now called the Large-Eddy Simulation (LES) manipulates the exact Navier-Stokes equations to remove only eddies that are smaller than the size of the filter. The large eddies are then computed in a time-dependent simulation. The LES is attractive since deviations from the mean flow (eddies) receive proportionately more computational attention and so any error induced by the turbulence model should be reduced in comparison with the RANS method. The application of LES to the field of industrial fluid simulations is, however, quite new when compared with the accepted models which rely on RANS. Thus a RANS model was chosen for use in this study.

7.4 Mesh Generation

The computational domain must be split into the small control-volumes required by the solver. The geometry of the cylinder into which the dual-fuel jets are injected in the current work is not complex in itself. Yet to effectively mesh this domain, it was necessary to split it into many smaller sub-domains. Further, the length scale difference between the gas nozzle and the cylinder dimension is in the order of 100. To resolve details of the velocity profile at the nozzle exit, one must compute at scales maybe 10 times smaller than the nozzle diameter [56]. Owing to *Fluent* having a built-in injection model, resolution this fine was not required for the diesel nozzle. In an effort to accurately resolve the under-expanded flow at the gas nozzle, however, a very fine mesh was used around the gas inlet with a slightly less-fine mesh in the expected vicinity of the standing shock wave or Mach disc.

7.4.1 Structure of the Mesh

To allow the meshing of the domain in a short amount of time, an unstructured mesh consisting of tetrahedral elements was at first considered. It was soon found though that despite rigidly specifying the density of the edge and face meshes, control of the coarseness of the volume meshes was difficult to achieve. Further, an excessive number of cells would result when using the unstructured volume meshes. Because of this, the majority of the volume was meshed using structured, hexahedral elements. Figure 7.4 shows an overall view of the domain whilst Figure 7.5 shows a cross-sectional view of a vertical plane through the axes of the injection nozzles.

In keeping with standard practice, [83], care was taken whilst constructing the mesh to ensure that the maximum skewness of any of the elements did not exceed 0.8 and that the aspect ratio did not exceed 10:1. Cells with high relative skewness allow numerical errors to enter the calculations. Cells with a high aspect-ratio favour computation of flow in a direction parallel to their longest axis. With the jets used in this case, such an issue may not have too great an effect on the results on the highly-directional flow near the nozzles. By choosing a low aspect ratio, however, calculation of the radial components of the jets' flow should be more accurately modelled.

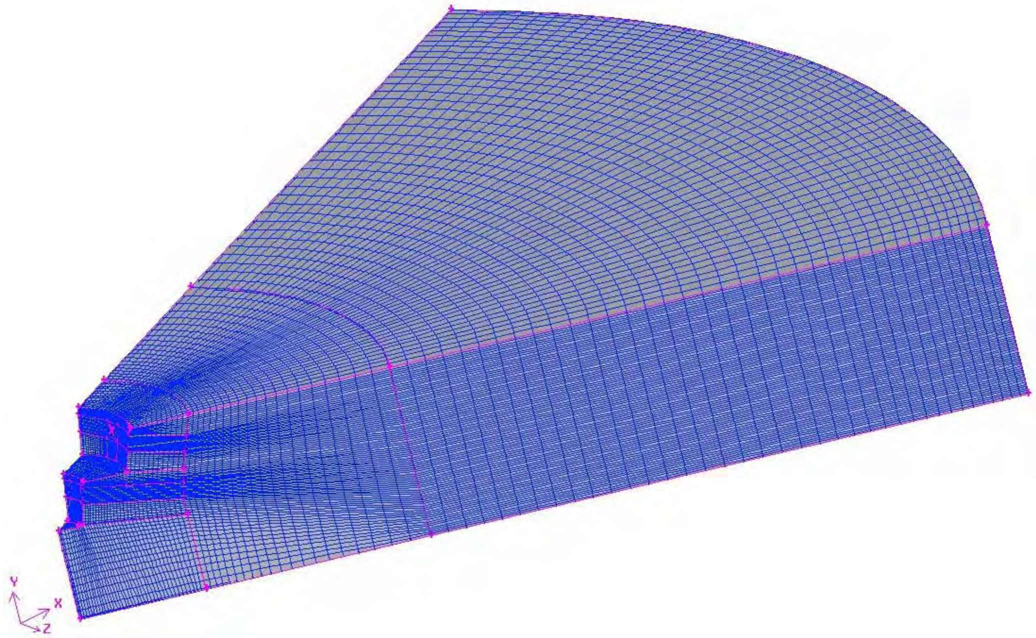

Figure 7.4. Overview of the entire mesh.

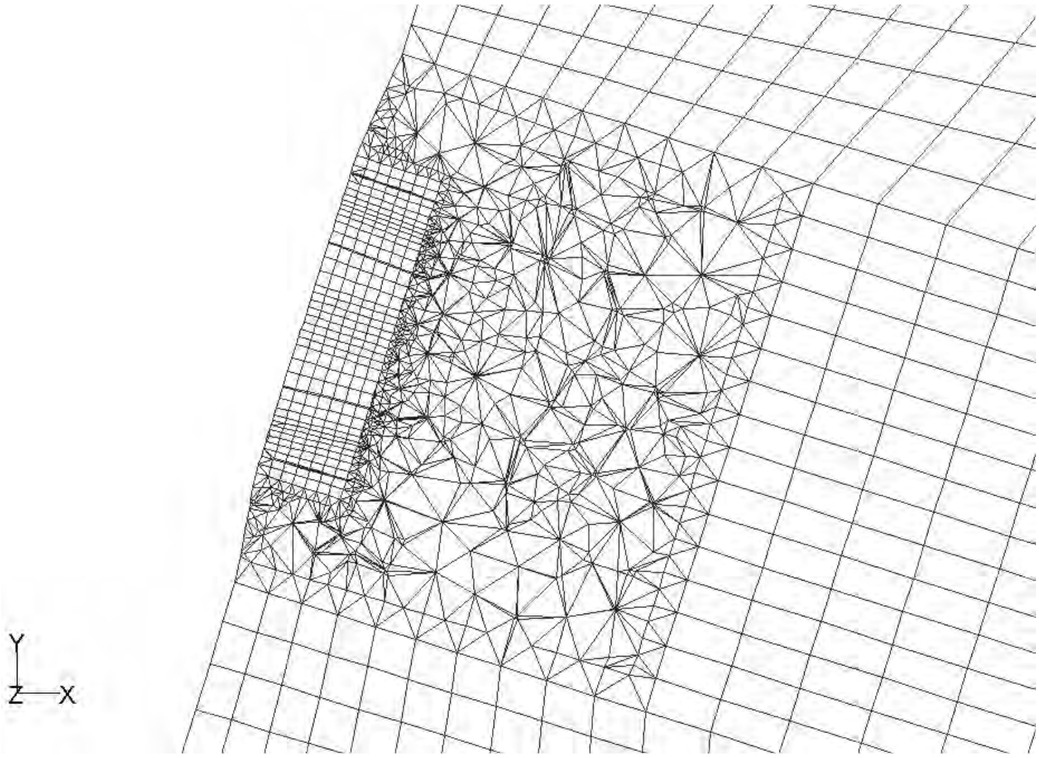

Figure 7.5. Unstructured, tetrahedral elements were used in the region connecting the circular gas inlet to the rest of the mesh.

7.4.2 Determining "Mesh Independence"

When using CFD, it is important to ensure that the results are not peculiar to a particular geometry of mesh. For each of the four DF injectors considered in the current work, meshes of different density were constructed so that the effects of mesh density on the results of the simulation could be quantified. Three meshes were constructed for each of the four injectors with the approximate number of cells for each mesh as shown in Table 7.1. With the arrival of the laboratory results as described in the previous chapter, attention focussed on the optimised injector.

To carry-out a more thorough analysis of the way in which the three different meshes affected the CFD results, it was planned initially to present penetration results from cases in which only diesel was injected and then for cases in which only gas was injected. However, a certain amount of randomness exists in the way the evaporation model for the diesel calculates droplet vaporisation. Thus it was found that results for the length of penetration of the diesel spray between the same cases running on the same processor for the diesel-only injection were not able to be repeated; at least for the small number of cases that could be run in a suitable amount of time. On the other hand, results for subsequent gas-only cases were identical. Thus only results from the gas-only cases have been considered in this analysis.

The main method used in this study of independence is changing the number of elements/cells in the mesh, ie. the overall cell density. Further refinement of the mesh may be achieved by modifying the distribution of the density of the cells, ie. the arrangement of the cells in the "boundary layer" near the walls of the computational domain. In determining independence of the mesh, a compromise must be made between how purely independent the mesh is from its cell density and the computing resources required to achieve this. In finding the "optimum" mesh to use, the "law of diminishing returns" applies. It is not worth making a mesh, say, twice as dense to achieve a gain of accuracy (measured against laboratory results) of only one or two percent if the computation time is doubled from, say, a week to two weeks.

7.4.2.1 Test Conditions

Each case was run with a gas mass-flow set to 0.001 kg/s which is about one-third of the peak gas flow under operating conditions for a real injector. The NG was modelled as methane which is a default fluid available in *Fluent*. The Realisable k-ε model (described in Appendix H) was used and so that wall-effects would not significantly affect the results, pressure-outlet boundaries were used for all domain boundaries except for the injector faces. These faces were modelled as wall-boundaries. The gas inlet was, as mentioned, set to the mass-flow inlet type boundary. A pressure-inlet boundary was first considered but difficulty in modelling such a nozzle with the physical relationships for sonic flow proved too difficult. Initial conditions in the computational domain were set to be quiescent with atmospheric pressure and a temperature of 293 K. The size of the time step was 1.0 μs.

For each of the twelve meshes studied here, two CFD cases were run. In the first case, the discretisation schemes for solving the equations for each variable of pressure, density, momentum and turbulent kinetic energy and dissipation-rate were calculated using a first-order solution. In the second case, a second-order solution was used for these variables. The *SIMPLEC* pressure-velocity coupling scheme was used in all cases.

Table 7.1 Comparison of the different meshes tested.

Name of Mesh	Approximate Number of Cells	Physical Memory (RAM) used for solution	Solution Time per Time Step*
A	1,000,000	~900 MB	22 minutes
B	385,000	~500 MB	10 minutes
C	160,000	~300 MB	4 minutes

*** Using a Pentium 4, 3 GHz processor which was available during the last 12 months of this project.**

7.4.2.2 Quantification of the Results

To measure the penetration of the gas jet, contours of the mass-fraction of methane were plotted in increments of 10%. So that results from each case could be directly compared with one another, the penetration of the gas jet was then taken to be the distance along the axis of the jet from the nozzle-orifice to the 10% contour line. The penetration was measured at 25 μs intervals for a period of 200 μs. In the case of the converging and optimised injectors, however, the 10% contour line had reached the boundary of the computational domain after just over 150 μs and so analysis for these geometries was carried-out only until this time.

7.4.2.3 Results

Figure 7.6 shows the results from analysis of the optimised mesh. In each case, the furthest penetration of the 10% contour of methane concentration is plotted against the solution time. For meshes A and B, gas penetrations at each measured time-step were in close agreement for the first-order cases. When mesh B was tested with the second-order discretisation scheme the results were also consistent. Using mesh B for the simulation of the dual-fuel injector thus seemed to be to be satisfactory for isolating the effects of grid density. Similar results were found for the other three injectors.

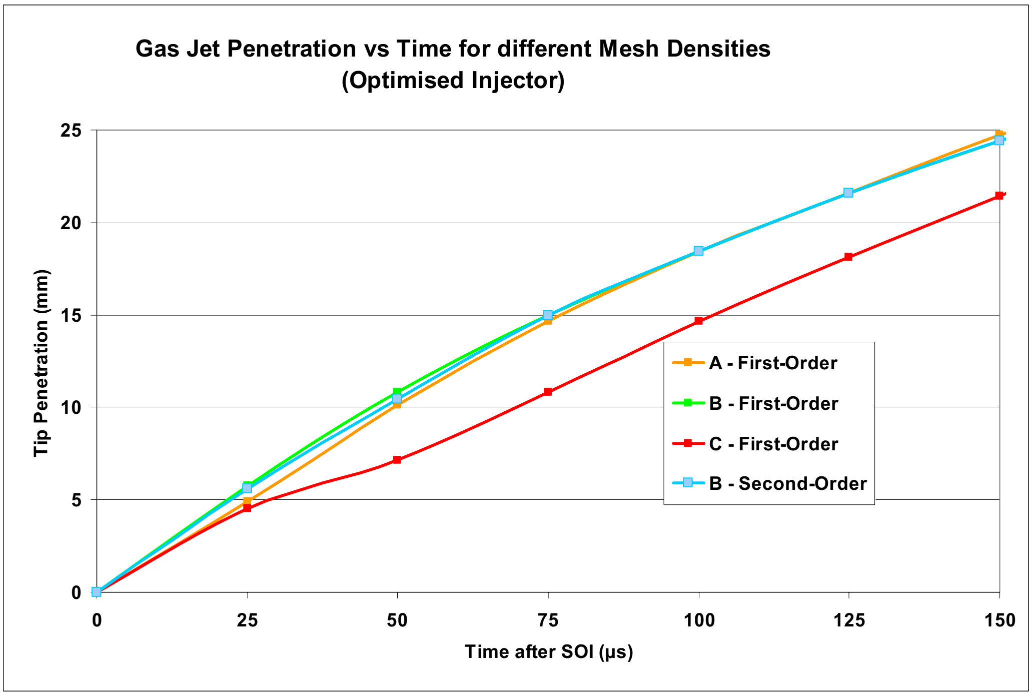

Figure 7.6. Results from the Mesh Independence Study.

7.4.2.4 Considerations for the Multi-Phase Flow

Simple tests for mesh independence of the liquid spray (similar to those described above for the gas jet) were carried out to ensure that the use of the reasonably fine Mesh B would not give results for jet penetration more than a few percent different to the less-fine Mesh C.

Whilst an increasingly-fine mesh will not necessarily affect the accuracy of the results in a single-phase (ie. gas-only) case, this is not so for the liquid injection studied here. Aneja and Abraham modelled atomising sprays using *KIVA* in 1998 [7] and found a sensitivity of the liquid penetration to the numerical resolution when the mesh was very fine. This was attributed to the dependence on grid density of the computed SMDs of the droplets. Different SMDs would result from different mesh densities because the collision frequency depended upon the density of the droplets within a cell. If the drops weren't evenly distributed, the number densities of drops within the cells could be different as the resolution is changed. Also, when vaporisation was present, distribution became markedly non-uniform. Grid dependence of computed SMR and liquid penetration was shown to arise from limitations of the collision and coalescence models. Such findings were confirmed in the study by Hill and Ouellette in 2000 [55].

7.5 Time-Step Independence

Upon establishing the cell-density of the numerical grid that would provide consistent and independent results, attention turned to the size of the time step that would be used. A study similar to that for determining mesh independence was performed with respect to the incremental time step used in the calculations. Figure 7.7 shows that independence was found when the time-step was reduced to 0.2 μs.

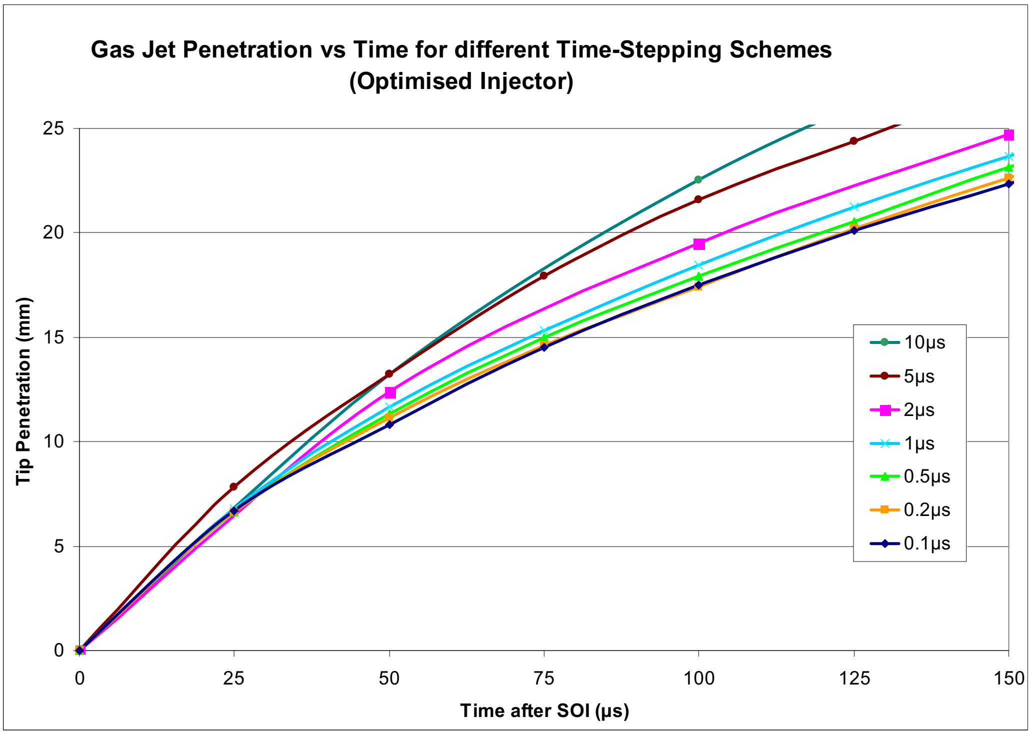

Figure 7.7. Results from the Time-Step Independence Study.

8. Chapter Eight: Numerical Work – Results

8.1 Simulation of the Diesel Spray

8.1.1 Calibrating the Diesel Spray

8.1.1.1 Setting the Flow-Rate for the Injection

The effective flow-rate of the HPCR diesel injector used in the laboratory was discussed in Chapter 5. As witnessed by Table 5.1, the mean flow rate for the 0.2 ms (electrical) pulse was unrealistically high. This is probably caused by opening and closing transients of the needle. From Table 5.1 and Figure 5.6 it can be seen that the average flow rate for the 0.3 ms injection lies between 4 and 5 g/s. Figure 8.1 shows that excellent agreement exists between laboratory and computational results for the growth-rate of the jet when the flow rate in the CFD is set to 5 g/s. Thus a mean flow rate of 5 g/s was chosen for the numerical simulation of the diesel spray. A more accurate result could perhaps have been achieved by varying the flow rate in the simulation to reflect the opening and closing transients of the needle. Figure 8.1 shows, however, that little could be gained.

8.1.1.2 Calibrating the "Wave" Model

As described in Section 7.3.1, setting the radius of the inlet corner to the nozzle hole in the atomiser model to 15 μm caused the orifice to cavitate. The Wave model for the aerodynamic break-up of the liquid spray was discussed in Section 3.4.3. The rate of break-up can be tuned by varying the value of the constants B_0 and B_1 as shown in equations 3.5. and 3.6 respectively.

$$r = B_0 \Lambda$$ **Equation 3.5 [120]**

$$\tau = \frac{3.726 B_1 a}{\Lambda \Omega}$$ **Equation 3.6 [120]**

The droplet radius constant, B_0 is generally set to 0.61 as described by Hong et al [61], Reitz [120], Reitz and Diwakar [123] and Tanner [143]. The value for the droplet break-up time constant, B_1, however, is often varied to help calibrate numerical results to those obtained through experiments. The effect of varying the value of B_1 for the diesel spray being studied here is shown in Figure 8.2. It can be seen that penetration in the far-field is not affected greatly by the value. A qualitative study of the distribution of injected particles was also performed but again little effect was noted.

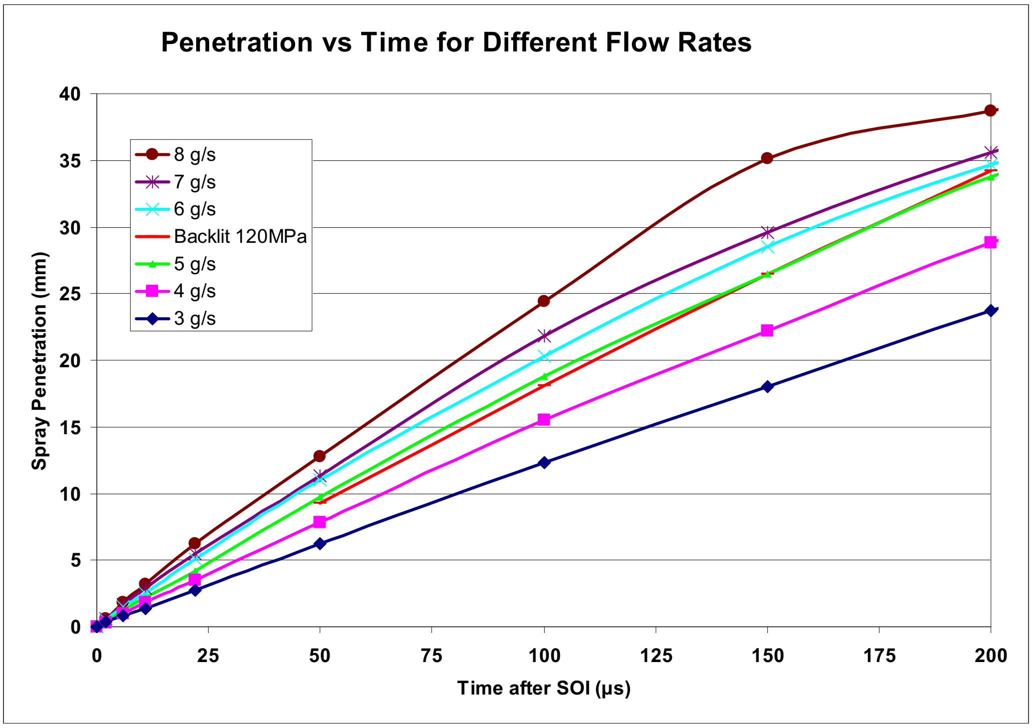

Figure 8.1. Tip penetration of the liquid phase in the diesel spray. Several flow-rates for the CFD are here compared with the laboratory result.

Reitz [120] and then Reitz and Diwakar [123] used B_1 = 20 and B_1 = 10 in their respective studies. The second study with B_1 = 10 resulted in a faster droplet stripping rate. Hong et al in 2000 [61] performed a similar study to the one carried-out in the current work but for non-evaporating sprays into ambient conditions. They used a "nozzle flow model" to simulate cavitation in conjunction with the Wave model although the injection pressures used were generally much lower than those in the current work. Figure 8.3 shows their results for a test in which the injection pressure was 10 MPa. The value of B_1 was also found to have little effect on penetration although the effect on the SMD of the resulting drops was significant. The best fit to their experimental data was found for $B_1 = 5$. For tests at higher pressures, they found that a higher value yielded better agreement with the experiments. A value of 20 was chosen for the current work.

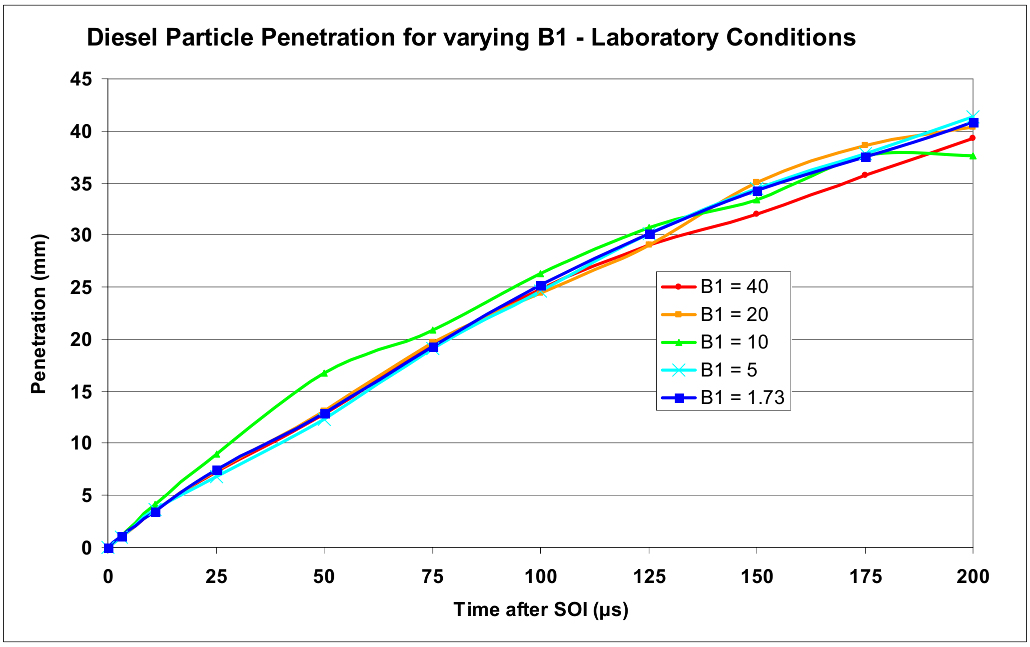

Figure 8.2. The effect of varying B_1 in the current work.

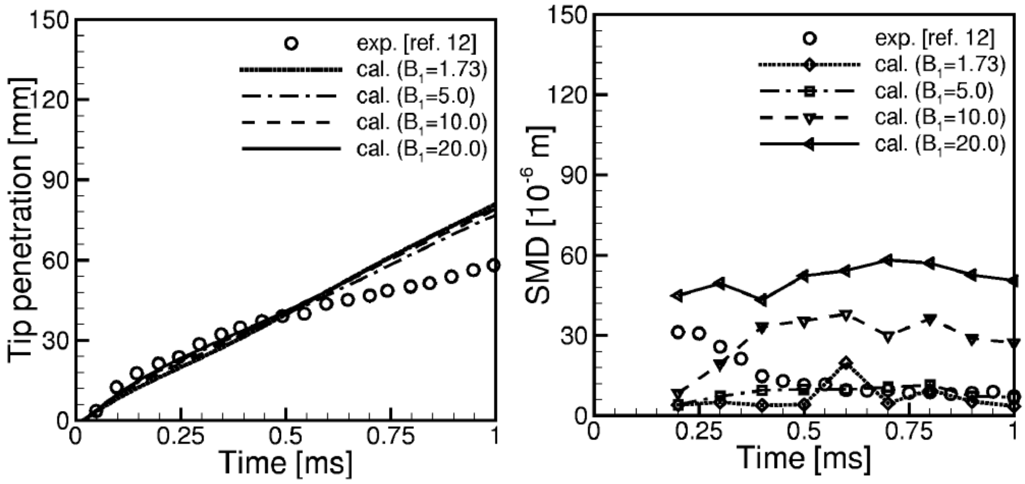

Figure 8.3. Laboratory results from Hong et al [61] for the variation of B_1. Measurements were taken 30 mm from the Ø0.2 mm nozzle. Injection pressure was 10 MPa.

8.1.2 Comparison with the Experiments

With the injection rate and atomisation models calibrated, cases for the parallel, converging and optimised injectors were solved using CFD. Owing to the poor mixing it displayed in the laboratory as described in the Section 6.1.1, the diverging injector was not simulated. Analysis of the numerical results confirmed that the optimised injector provided the best mixing. Thus all subsequent analysis in this chapter is with respect to injection from the optimised injector geometry. Since the actual diesel nozzle was the same for each of the different gas nozzles, results for the diesel spray hold for each of the different injectors tested.

Photo Set 8.1 shows frames from high-speed schlieren video of the diesel spray in the laboratory compared with frames from the CFD. The view chosen for representation of the numerical results is a two-dimensional slice taken vertically through the centre of the computational domain. This is therefore the same plane upon which lie the axes of both the gas and diesel nozzles. Note that the two jets can each be considered to be axi-symmetric until such time as they interact.

Fluent displays the relative concentration of liquid diesel droplets using “particles”. Each particle does not necessarily represent an actual diesel droplet but the area-density of the particles shown is representative of the concentration of the liquid diesel in the particular plane shown. In the frames in the right-hand side column Photo Set 8.1, the velocity of each particle is represented by its colour. Ten levels of colour exist between red (300 m/s) and Blue (zero). A small number of particles close to the nozzle were found to have a velocity just exceeding 300 m/s.

Agreement between the two columns for the penetration length of the liquid diesel is reasonable considering that, in the photo frames, the droplets around the periphery of the jet will not show-up very well. This is because the droplets are so finely atomised that light will bend enough between the test-section and the camera to effectively cover the shadow caused by the droplet.

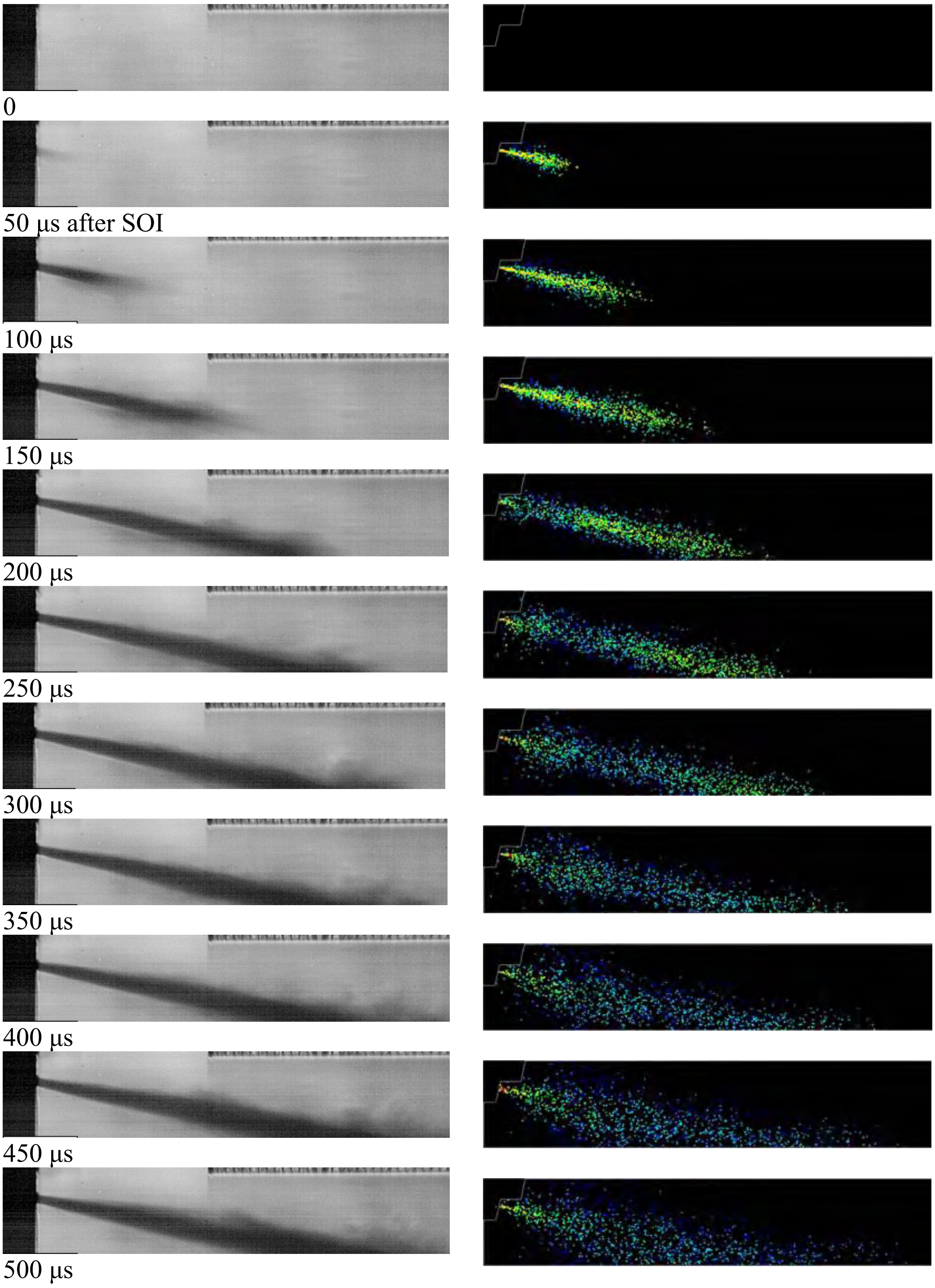

Photo Set 8.1. Schlieren images of the diesel spray (left-hand column) compared with CFD results (right-hand column).

8.1.3 Entrainment of the Surroundings into the Diesel Spray

Evaporation of the diesel droplets/particles in the spray, caused by interaction between the droplets and the air in the chamber, can be seen in Photo Set 8.2. The left-hand side column shows particle plots for every 50 μs through the simulation. The right-hand column shows the concentration of diesel vapour with respect to air in the cylinder. The mass-fraction of diesel is plotted in contours. The red contours indicate a mass fraction of 0.1 (10%) whilst blue represents a concentration of zero. There are a total of ten colours of contour and so each intermediate contour represents the mean concentration in increments of 0.01 (1%).

Figure 8.4 shows vectors of velocity in the near-field of the diesel spray. One vector arrow is shown here for every two cells in the vertical plane of interest through the centre of the mesh. It can be seen that air is being entrained into the "penetration" part of the spray as described by Sato et al [129] in Section 3.9.

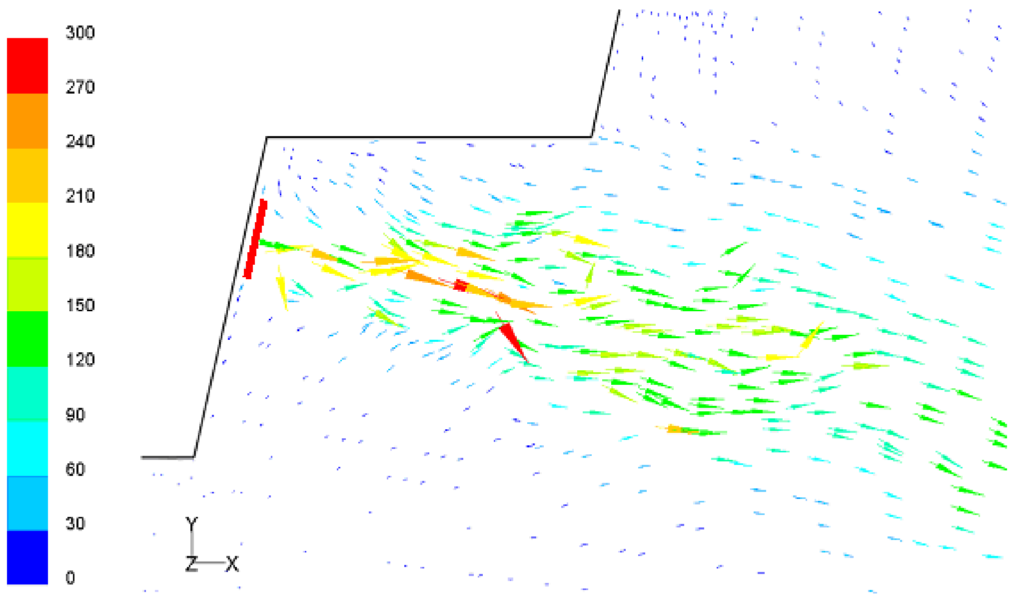

Figure 8.4. Vectors of velocity of the air/diesel vapour mixture in the chamber near the diesel injector at the instant of EOI (0.5 ms after SOI). The vectors are scaled and coloured according to the values (m/s) in the legend on the left. The location of the virtual nozzle is shown as a red line. The chamber initially contains atmospheric air at 293K.

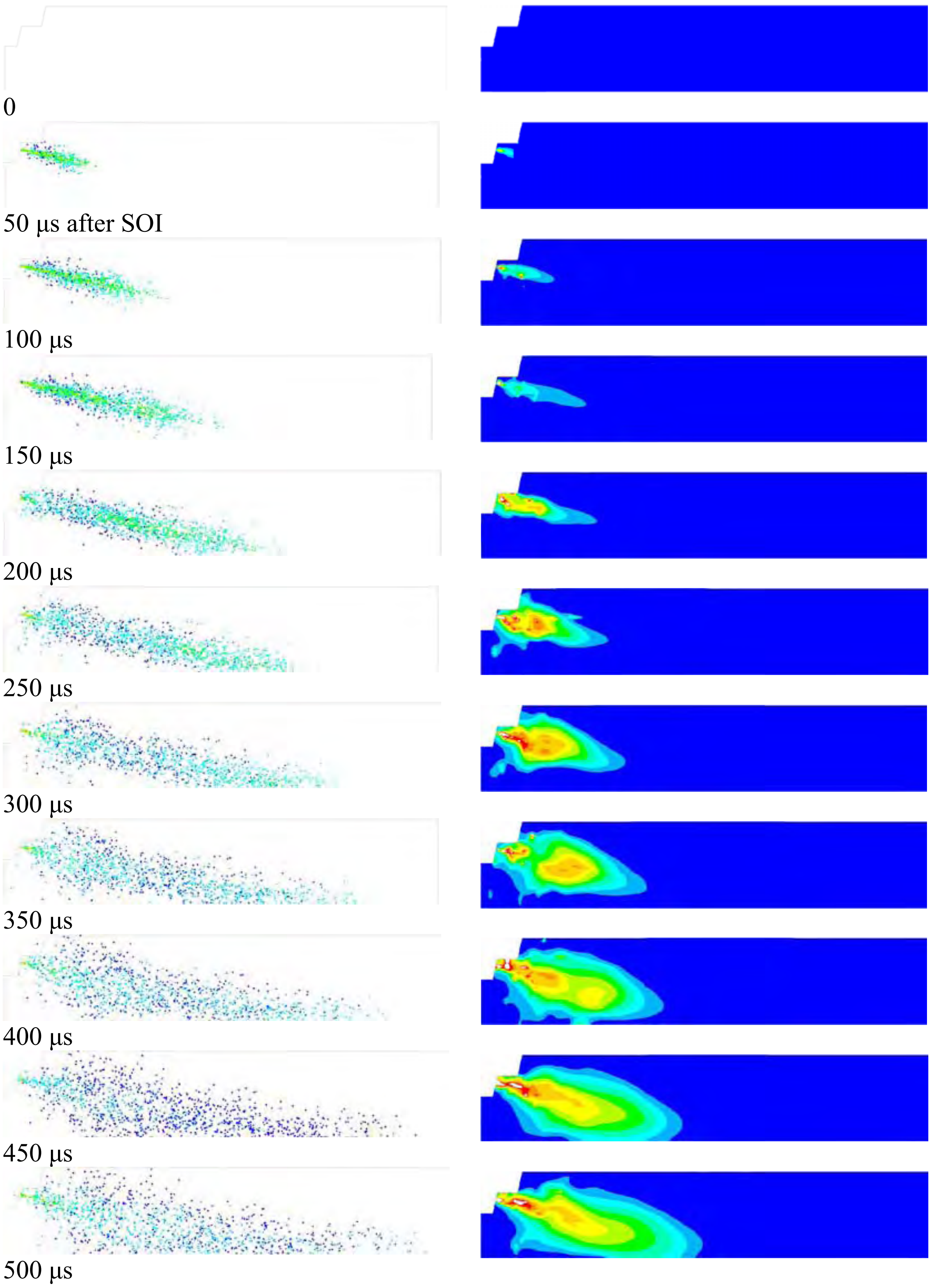

Photo Set 8.2. The column on the left shows the penetration and speed of the diesel particles as shown previously in Photo Set 8.1. In the column on the right, contours of the mass-fraction of diesel vapour are plotted in ten increments ranging between 0 and 0.1.

Photo Set 8.2 shows a result which is analogous to that presented in Photo Sets 5.25 and 5.26 where shadowgraph images of the spray were compared with backlit photos. Regions of vapour form in the chamber after the spray has passed and some of the liquid evaporates.

Figure 8.5 shows contours of velocity of the diesel spray at 0.5 ms after SOI. The decrease in speed of the spray as it progresses across the chamber can be seen to be mostly linear as the momentum of the droplets is transferred to the surrounding air.

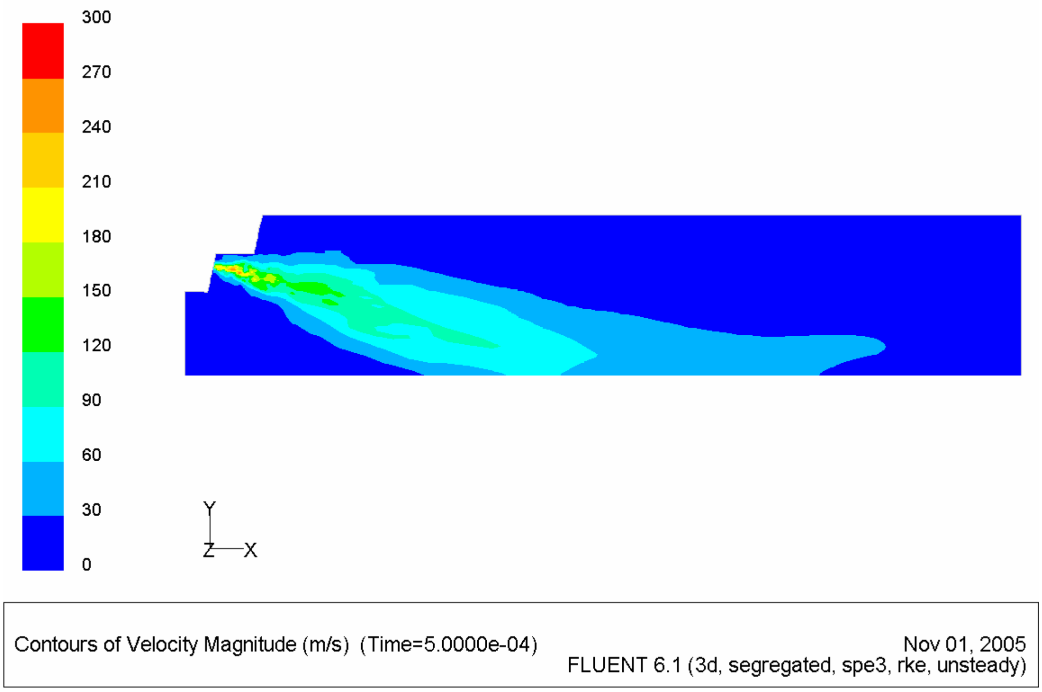

Figure 8.5. A screen-shot from *Fluent* taken 0.5 ms after SOI of the diesel injection. The velocity of the gas in the chamber (both air and diesel vapour) is shown in contours in ten increments. The peak velocity is 281 m/s.

8.2 Simulation of the Gas Jet

8.2.1 Calibrating the Gas Jet

As described in Section 5.3, the flow rate of the NG into the chamber from the nozzle builds-up over a few milliseconds. The rate of build-up was shown graphically in Figure 5.9. Gas pressure to the GCV was set at 16 MPa during those tests which, by calculation for a choked nozzle, should have yielded a final, steady flow-rate of 3.5 g/s for the ambient laboratory conditions at 293 K.

Accordingly, CFD simulations were made in which the flow-rate of the gas jet was slowly increased over a period of time. Table 8.1 shows the flow rates used in the respective time intervals so that penetration of the gas jet in the CFD matched the penetration in the laboratory tests.

Table 8.1. The gas flow rates used in the CFD so that penetration of the jet matched that measured in the laboratory.

Time (ms)	Injection Pressure (MPa)	Gas Flow (g/s)
0 - 0.1	0.044	0.01
0.1 - 0.2	0.088	0.02
0.2 – 0.3	0.224	0.05
0.3 – 0.5	0.450	0.10
0.5 – 0.8	1.126	0.25
0.8 – 1.0	2.256	0.50
1.0 – 1.3*	4.512	1.00
1.3 -1.8	6.768	1.50
1.8-2.5	9.024	2.00
2.5-3.0	11.280	2.50
3.0-4.0	13.536	3.00
>4.0	16.000	3.50

*** The 10% contour of mass-fraction had by this time exceeded the bounds of the domain. Subsequent time-step intervals and flow rates were approximated based upon the development of the jet observed in the schlieren video.**

8.2.2 Comparison with the Experiments

8.2.2.1 Growth Rate of the Jet

Photo Set 8.3 shows frames from the high-speed schlieren video of injection from the optimised injector compared with results from the CFD. In the frames from the CFD, the concentration of methane is plotted in contours of concentration of mass-fraction. The red contours indicate a mass fraction of 1.0 (100%) whilst blue represents a concentration of zero. There are ten levels/colours of contour such that each band represents the mean concentration in increments of 0.1 (10%). Growth of the jet in the CFD matched the penetration witnesses in the laboratory within a few millimetres until the perimeter of the gas jet had exceeded the bounds of the domain at about 1.3 ms after SOI. The subsequent ramp-up of flow in the CFD was chosen to reflect the build-up in the gas nozzle determined in the laboratory from the location of the Mach disc.

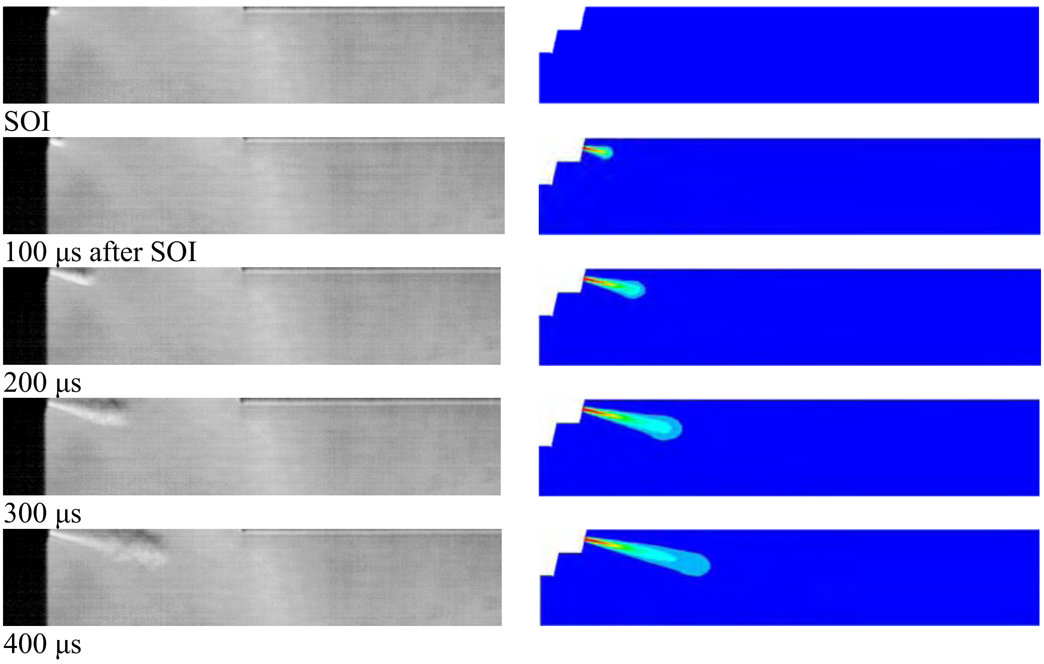

Photo Set 8.3. Schlieren video of the development of the gas jet from the optimised nozzle. The injection pressure was 16 MPa.

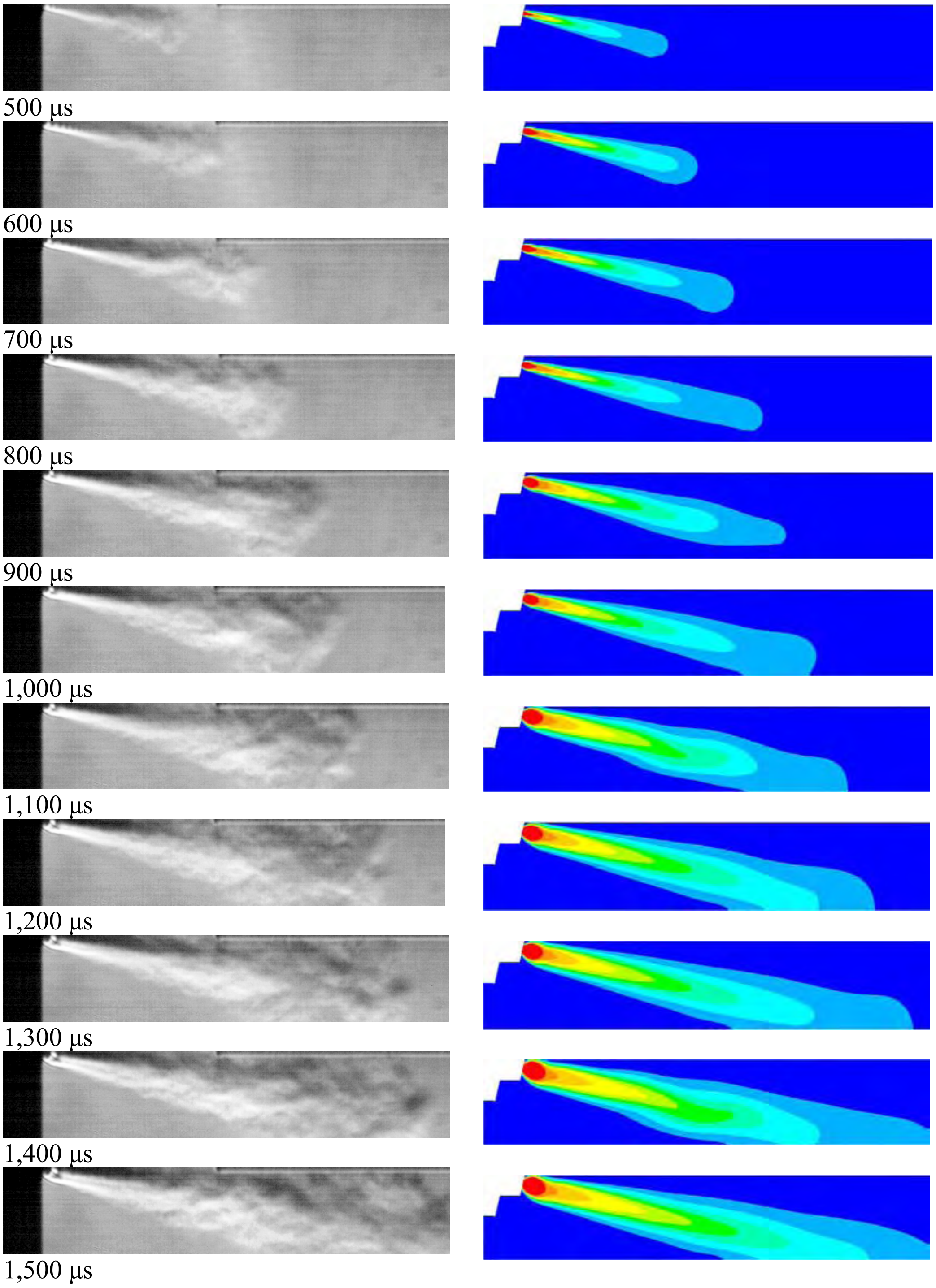

(Continuation of Photo Set 8.3.)

8.2.2.2 Location of the Mach Disc and Expansion of the Jet

From the shadowgraph images presented in Section 5.3.2, it was calculated that the area ratio of the normal shock to that of the nozzle exit was about 4.7, which indicates that the flow into the normal shock has a velocity of around 870 m/s at a Mach number of about 2.9. Downstream of the normal shock, the velocity could then be estimated as 200 m/s (Mach number 0.46). The methodology used for these calculations is summarised in Appendix E.

Figure 8.6 shows contours of Mach number for the gas jet at 1.3 ms after its SOI. Fair agreement of the location of the Mach disc and its size exists between this plot and the results from the laboratory as presented in Section 5.3.2. The speed at the nozzle exit can be seen to be at Mach 1 as required for a choked nozzle. Expansion takes the peak speed to just over Mach 3 before the speed drops back to subsonic over the shock wave.

Figure 8.7 shows a comparison between the location of the Mach disc seen in the laboratory and that from the CFD. The location of the Mach disc in the CFD indicates that the rate of pressure build-up in the numerical models is higher than that observed in the laboratory. There are two likely causes for this:

- The rate of jet growth was the only determining factor in the calibration of the flow rate of the jet in the CFD. The 10% contour of mass-fraction was used in the CFD whereas the concentration of gas at the boundary of the jet in the schlieren images is uncertain. Thus the increase in pressure/flow in the CFD could have occurred more rapidly than was really the case in the experiments, especially if the visible boundary of the jet in the experiments occurred at a very low concentration of gas, ie. below 10% concentration.

- The pressure drop through the nozzle was not included in the CFD and the offset so caused is clearly visible in Figure 8.7.

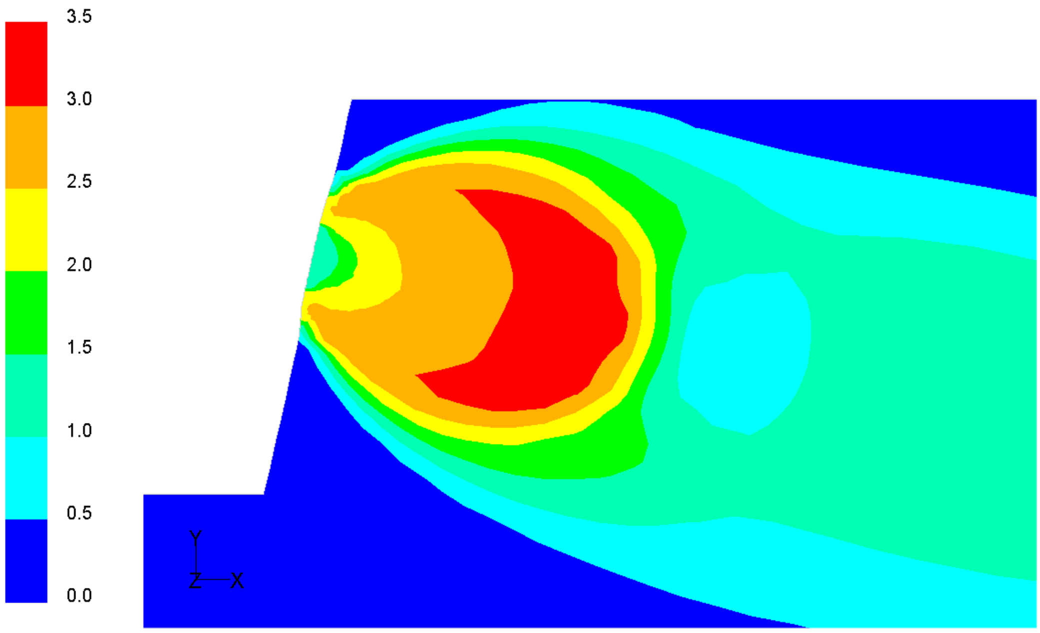

Figure 8.6. Contours of Mach number for the gas jet, 1.3 ms after SOI.

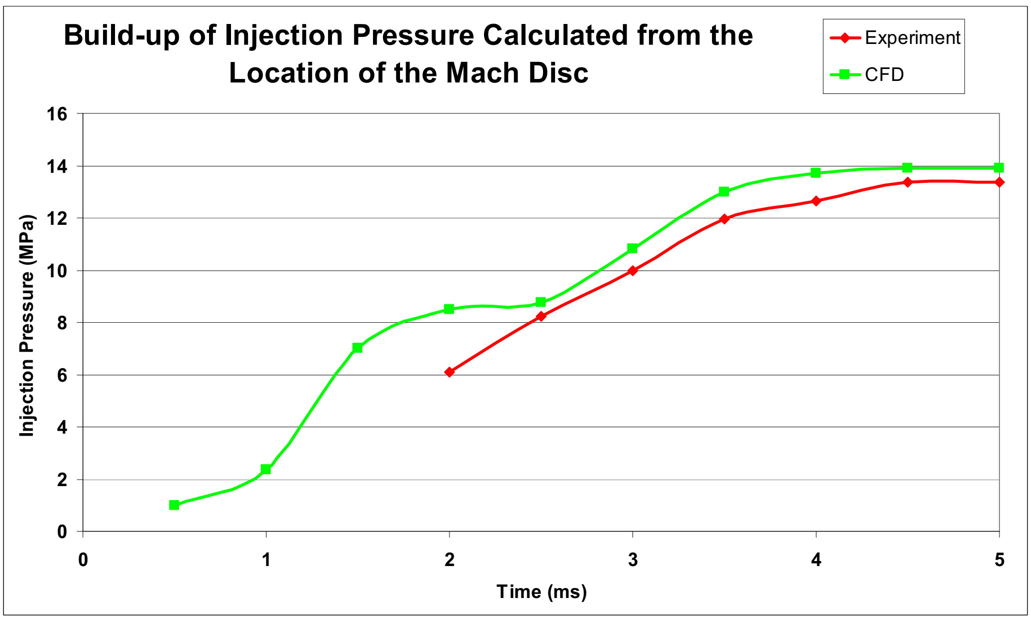

Figure 8.7. Injection pressure calculated from the location of the Mach disc – Laboratory results compared with the CFD.

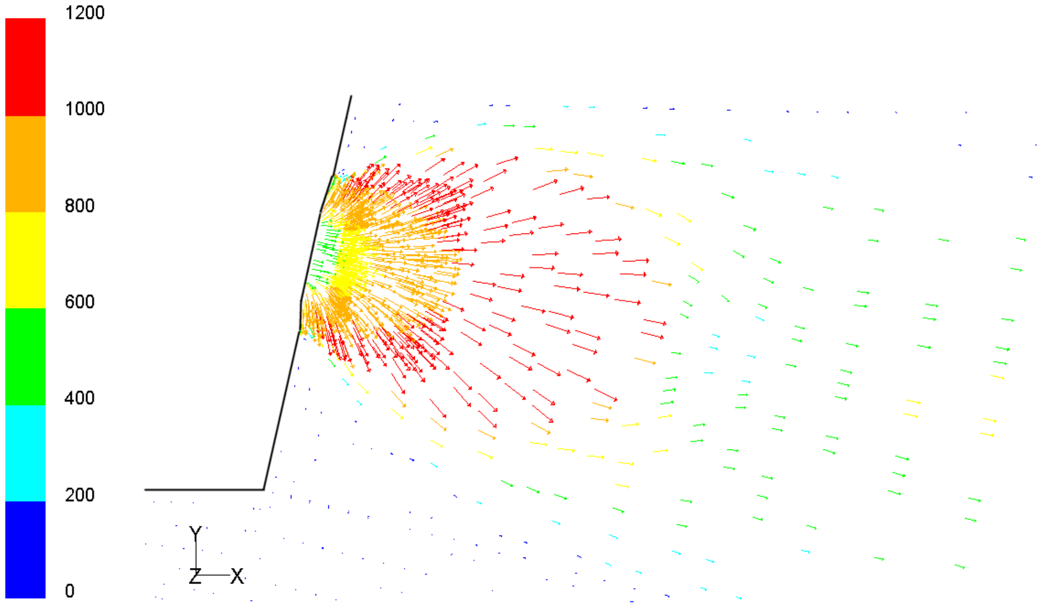

Figure 8.8. Vectors of velocity (coloured by speed in m/s) in the near-field of the gas nozzle.

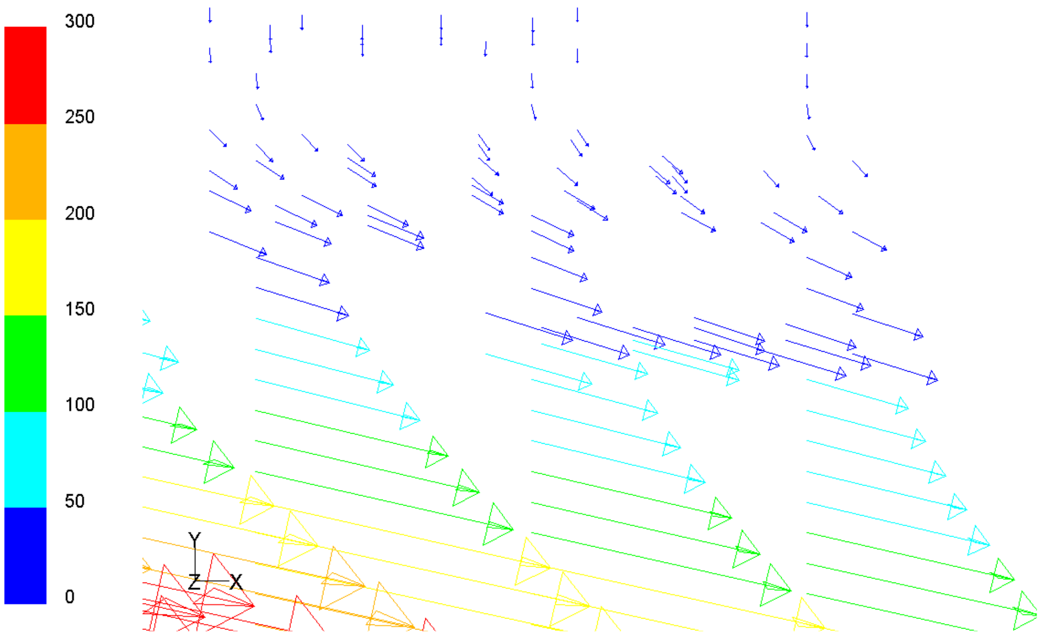

Figure 8.9. Vectors of velocity (coloured by speed in m/s) in the far-field of the gas nozzle.

8.2.3 Entrainment of the Surroundings into the Gas Jet

Figures 8.8 and 8.9 show velocity vectors in and around the gas jet in the near-field and far-field of the nozzle respectively. In common with the diesel spray, the surroundings can be seen to be entrained into the relatively low pressure periphery of the jet. Entrainment into gas jets was described in Section 3.8.2. The work of Abraham [2] revealed that the total mass entrained is shown to have a cubic dependence on axial penetration of the jet as per Equation 3.10.

$$M_e = \frac{1}{0.7}\left(\frac{8\pi}{3}\right)^2\left(\frac{K}{4\pi^{3/2}}\right)^2 \rho_a X_t^{\,3} \qquad \textbf{Equation 3.10 [2]}$$

8.2.3.1 An Approximation

Before applying Equation 3.10 to the CFD results in the current work, an alternative analysis was performed. Figure 8.10 shows an enlargement of the frame taken from Photo Set 8.3 at 1,300 μs after SOI. The penetration length of the gas jet (ie. the axial distance from the orifice to the outer limit of the 10% contour of mass-fraction) is 48.5 mm. Figure 8.11 shows a frame at the same time but here the contours are of density. These contours are plotted in twenty levels with a density range between 0 and 2 kg/m^3 and thus each contour represents a density band of 0.1 kg/m^3.

Five planes, each situated normal to the axis of the gas jet, have been drawn on both Figures 8.10 and 8.11. At each of the five planes, the air entrained into the jet was calculated on a mass per unit-length basis across the section of the jet. This was achieved by superimposing the plot of the contours of mass-fraction over the plot of contours of density. The mass per unit-length, m', for the annular area of each contour of mass-fraction, A, was then calculated using $m' = \rho \cdot c \cdot A$ where c was the mass-fraction of methane in the jet in the respective annular area and ρ the average density in the annulus. The mass of gas per unit-length in each annulus was then summed to find the total mass per unit-length of each of the five sections through the jet. The boundary of the jet in each case was taken to be the contour of 10% mass-fraction. Figure 8.12 shows the results from this calculation.

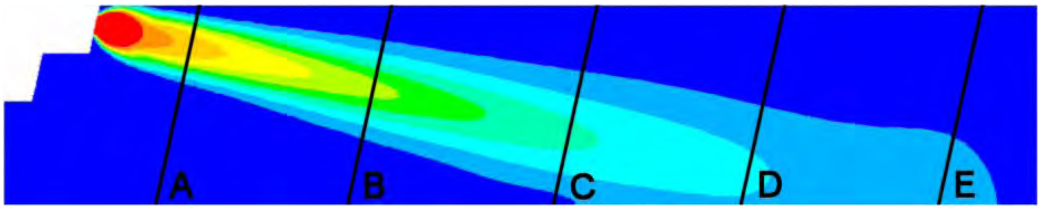

Figure 8.10. Enlargement of the 1,300 μs frame of gas concentration taken from Photo Set 8.3.

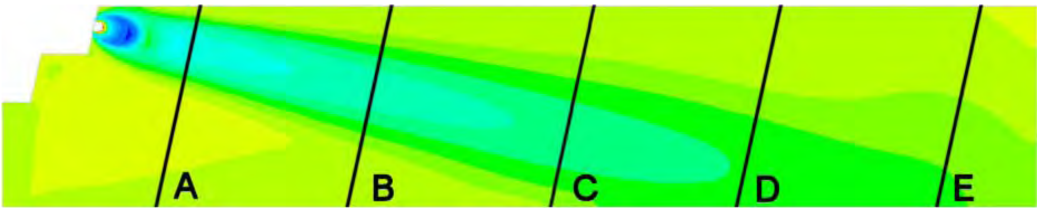

Figure 8.11. 1,300 μs frame showing contours of density in twenty levels between 0 and 2.0 kg/m³. The pale green (in the top right-hand corner) represents density between 1.1 and 1.2 kg/m³.

The total mass of air entrained into the jet could then be approximated by integrating the results for the individual planes as follows:

$$M_e = \int_{Orifice}^{Tip} m' dx \qquad \textbf{Equation 8.1}$$

Where x represents the penetration length of the jet in millimetres. Then for a jet length of 48.5 mm, Equation 8.1 can be re-written as:

$$M_e = \int_{0}^{48.5mm} (\rho \cdot c \cdot A) dx \qquad \textbf{Equation 8.2}$$

The individual values of m' were discretely summed as shown in Table 8.2 to yield an approximate mass of the total air entrained into the jet of 1.37 mg.

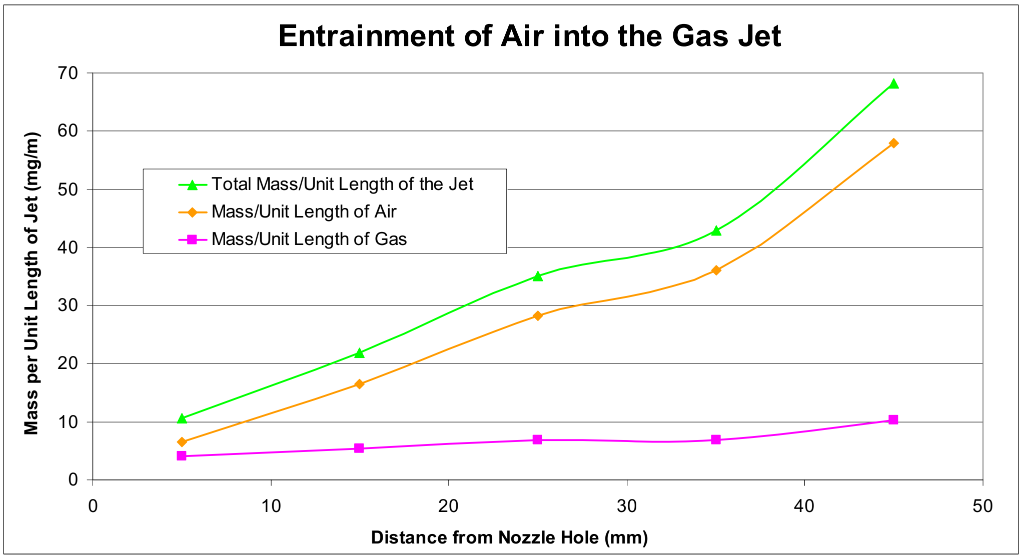

Figure 8.12. Entrainment of air into the gas jet.

Table 8.2. Integration of the individual entrainments to yield the mass of the jet.

Jet Region (mm)	Plane Used	Length (mm)	Entrainment at Plane (mg/m)	Entrainment in Region (mg)	TOTAL
0-10	A	10	6.58	0.066	
10-20	B	10	16.44	0.164	
20-30	C	10	28.18	0.282	
30-40	D	10	36.04	0.360	
40-48.5	E	8.5	57.95	0.493	**1.37 mg**

8.2.3.2 Abraham's Method

Now returning to Equation 3.10 of Abraham [2], the appropriate values for the jet analysed above are ρ_a = 1.2 kg/m^3 and X_t = 0.0485 m. Abraham suggested a value of K between 0.21 and 0.23 for nozzles such as that used in the current work. Table 8.3 shows the amount of air entrained into the jet when using Abraham's equation for several values of K. A value for K, calculated from the value of air entrained using the approximation in the section above, can be seen to lie within the bounds suggested by Abraham.

Table 8.3. Comparison of the amount of air entrained into the gas jet at *X* = 48.5 mm using both Abraham's equation and the approximation described above.

Calculation Method	Value of *K*	Mass entrained into the Jet (mg)
Abraham	0.21	*1.68*
Abraham	0.22	*1.85*
Abraham	0.23	*2.02*
Approximation	*0.223*	1.96

The gas jet modelled in the CFD thus represents the jet in the experiments quite well and behaves in a manner similar to that achieved by previous researchers. With the gas jet calibrated in this way, attention could be turned to the simulation of dual-fuelling.

8.3 Simulation of the Dual-Fuel Injection

8.3.1 Injection under Laboratory Conditions

The goal of developing the computational models in the current work was to be able to simulate DF injection into a combustion chamber. Visualising the flow-fields inside a combustion chamber is beyond what is presently achievable within the School. Thus validation of the CFD of the DF jets was only possible by comparing the CFD to results from DF injection in the JVR in the laboratory. If the CFD matched the laboratory results for the DF injection in the JVR then simulation of the DF injection under conditions of high pressure and temperature (ie. "engine" conditions) could be carried-out with some confidence.

8.3.1.1 Comparison with Experiments

Photo Set 8.4 shows results from DF injection with the optimised injector. SOI of both the diesel spray and the gas jet was simultaneous. The frames in the column on the left-hand side are from the schlieren video and are the same as those shown in Photo Set 6.7. The right-hand column shows frames from the CFD simulation. Liquid diesel is represented by particles (as described previously) and the gas jet by contours of mass-fraction.

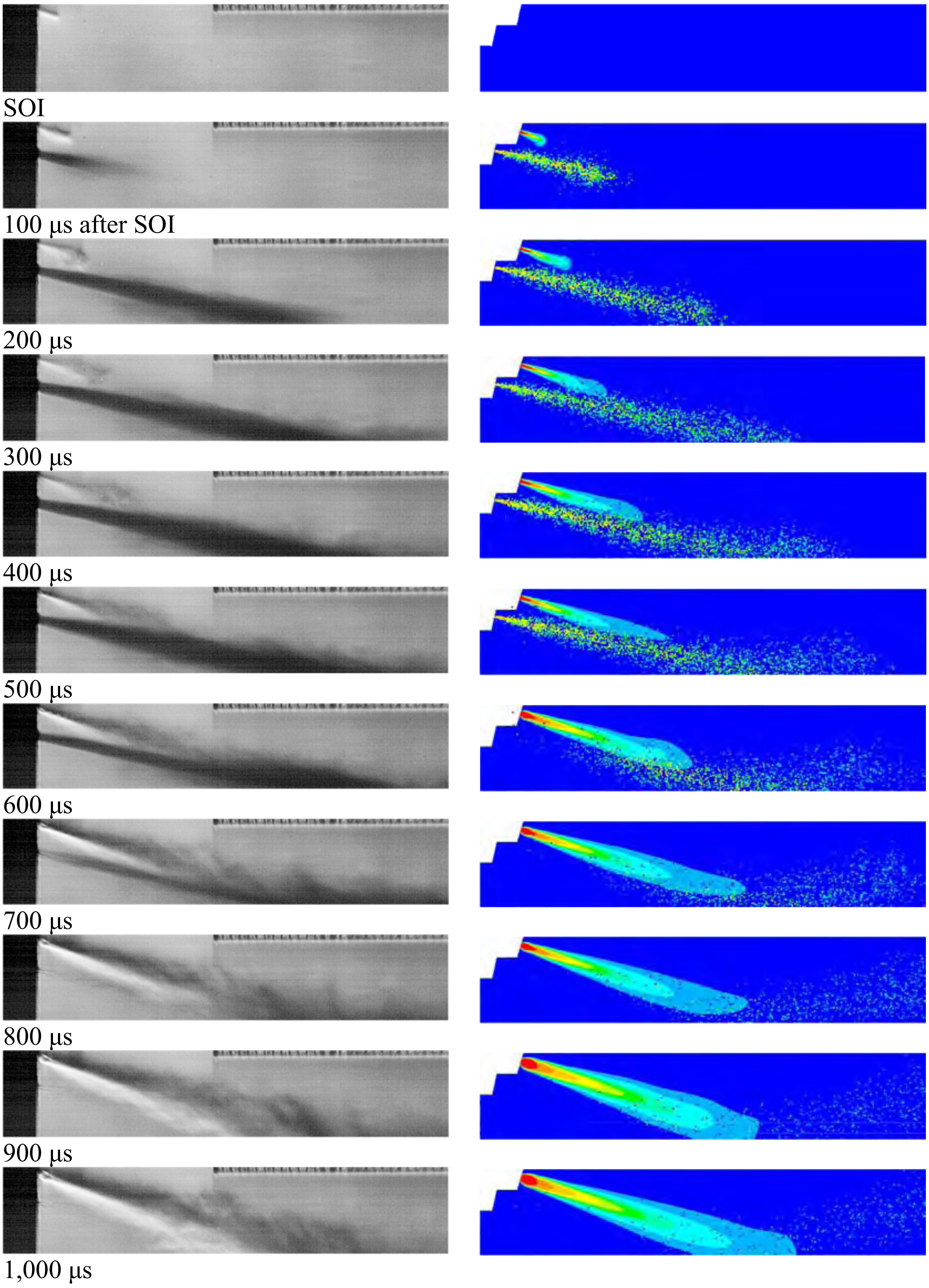

Photo Set 8.4. High-speed schlieren video of the optimised injector compared with results from the CFD simulation.

8.3.1.2 Interlace Angle

In all of the cases tested here, both the diesel and gas nozzle orifices lay on the same vertical plane. Thus, if each injector had six equi-spaced holes then each of the holes in the gas injector would be in the same vertical plane as a hole in the diesel injector. Li et al [85] carried-out numerical modelling to investigate the effect of rotating the axis of the gas nozzle with respect to the diesel nozzle from 0 degrees (ie. where each pair of nozzle holes are co-planar, as tested here). They defined the angle between the axis of the diesel nozzle and the axis of the gas nozzle (when measured on a plane perpendicular to the axis of the injector) as the "interlace" angle. They tested interlace angles of 0, 15 and 30 degrees as shown in Figure 8.13. Performance of the 15° angle was found to be similar to the 0 degree case. When the interlace angle was 30º, however (ie. when each of the gas holes was placed evenly between the diesel holes), the heat release rate was substantially lower. This was attributed to poor ignition of the NG. Since NG has a low cetane number, it is ignited by the hot diesel flame or its burnt products, not by auto-ignition. Thus the distribution and evolution of the pilot diesel with respect to the NG jet plays a key role in the ignition of the natural gas. With a low interlace angle, the burning diesel can more-effectively ignite the gas.

8.3.2 Simulating DF Injection under Engine Conditions

Experiments performed in the laboratory have been used to validate the CFD simulations. With confidence in the CFD models established, cases were run to simulate DF injection under the conditions found in an operating engine. In future, combustion testing will be carried-out in the RCM using the nozzle geometry that has been suggested in this study. Thus the optimised mesh of the RCM's chamber, which was used in the simulations under atmospheric conditions, was retained here. The previously open, "pressure-outlet"-type boundaries of the domain were replaced with steel "wall"-type boundaries. Two configurations for the initial conditions inside the chamber were simulated, as described in Table 8.4.

8.3.2.1 Quiescent Conditions

In the first instance, the cylinder was initialised to simulate the pressure and temperature that should, in theory, exist at the top of the RCM's compression stroke. Since the RCM does have an intake stroke *per se*, ie. air is not introduced into the chamber through poppet valves, there is no swirl-induced turbulence in the chamber at the start of combustion. Thus the air in the chamber may be considered to be quiescent.

8.3.2.2 Turbulent Conditions

A means of introducing initial turbulence into the chamber of the RCM is to be a priority during its future development. This is so that the RCM may provide a somewhat more accurate indication of combustion in a "real" engine. Initially-turbulent conditions were thus also devised for CFD simulation of injection into the RCM. This will enable future combustion testing with an improved RCM to be compared with the numerical work presented here. Determination of the turbulence level used is described in Appendix H.

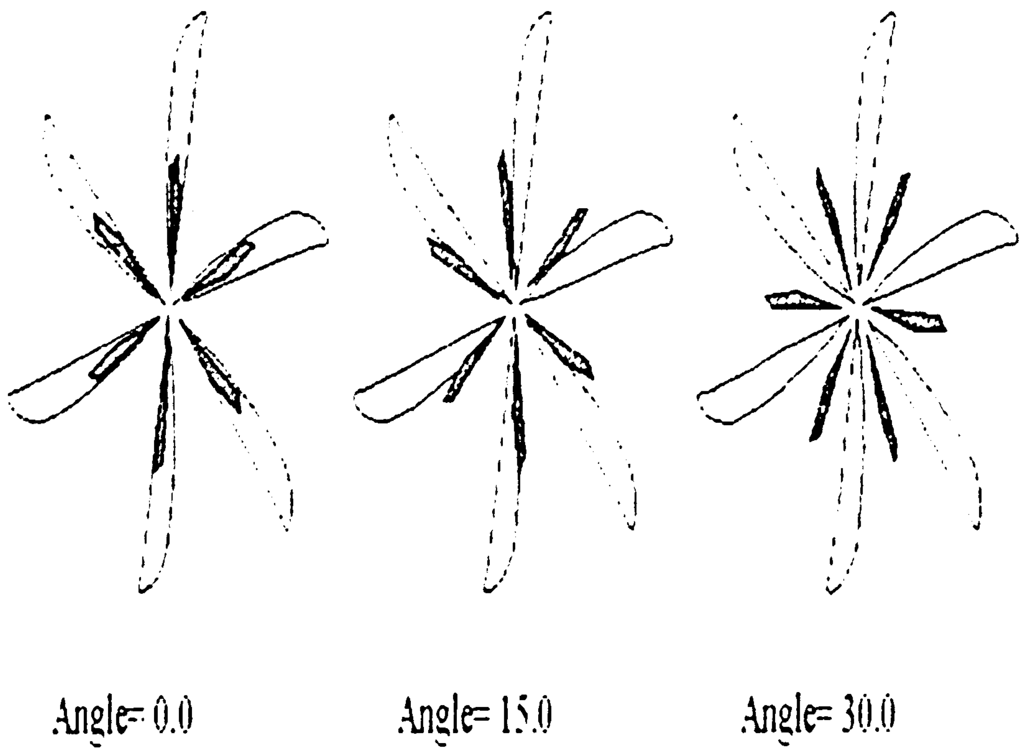

Figure 8.13. Interlace angles tested by Li et al [85].

Table 8.4. Initial chamber properties for the simulation of engine conditions.

Parameter	Quiescent	Turbulent
Pressure	7.28 MPa	7.28 MPa
Temperature	1,070 K	1,070 K
Turbulence Kinetic Energy	0	17 m^2/s^2
Turbulence Dissipation Rate	0	1,188 m^2/s^3

8.3.3 "Liquid Length" of the Diesel

8.3.3.1 Previous Work

In 1998, Siebers [136] used Mie-scattered light imaging to investigate the liquid-phase fuel penetration in conditions similar to that found in the cylinder of an engine. This work showed that liquid fuel initially defines the penetrating tip of a diesel spray. This continues until the liquid fuel penetrates to a point where the total fuel evaporation rate in the spray equals the fuel injection rate. When this condition occurs, the tip of the liquid region stops penetrating and begins fluctuating about a mean axial location with only vapour-phase fuel penetrating beyond that location. Parameters that were found to affect the location of the tip of the liquid-phase fuel included the injector orifice diameter, the ambient gas conditions and fuel volatility. Perhaps surprisingly, injection pressure had little effect. Figure 8.14 shows a graph of liquid length versus orifice diameter for a wide range of conditions.

From these results, Siebers [137] developed a scaling law for liquid length as given in Equation 8.3. This law was developed from an idealised diesel spray model using the principles of conservation of mass, momentum and energy. The idealised spray was assumed to have quasi-steady flow with a uniform growth rate (ie. a constant spreading angle). Uniform velocity, fuel concentration and temperature profiles (ie. perfect mixing inside the spray boundaries) were also assumed and no consideration was given in the spray model to the atomisation process or droplets. The idealised model treats the spray more as a locally homogeneous flow where the transport rates between phases at droplet surfaces are fast relative to the transport rates as a result of the mixing processes in the spray.

$$L = \frac{b}{a} \cdot \sqrt{\frac{\rho_f}{\rho_a}} \cdot \frac{\sqrt{C_a} \cdot D}{\tan(\theta/2)} \sqrt{\left(\frac{2}{B(T_a, P_a, T_f)} + 1\right)^2 - 1}$$

Equation 8.3 [137]

In Equation 8.3, a and b are constants and B is a function of the chamber's ambient temperature and pressure and the temperature of the injected fuel. D is the diameter of the injection orifice and C_a is the coefficient of area contraction of the spray.

Kim et al in 2002 [72] furthered the work of Siebers by using Raman-spectroscopy to find the penetration length of both the liquid and vapour phases of the diesel injection. Vapour concentration measurements were performed for two unit injectors typically found in small- and medium-bore engines under evaporating conditions similar to those experienced in an engine.

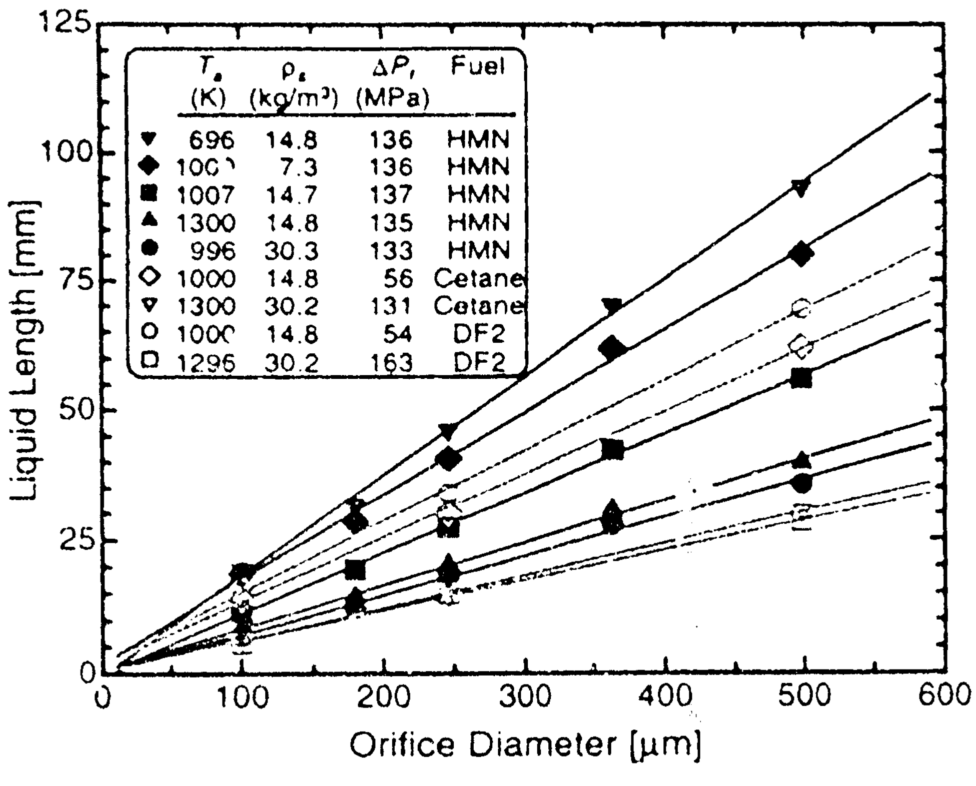

Figure 8.14. **Liquid Length vs. orifice diameter for a wide range of conditions as tested by Siebers in 1998. The terms in the legend represent the ambient gas temperature and density, the pressure drop across the orifice and the type of fuel used [137].**

8.3.3.2 Current Work

For the current work, the injection pressure was set to simulate 120 MPa as described in Chapter 5. The effect of varying the value of the droplet break-up time constant in the Wave Model, B_1, when injecting into laboratory (atmospheric) conditions was discussed in Section 8.1.1.

For the first simulation of injecting into conditions found in an engine, the domain was initialised to the quiescent conditions from Table 8.4. Thus the ambient temperature and density in the chamber were 1,070 K and 23.7 kg/m^3 respectively which should represent the upper-end of conditions in the RCM at TDC. Tests to gauge the effect of varying B_1 were repeated for the CFD domain under these conditions of high temperature and pressure. Results from these tests are shown in Figure 8.15.

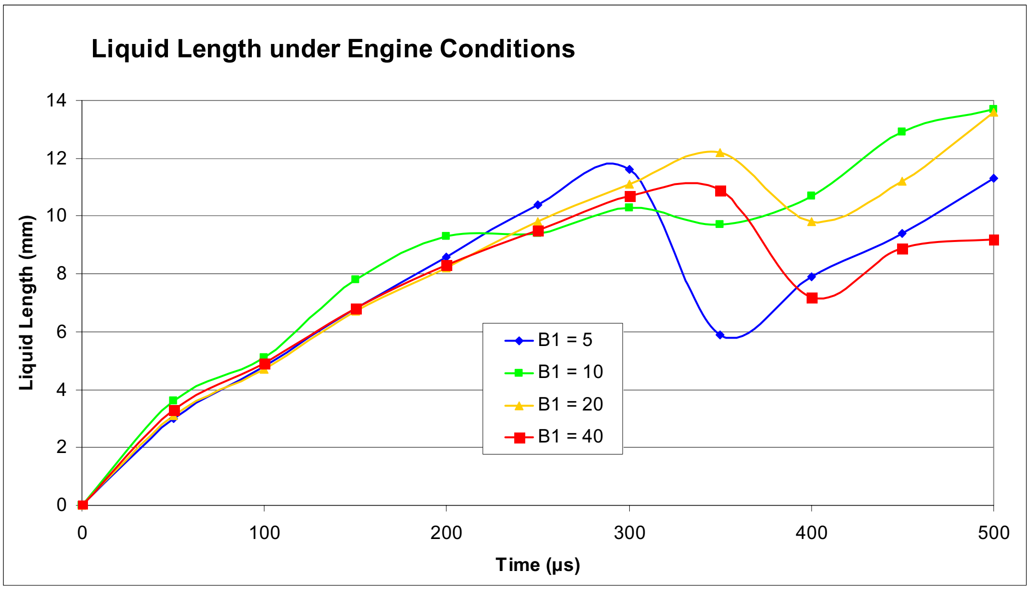

Figure 8.15. Liquid length found from the CFD in the current work for varying values of B_1.

Conditions for the injection in the current work, when compared with the test cases shown Figure 8.14, are perhaps closest to those in the fifth case from the top of the legend (the filled circle). The liquid length measured by Siebers in Case 5 was, for a diameter 0.20 mm nozzle-hole (similar to that used in the current work), estimated to be around 12 mm.

Varying B_1 when injecting into engine conditions can be seen to have somewhat more of an effect than when injecting into atmospheric conditions. For the limited time-frame studied in the current work, a low value of B_1 seems to result in the spray reaching its "liquid length" earlier than for a higher value, ie. a peak is reached and then fluctuation around a mean point begins earlier. Yet the actual liquid length achieved does not vary greatly between the four cases. In each case, fluctuation looks to be going to occur at a liquid length of between about 8 and 14 mm. The average of these two extremities, 11 mm, compares well with the 12 mm found by Siebers.

8.3.4 Predicting Ignition Sites

As has been discussed in Section 2.3.3, there exist both correlations as well as actual experimental data for predicting the ignition delay of diesel. Where in the cylinder the actual ignition takes place, however, remains a more elusive parameter and different researchers maintain different beliefs. The composition of the mixture, ie. the mixture strength at the point of ignition is important insofar as it can greatly affect visible (particulate) emissions from the engine.

8.3.4.1 Previous Work

The Importance of the Mixture Strength at Ignition

Flynn et al [40] stated that rich regions were responsible for particulate precursors, poly-aromatic hydrocarbons, which later form soot within the hot, oxygen-depleted zone within the diffusion flame. Most recently, Siebers and Higgins [138] have described how early air entrainment into the fuel spray coupled with the flame lift-off length can greatly affect the final output level of particulates. Therefore, the Equivalence Ratio distribution at the ignition time defines the initial flame development and combustion characteristics and also defines the production of pollutant emissions.

Where Ignition Begins

Recent work on the effect of early spray development on ignition and emissions has shown that the local air-fuel ratios play an important role. The following research is pertinent to the work here:

- Rife and Heywood [125] have shown that the auto-ignition of diesel jets occurs in a diesel vapour concentration band between the Equivalence Ratios of 1 and 1.5.

- Baritaud et al [16] used the exciplex method to determine the vapour concentration near the ignition site. They suggested that ignition occurs near the end of the liquid core where vapour concentration is the highest.

The actual value of the highest concentration of diesel vapour that occurs in the cylinder has been the focus of several researchers. Both numerical and laboratory studies have been used to quantify the value. Table 8.5 summarises some of these findings. In each case, modern, high-pressure injectors were used.

Table 8.5. Previous studies of the maximum Equivalence Ratio, Φ, of diesel vapour in a chamber.

Reference	Researcher	Study	P, T and Density	Max Value
66	Iyer (2002)	CFD	1,000 K, 30.2 kg/m^3	ER 3.75
18	Beckman (2001)	Exciplex LIF	1000 K, 15 kg/m^3	ER 3.5
			1200 K, 15 kg/m^3	ER 4.0
73	Kim et al. (2002)	Exciplex LIF	3.0 MPa, 800 K, 15 kg/m^3	ER >3.0
			3.5 MPa, 1000 K, 15 kg/m^3	ER >3.0
(Current)			*7.3 MPa, 1070 K, 24 kg/m^3*	

8.3.4.2 Current Work

The images in Photo Sets 8.5 through 8.8 show results from simulation using the initially quiescent conditions described in Table 8.4. Each set of frames is from a case which has a particular staging of the NG jet relative to the diesel spray. The staging is the same as studied in the laboratory work, ie. simultaneous SOI of the two jets and then SOI of the gas jet delayed by 0.25, 0.50 and 0.75 ms after SOI for the diesel pilot.

Two important differences in the both the actual simulations and the presentations of the results exist for this section:

- The rate of increase of injection pressure (and thus mass-flow) of the NG jet has been increased for these cases of high chamber pressure and temperature. The rate of pressure rise for the cases simulated under laboratory conditions was described in Table 8.1. In the simulation of RCM-conditions, the injection pressure started at 2.67 MPa and was increased by 2.67 MPa every 50 µs such that a final injection pressure of 16 MPa was achieved at 300 µs after SOI. This change was made to more-accurately reflect the flow which should be able to be achieved in a production-intent injector, ie. one where the GCV is able to be placed closer to the nozzle orifices as described in Section 4.3.4.

- For the results presented in the following Photo Sets, the frames have been enlarged so that only the relatively near-field of the injector is shown. One-half of the width of the chamber is shown, ie. the image represents the 27 mm closest to the injector rather than the full radius of 54 mm. This is so that detail of the injection close to the injector is better represented.

The images in the left-hand column of each Photo Set show contours of mass-fraction of NG superimposed on contours of Equivalence Ratio of the vaporised diesel. A key for the colour-coding of the contours is shown in Figure 8.16. The contours for the gas jet are shown in ten levels, each level representing a band of mass-fraction of 10%. The contours for the diesel are shown in five levels, each representing a range of Equivalence Ratio. The images in the right-hand column show mass-fraction of air in the chamber. These contours, like those for the NG in the left-hand column, are shown in ten levels.

By plotting the results in this way, likely ignition sites for the pilot can be compared with the results of both Rife and Heywood [125] and Baritaud et al [16]. The location of the head of the gas jet can then be seen at the time of the ignition of the pilot.

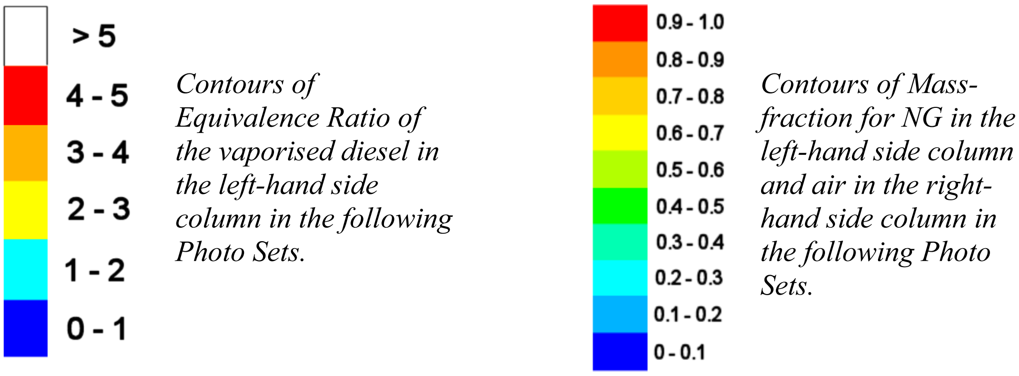

Figure 8.16. Key for the contours in Photo Sets 8.5 through 8.9.

During this analysis, it is worthwhile to consider the findings of Kuo et al in 1983 [78] who used numerical models to analyse the ignition process in diesels. As mentioned in Section 2.3.1, they found that under normal diesel engine conditions, 70 to 95% of the injected fuel is in the vapour phase at the start of combustion. Evaporation is more than 90% complete after 1 ms. However, only 10 to 35% of the vaporised fuel has mixed to within flammability limits in a typical medium-speed DI diesel engine. Thus combustion is largely mixing-limited rather than evaporation-limited. Of course, under cold-starting conditions, evaporation becomes a major constraint. In the current study and with modern, high-compression/turbocharged engines, the ignition delay can be estimated to be between 0.3 and 0.5 ms as described in Section 2.3.3. Since the injection time of the diesel pilot is approximately equal to or less than this time, there exists the possibility that all of the pilot is injected before ignition occurs.

8.3.5 Optimising the Staging of the Injection

8.3.5.1 Considerations for Analysing the Results of the Simulation

From the results above, there exist some regions where the ER is higher than the maximum of 4.0 found by Beckman and Farrell [18]. The maximum value recorded in the current work was about 5.0 in the initially quiescent cases. Possible reasons for this increased value in the current work include grid density as described in Section 7.4.2 and different chamber conditions as shown in Table 8.4.

Another phenomenon that must be noted is that penetration of the gas jet under chamber conditions of high pressure and temperature appears to be much slower than under laboratory/ambient conditions. Under laboratory conditions at a time of, say, 1.3 ms after SOI of the gas jet, the contour of 10% mass-fraction of the gas has mostly reached the cylinder wall in both photos from the laboratory and in the numerical simulations. Under engine conditions, however, this same 10% contour has not quite reached half-way across the full chamber width, ie. it has not yet reached the right-hand side of the frame in the Photo Sets above. This occurs despite the increased rate of pressure/mass-flow rise compared with the simulations of the laboratory experiments.

A factor in considering this anomaly is that with the increased chamber pressure relative to the injection pressure, the gas jet will not be choked until the injection pressure rises to about 13 MPa (for the chamber pressure of 7.28 MPa and a critical choking pressure ratio for NG of 1.86 as described previously). Thus the nozzle is not choked in the early stages of injection. Yet the actual injection rate should still be higher for the cases simulating engine conditions. The actual reason for the apparently reduced penetration rate is likely to be the increased rate of diffusion of the gas at the higher chamber temperatures and density. For a given rate of injection, the actual penetration of the head of the jet will be retarded since more mass of NG is “delayed” in its journey across the chamber by the more-dense air with which it has to mix.

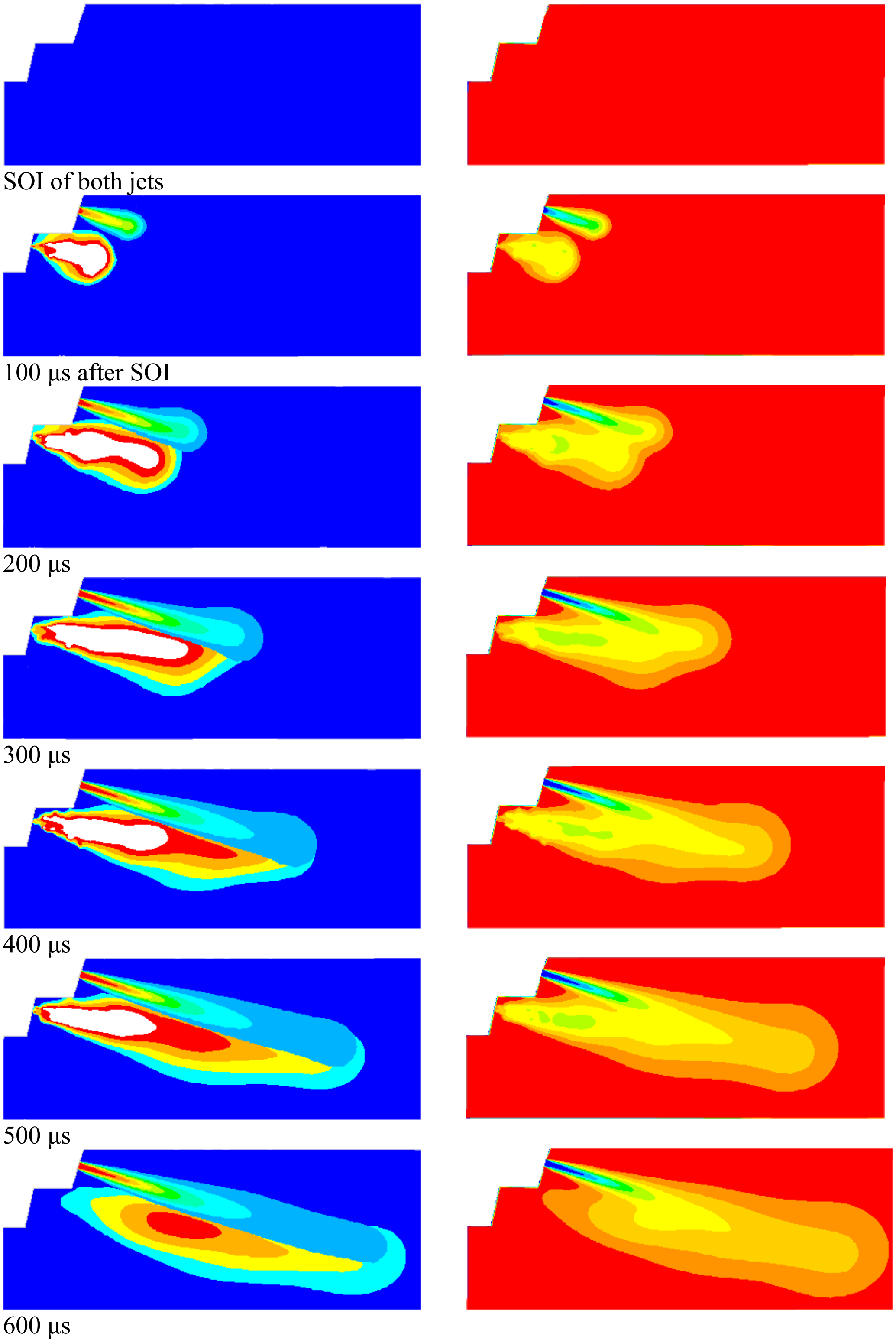

Photo Set 8.5. DF Injection under engine conditions – Simultaneous SOI.

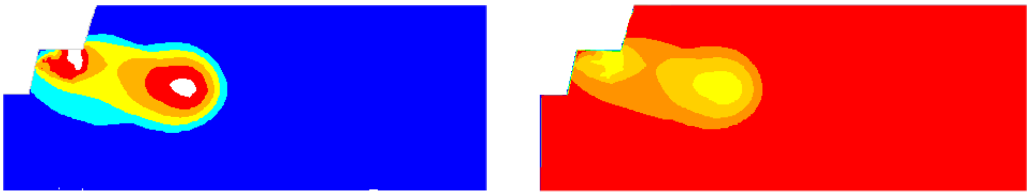

250 µs after SOI of the pilot

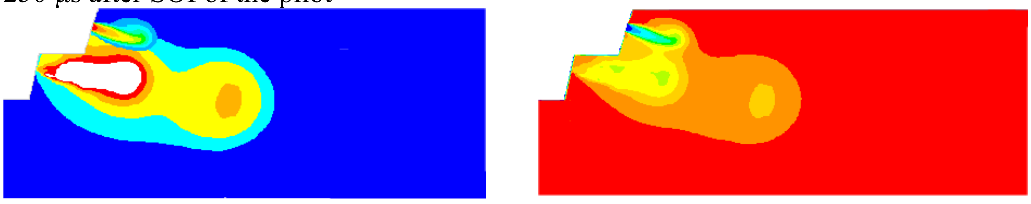

350 µs

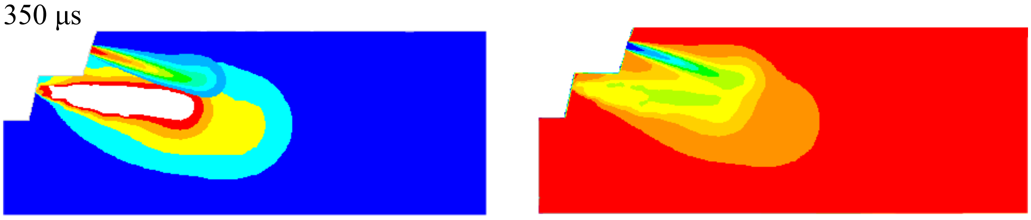

450 µs

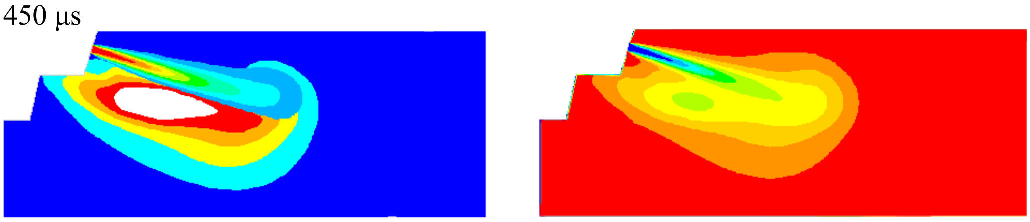

550 µs

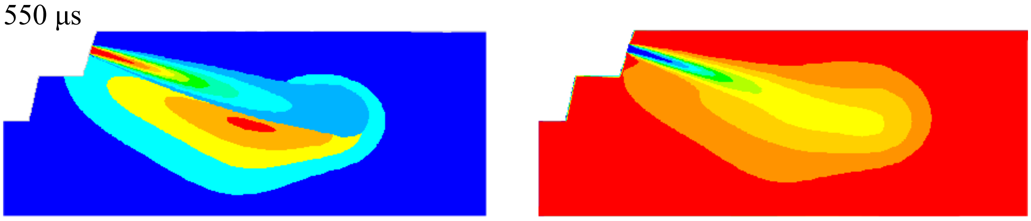

650 µs

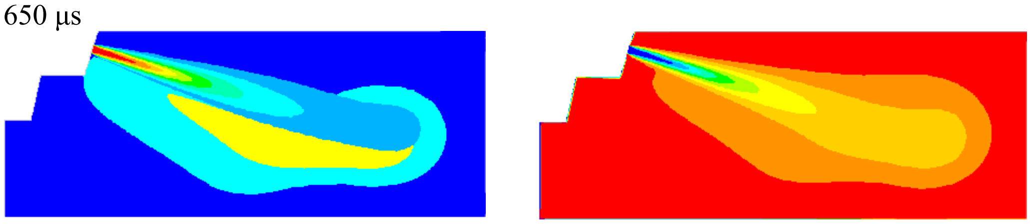

750 µs

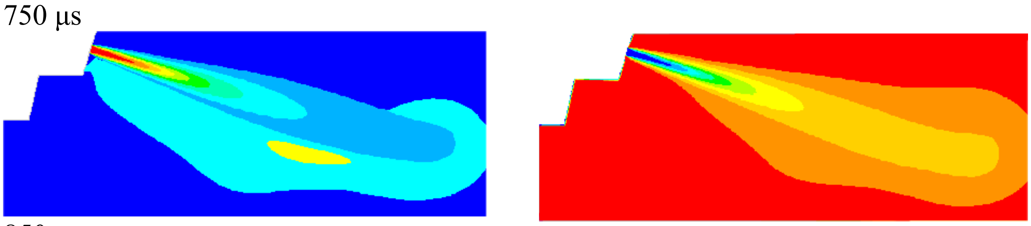

850 µs

Photo Set 8.6. DF Injection under engine conditions – SOI of NG is 0.25 ms after diesel.

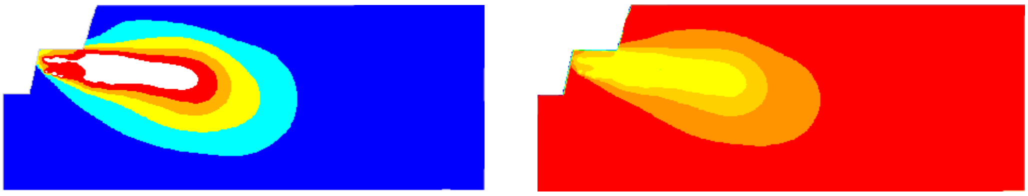

500 μs after SOI of the pilot

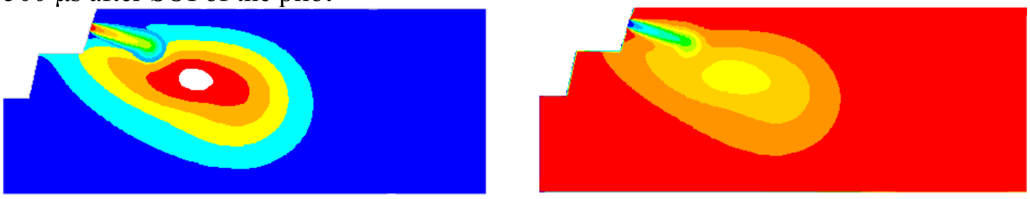

600 μs

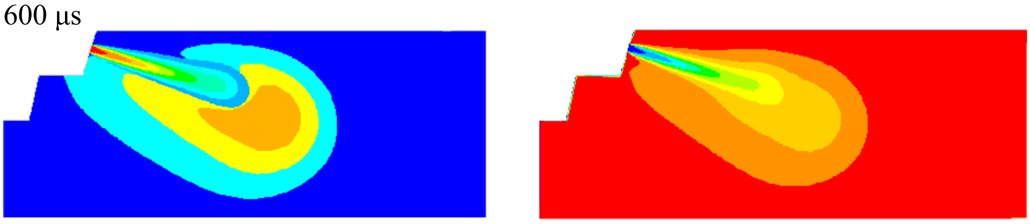

700 μs

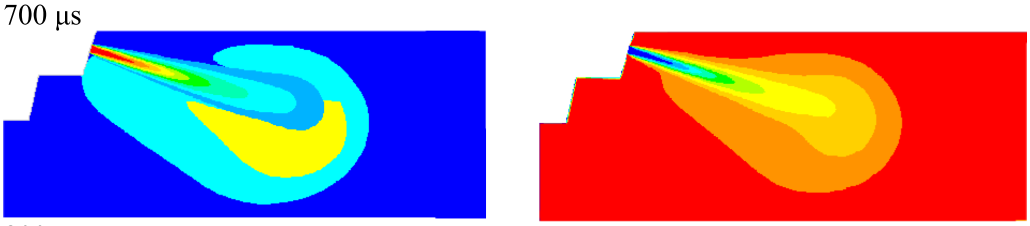

800 μs

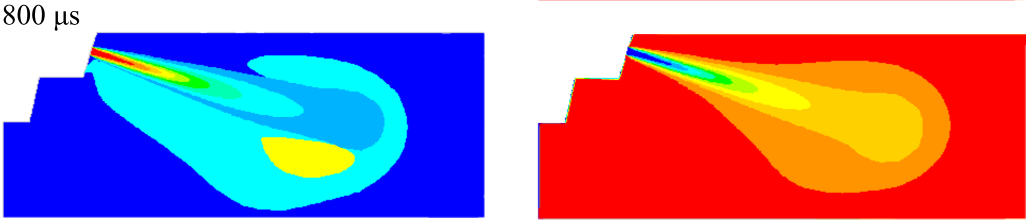

900 μs

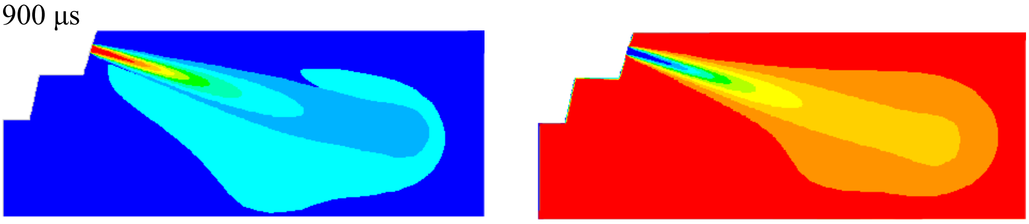

1,000 μs

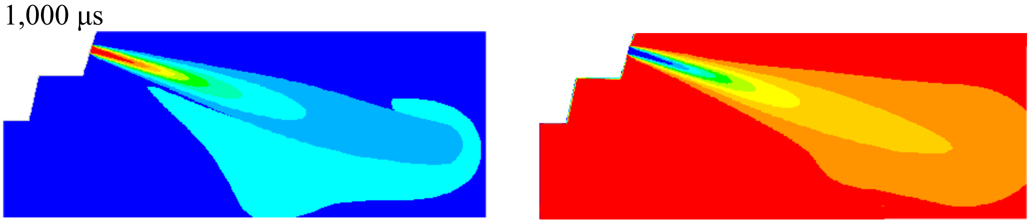

1,100 μs

Photo Set 8.7. DF Injection under engine conditions – SOI of NG is 0.50 ms after diesel.

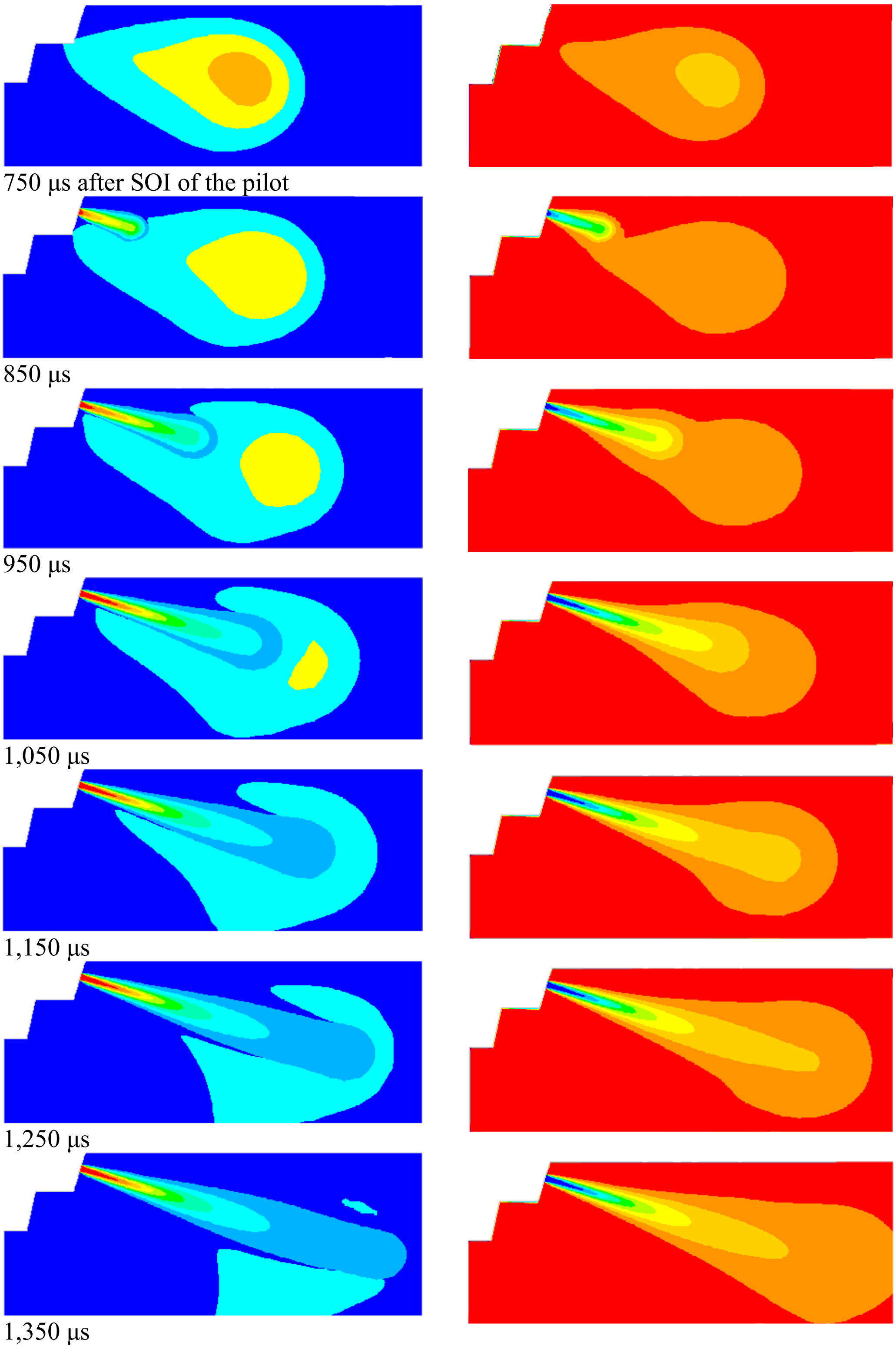

Photo Set 8.8. DF Injection under engine conditions – SOI of NG is 0.75 ms after diesel.

8.3.5.2 Analysis of the Results

As previously described, Rife and Heywood [125] suggested that ignition of the diesel will occur in areas within the chamber where the Equivalence Ratio is between 1 and 1.5. Baritaud et al [16], on the other hand, suggest that ignition will occur where the mixture is richest. Irrespective of whichever of these two theories holds more true, ignition is likely to occur somewhere between 0.3 and 0.5 ms after SOI of the diesel. The gradient of the Equivalence Ratio is quite high near the extremity of penetration of diesel vapour. Thus the axial distance between the contour band of $1 < \Phi < 2$ and $\Phi > 4$ is only a few millimetres. The practical difference between the location of the first ignition sites according to either Rife and Heywood or Baritaud is of limited significance.

Figures 8.17 through 8.20 each show an enlargement of a single frame from Photo Sets 8.5 through 8.8 respectively. For the purposes of the following commentary, an ignition delay time of 0.4 ms will be assumed. The location of the first ignition sites will be taken to be along the axis of the diesel jet where Φ is about 4. This location is shown as the black star in Figure 8.17.

In Figure 8.17, where the SOI of the two jets is simultaneous, the head of the gas jet can be seen to have just passed the likely ignition site of the pilot. Ignition of the pilot is likely to be delayed by the presence of the gas as described in Section 2.7.2 and so some delay between SOI of the pilot and SOI of the gas should be established.

Figure 8.18 shows the earliest relevant frame from the case where SOI of the gas jet is delayed by 250 μs with respect to the pilot. Assuming a similar time and location of ignition of the pilot as in Figure 8.17, a flame should just be established by the time the gas jet reaches the location of ignition. For a delay of the gas jet of 500 μs as shown in Figure 8.19, more of the diesel will have burnt and the ignition delay of the gas will be somewhat shorter.

For a delay of 750 μs as shown in Figure 8.20, most of the diesel could have burnt by the time the gas jet is established. Whilst it is unlikely that the pilot will be extinguished by the time the gas is injected, this staging delay is perhaps a little long. A reduction in formation of particulates may also be expected if ignition of the gas starts earlier and a more-constant rise in cylinder pressure may be achieved. Such speculation can only be resolved by a more advanced numerical study which includes combustion models or by actual combustion testing in the RCM and ultimately in an actual engine.

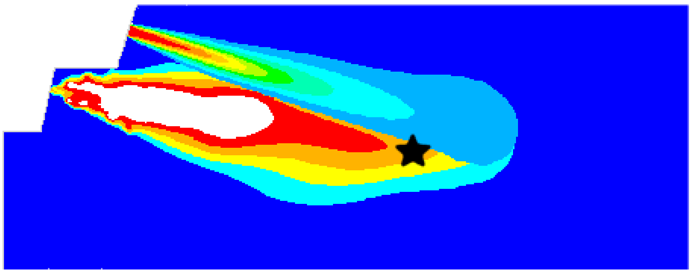

Figure 8.17.

Enlargement from Photo Set 8.5 (Simultaneous SOI of the two jets). This frame is taken 400 µs after Simultaneous SOI.

The likely location of the first ignition of the pilot is shown by the black star.

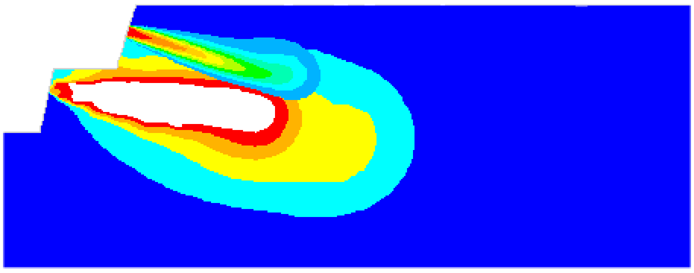

Figure 8.18.

Enlargement from Photo Set 8.6 (SOI of the gas jet delayed by 250 µs). This frame is taken 450 µs after SOI of the pilot.

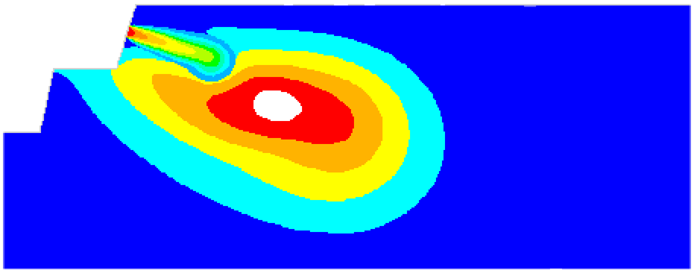

Figure 8.19.

Enlargement from Photo Set 8.7 (SOI of the gas jet delayed by 500 µs). This frame is taken 600 µs after SOI of the pilot.

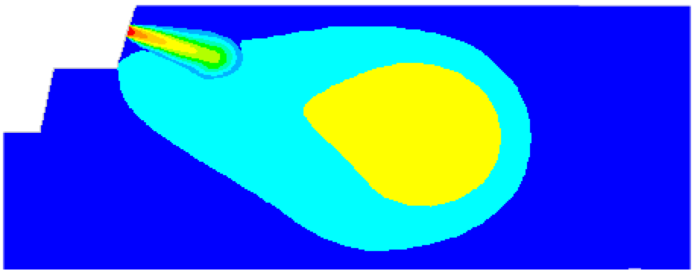

Figure 8.20.

Enlargement from Photo Set 8.8 (SOI of the gas jet delayed by 750 µs). This frame is taken 850 µs after SOI of the pilot.

Optimum dual-fuel combustion is thus likely to exist with a delay of SOI for the gas jet of between 250 and 500 μs after SOI of the diesel. Perhaps co-incidentally, since there is a significant difference in penetration of the gas jet between the ambient and high chamber-pressure cases, this is consistent with the expectation from the findings presented for the laboratory work in Chapter 6.

These results should hold even in an actual, reciprocating engine since the rate of jet penetration and the evaporation rate of the diesel can be expected to be similar to those seen here. Aneja and Abraham [7] used both numerical and experimental methods to study diesel injection into an engine in 1998. For an SOI of diesel at 10º BTDC, steady penetration of liquid diesel was achieved by 3º after TDC at an engine speed of 1,200 rpm, ie. in a time of about 1.8 ms. Of significance was that the conditions inside the chamber changed very little during this time: density by only 3% and temperature by only 2%. Thus for the short variation in staging times studied in the current work, ie. less than 1 ms, the change in conditions within the chamber should be negligible.

Other useful information from Photo Sets 8.5 through 8.8 can be seen here. In the latter frames of each set, the remaining diesel vapour is "sucked" into the near-field of the gas jet. Assuming that this region of diesel vapour has already burned, these high-temperature residuals will improve combustion of the gas. If this vapour has not yet burned, its entrainment into the gas will ensure its subsequent combustion.

8.3.5.3 The Effect of Turbulence

The above analysis was performed for cases in which there existed no initial turbulence in the chamber. To study any variation in the trends witnessed for these results for a chamber that is turbulent at the time of injection, a simulation was performed under the initially turbulent conditions as described in Table 8.4. From the above analysis, a delay of the gas jet of about 0.5 ms was proposed to be suitable under most conditions. Thus it was for this injection staging that a case was analysed under conditions of initial turbulence. Photo Set 8.9 shows results from the case in which swirl has been simulated.

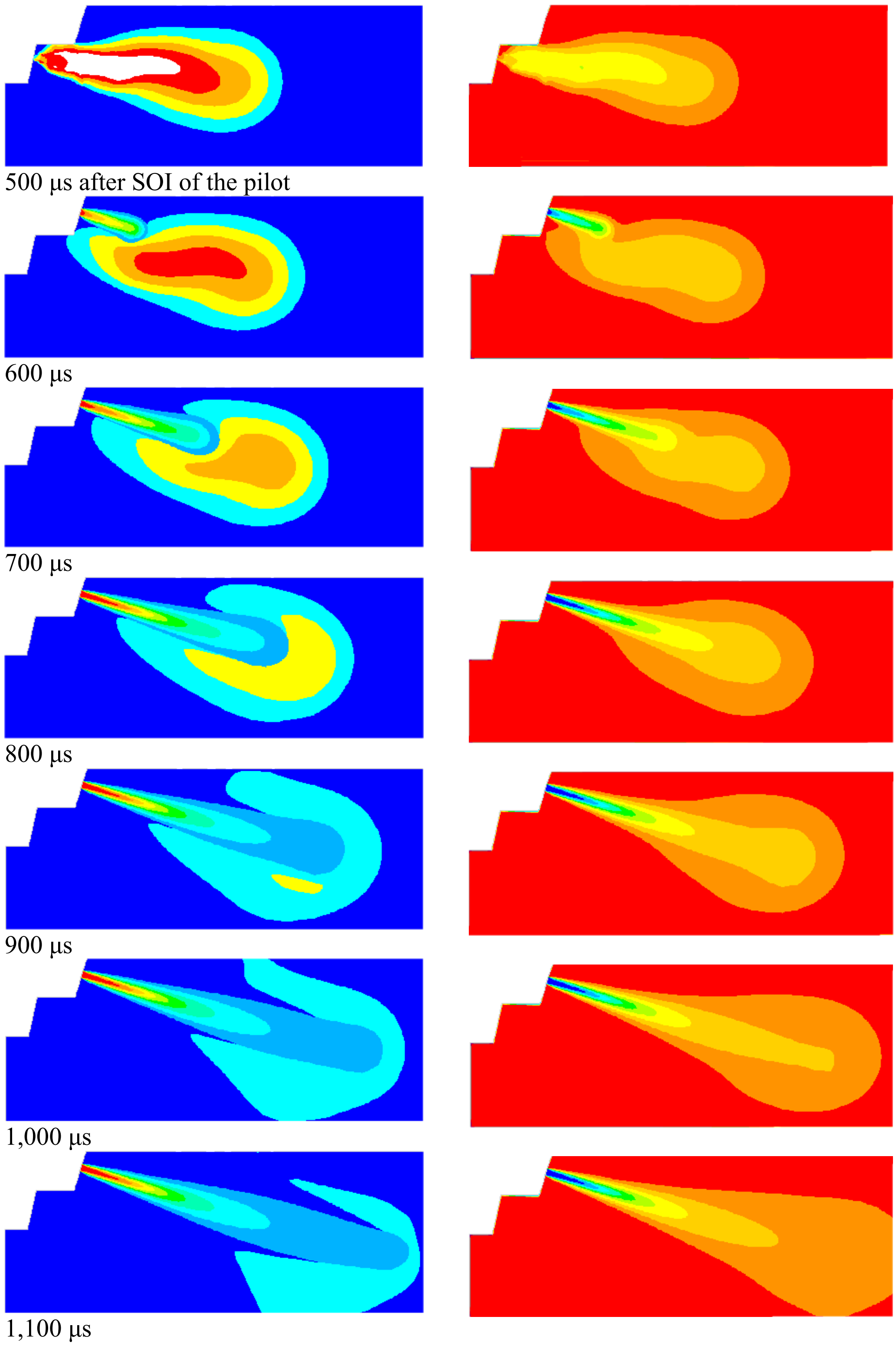

Photo Set 8.9. DF Injection under engine conditions with initial chamber turbulence – SOI of the NG is 0.50 ms after SOI of the diesel.

Siebers [136] found that the liquid length of the diesel spray was controlled mainly by turbulent mixing processes and that a high level of turbulence could result in variations around the mean length of ± 11%. Hill and Ouellette [56] found that with an initial turbulence kinetic energy of 0.5 m^2/s^2, penetration of the gas jet was reduced by 5%. When turbulence was increased to 5 m^2/s^2, penetration was reduced by another 2%.

In the current work, the inclusion of chamber turbulence seems to have little effect. Of note, however, is that dispersion of the diesel vapour appears to occur more rapidly in the case with initial turbulence. This is evident by comparing the area covered by the band of $1 < \Phi < 2$ in the latter frames of Photo Sets 8.7 and 8.9. Less area is covered by this band in Photo Set 8.9 which indicates that the chamber turbulence has helped with mixing.

8.3.5.4 Nozzle Size and Injection Rate

Dual-fuelling scenarios for an engine consisting of cylinders the size of that in the RCM were described in Section 5.4. In a case of high load and high gas substitution (such as Case 2 in Table 5.2), the duration of the gas injection is about 4 ms. This may prove to be too long in an actual engine. For example, one engine stroke at 2,000 rpm takes only 15 ms. In a production injector there would be some benefit in making the gas orifices say, 0.6 mm in diameter rather than the 0.4 mm modelled here. A 0.4 mm nozzle was chosen here to enable controlled switching of the gas in the laboratory environment. By making the nozzle only 0.4 mm in diameter, the flow time required to deliver the correct mass of gas through the injector was high enough to be achieved accurately.

Yet there may actually be a nett benefit in engines for some applications in having an injection as “slow” as that modelled here. This slow injection rate and subsequent burning would help with control of NO_x emissions which often occur as a result of the rapid energy release with modern, high-pressure diesel injectors. Again, such speculation can only be accurately resolved with more-advanced CFD models and laboratory facilities.

9. Chapter Nine: Concluding Remarks

A high-pressure dual-fuelling system was developed for the study of a diesel jet, a natural gas jet and combined, dual-fuel jets in the laboratory. High-speed liquid and gas jets were generated that were suitable for direct-injection into the cylinder of an engine. Injection of the jets was able to be achieved both discretely and simultaneously with independent control over the flow duration and timing of both jets. Experimental apparatus allowed visual capture of the jets at various times during their respective life cycles. The jets were then successfully modelled using computational methods. These calculations allowed the jets to be studied quantitatively in a way that was not possible in the laboratory.

9.1 Review of the Laboratory Work

9.1.1 Effectiveness of the Visualisation Techniques

9.1.1.1 Imaging Techniques

- Backlighting provided adequate detail for qualitative analysis of the diesel spray. The boundaries of the spray could be clearly seen. Some information about the relative size of the atomised fuel could be gathered by varying the intensity of the light source between photo sets. When used with the high-speed video camera, the growth of turbulent structures was able to be witnessed.
- Shadowgraph analysis of the diesel spray allowed the regions of vaporised fuel to be distinguished from the atomised fuel. This allowed comparison of the relative performance of the nozzle to atomise the fuel at different injection pressures. This technique was also a useful aid in calibrating the spray models in *Fluent*.
- Owing to its dependence on a high pressure gradient in the flow, the boundary of the jet in the far-field was not able to be clearly seen with the shadowgraph. But shadowgraph analysis of the near-field of the gas jet enabled the location and size of the Mach disc to be determined. This allowed the actual injection pressure to be calculated with some confidence and so assisted with calibration of the CFD models.

- The schlieren method, when used with the high-speed video camera, provided adequate detail to define the boundary of the gas jet. As was the case for the diesel spray, the growth of turbulent structures was clearly visible when the intensity of lighting was set correctly. Photos taken with the schlieren method were thus used in calibrating the mass-flow rate of the gas in the CFD and for all analysis of the dual-fuel jets

A sound, qualitative understanding was gained of the nature of the development of fuel jets for direct-injection dual-fuelling. The rate of growth of the jets was able to be described numerically and estimates made into the rate of entrainment into the individual jets. The techniques used in this laboratory study cannot, of course, provide quantitative data regarding the concentration of any part of the jet. More advanced systems such as laser interferometry [134] or ultimately the use of a mass spectrometer would be required for this.

9.1.1.2 The High-speed Video Camera

Camera Resolution

The CCD element within the X-Stream XS-4 consisted of 512 x 512 pixels. All of these pixels could be used to capture an image up to a camera speed of around 5,000 frames per second (5 kfps). In most of the experiments in this project, this capture area was reduced to 512 x 128 pixels so that a frame rate of 20 kfps could be achieved. Owing to the high “aspect ratio” nature of the fuel jets, this rectangular field of view was adequate for the purposes of the work carried-out here. The resolution of the image (ie. 512 pixels covering a jet length of about 50mm) was, however, marginal for a detailed study of the turbulent structures within the jets. A camera capable of higher resolution at the chosen frame rate – say 1,024 x 1,024 pixels at 20 kfps - would result in much better images of vortices on the surface of the jet.

Camera Speed

Most of the laboratory work was carried-out using a camera speed of 20 kfps. This speed was chosen since it provided the best balance of available exposure time for a bright image (47 μs per frame) and a large-enough image capture area (512 x 128 pixels). Further refinement of the optical system (ie. the use of improved light-sources and lenses) would perhaps allow higher frame rates to be used and thus provide a better understanding of the growth of turbulent structures on the surface of the jets. With the current camera, however, a loss of image size/resolution must be accepted if an increase in frame rate is desired.

9.2 Usefulness of the CFD

9.2.1 General Modelling of the Flow

For a given flow rate from the diesel injector in the laboratory, the penetration of the liquid diesel calculated using *Fluent* was accurate within a few percent. Of particular significance were the results achieved in the cases simulating injection into the chamber under conditions of high temperature and pressure. The evaporation sub-model accurately predicted the liquid-length of the diesel spray when compared with the work of previous researchers [72, 136]. The actual concentration of vapour in the chamber was perhaps over-predicted when compared with previous studies which used both laboratory and simulation techniques to model conditions in a cylinder at the time of ignition. This anomaly could possibly be resolved with some minor modification of the numerical parameters available in the injection sub-model.

Most features of the gas jet were also well-modelled. Under-expanded flow from the gas injector resulted in the formation of a shock wave as described in Chapter 3. The location and size of this Mach disc was very similar to that seen in the laboratory. The rate of growth of the modelled gas jet was successfully matched.

Fluent appears to model the dual-fuel injection reasonably well. The growth and spreading rate of both the liquid and gas jets was able to be calibrated to reflect the jets observed in experiments. As described in Section 8.3.5, entrainment of the atomised diesel spray into the gas jet was able to be clearly seen, indicating that species mixing was well accounted-for in the simulation.

9.2.2 Deficiencies in the Modelling

Fluent does not appear to adequately resolve instabilities on the surface of the jet. Photo 9.1 and Figure 9.1 respectively show a frame taken from schlieren video in the laboratory and a frame from the CFD simulation of the same injection. Turbulent structures can be seen on the surface of the jet in Photo 9.1. (The actual development of this turbulence can be better seen in Photo Set 5.27 and in the Photo Sets in Section 6.1.) The variation in the intensity of the schlieren images are caused by fluctuations in the density of the gas in the test section. These fluctuations can be caused by non-uniform pressure variations in the flow but more likely because of variations in the relative mixture of NG and air in the jet.

Despite setting a high level of turbulence in the injected jets, Figure 9.1 shows how such fluctuations in the concentration of NG are not reflected in the CFD results. The contours of mass-fraction in the CFD are relatively smooth along the length of the jet. Figure 9.2 shows a plot of contours of Turbulence Kinetic Energy, *k*, for the same jet in ten levels between 0 and 10,000 m^2/s^2. Turbulence does exist in the simulated jets but does not manifest itself in fluctuations of concentration as it seems to in the laboratory.

9.3 Findings from the Current Work

9.3.1 Literature Review

A comprehensive review of literature, pertinent to the dual-fuelling of CI engines using diesel and natural gas, was carried-out in the first twelve months of the project. Journals were then closely monitored for the duration of the project. Dual-fuelling using HPDI has received much research attention, especially in the last decade. The use of HPCR diesel injectors as a basis for HPDI has been achieved and documented by Ouellette and Welch [110]. Yet there remains much potential for the development of HPDI for larger engines. Of particular interest is the development of a DF injector using the HEUI originally developed within the School by Yudanov [159]. The extremely high injection pressure but low control-side pressure of the HEUI allows large quantities of fuel to be injected but with very precise control. Owing to its high turn-down ratio, this HEUI is especially suited to high-substitution dual-fuelling in very large engines.

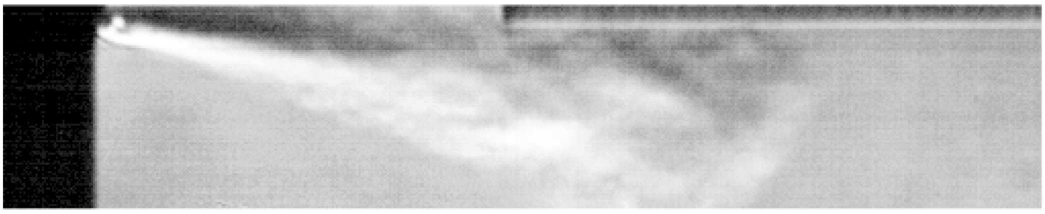

Photo 9.1. Frame taken from schlieren video of the gas jet, 0.8 ms after SOI. Turbulence can be seen as variations in the light intensity on the surface of the jet.

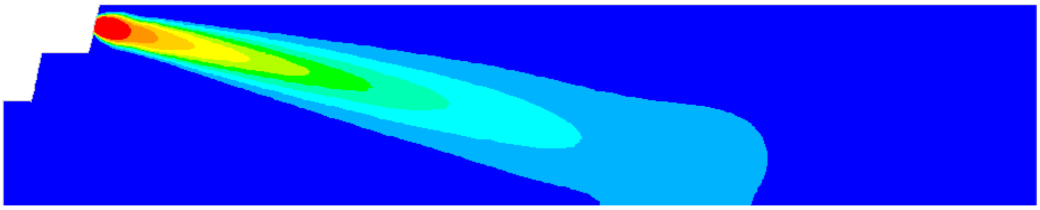

Figure 9.1. Frame taken from the CFD simulation of the gas jet under the same conditions as in Figure 9.1. Contours of the mass-fraction of gas are shown in ten levels between 0 and 100%.

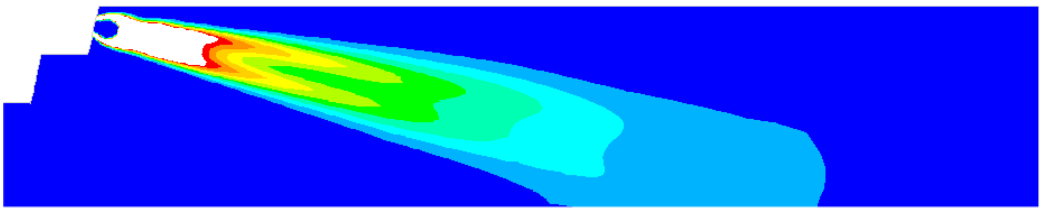

Figure 9.2. Frame taken from the same CFD case as Figure 9.1. Turbulence Kinetic Energy, k, is shown in ten levels between 0 and 10,000 m^2/s^2.

9.3.2 Optimum Injection Pressure

Extensive laboratory testing of the HPCR diesel injector was carried-out to determine its injection properties at different injection pressures. The most highly-atomised spray was found to issue from the particular nozzle used here when the injection pressure was set at 120 MPa. This was close to the design pressure of the HPCR system as described in Section 5.2.1.

The growth rate for the gas jet under different injection pressures was also studied. The maximum pressure was limited by that available from the gas cylinder – about 16 MPa. The gas is not required to atomise and evaporate before combustion. The rate of entrainment of the surroundings and thus mixing is largely dependent on the rate of growth of the jet which is in turn dependent on the rate of injection as detailed in Section 3.8. Laboratory testing of the dual-fuel injection was thus carried-out at 16 MPa to maximise the potential for entrainment of the gas jet. Further, this high injection pressure should help ensure that the entire duration of combustion does not exceed 40 to 50 crank degrees as recommended by Heywood [54] and described in Section 8.3.5.

9.3.3 Injector Geometry

9.3.3.1 Nozzle Hole Size

The DF injector studied in the current work was designed for the RCM as described in Section 5.4 and in Appendix G. Since a propriety diesel injector was used as the foundation for the DF injector, its standard nozzle holes were left standard. This nozzle had equi-spaced nozzle holes, each with a diameter of 0.2 mm.

Li et al [85] suggested that for HPDI through a common injector, the number of holes in the gas nozzle should equal the number of holes in the diesel nozzle. The diameter of the six holes in the gas nozzle was set to 0.4 mm. Section 8.2.1 details how this size ultimately yielded an injection rate of 3.5 g/s per nozzle hole. This rate meant that the injection time was long enough to accurately control in the laboratory but short enough such that the combustion time in a real engine would be acceptably short. As described in Section 8.3.5, the gas injection time into an RCM-sized cylinder operating at over 90% gas-substitution level and at full load would be around 4 ms.

9.3.3.2 Convergence Angle of the Fuel Jets

Both laboratory testing and simulation using CFD indicated an optimum converging angle of only a few degrees between the two fuel jets. The angle using for the "optimised" injector geometry was 5° as described in Section 6.1. Some mixing was present when the jets were injected parallel to each other and also when there was a high convergence angle (12.5°). But the best combustion characteristics could be expected in a range between, say, 3 and 7°.

9.3.4 Injection Staging

A simultaneous start time for the two injections provides good mixing although the presence of the natural gas is likely to delay the ignition of the pilot diesel (as described in Section 2.7.2.2). Any delay above the maximum that was tested here, 0.75 ms, is too great since the diesel has moved too far away from the nozzle by the time the gas is injected. A delay in SOI of about 0.5 ms should provide a reasonable compromise between maximising the mixing and minimising the ignition delay for both jets. Further details are given in Sections 6.2 and 8.3.4.

9.4 Continuing the Current Project

9.4.1 CFD Work

9.4.1.1 Improvements to the Modelling

Apart from what seems to be the requirement to more-accurately model turbulence in the jets, there remains some potential to resolve the formation of the Mach disc near the gas injector with higher fidelity. A Mach disc is essentially a discontinuity in flow. Owing to their foundation using the Navier-Stokes equations (described in Chapter 7 and Appendix H), CFD codes in general rely on considering flow to be continuous. Thus discontinuities such as shock waves require a number of cells to resolve the rapid change in pressure, temperature and density across the shock wave. Typically, approximation of a shock wave as a continuous gradient takes between two and three cells [92]. Thus the Mach disc in the CFD has a "thickness" of two cells when in reality the shock wave will be infinitesimally thin. A more precise location of the Mach disc could be found if a finer mesh is used in the region where it forms. Implementation of a "coupled" solver would also be an advantage.

9.4.1.2 Refinement of the Validation Procedure

More-advanced imaging techniques could also be implemented in the laboratory so that the boundaries of the gas can be identified with more confidence. Techniques such as Raman spectroscopy or planar laser-induced fluorescence (PLIF) could not only locate the exact boundary of the jet but provide information about the flow-field within the jet, thus assisting with development and further validation of the CFD.

9.4.1.3 Future Models

The computational domains developed in the current work appear to be adequate for simulation of combustion in the Rapid Compression Machine. Work should soon begin on modelling a combustion chamber such as that found in a modern, direct-injection diesel engine. *Fluent* is also capable of simulating a reciprocating engine in that its mesh-generation module, *Gambit*, supports construction of moving meshes, ie. a mesh in which the number of elements remains constant but in which the cells can deform between each time step in the simulation. Successful implementation of this feature would allow modelling of the inlet and compression strokes of the engine and perhaps even flow through the valves.

9.4.2 Development of the DF Injector

Continuation of the work described in this volume will require development of both the laboratory rig and of the numerical models. As described in Section 4.3.4 and referred back to many times, a gas injection valve needs to be integrated closer to the nozzle of the DF injector. This would result in less "dead" volume than that used in the current work. This will then allow a more favourable rate of injection to be achieved whilst allowing fitment to either the RCM or an engine. The final DF injector can be expected to look something like the one proposed by Kloeckner [74], described in Appendix B.

The actual injection parameters for the new DF injector have been well-established in this volume and summarised in the previous section. Mechanical, hydraulic and electronic design can now proceed with confidence that the resulting injector will be suitable for direct fitment to an engine. Tran [150] used the software packages *Matlab* and *Simulink* to model the mechanical response of an HPCR injector. A similar study of the proposed DF injector should be carried-out. Several commercial software packages are available to facilitate this. The power of even desktop computers these days allows all aspects of an injector's function to be simulated before committing a design to the machine shop. CFD is only one such tool available to allow both time and money to be saved by optimising the mechanical design before an injector is actually built.

9.4.3 Laboratory Testing

The logical starting-place for empirical testing of the HPDI concept is in the Rapid Compression Machine. The RCM was not actually used as part of the current work although the Diesel Delivery System, described in Section 4.3.2, may now be fitted directly to it. Early in the project, before it was realised that a suitable gas injector to be used with both the JVR and the RCM would be unable to be developed, the RCM was modified to accept an HPCR injector. Photo 9.2 shows how the head of the RCM was modified by the author for this purpose.

Testing of the combustion characteristics of the HPCR injector is a worthwhile process in itself but testing DF combustion will probably require construction of a combined injector as described by Kloeckner. Control of the gas injection must be achieved using a needle very close to the injection holes so that the delay in the pressure-rise of the gas injection is maximised whilst minimising the potential of the nozzle to be contaminated with combustion products.

9.4.4 Legacy of this Project

The current work has established research into HPDI within the School. The foundation has been laid for more-specialised research into controlling the gas injection and packaging the system for fitment to an engine. With increasingly-stringent emissions laws, the rising price of fuel and Australia's vast reserves of natural gas, HPDI is a technology ideally suited for development and ultimately commercialisation at UNSW.

Photo 9.2. The head of the RCM was modified as part of the current work. Here, the HPCR injector is mounted to a dummy gas nozzle sleeve in the head.

10. Chapter Ten: References

1. G.H. Abd Alla, H.A. Soliman, O.A. Badr and M.F. Abd Rabbo, *Effect of Pilot Fuel Quantity on the Performance of a Dual Fuel Engine*, SAE Paper 1999-01-3597.
2. J. Abraham, *Entrainment Characteristics of Transient Jets*, Numerical Heat Transfer, Volume 30, Part A, 1996.
3. J. Abraham and F.V. Bracco, *Effects of Combustion on In-Cylinder Mixing of Gaseous and Liquid Jets*, SAE Paper 950467.
4. J. Abraham, V. Magi, J. MacInnes and F.V. Bracco, *Gas Versus Spray Injection: Which Mixes Faster?* SAE Transactions, Volume 103, 1995.
5. S. Abramovich and A. Solan, *The Initial Development of a Submerged Laminar Round Jet*, Journal of Fluid Mechanics, Volume 59, 1973.
6. A.A. Amsden, P.J. O'Rourke and T.D. Butler, *KIVA II: A Computer Program for Chemically Reactive Flows and Sprays*, Los Alamos National Laboratory, 1989.
7. R. Aneja and J. Abraham, *How Far does the Liquid Penetrate in a Diesel Engine: Computer Results vs. Measurements?* Combustion Science and Technology, Volume 138, 1998.
8. C. Arcoumanis and M. Gavaises, *Linking Nozzle Flow with Spray Characteristics in a Diesel Fuel Injection System*, Atomization and Sprays, Volume 8, Number 3, 1998.
9. C. Arcoumanis, M. Gavaises and B. French, *Effect of Fuel Injection Processes on the Structure of Diesel Sprays*, SAE Paper 970799.
10. H. Ashkenaz and F.S. Sherman, *Rarefied Gas Dynamics*, Volume 1, Academic Press, New York, 1966.
11. A. Asmus and B. Wellington, *Diesel Engines and Fuel Systems,* Third Edition, Longman Cheshire, 1992.
12. *Natural Gas Falcon Production Starts*, www.autoweb.com.au, 1 August 1997.
13. *Green Falcon Provides Relief from Petrol Price Pain*, www.autoweb.com.au, 18 July 2000.

14. C. Badock, R. Wirth, A. Fath and A. Leipertz, *Investigation of Cavitation in Real Size Diesel Injection Nozzles*, International Journal of Heat and Fluid Flow, 1999.

15. C. Bai and A.D. Gosman, *Development of Methodology for Spray Impingement Simulation*, SAE Paper 950283.

16. T.A. Baritaud, T.A. Heinze and J.F. Le Coz, *Spray and Self-Ignition Visualization in a DI Diesel Engine*, SAE Paper 940681.

17. N.J. Beck, W.P. Johnson, A.F. George, P.W. Petersen, B. van der Lee and G. Klopp, *Electronic Fuel Injection for Dual Fuel Diesel Methane*, SAE Paper 891652.

18. M.S. Beckman and P.V. Farrell, *Simultaneous Liquid and Vapour Diesel Fuel Spray Images from a HEUI Injector*, 12th ILASS Americas, 21-23 May 2001, Dearborn, Michigan.

19. W. Bergwerk, Proceedings of the Institute of Mechanical Engineers, Volume 173, 1959.

20. A.D. Birch, *The Turbulent Concentration Field of a Methane Jet*, Journal of Fluid Mechanics, Volume 88, 1978.

21. *Automotive Handbook*, Fourth Edition, Robert Bosch GmbH, 1996.

22. *The Diesel Engine with Bosch,* Robert Bosch GmbH, DVD Version 5.0, 2005.

23. X. Boyan and M. Furuyama, *Jet Characteristics of CNG Injector with MPI System*, JSAE Review 19, 1998.

24. K. Bremhorst and P.G. Hollis, *Velocity field of an Axisymmetric, Pulsed, Subsonic Air Jet*, AIAA Journal, Volume 28 (12), 1990.

25. K.S. Burn and G.A. Karim, *The Combustion of Gaseous Fuels in Dual Fuel Engines of the Compression Ignition Type with Particular Reference to Cold Intake Temperature Conditions*, SAE Paper 800263.

26. P. Calais and R. Sims, *A Comparison of Life-Cycle Emissions of Liquid Biofuels and Gaseous Fossil Fuels in the Transport Sector*, Proceedings of Solar 2000, Brisbane, 2000.

27. A. Castleman, NACA Report, Number 440, 1932.

28. D. Chew, *Designing and Building a Single-Shot Injection System for a Rapid Compression Machine*, ME Thesis, School of Mechanical and Manufacturing Engineering, UNSW, December 2001.

29. G.E. Cossali, A. Coghe and L. Araneo, *Near-Field Entrainment in an Impulsively Started Turbulent Gas Jet*, AIAA Journal, Volume 39, Number 6, June 2001.

30. T. Dan, S. Takagishi, J. Senda and H. Fujimoto, *Organised Structure and Motion in Diesel Spray*, SAE Paper 970641.

31. K.J. de Juhasz, Transactions of the ASME, Volume 53, 1931.

32. *Diesel Nozzles and Injectors*, Delphi Diesel Systems Limited, Solihull, England, 2000.

33. *Westport Innovations set to Demonstrate Natural Gas Technology on Heavy-duty Trucks*, Diesel Progress (North American Edition), March 2000.

34. U. Dohle, M. Duernholz, S. Kampmann, J.N Hammer, C. Hinrichsen, *4th Generation Common Rail Injection System for Future Emission Legislation*, FISITA Conference 2004, Paper V271.

35. B. Douville, P. Ouellette, A. Touchette and B. Ursu, *Performance and Emissions of a Two-Stroke Engine Fuelled using High-Pressure Direct Injection of Natural Gas*, SAE Paper 981160.

36. P.M. Einang, S. Koren, R. Kvamsdal, T. Hansen and A. Sarsten, *High-Pressure Digitally Controlled Injection of Gaseous Fuel in a Diesel Engine with Special Reference to Boil-Off from LNG Tankers*, CIMAC '83 Conference Proceedings, Paris, June 1983.

37. M. Favre-Marinet, E.B. Camano and J. Sarboch, *Near-Field of Coaxial Jets with Large Density Differences,* Experiments in Fluids, Volume 26, 1999.

38. *FIRE 5.1 User's Guide*, 2nd Edition, AVL, 1993.

39. *Fluent 6.1.18 User's Guide*, Fluent Inc., 28 January 2003.

40. P.F. Flynn, D.P. Russell, G.L. Hunter, A.O. zur Loye, O.C. Akinyemi, J.E. Dec and C. Westbrook, *Diesel Combustion: An Integrated View Combining Laser Diagnostics, Chemical Kinetics and Empirical Validation*, SAE Paper 1999-01-0509.

41. R.A. Fraser, D.L. Siebers and C.F. Edwards, *Autoignition of Methane and Natural Gas in a Simulated Diesel Environment*, SAE Paper 910227.

42. P. Gaillard, *Multidimensional Numerical Study of the Mixing of an Unsteady Gaseous Fuel Jet with Air in Free and Confined Situations*, SAE Paper 840225.
43. L.C. Ganippa, G. Bark, S. Andersson and J. Chomiak, *Comparison of Cavitation Phenomena in Transparent Scaled-Up Single-Hole Diesel Nozzles*, CAV2001 Session A9.005.
44. P. Gastaldi, B. Argueyrolles, D. Passerel and M. Truant, *3D Simulation for the Development of CR Diesel Combustion Chambers*, Auto Technology, Volume 3, 2003.
45. K. Gebert, N.J. Beck, R.L. Barkheimer, H.C. Wong and A.D. Wells, *Development of a Pilot Fuel Injection System for a CNG Engine*, SAE Paper 961100.
46. J.M. Gordillo, M. Perez-Saborid and A.M. Ganan-Calvo, *Linear Stability of Co-flowing Liquid-gas Jets*, Journal of Fluid Mechanics, Volume 448, 2001.
47. U.D. Grebe and R. Imarisio, *Gasoline or Diesel Engine - the Race is On!* FISITA Conference 2004, Paper V097.
48. www.greenhouse.gov.au, 1 August 2005.
49. E. Griffen and A. Muraszew, *The Atomization of Liquid Fuels*, Wiley, New York, 1953.
50. M. Grossner, *Diesel: the Man and the Engine*, Antheneum, New York, 1978.
51. C. Gunea, M.R.M. Razavi and G.A. Karim, *The Effects of Pilot Fuel Quality on Dual Fuel Engine Ignition Delay*, SAE Paper 982453.
52. H.O. Hardenberg and F.W. Hase, *An Empirical Formula for Computing the Pressure Rise Delay of a Fuel from its Cetane Number and the Relevant Parameters of Direct-Injection Diesel Engines*, SAE Paper 790493.
53. C. Hasse and N. Peters, *Simulation of Multiple Injections in DI Diesel Engines Using a Two-Dimensional Flamelet Model*, Proceedings of the European Combustion Meeting, Aachen, 2003.
54. J.B. Heywood, *Internal Combustiton Engine Fundamentals*, McGraw Hill Book Company, 1988.
55. P.G. Hill and P. Ouellette, *Transient Turbulent Gaseous Fuel Jets for Diesel Engines*, Journal of Fluids Engineering, Volume 121, 1999.
56. P.G. Hill and P. Ouellette, *Turbulent Transient Gas Injections*, ASME Journal of Fluids Engineering, Volume 122, 2000.

57. H. Hiroyasu, M. Arai and M. Shimizu, ICLASS-91, Gaithersburg, 1991.

58. H. Hiroyasu and T. Kadota, *Fuel Droplet Size Distribution in Diesel Combustion Chamber*, SAE Paper 740715.

59. K.B. Hodgins, H. Gunawan and P.G. Hill, *Intensifier-Injector for Natural Gas Fuelling of Diesel Engines*, SAE Paper 921553.

60. K.B. Hodgins, P.G. Hill, P. Ouellette and P. Hung, *Directly Injected Natural Gas Fuelling of Diesel Engines*, SAE Paper 961671.

61. K.B. Hong, H.S. Ryou, G.H. Ko and H. Lee, *The Influence of Break-up Time Constant and Cavitation Modeling on Numerical Simulation of High-Pressure Diesel Sprays*, ILASS Asia ’00, Tsukuba, Japan, 14-15 December 2000.

62. K.Y. Huh and A.D. Gosman, *A Phenomenological Model of Diesel Spray Atomisation*, Proceedings of the International Conference on Multiphase Flows, Tsukuba, 24-27 September 1991.

63. G.S. Hyun, M. Nogami, J. Senda and H. Fujimoto, *Study on Unsteady Gas Jet and Wall Jet Impingement Jet - Comparison of Experimental Results with Numerical Analysis by Distance Vortex Method*, JSAE Review 17, 1996.

64. V. Iyer and J. Abraham, *Penetration and Dispersion of Transient Gas Jets and Sprays*, Combustion Science and Technology, Volume 130, 1997.

65. V.A. Iyer, J. Abraham and V. Magi, *Exploring Injected Droplet Size Effects on Steady Liquid Penetration in a Diesel Spray with a Two-Fluid Model*, International Journal of Heat and Mass Transfer, Volume 45, Number 3, 2002.

66. L. Johansson and M. Lundqvist, *CFD Simulation of Laminar Methane-Air Diffusion Flame*, UNSW 2002.

67. *Journal of Fluids Engineering Editorial Policy Statement on the Control of Numerical Accuracy*, www.divisions.asme.org/fed/divisionadmin/Current%20JFE %20Publication%20Policy.pdf, November 2004.

68. G.A. Karim, W. Jones and R.R. Raine, *An Examination of the Ignition Delay Period in Dual Fuel Engines*, SAE Paper 892140.

69. G.A. Karim and Z. Liu, *The Ignition Delay Period in Dual Fuel Engines*, SAE Paper 950466.

70. S.M. Kato, B.C. Groenwegen and R.E. Briedenthal, *Turbulent Mixing in Nonsteady Jets*, AIAA Journal, Volume 25, Number 1, 1987.

71. J.H. Kim, K. Nishida, T. Yoshizaki and H. Hiroyuki, *Characterisation of Flows in the Sac Chamber and the Discharge Hole of a DI Diesel Injection Nozzle by using a Transparent Model Nozzle*, SAE Paper 972942.

72. T. Kim, M.S. Beckman, P.V. Farrell and J.B. Ghandi, *Evaporating Spray Concentration Measurements from Small and Medium Bore Diesel Injectors*, SAE Paper 2002-01-0219.

73. G. Kleinstein, *Mixing in Turbulent Axially Symmetric Free Jets*, Journal of Spacecraft and Rockets, Volume 1, Number 4, 1964.

74. S. Kloeckner, *Analysis of a Preliminary Design of a Hydraulically-Actuated Natural Gas Injector*, ME Thesis, School of Mechanical and Manufacturing Engineering UNSW, June 2000.

75. S.C. Kong, P.K. Senecal and R.D. Reitz, *Developments in Spray Modelling in Diesel and Direct-Injection Gasoline Engines*, Oil & Gas Science and Technology, Volume 54, Number 2, 1999.

76. H. Kouros, R. Medina and H. Johari, *Spreading Rate of an Unsteady Turbulent Jet*, AIAA Journal, Volume 31, Number 8, 1993.

77. T.W. Kuo and F.V. Bracco, *On the Scaling of Transient Laminar, Turbulent and Spray Jets*, SAE Paper 820038.

78. T. Kuo, R.C. Yu and S.M. Shahed, *A Numerical Study on the Transient Evaporating Spray Mixing Process in the Diesel Environment*, SAE Paper 831735.

79. www.global.kyocera.com/application/automotive/environment/piezo.html, 4 September 2003.

80. M. Langford, *Basic Photography*, Chapter 2 - Light and Image Forming, Focal Press, 1996.

81. J.C. Lasheras and E.J. Hopfinger, *Liquid Jet Instability and Atomization in a Coaxial Gas Stream*, Annual Review of Fluid Mechanics, Volume 32, 2000.

82. C.H. Lee and R.D. Reitz, *An Experimental Study of the Effect of Gas Density on the Distortion and Breakup Mechanism of Drops in High-Speed Gas Stream*, International Journal of Multiphase Flow, Volume 26, 2000.

83. E. Leonardi and T.J. Barber, Class Notes for MECH9620, School of Mechanical and Manufacturing Engineering, UNSW, 2002.

84. H. Lettmann, J. Seebode and G.P. Merker, *Numerical and Experimental Evaluation of DI-Diesel Soot and Nitrogen Emissions in Respect of Different Injection Strategies*, FISITA Conference 2004, Paper V240.

85. G. Li, P. Ouellette, S. Dumitrescu and P.G. Hill, *Optimization Study of Pilot-Ignited Natural Gas Direct-Injection in Diesel Engines*, SAE Paper 1999-01-3556.

86. Y. Li, A. Kirkpatrick, C. Mitchell and B. Willson, *Characteristic and Computational Fluid Dynamics Modeling of High-Pressure Gas Jet Injection*, Transactions of the ASME - Journal of Engineering for Gas Turbines and Power, Volume 126, Number 1, January 2004.

87. T.M. Liou, M. Hall, D.A. Santavicca, and F.V. Bracco, *Laser Doppler Velocimetry Measurements in Valved and Ported Engines*, SAE Paper 840375.

88. Z. Liu, *An Examination of the Combustion Characteristics of Compression Ignition Engines Fuelled with Gaseous Fuels*, PhD Thesis, Department of Mechanical Engineering, University of Calgary, Alberta, Canada, 1995.

89. B.S. Massey, *Mechanics of Fluids*, Sixth Edition, Van Nostrand Reinhold (International), 1989.

90. M. Mbarawa, *Problems Related to the Combustion of the Gaseous Fuel (Natural Gas) in Diesel Engines*, PhD Thesis, School of Mechanical and Manufacturing Engineering, UNSW, 1998.

91. H. Miao, *Fundamental Studies of Combustion Phenomena in Dual Fuel Engines*, PhD Thesis, School of Mechanical and Manufacturing Engineering, UNSW, August 2001.

92. Personal Memorandum from J.M. Middelberg, PhD Candidate in Mechanical Engineering at UNSW, 14 October 2005.

93. R.L. Miller, K.P. Duffy, M.A. Flinn, S.A. Faulkner and M.A. Graham, *Caterpillar Light Truck Clean Diesel Program*, SAE Paper 1999-01-2243.

94. B.E. Milton, *Thermodynamics, Combustion and Engines*, School of Mechanical and Manufacturing Engineering, UNSW, 2001.

95. M. Miyake, T. Biwa, Y. Endoh, M. Shimotsu, S. Murakami and T. Komoda, *The Development of High Output, Highly Efficient Gas Burning Diesel Engines,* CIMAC '83 Conference Proceedings, Paris, June 1983.

96. P.L. Mtui and P.G. Hill, *Ignition Delay and Combustion with Natural Gas Fuelling of Diesel Engines*, SAE Paper 961933.

97. www.myfreelander.com/fuelsystem.htm, 25 August 2003.

98. J.D. Naber, and D.L. Siebers, S.S. di Julio and C.K. Westbrook, *Effects of Natural Gas Composition on Ignition Delay under Diesel Conditions*, Combustion and Flame, Volume 99, 1994.

99. J.D. Naber, D.L. Siebers, C.K. Westbrook, J.A. Caton and S.S. di Julio, *Natural Gas Autoignition Under Diesel Conditions: Experiments and Chemical Kinetic Modeling*, SAE Paper 942034.

100. National Alternative Fuels Training Consortium, www.naftc.wvu.edu, 7 August 2005.

101. O.B. Nielsen, B. Qvale and S. Sorenson, Ignition Delay Period in the Dual Fuel Engine, SAE Paper 870589.

102. A. Nishimura and D.N. Assanis, *A Model for Primary Diesel Fuel Atomization Based on Cavitation Bubble Collapse Energy*, ICLASS 2000, Pasadena California, 16-20 July 2000.

103. W.H. Nurick, *Orifice Cavitation and Its Effects on Spray Mixing*, Journal of Fluids Engineering, Volume 98, 1976.

104. O.M.I. Nwafor and G. Rice, *Combustion Characteristics and Performance of Natural Gas in a High-Speed Indirect Injection Diesel Engine*, Renewable Energy, Volume 5, Numbers 5-8, 1994.

105. P.J. O'Rourke and A.A. Amsden, *The TAB Method for Numerical Calculation of Spray Droplet Breakup*, SAE Paper 872089.

106. P. Ouellette, *Direct Injection of Natural Gas for Diesel Engine Fuelling*, PhD Thesis, The University of British Columbia, May 1996.

107. P. Ouellette, B. Douville, P.G. Hill and B. Ursu, *NO_x Reduction in a Directly Injected Natural Gas Engine*, 13 February 2002. www.westport.com/ userupload/uploadfile/ice98.pdf.

108. P. Ouellette and P.G. Hill, *Visualization of Natural Gas Injection for a Compression Ignition Engine*, SAE Paper 921555.

109. P. Ouellette, P.L. Mtui and P.G. Hill, *Numerical Simulations of Directly Injected Natural Gas and Pilot Diesel Fuel in a Two-Stroke Compression Ignition Engine*, SAE Paper 981400.

110. P. Ouellette and A. Welch, *Progresses in High Pressure Direct Injection (HPDI) of Natural Gas in Automotive Diesel Engines*, WORLD NGV2002, 8th International & 20th National Conference & Exhibition on Natural Gas Vehicles, Washington D.C., 8-10 October 2002.

111. T. Park, R.J. Atkinson, N.N. Clark, M.L. Traver and C.M. Atkinson, *Operation of a Compression Ignition Engine with a HEUI Injection System on Natural Gas with Diesel Pilot Injection*, SAE Paper 1999-01-3522.

112. M.A. Patterson and R.D. Reitz, *Modelling the Effects of Fuel Spray Characteristics on Diesel Engine Combustion and Emissions*, SAE Paper 980131.

113. J. Plateau, *Stattique Experimentale et Theoretique des Liquids Soumie Aux Seules Forces Moleicularies, Chanthier Vallars*, Paris, 1873.

114. S.B. Pope, *An Explanation of the Turbulent Round-Jet/Plane-Jet Anomaly*, AIAA Journal, March 1978.

115. G. Prakash, A.B. Shaik and A. Ramesh, *An Approach for Estimation of Ignition Delay in a Dual Fuel Engine*, SAE Paper 1999-01-0232.

116. J.Q. Qin, T. Dan and M.C. Lai, E. Schwartz and W. Brkyzik, *Correlating the Diesel Spray Behavior to Nozzle Design*, SAE Paper 1999-01-3555.

117. W.E. Ranz, Cambridge Journal of Chemical Engineering, Volume 36, 1958.

118. Lord Rayleigh, *On the Instability of Jets*, London Mathematical Society, 10:361-71, 1878.

119. *The Australian Car Book*, Reader's Digest Services Pty Ltd, Sydney, 1984.

120. R.D. Reitz, *Modelling Atomization Process in High-Pressure Vaporising Sprays*, Atomization and Spray Technology, Volume 3, 1987.

121. R.D. Reitz and F.V. Bracco, *Mechanism of Atomization of a Liquid Jet*, Physics of Fluids, Volume 25, 1982.

122. R.D. Reitz and F.V. Bracco, *Mechanisms of Break-up of Round Liquid Jets*, Encyclopaedia of Fluid Mechanics, Volume 3, Gulf Publishing, NJ, 1986.

123. R.D. Reitz and R. Diwakar, *Structure of High-Pressure Fuel Sprays*, SAE Paper 870598.

124. R.D. Reitz and C.J. Rutland, *Development and Testing of Diesel Engine CFD Models*, Progress in Energy Combustion Science, Volume 21, 1995.

125. J. Rife and J.B. Heywood, *Photographic and Performance Studies of Diesel Combustion in a Rapid Compression Machine*, SAE Paper 740948.

126. W. Rizk, *Experimental Studies of the Mixing Processes and Flow Configurations in Two-Cycle Engine Scavenging*, Proceedings of the Institution of Mechanical Engineers, Series E, Volume 172, 1958.

127. P.J. Rubas, M.A. Paul, G.C. Martin, R.E. Coverdill, R.P Lucht, J.E. Peters and K.A. del Vecchio, *Methane Jet Penetration in a Direct-Injection Natural Gas Engine*, SAE Paper 980143.

128. R. Sadek, Proceedings of the Institute of Mechanical Engineers, Volume 173, 1959.

129. G.T. Sato, H. Tanabe, T. Sorihashi and H. Fujimoto, *Experimental Study on Transient Gas Jet*, Proceedings of the 20th FISITA Congress, Number 845036, 1984-5.

130. D.P. Schmidt and M.L. Corradini, *Analytical Prediction of the Exit Flow of Cavitating Orifices*, Atomization and Sprays Volume 7, Number 6, 1997.

131. D.P. Schmidt, C.J. Rutland and M.L. Corradini, *A Numerical Study of Cavitating Flow Through Various Nozzle Shapes*, SAE Paper 971597.

132. D.P. Schmidt, T.F. Su, K.H. Goney, P.V. Farrell and M.L. Corradini, *Detection of Cavitation in Fuel Injector Nozzles*, www.cobia.ecs.umass.edu/ISTP.pdf, 30 May 2003.

133. B. Schneider, *Experimental Investigation of Diesel Sprays*, 21st CIMAC Congress, Interlaken, 16 May 1995.

134. A.H. Shapiro, *Introductory Concepts to Compressible Flow*, Ronald Press, New York, 1958.

135. J. Sharp, Memorandum e-mail - Bosch CP-1 Pump Specifications, 1 July 2003.

136. D.L. Siebers, *Liquid-Phase Penetration in Diesel Sprays*, SAE Paper 980809.

137. D.L. Siebers, *Scaling Liquid-Phase Fuel Penetration in Diesel Sprays Based on Mixing-Limited Vaporisation*, SAE Paper 1999-01-0528.

138. D. Siebers and B. Higgins, *Flame Lift-Off on Direct-Injection Diesel Sprays under Quiescent Conditions*, SAE Technical Paper 2001-01-0530.

139. R.E. Sonntag and G.J. van Wylen, *Introduction to Thermodynamics*, Third Edition, John Wiley & Sons, 1991.

140. C. Soteriou, R. Andrews and M. Smith, *Direct Injection Diesel Sprays and the Effect of Cavitation and Hydraulic Flip on Atomisation*, SAE Paper 950080.

141. C. Soteriou, R. Andrews and M. Smith, *Further Studies of Cavitation and Atomisation in Diesel Injection*, SAE Paper 1999-01-1486.

142. C. Soteriou, R. Andrews, M. Smith, N. Torres and S. Sankhalpara, *The Flow Patterns and Sprays of Variable Orifice Nozzle Geometries for Diesel Injection*, SAE Paper 2000-01-0943.

143. F.X. Tanner, *Liquid Jet Atomization and Droplet Breakup Modeling of Non-Evaporating Diesel Fuel Sprays*, SAE Paper 970050.

144. F.X. Tanner, G.S. Zhu and R.D. Reitz, *A Turbulence Dissipation Correction to the k-Epsilon Model and its Effect on Turbulence Length Scales in Engine Flows*, International Multidimensional Engine Modeling Users Group Meeting at the SAE Congress, Detroit, 4 March 2001.

145. Y. Tao, K.B. Hodgins and P.G. Hill, *NO_x Emissions from a Diesel Engine Fuelled with Natural Gas*, Transactions of the ASME, Volume 117, December 1995.

146. J.W. Telford, *The Convective Mechanism in Clean Air*, Journal of the Atmospheric Sciences, Volume 23, Number 6, 1966.

147. www.theimagingsource.com/prod/opt/opticsintro_2.htm, 11 June 2005.

148. www.thepowershop.com/HEUI.htm, 5 November 2002.

149. E. Tomita, Y. Hamamoto, H. Tstsumi and S. Takasaki, *Ambient Gas Entrainment into a Transient Gas Jet (Visualisation of Surrounding Air Motion and Estimation of Entrainment Amount by Path Line Method)*, JSME Journal, Series B, Volume 39, Number 3, 1996.

150. X.T. Tran, *Modelling and Simulation of Electronically Controlled Diesel Injectors*, ME Thesis, School of Mechanical and Manufacturing Engineering UNSW, 2003.

151. J.S. Turner, *The Starting Plume in Neutral Surroundings*, Journal of Fluid Mechanics, Volume 13, 1962.

152. M. van Dyke (Editor), *An Album of Fluid Motion*, The Parabolic Press, Stanford, California, 1982.

153. H.K. Versteeg and W. Malalasekera, *An Introduction to Computational Fluid Dynamics*, Prentice-Hall, Harlow, England, 1995.

154. J.F. Wakenell, G.B. O'Neal and Q.A. Baker, *High-Pressure Late-Cycle Direct Injection of Natural Gas in a Rail Medium Speed Diesel Engine*, SAE Paper 872041.

155. C. Weber, *On the Disruption of Liquid Jets*, Journal of Mathematics and Mechanics, Volume 2, Number 2, 1931.

156. T.R. White, *The Effect of Spark-Knock on the performance of a Modern, Spark-Ignition Engine*, BE Thesis, School of Mechanical and Manufacturing Engineering, UNSW, November 1999.

157. P.O Witze, The *Impulsively Started Incompressible Turbulent Jet*, Sandia Laboratories Report, Number SAND80-8617, Livermore, California, October 1980.

158. P.O. Witze, *Hot-Film Anemometer Measurements in a Starting Turbulent Jet*, AIAA Journal Volume 21, Number 2, 1983.

159. S.V. Yudanov, *Development of the Hydraulically-actuated Electronically-controlled Unit Injector for Diesel Engines*, SAE Paper 952057.

160. S. Zakrzewski, *A Numerical and Experimental Investigation of High-Speed Liquid Jets - Their Characteristics and Dynamics*, PhD Thesis, School of Mechanical and Manufacturing Engineering, UNSW, 2001.

161. J. Zhang, R.A. Fraser and A.B. Strong, *Modelling Diesel Engine Natural Gas Injection: Injector/Cylinder Boundary Conditions*, SAE Paper 940329.

Appendix A: Properties of Transport Fuels

Table A.1. Data for some Automotive Fuels [100].

	Methane	Propane	Gasoline	Diesel	Hydrogen	Methanol	Ethanol
Chemical Formula	CH_4	C_3H_8	C_8H_{18}	$C_{12}H_{26}$	H_2	CH_3OH	C_2H_5OH
RON	130	112	91-98	N.A	130+	107	108
MON	130	97	83-90	N.A	N.A	91	92
CN	-10	5-10	8-14	40-65	N.A	3	8
ρ of Liquid Fuel (kg/L)	N/A	0.509	0.746	0.808	0.0708	0.79	0.783
ρ of Gas (kg/m^3)	0.6512	0.508	4.4		0.0838		
Boiling Point (°C)	-162	-42	27-240		-252.7		
LHV (kJ/kg)	49,913	46,238	42,661	43,419	119,444	19,859	26,855
Energy Content (BTU/USgal)	121,459	84,448	114,194	125,881	N/A	N/A	57,449
Energy cf. Gasoline	65%	72%	100%	113%	26%	47%	66%
Energy cf. Diesel	57%	64%	88%	100%	23%	41%	58%
Stoichiometric A/F Ratio (by mass)	17.3	15.7	14.7	15	34.3	6.5	9
Heat of Boiling (kJ/kg)	507	423	355	286	N.A	1186	842
Energy of Stoichiometric Mixture (Vapour)	3.58	3.79	3.55	3.61	3.58	3.45	3.46
Auto-ign. Temp (°C)	540	482	257	316	574	464	423
Peak Flame Temp (°C)	1790	1990	1977	2054	2045		
Spark Ignition Energy (MJ)	0.29	0.305	0.24	0.24	0.02		
Flammability Limits (% volume)	5.3-15	2.1-10.4	1.4- 7.6	0.6-5.5	4-75		
Maximum Burning Velocity in ambient air (cm/s)	37-45	43-52	37-43				
Specific Gravity at ambient (°F)	0.55	1.52	2-4	4-6			
Reid Vapour Pressure (psi)	2400	208	8-15	0.2		4.6	2.3
Relative Flame Visibility	0.6	0.6	1	1			
Flash Point (°F)	-300	-100 to -150	-45	165		52	55

* @ 3500 psi

Table A.2. Full fuel-cycle CO_2 emissions for a range of transport fuels– gCO_2/MJ [26].

Process	Diesel	LS[1] diesel	ULS[2] diesel	LPG	CNG	LNG	E95[3]	BD20[4]	BD100[5]
Fuel production	11	12	13	11	6	9	-29	2	-41
Combustion	69	69	69	69	54	55	65	73	89
Total	**80**	**81**	**82**	**80**	**60**	**64**	**36**	**75**	**48**
Reduction in emissions cf. stnd diesel (%)	**0**	**+1.25**	**+2.5**	**0**	**-25**	**-20**	**-55**	**- 6.25**	**-40**

LS = Low Sulphur

ULS = Ultra-Low Sulphur

E = Ethanol

BD = Bio-diesel

Table A.3. Composition of Natural Gas as used in the Current Work, from Miao [91].

Component		Percentage by Volume	Percentage by Mass
Methane	CH_4	94.1	88.5
Ethane	C_2H_6	2.8	4.9
Propane	C_3H_8	0.1	0.3
Carbon Dioxide	CO_2	1.5	3.8
Nitrogen	N_2	1.5	2.5

Appendix B: Kloeckner's Proposed DF Injector

Sven Kloeckner submitted a thesis as part of a Master's degree at the School in June of 2000 [74]. The objective of the project was "to develop an engine fuel system that was able to supply the engine with both low cetane number gaseous fuel and high cetane number diesel fuel simultaneously with the ultimate aim of making engines run smoother, cleaner and more cost-efficient." It was hoped to base this DF/HPDI injector on the HEUI developed within the School by Yudanov [159]. The injector was designed for fitment to the School's Volvo test engine, the specifications of which are given in Table B.1.

Table B.1. Specifications of the School's Volvo Test Engine [74].

Model	**Volvo 7B-230**
Number of Cylinders	Six
Swept Volume	6.7 L
Rated Power	230 hp/169 kW at 2,200 rpm
Bore x Stroke	104.8 x 130 mm
Compression ratio	18:1
Max cylinder pressure	4.5 MPa
Injector opening pressure	25 MPa

From this data, Kloeckner calculated the requirements of a dual-fuel injector to suit the Volvo engine whilst operating at its design speed of 2,000 rpm. These requirements are given in table B.2.

The result from this work was the design of an HPDI injector as shown in Figure B.1.

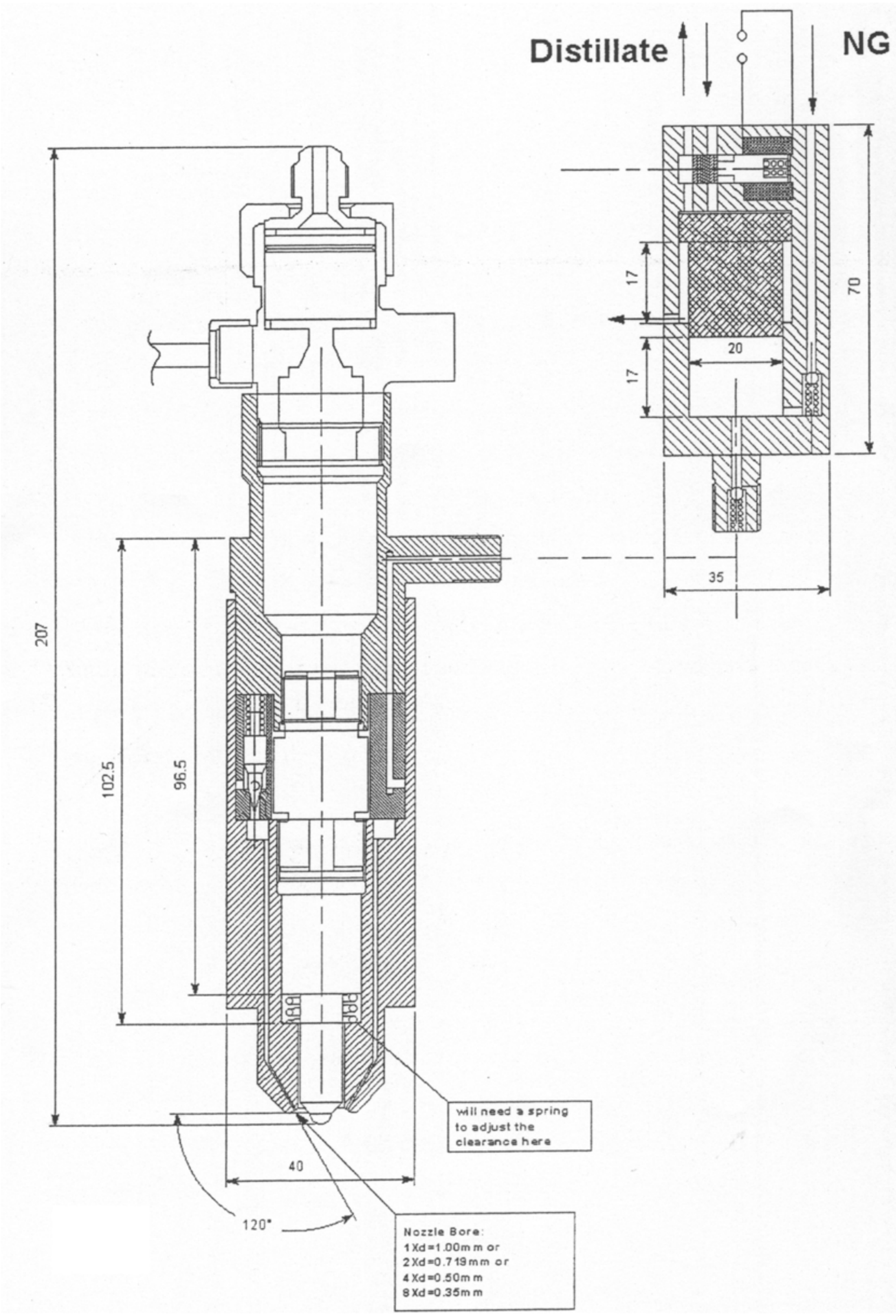

Figure B.1. Schematic diagram of Kloeckner's proposed HPDI injector [74].

Table B.2. Parameters for the Design of a Dual-Fuel injector [74].

Engine speed	2,000 rpm
Injection time	Ranges between 0.7 ms and 5 ms
Maximum NG mass per cycle	0.056 g
Maximum NG volume per cycle	724 mm^3
Total Nozzle Area:	0.79 mm^2
Injection Pressure	20 MPa
NG injection Density	85.6 kg/m^3
NG injection Temperature	500 K

Appendix C: Manufacturing Drawings of the Major Components of the Test Rig

Table C.1. Drawing List.

Part Number	**Description**
	Diesel Delivery System
TRW-P-003	Assembly – Diesel Delivery System
TRW-P-022	Base Plate
TRW-P-054	Tank
TRW-P-034	Fuel Rail Bracket
TRW-P-014	Assembly - Pump
TRW-P-032	Pump Bracket
TRW-P-062	Pump Shaft
TRW-P-073	Pump Shaft Housing
TRW-P-084	Pump Manifold
TRW-P-087	Pump Manifold Runners
TRW-P-114	Intensifier Assembly
	Gas Delivery System
TRW-G-214	Assembly – DF Injector
TRW-G-226	Gas Nozzle Sleeve
TRW-G-242	Gas Reservoir
	Jet Visualisation Box
TRW-V-408	JVB Parts List
TRW-V-422	JVB Head
TRW-V-444	Bulb Holder – Halogen Lamp for MVL Housing

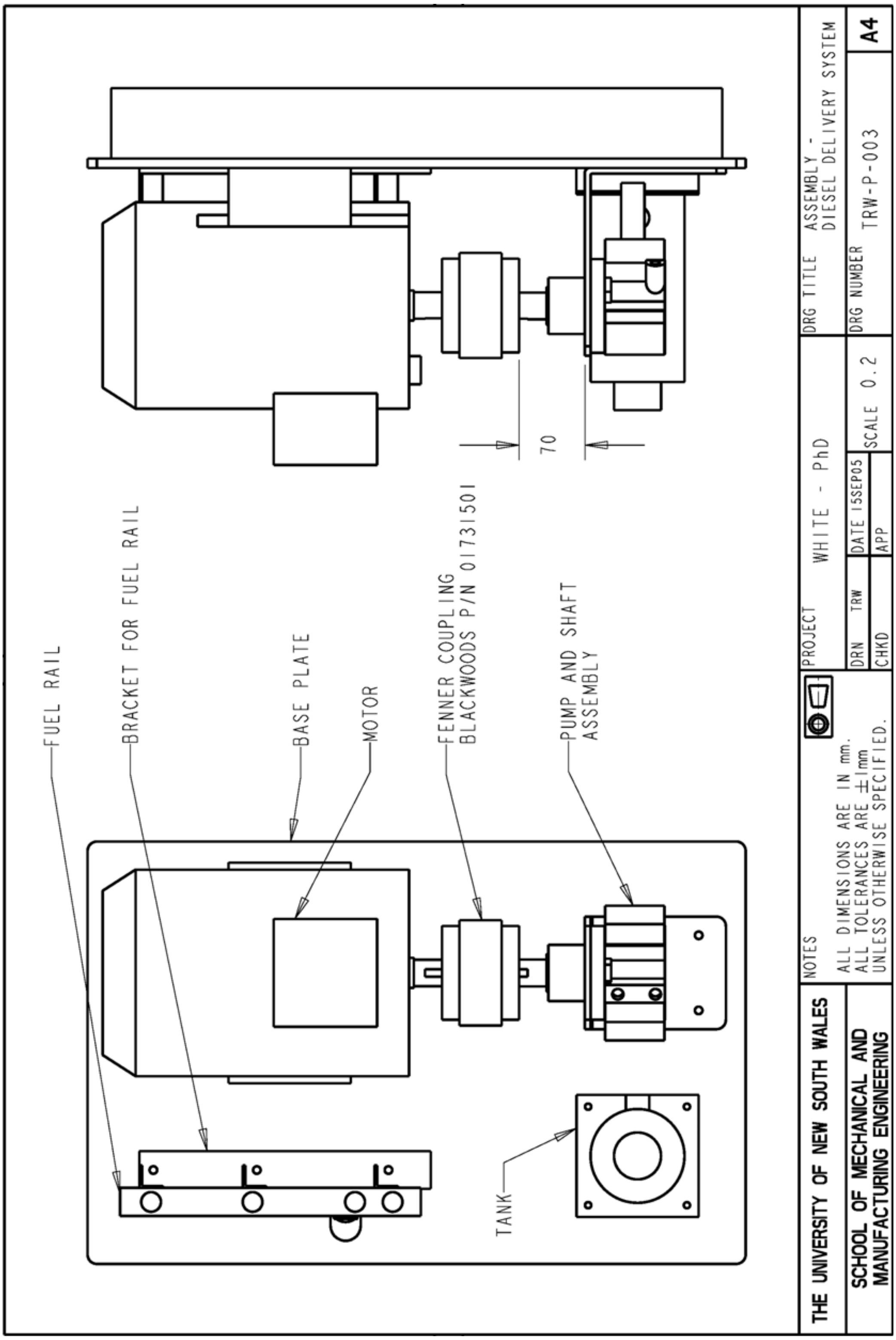
FUEL RAIL
BRACKET FOR FUEL RAIL
BASE PLATE
MOTOR
FENNER COUPLING
BLACKWOODS P/N 01731501
PUMP AND SHAFT
ASSEMBLY
TANK
70
THE UNIVERSITY OF NEW SOUTH WALES
SCHOOL OF MECHANICAL AND
MANUFACTURING ENGINEERING
NOTES
ALL DIMENSIONS ARE IN mm.
ALL TOLERANCES ARE ±1mm
UNLESS OTHERWISE SPECIFIED.
PROJECT WHITE - PhD
DRN TRW
DATE 15SEP05
CHKD
APP
DRG TITLE ASSEMBLY -
DIESEL DELIVERY SYSTEM
SCALE 0.2
DRG NUMBER TRW-P-003
A4

Figure C.1

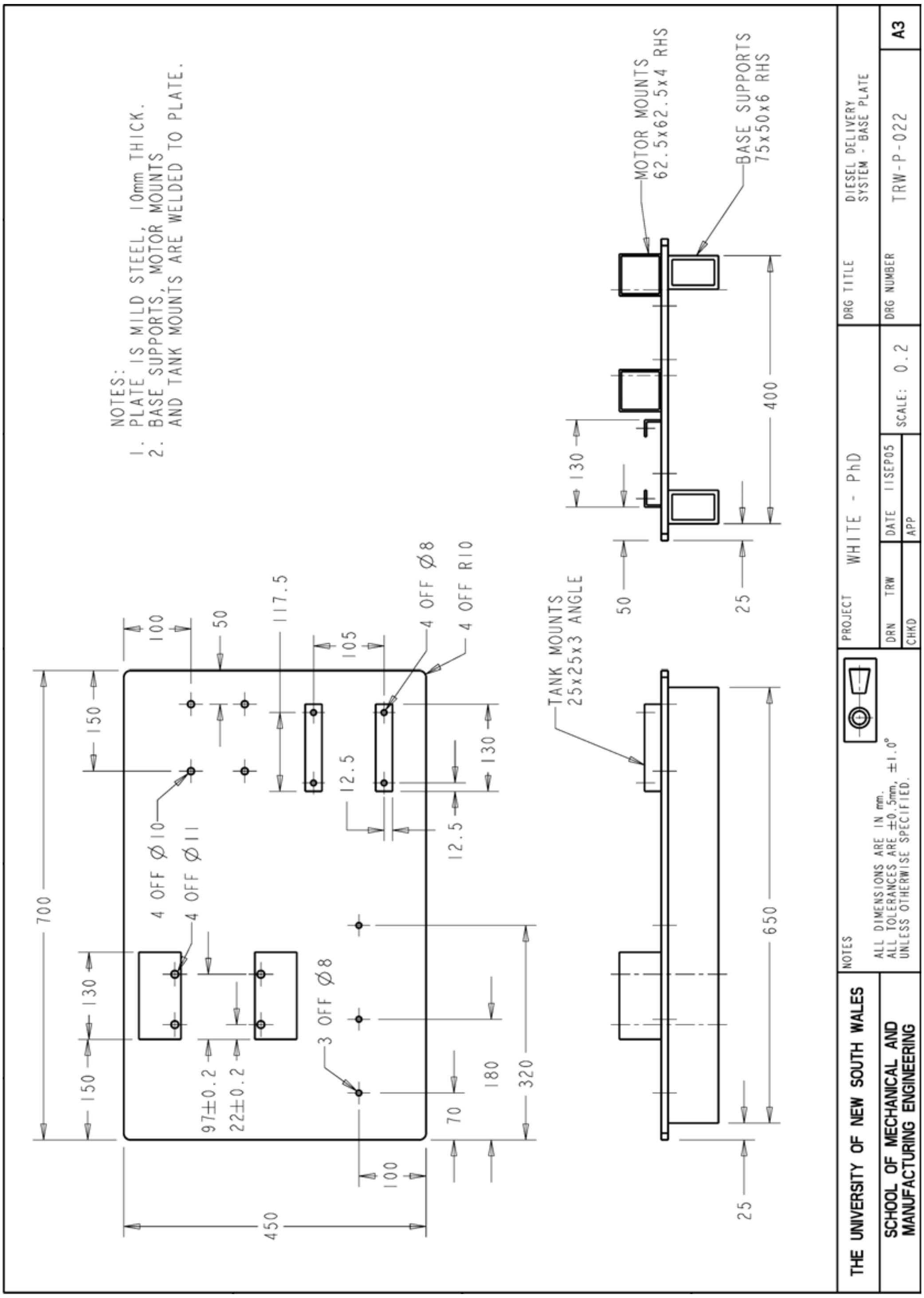
NOTES:
1. PLATE IS MILD STEEL, 10mm THICK.
2. BASE SUPPORTS, MOTOR MOUNTS AND TANK MOUNTS ARE WELDED TO PLATE.
MOTOR MOUNTS 62.5x62.5x4 RHS
BASE SUPPORTS 75x50x6 RHS
TANK MOUNTS 25x25x3 ANGLE
4 OFF Ø8
4 OFF R10
4 OFF Ø10
4 OFF Ø11
3 OFF Ø8
97±0.2
22±0.2
700
450
650
400
320
180
150
130
117.5
105
100
70
50
25
12.5
THE UNIVERSITY OF NEW SOUTH WALES
SCHOOL OF MECHANICAL AND MANUFACTURING ENGINEERING
NOTES
ALL DIMENSIONS ARE IN mm.
ALL TOLERANCES ARE ±0.5mm, ±1.0°
UNLESS OTHERWISE SPECIFIED.
PROJECT WHITE - PhD
DRN TRW
CHKD
DATE 11SEP05
APP
SCALE: 0.2
DRG TITLE DIESEL DELIVERY SYSTEM - BASE PLATE
DRG NUMBER TRW-P-022
A3

Figure C.2

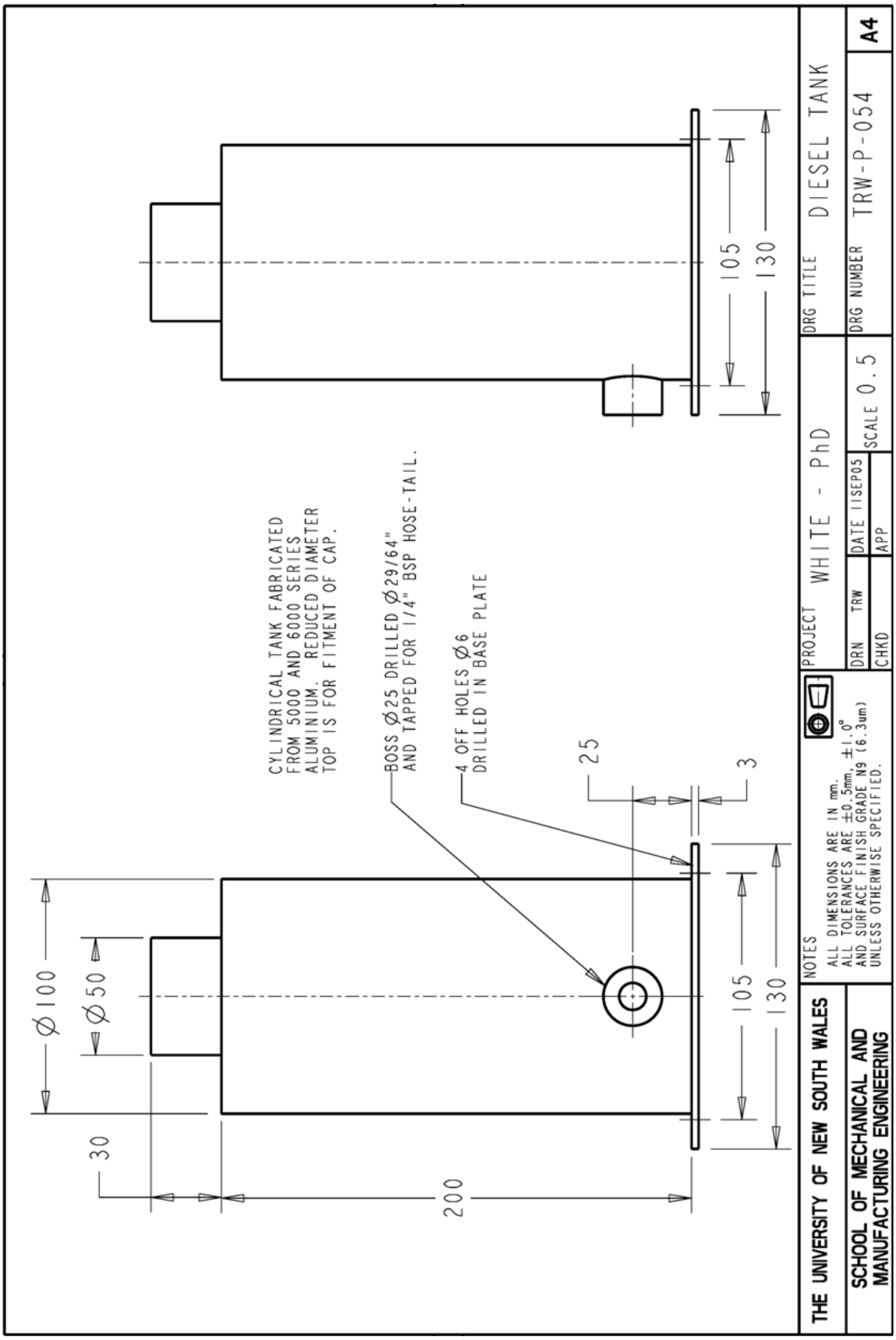
CYLINDRICAL TANK FABRICATED FROM 5000 AND 6000 SERIES ALUMINIUM. REDUCED DIAMETER TOP IS FOR FITMENT OF CAP.
BOSS Ø25 DRILLED Ø29/64" AND TAPPED FOR 1/4" BSP HOSE-TAIL.
4 OFF HOLES Ø6 DRILLED IN BASE PLATE
Ø100
Ø50
30
200
25
3
105
130
105
130
THE UNIVERSITY OF NEW SOUTH WALES
SCHOOL OF MECHANICAL AND MANUFACTURING ENGINEERING
NOTES
ALL DIMENSIONS ARE IN mm.
ALL TOLERANCES ARE ±0.5mm, ±1.0°
AND SURFACE FINISH GRADE N9 (6.3um)
UNLESS OTHERWISE SPECIFIED.
PROJECT WHITE - PhD
DRN TRW
DATE 11SEP05
CHKD
APP
SCALE 0.5
DRG TITLE DIESEL TANK
DRG NUMBER TRW-P-054
A4

Figure C.3

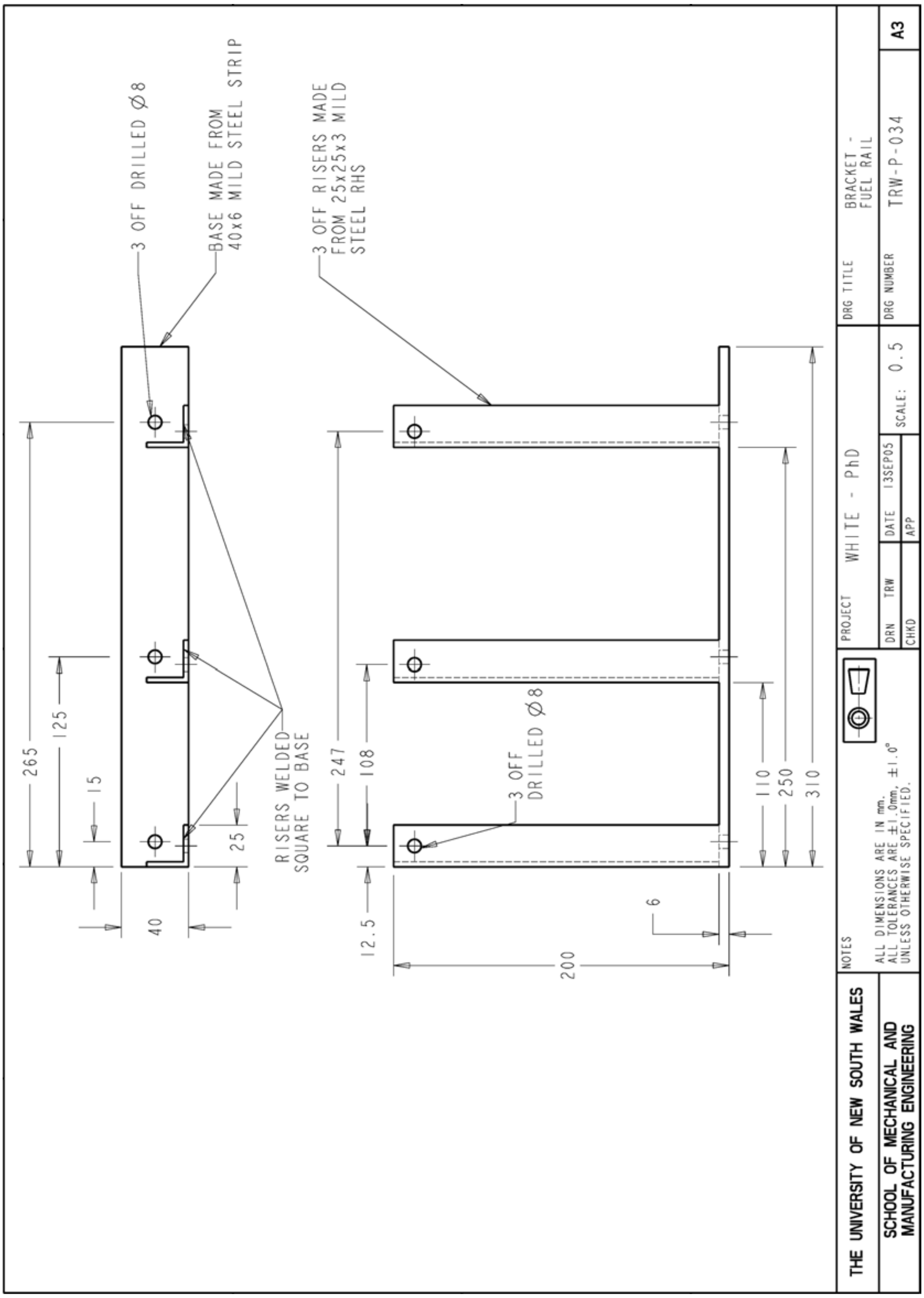
3 OFF DRILLED Ø8
BASE MADE FROM 40x6 MILD STEEL STRIP
3 OFF RISERS MADE FROM 25x25x3 MILD STEEL RHS
RISERS WELDED SQUARE TO BASE
3 OFF DRILLED Ø8
265
125
15
25
40
247
108
12.5
6
200
110
250
310
NOTES
ALL DIMENSIONS ARE IN mm.
ALL TOLERANCES ARE ±1.0mm, ±1.0°
UNLESS OTHERWISE SPECIFIED.
PROJECT WHITE - PhD
DRN TRW
DATE 13SEP05
CHKD
APP
SCALE: 0.5
DRG TITLE BRACKET - FUEL RAIL
DRG NUMBER TRW-P-034
A3
THE UNIVERSITY OF NEW SOUTH WALES
SCHOOL OF MECHANICAL AND MANUFACTURING ENGINEERING

Figure C.4

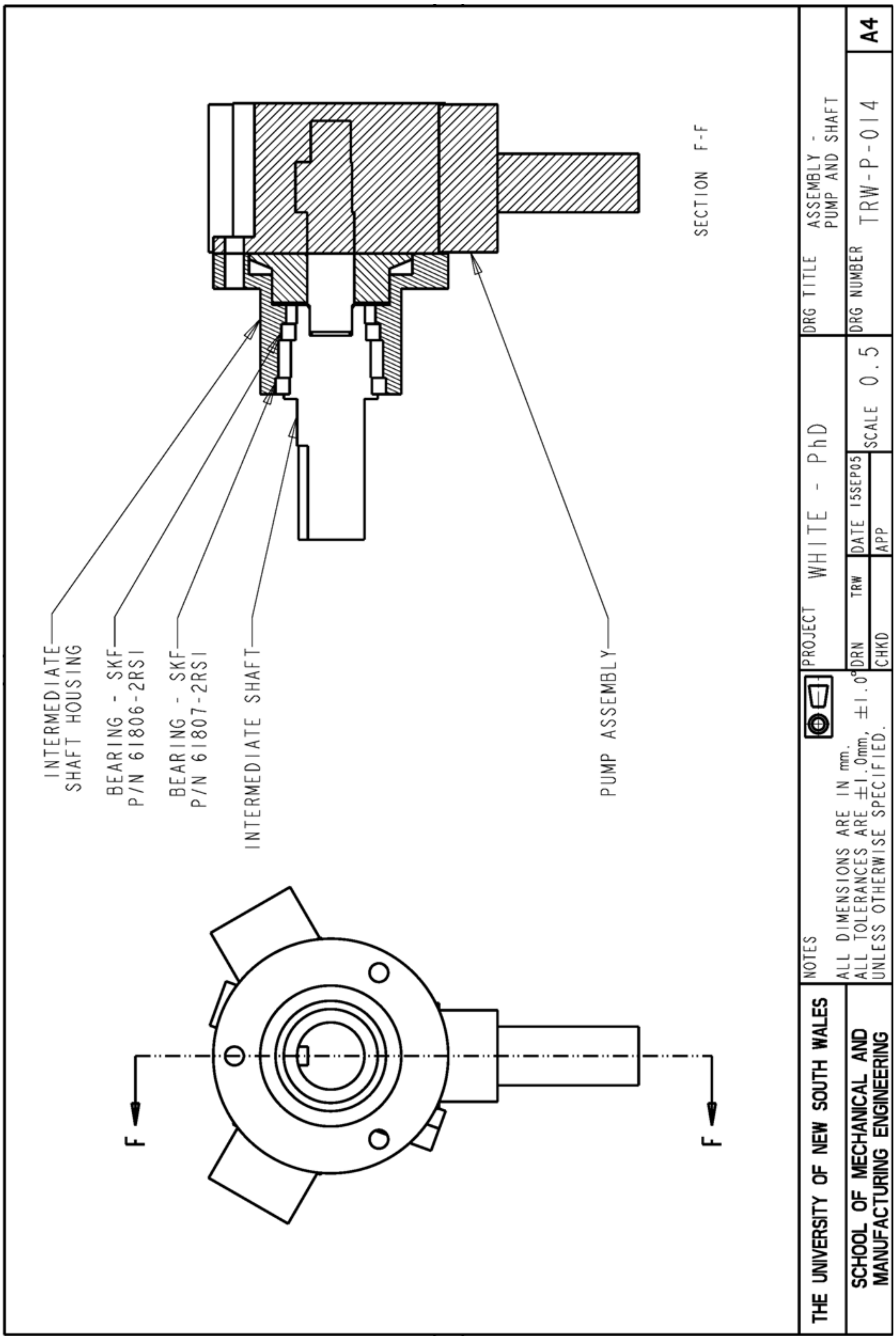
INTERMEDIATE SHAFT HOUSING
BEARING - SKF P/N 61806-2RSI
BEARING - SKF P/N 61807-2RSI
INTERMEDIATE SHAFT
PUMP ASSEMBLY
SECTION F-F
F
F
THE UNIVERSITY OF NEW SOUTH WALES
SCHOOL OF MECHANICAL AND MANUFACTURING ENGINEERING
NOTES
ALL DIMENSIONS ARE IN mm.
ALL TOLERANCES ARE ±1.0mm, ±1.0°
UNLESS OTHERWISE SPECIFIED.
PROJECT WHITE - PhD
DRN TRW
DATE 15SEP05
CHKD
APP
SCALE 0.5
DRG TITLE ASSEMBLY - PUMP AND SHAFT
DRG NUMBER TRW-P-014
A4

Figure C.5

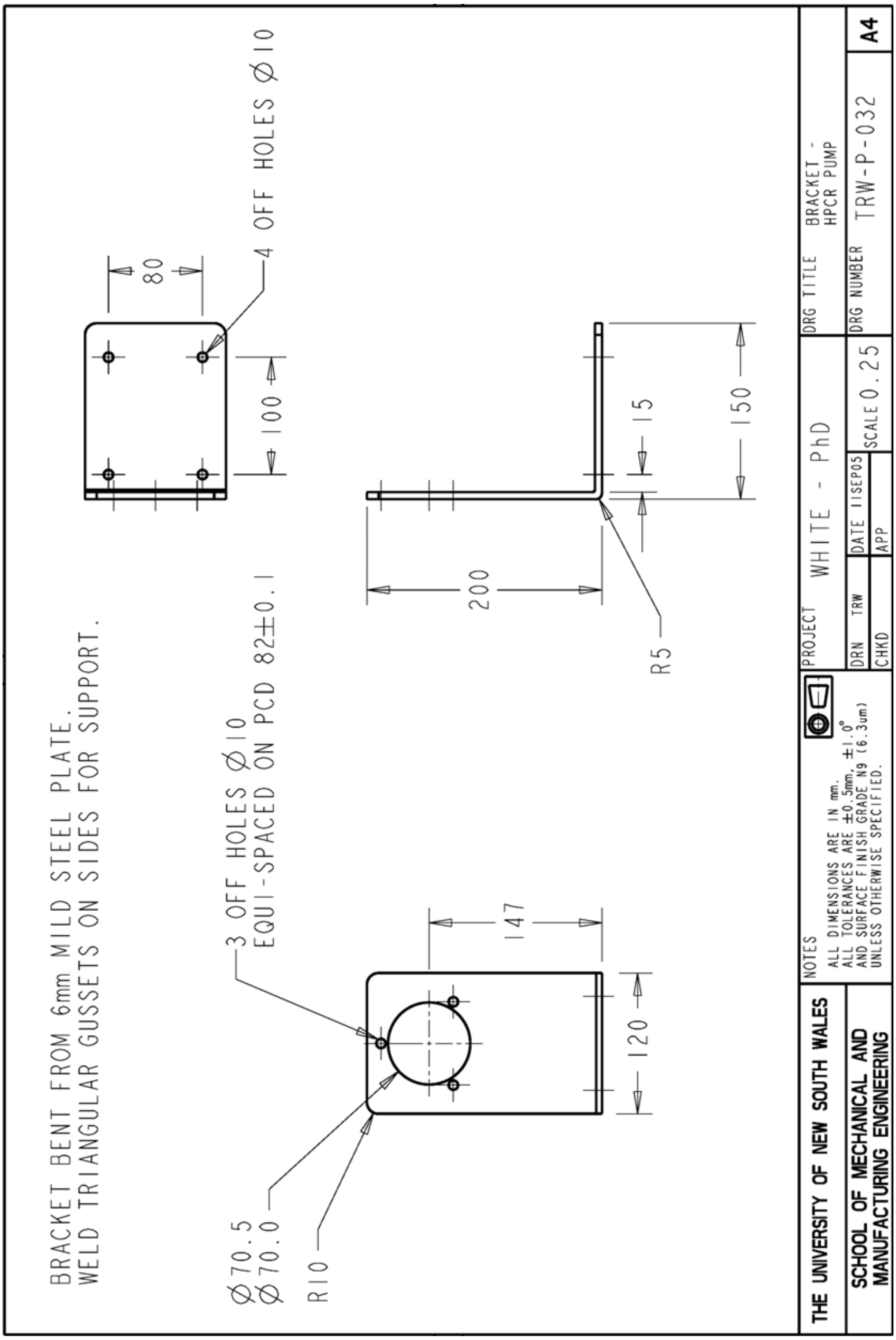
BRACKET BENT FROM 6mm MILD STEEL PLATE.
WELD TRIANGULAR GUSSETS ON SIDES FOR SUPPORT.
3 OFF HOLES Ø10
EQUI-SPACED ON PCD 82±0.1
4 OFF HOLES Ø10
Ø70.5
Ø70.0
R10
147
120
80
100
15
150
200
R5
THE UNIVERSITY OF NEW SOUTH WALES
SCHOOL OF MECHANICAL AND MANUFACTURING ENGINEERING
NOTES
ALL DIMENSIONS ARE IN mm.
ALL TOLERANCES ARE ±0.5mm, ±1.0°
AND SURFACE FINISH GRADE N9 (6.3um)
UNLESS OTHERWISE SPECIFIED.
PROJECT
WHITE - PhD
DRN TRW
DATE 11SEP05
CHKD
APP
SCALE 0.25
DRG TITLE
BRACKET - HPCR PUMP
DRG NUMBER
TRW-P-032
A4

Figure C.6

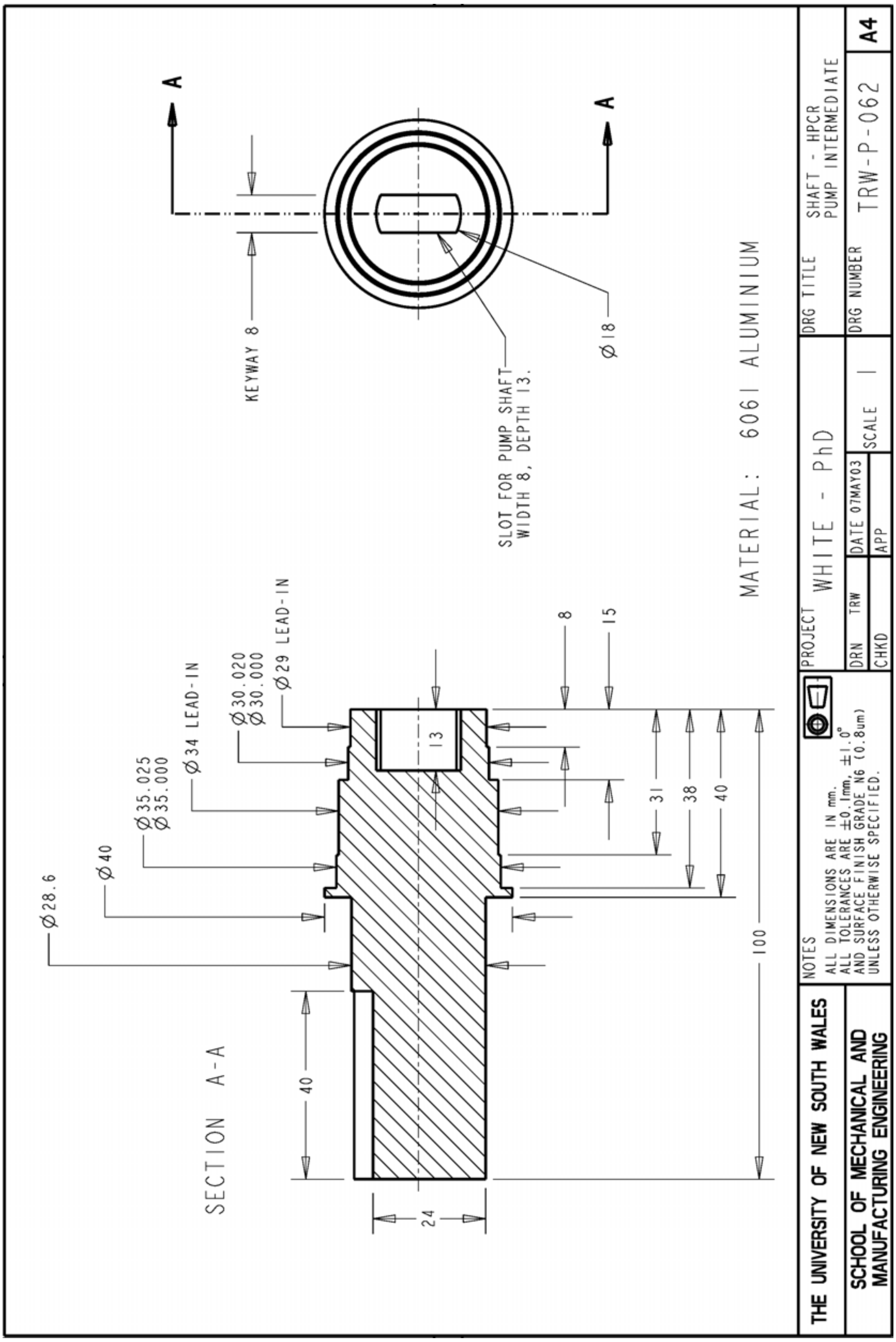
SECTION A-A
Ø28.6
Ø40
Ø35.025
Ø35.000
Ø34 LEAD-IN
Ø30.020
Ø30.000
Ø29 LEAD-IN
13
8
15
31
38
40
100
40
24
A
A
KEYWAY 8
SLOT FOR PUMP SHAFT
WIDTH 8, DEPTH 13.
Ø18
MATERIAL: 6061 ALUMINIUM
THE UNIVERSITY OF NEW SOUTH WALES
SCHOOL OF MECHANICAL AND MANUFACTURING ENGINEERING
NOTES
ALL DIMENSIONS ARE IN mm.
ALL TOLERANCES ARE ±0.1mm, ±1.0°
AND SURFACE FINISH GRADE N6 (0.8um)
UNLESS OTHERWISE SPECIFIED.
PROJECT
WHITE - PhD
DRN TRW
DATE 07MAY03
CHKD
APP
SCALE 1
DRG TITLE
SHAFT - HPCR PUMP INTERMEDIATE
DRG NUMBER
TRW-P-062
A4

Figure C.7

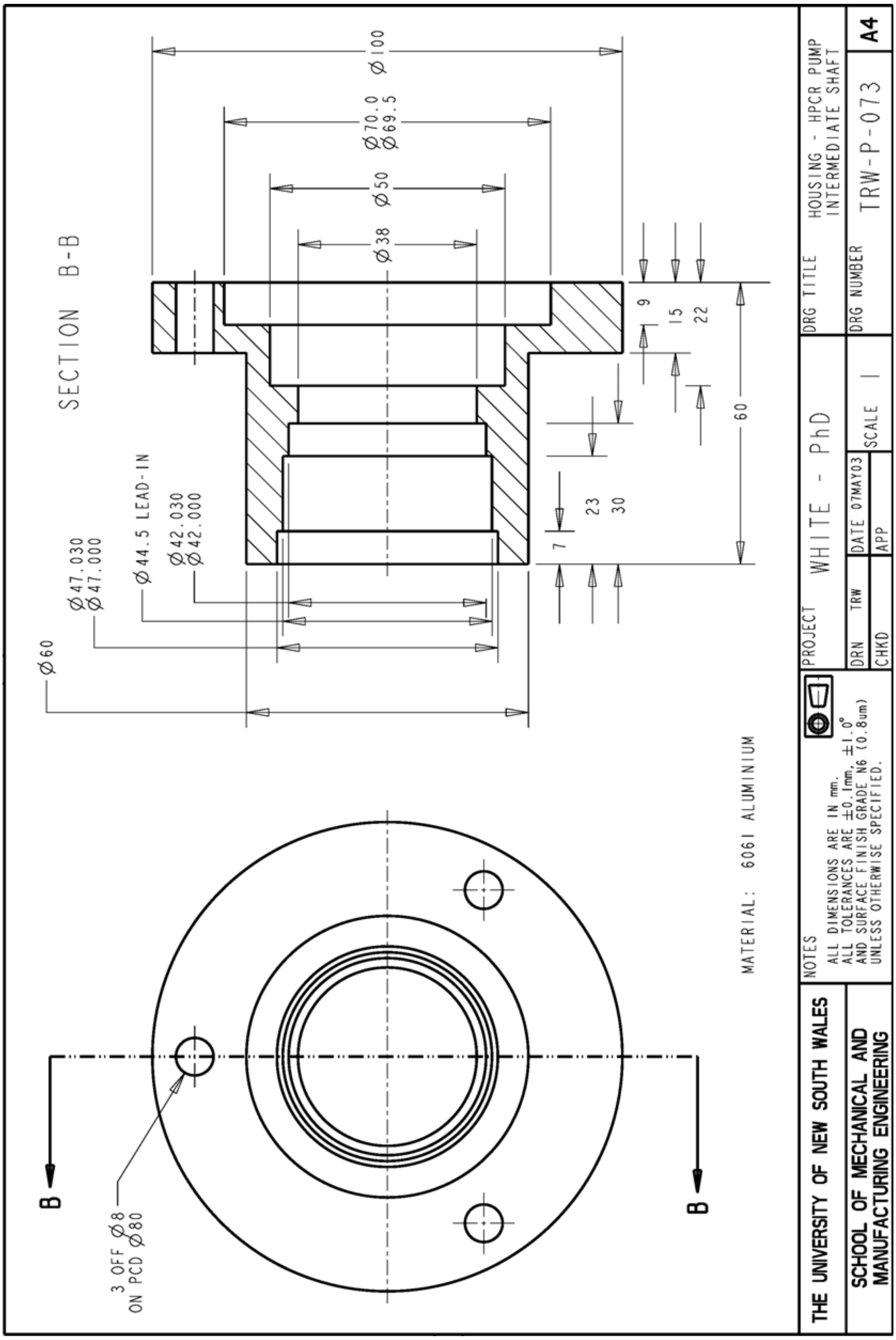
SECTION B-B
Ø100
Ø70.0
Ø69.5
Ø50
Ø38
Ø47.030
Ø47.000
Ø44.5 LEAD-IN
Ø42.030
Ø42.000
Ø60
9
15
22
60
7
23
30
3 OFF Ø8
ON PCD Ø80
B
B
MATERIAL: 6061 ALUMINIUM
NOTES
ALL DIMENSIONS ARE IN mm.
ALL TOLERANCES ARE ±0.1mm, ±1.0°
AND SURFACE FINISH GRADE N6 (0.8um)
UNLESS OTHERWISE SPECIFIED.
THE UNIVERSITY OF NEW SOUTH WALES
SCHOOL OF MECHANICAL AND
MANUFACTURING ENGINEERING
PROJECT WHITE - PhD
DRN TRW
CHKD
DATE 07MAY03
APP
SCALE 1
DRG TITLE HOUSING - HPCR PUMP
INTERMEDIATE SHAFT
DRG NUMBER TRW-P-073
A4

Figure C.8

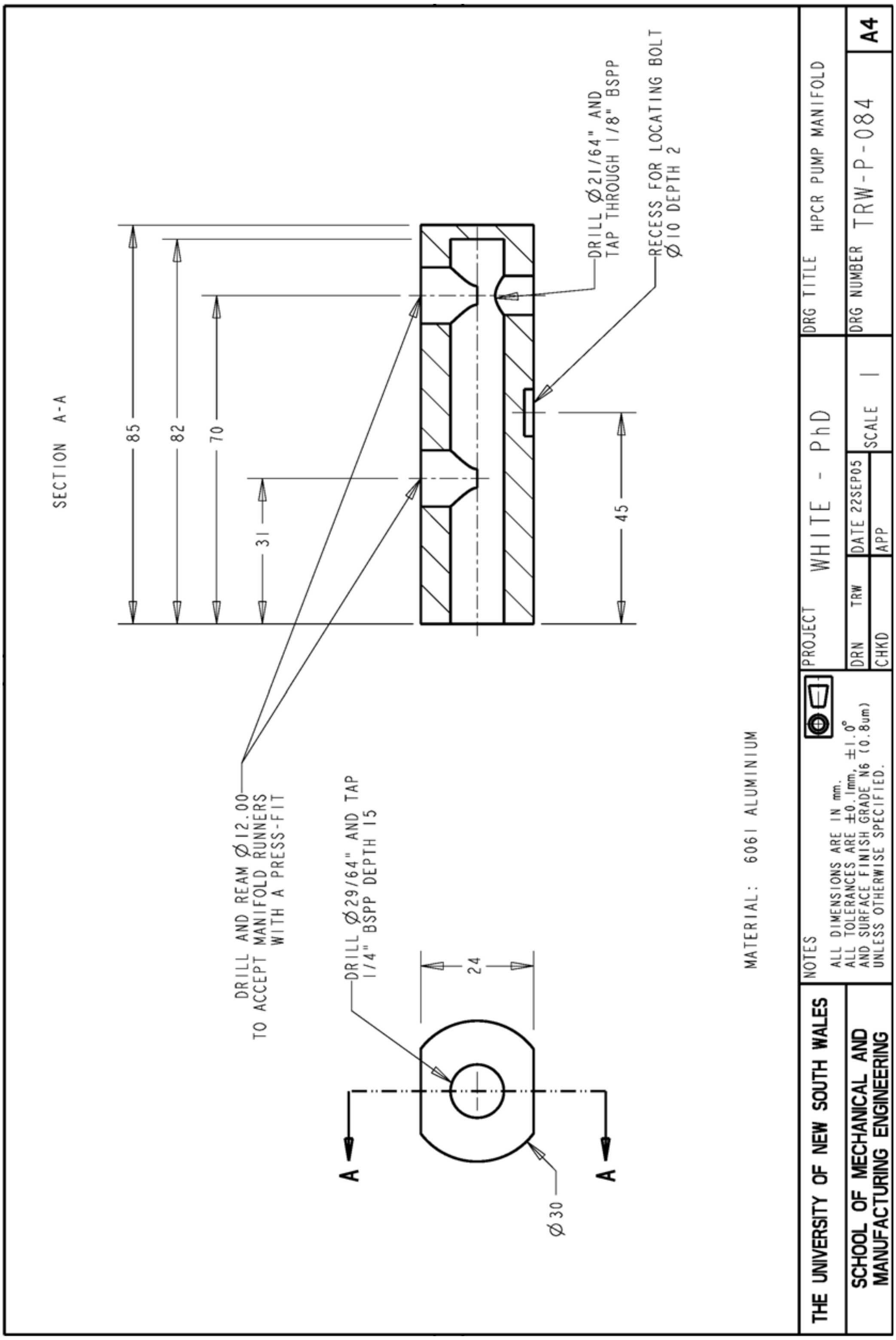
SECTION A-A
85
82
70
31
45
DRILL Ø21/64" AND TAP THROUGH 1/8" BSPP
RECESS FOR LOCATING BOLT Ø10 DEPTH 2
DRILL AND REAM Ø12.00 TO ACCEPT MANIFOLD RUNNERS WITH A PRESS-FIT
DRILL Ø29/64" AND TAP 1/4" BSPP DEPTH 15
24
Ø30
A
A
MATERIAL: 6061 ALUMINIUM
NOTES
ALL DIMENSIONS ARE IN mm.
ALL TOLERANCES ARE ±0.1mm, ±1.0°
AND SURFACE FINISH GRADE N6 (0.8um)
UNLESS OTHERWISE SPECIFIED.
THE UNIVERSITY OF NEW SOUTH WALES
SCHOOL OF MECHANICAL AND MANUFACTURING ENGINEERING
PROJECT WHITE - PhD
DRN TRW
CHKD
DATE 22SEP05
APP
SCALE 1
DRG TITLE HPCR PUMP MANIFOLD
DRG NUMBER TRW-P-084
A4

Figure C.9

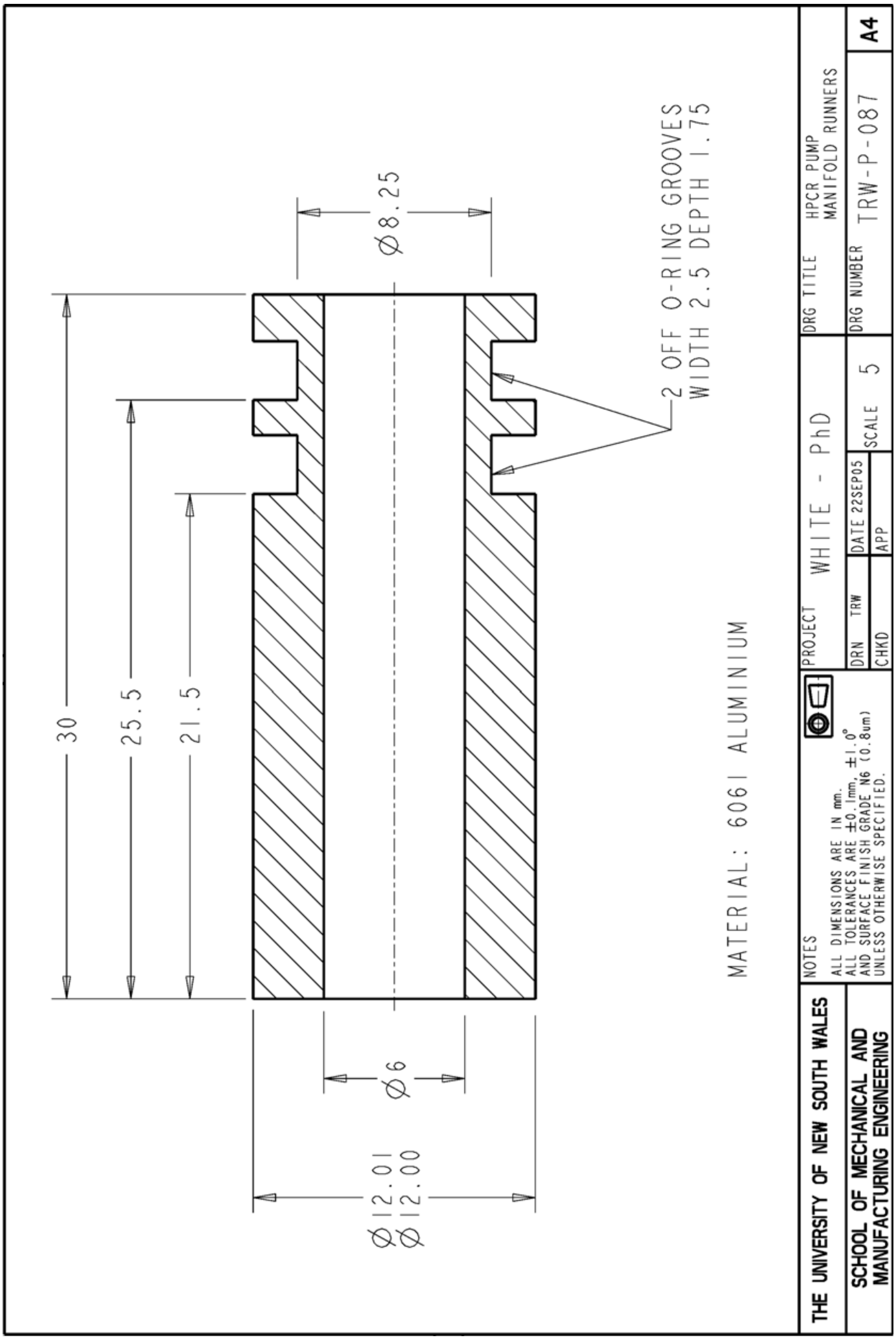
2 OFF O-RING GROOVES
WIDTH 2.5 DEPTH 1.75
Ø8.25
30
25.5
21.5
Ø6
Ø12.01
Ø12.00
MATERIAL: 6061 ALUMINIUM
THE UNIVERSITY OF NEW SOUTH WALES
SCHOOL OF MECHANICAL AND MANUFACTURING ENGINEERING
NOTES
ALL DIMENSIONS ARE IN mm.
ALL TOLERANCES ARE ±0.1mm, ±1.0°
AND SURFACE FINISH GRADE N6 (0.8um)
UNLESS OTHERWISE SPECIFIED.
PROJECT WHITE - PhD
DRN TRW
CHKD
DATE 22SEP05
APP
SCALE 5
DRG TITLE HPCR PUMP MANIFOLD RUNNERS
DRG NUMBER TRW-P-087
A4

Figure C.10

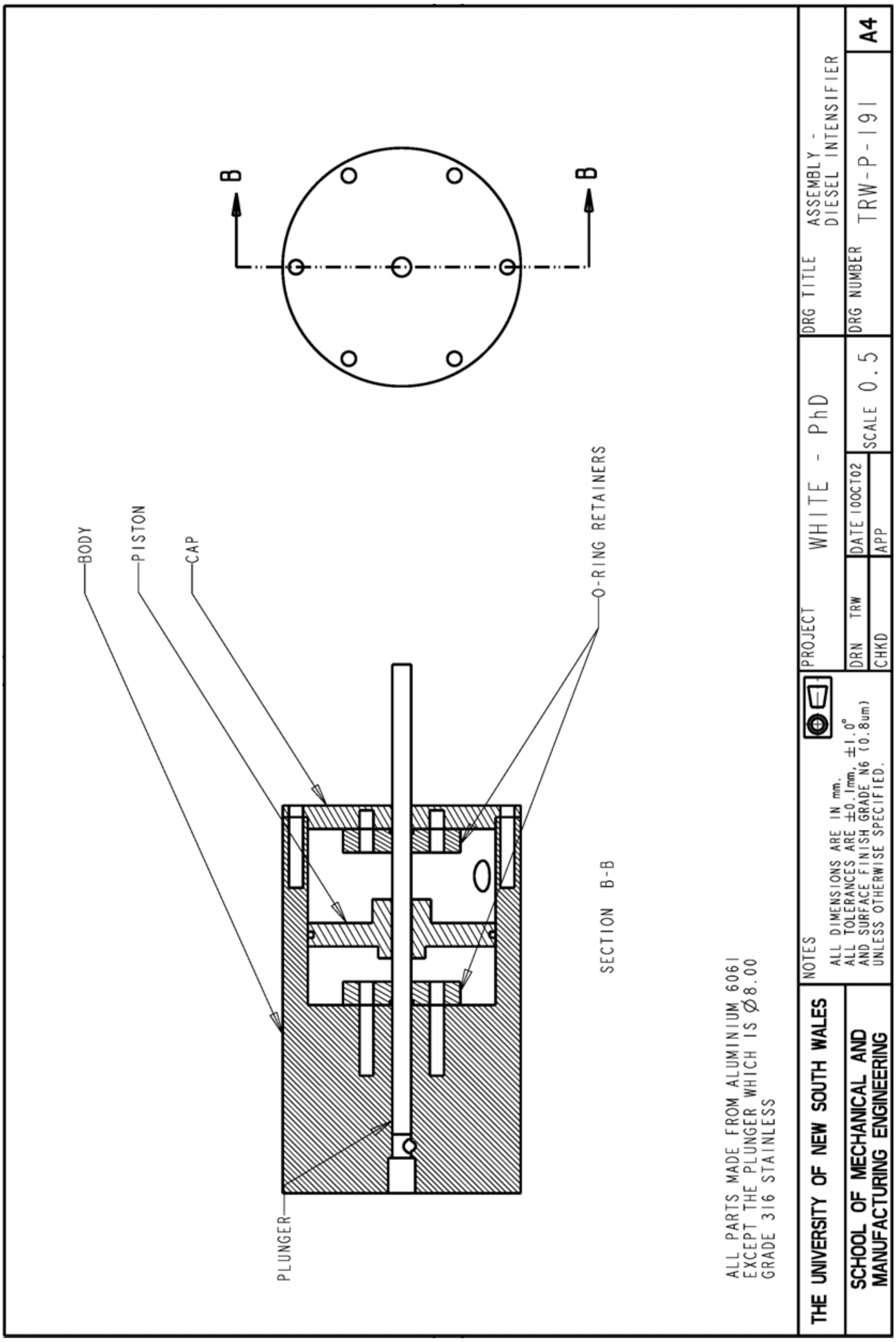
B
B
BODY
PISTON
CAP
O-RING RETAINERS
PLUNGER
SECTION B-B
ALL PARTS MADE FROM ALUMINIUM 6061
EXCEPT THE PLUNGER WHICH IS Ø8.00
GRADE 316 STAINLESS
THE UNIVERSITY OF NEW SOUTH WALES
SCHOOL OF MECHANICAL AND
MANUFACTURING ENGINEERING
NOTES
ALL DIMENSIONS ARE IN mm.
ALL TOLERANCES ARE ±0.1mm, ±1.0°
AND SURFACE FINISH GRADE N6 (0.8um)
UNLESS OTHERWISE SPECIFIED.
PROJECT
WHITE - PhD
DRN TRW
DATE 10OCT02
CHKD
APP
SCALE 0.5
DRG TITLE
ASSEMBLY -
DIESEL INTENSIFIER
DRG NUMBER
TRW-P-191
A4

Figure C.11

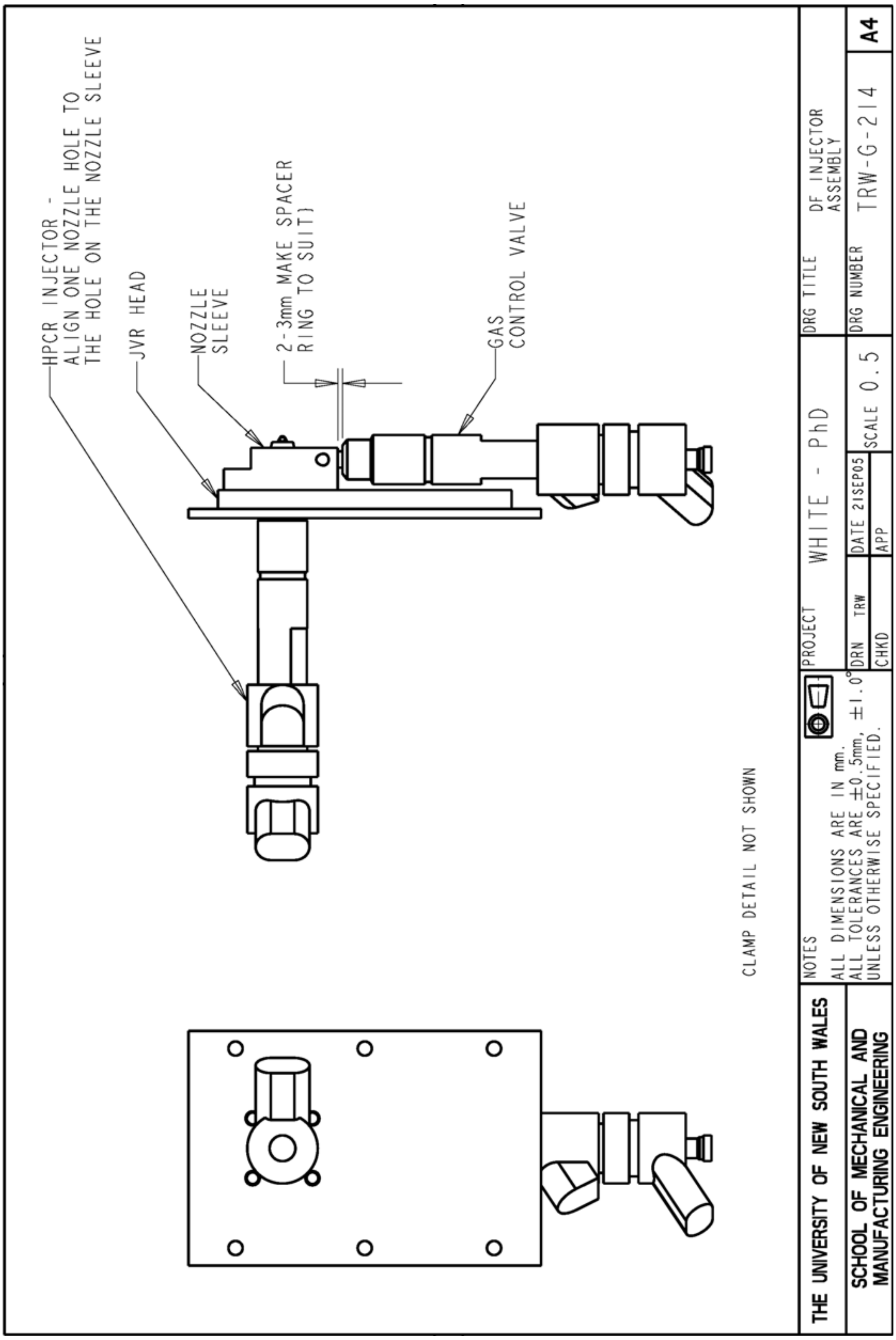
HPCR INJECTOR - ALIGN ONE NOZZLE HOLE TO THE HOLE ON THE NOZZLE SLEEVE
JVR HEAD
NOZZLE SLEEVE
2-3mm MAKE SPACER RING TO SUIT)
GAS CONTROL VALVE
CLAMP DETAIL NOT SHOWN
NOTES
ALL DIMENSIONS ARE IN mm.
ALL TOLERANCES ARE ±0.5mm, ±1.0°
UNLESS OTHERWISE SPECIFIED.
PROJECT
WHITE - PhD
DRG TITLE
DF INJECTOR ASSEMBLY
DRN TRW
CHKD
DATE 21SEP05
APP
SCALE 0.5
DRG NUMBER
TRW-G-214
A4
THE UNIVERSITY OF NEW SOUTH WALES
SCHOOL OF MECHANICAL AND MANUFACTURING ENGINEERING

Figure C.12

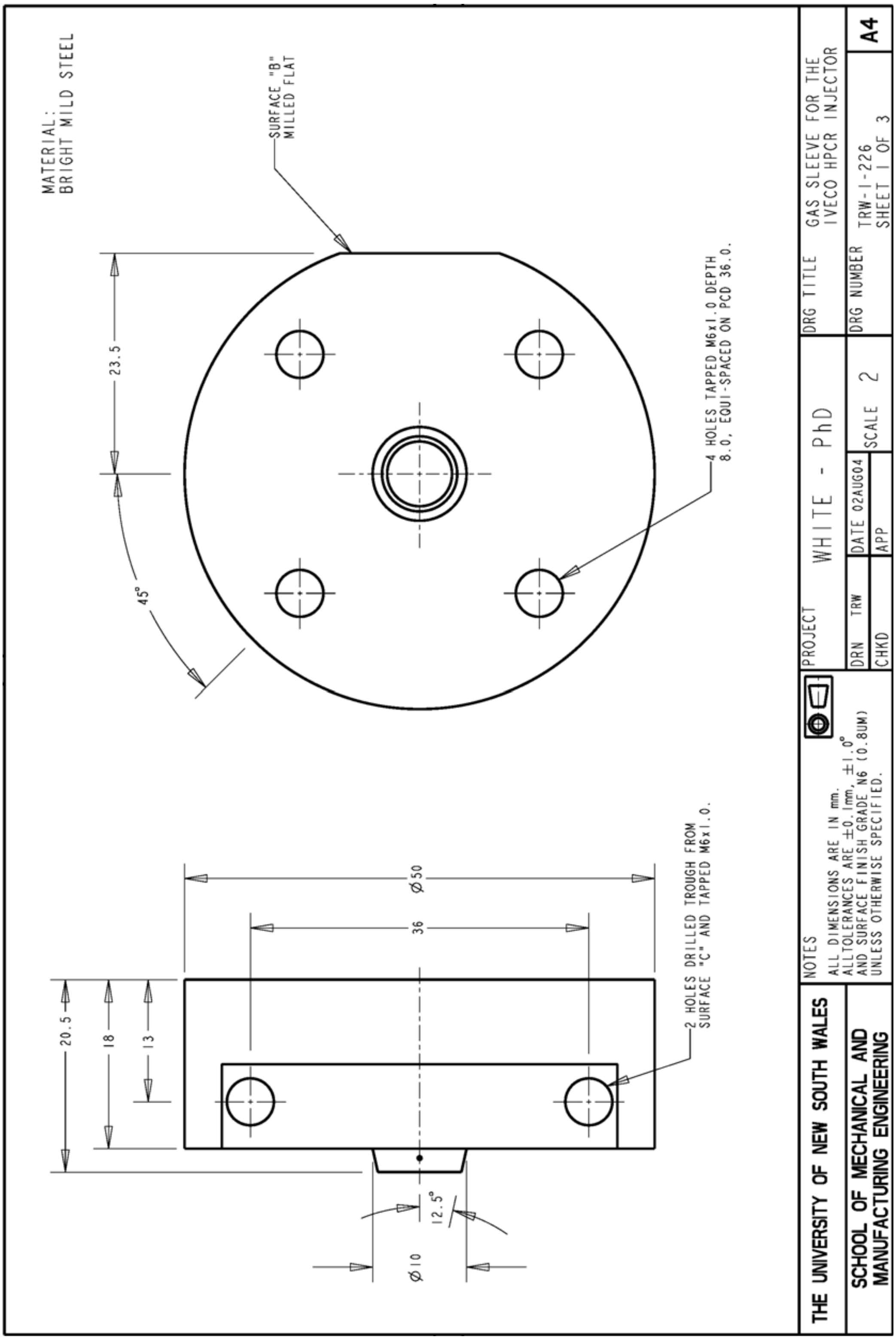
MATERIAL:
BRIGHT MILD STEEL
SURFACE "B"
MILLED FLAT
23.5
45°
4 HOLES TAPPED M6x1.0 DEPTH
8.0, EQUI-SPACED ON PCD 36.0.
2 HOLES DRILLED TROUGH FROM
SURFACE "C" AND TAPPED M6x1.0.
Ø50
36
20.5
18
13
12.5°
Ø10
THE UNIVERSITY OF NEW SOUTH WALES
SCHOOL OF MECHANICAL AND
MANUFACTURING ENGINEERING
NOTES
ALL DIMENSIONS ARE IN mm.
ALL TOLERANCES ARE ±0.1mm, ±1.0°
AND SURFACE FINISH GRADE N6 (0.8UM)
UNLESS OTHERWISE SPECIFIED.
PROJECT
WHITE - PhD
DRN TRW
DATE 02AUG04
CHKD
APP
SCALE 2
DRG TITLE
GAS SLEEVE FOR THE
IVECO HPCR INJECTOR
DRG NUMBER
TRW-1-226
SHEET 1 OF 3
A4

Figure C.13

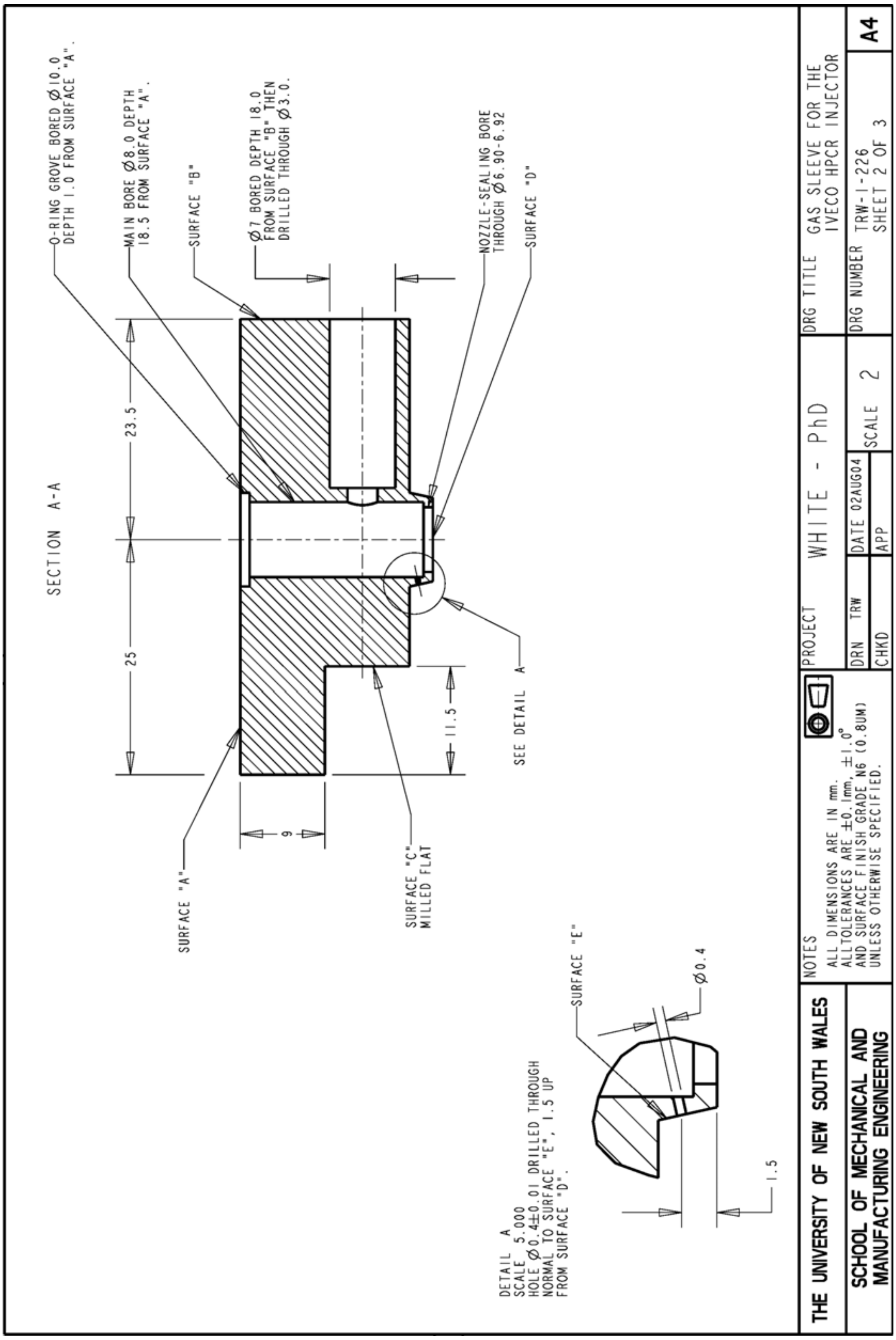
SECTION A-A
O-RING GROVE BORED Ø10.0 DEPTH 1.0 FROM SURFACE "A".
MAIN BORE Ø8.0 DEPTH 18.5 FROM SURFACE "A".
SURFACE "B"
Ø7 BORED DEPTH 18.0 FROM SURFACE "B" THEN DRILLED THROUGH Ø3.0.
NOZZLE-SEALING BORE THROUGH Ø6.90-6.92
SURFACE "D"
23.5
25
11.5
6
SEE DETAIL A
SURFACE "A"
SURFACE "C" MILLED FLAT
SURFACE "E"
Ø0.4
1.5
DETAIL A
SCALE 5.000
HOLE Ø0.4±0.01 DRILLED THROUGH NORMAL TO SURFACE "E", 1.5 UP FROM SURFACE "D".
NOTES
ALL DIMENSIONS ARE IN mm.
ALL TOLERANCES ARE ±0.1mm, ±1.0°
AND SURFACE FINISH GRADE N6 (0.8UM)
UNLESS OTHERWISE SPECIFIED.
THE UNIVERSITY OF NEW SOUTH WALES
SCHOOL OF MECHANICAL AND MANUFACTURING ENGINEERING
PROJECT WHITE - PhD
DRN TRW
CHKD
DATE 02AUG04
APP
SCALE 2
DRG TITLE GAS SLEEVE FOR THE IVECO HPCR INJECTOR
DRG NUMBER TRW-I-226
SHEET 2 OF 3
A4

Figure C.14

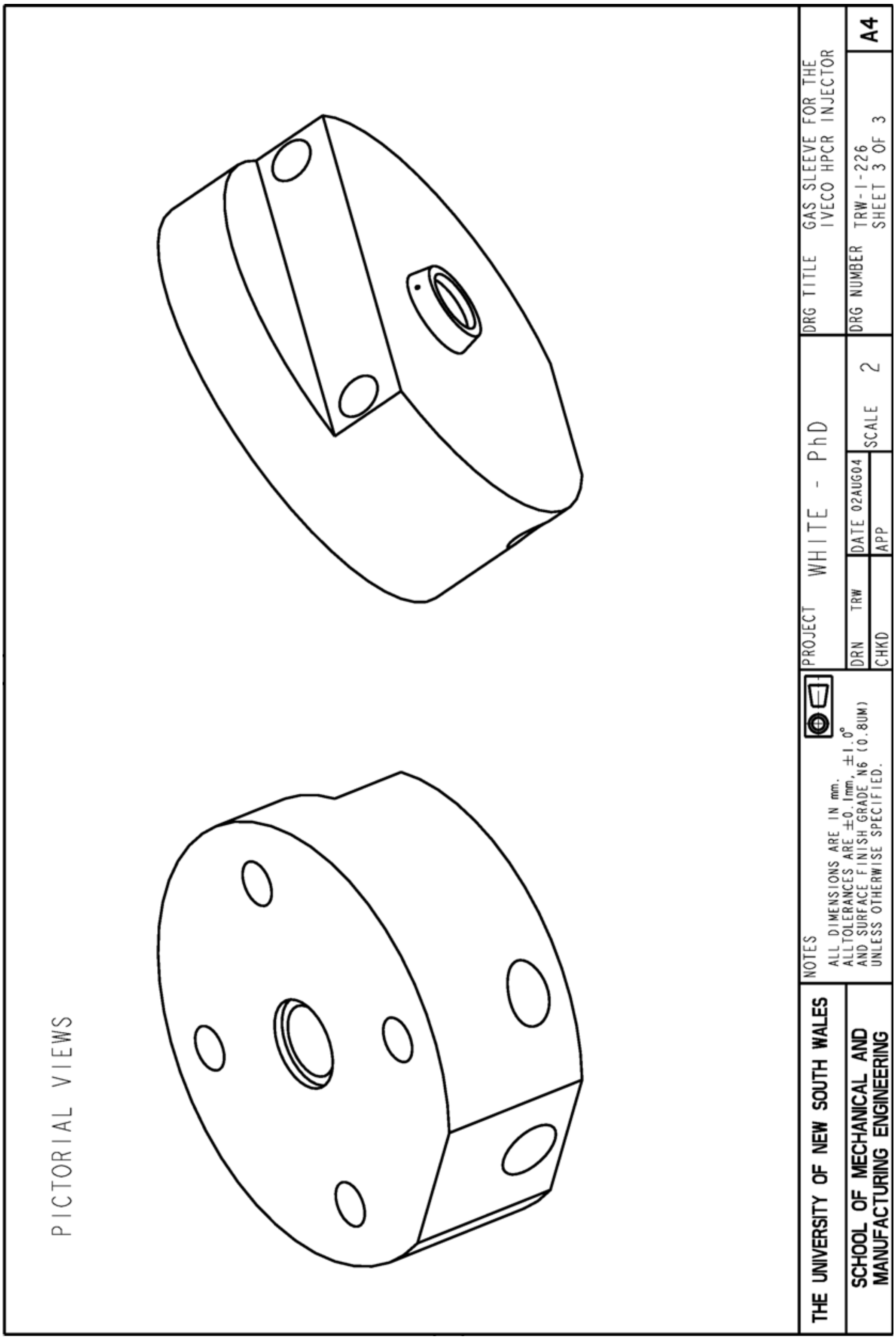
PICTORIAL VIEWS
THE UNIVERSITY OF NEW SOUTH WALES
SCHOOL OF MECHANICAL AND MANUFACTURING ENGINEERING
NOTES
ALL DIMENSIONS ARE IN mm.
ALL TOLERANCES ARE ±0.1mm, ±1.0°
AND SURFACE FINISH GRADE N6 (0.8UM)
UNLESS OTHERWISE SPECIFIED.
PROJECT WHITE - PhD
DRN TRW
DATE 02AUG04
CHKD
APP
SCALE 2
DRG TITLE GAS SLEEVE FOR THE IVECO HPCR INJECTOR
DRG NUMBER TRW-I-226
SHEET 3 OF 3
A4

Figure C.15

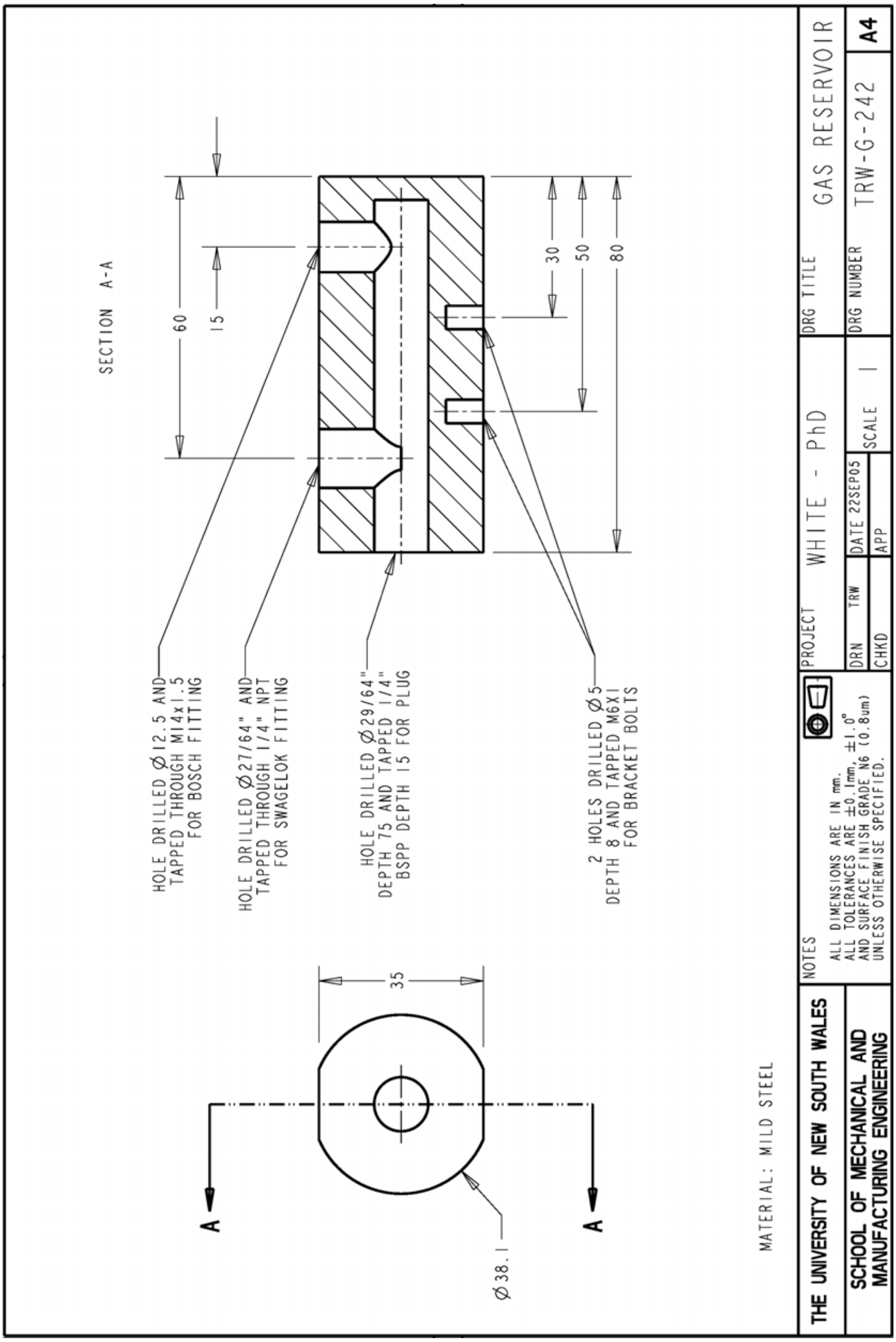
SECTION A-A
60
15
30
50
80
35
A
A
Ø38.1
MATERIAL: MILD STEEL
HOLE DRILLED Ø12.5 AND
TAPPED THROUGH M14x1.5
FOR BOSCH FITTING
HOLE DRILLED Ø27/64" AND
TAPPED THROUGH 1/4" NPT
FOR SWAGELOK FITTING
HOLE DRILLED Ø29/64"
DEPTH 75 AND TAPPED 1/4"
BSPP DEPTH 15 FOR PLUG
2 HOLES DRILLED Ø5
DEPTH 8 AND TAPPED M6X1
FOR BRACKET BOLTS
THE UNIVERSITY OF NEW SOUTH WALES
SCHOOL OF MECHANICAL AND
MANUFACTURING ENGINEERING
NOTES
ALL DIMENSIONS ARE IN mm.
ALL TOLERANCES ARE ±0.1mm, ±1.0°
AND SURFACE FINISH GRADE N6 (0.8um)
UNLESS OTHERWISE SPECIFIED.
PROJECT
WHITE - PhD
DRN TRW
CHKD
DATE 22SEP05
APP
SCALE 1
DRG TITLE
GAS RESERVOIR
DRG NUMBER
TRW-G-242
A4

Figure C.16

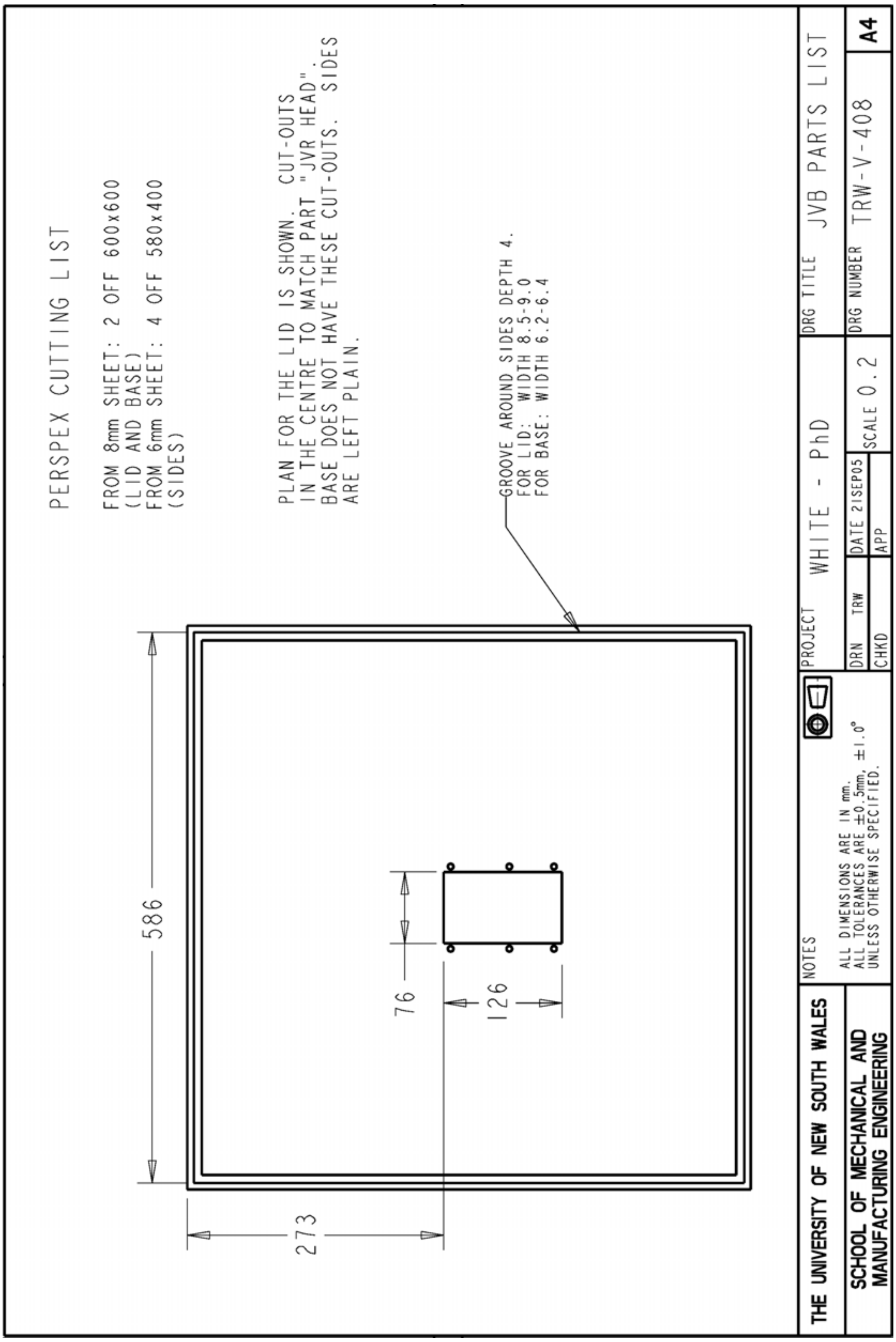

PERSPEX CUTTING LIST
FROM 8mm SHEET: 2 OFF 600x600
(LID AND BASE)
FROM 6mm SHEET: 4 OFF 580x400
(SIDES)
PLAN FOR THE LID IS SHOWN. CUT-OUTS
IN THE CENTRE TO MATCH PART "JVR HEAD".
BASE DOES NOT HAVE THESE CUT-OUTS. SIDES
ARE LEFT PLAIN.
GROOVE AROUND SIDES DEPTH 4.
FOR LID: WIDTH 8.5-9.0
FOR BASE: WIDTH 6.2-6.4
586
76
126
273
THE UNIVERSITY OF NEW SOUTH WALES
SCHOOL OF MECHANICAL AND
MANUFACTURING ENGINEERING
NOTES
ALL DIMENSIONS ARE IN mm.
ALL TOLERANCES ARE ±0.5mm, ±1.0°
UNLESS OTHERWISE SPECIFIED.
PROJECT WHITE - PhD
DRN TRW
CHKD
DATE 21SEP05
APP
SCALE 0.2
DRG TITLE JVB PARTS LIST
DRG NUMBER TRW-V-408
A4

Figure C.17

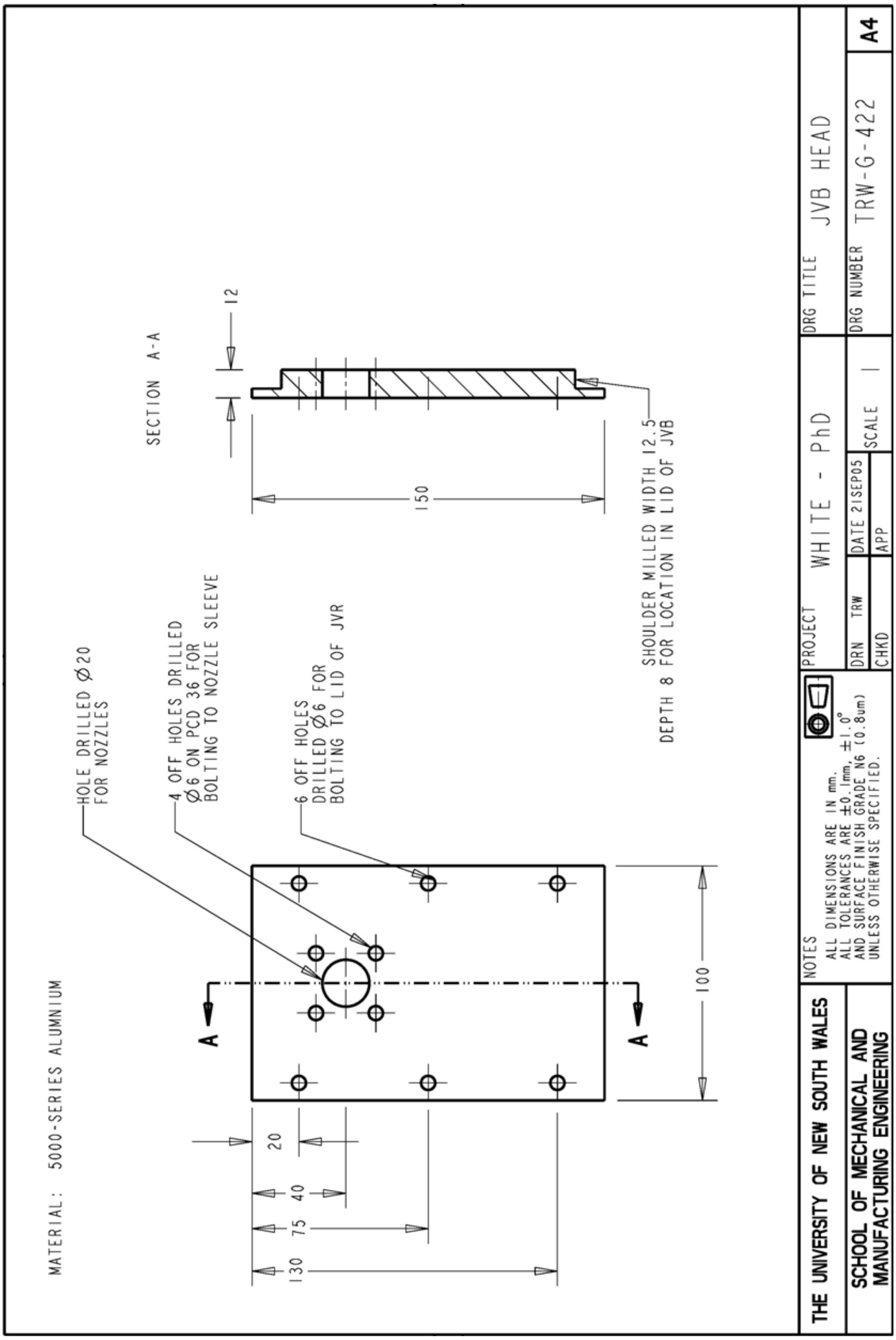

MATERIAL: 5000-SERIES ALUMINIUM
HOLE DRILLED Ø20
FOR NOZZLES
4 OFF HOLES DRILLED
Ø6 ON PCD 36 FOR
BOLTING TO NOZZLE SLEEVE
6 OFF HOLES
DRILLED Ø6 FOR
BOLTING TO LID OF JVR
SECTION A-A
12
150
SHOULDER MILLED WIDTH 12.5
DEPTH 8 FOR LOCATION IN LID OF JVB
A
A
20
40
75
130
100
THE UNIVERSITY OF NEW SOUTH WALES
SCHOOL OF MECHANICAL AND
MANUFACTURING ENGINEERING
NOTES
ALL DIMENSIONS ARE IN mm.
ALL TOLERANCES ARE ±0.1mm, ±1.0°
AND SURFACE FINISH GRADE N6 (0.8um)
UNLESS OTHERWISE SPECIFIED.
PROJECT WHITE - PhD
DRN TRW
CHKD
DATE 21SEP05
APP
SCALE 1
DRG TITLE JVB HEAD
DRG NUMBER TRW-G-422
A4

Figure C.18

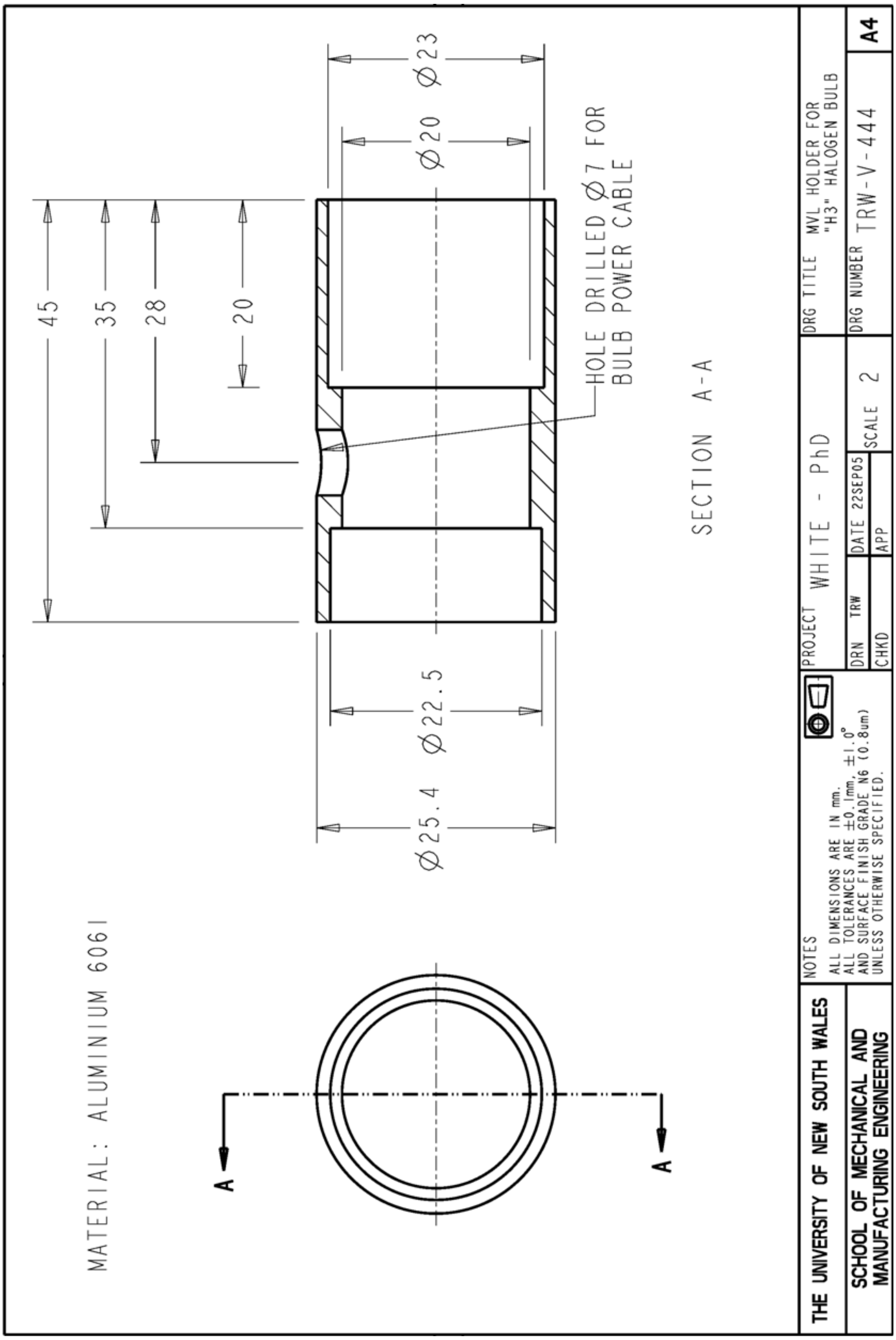
MATERIAL: ALUMINIUM 6061
Ø25.4
Ø22.5
Ø20
Ø23
45
35
28
20
HOLE DRILLED Ø7 FOR
BULB POWER CABLE
SECTION A-A
A
A
THE UNIVERSITY OF NEW SOUTH WALES
SCHOOL OF MECHANICAL AND
MANUFACTURING ENGINEERING
NOTES
ALL DIMENSIONS ARE IN mm.
ALL TOLERANCES ARE ±0.1mm, ±1.0°
AND SURFACE FINISH GRADE N6 (0.8um)
UNLESS OTHERWISE SPECIFIED.
PROJECT WHITE - PhD
DRN TRW
CHKD
DATE 22SEP05
APP
SCALE 2
DRG TITLE MVL HOLDER FOR
"H3" HALOGEN BULB
DRG NUMBER TRW-V-444
A4

Figure C.19

Appendix D: Modification of an HPCR Diesel Injector to make it Usable as a Gas Control Valve

D.1 Operation of an HPCR Diesel Injector

A schematic diagram of a Bosch HPCR injector as used in the current work is shown in Figure D.1. The injector works as follows:

- The Inlet Port is supplied with diesel from the fuel rail at a nominal pressure of 135 MPa. This high pressure exists permanently in the Needle Chamber (10). When the injector is at rest, this pressure also exists in the Working Chamber (6) which is connected to the Inlet Port via the Inlet Orifice (4).
- Pressure in the Working Chamber creates a net hydraulic force that holds the Piston (7) is its down-most position. The Piston transfers this downward force via the pre-loaded Needle Spring (8) and its bush to the Needle (9). The needle is thus held closed.
- When the Solenoid (1) is energised, the Ball (3) is allowed to lift from its seat which in turn allows diesel to flow from the Working Chamber through the Outlet Orifice (5). Since diesel flow into the Working Chamber is throttled through the Inlet Orifice (4), the pressure in the Working Chamber falls.
- This falling pressure on top of the Piston allows the pre-loaded Needle Spring to move the Piston upwards. This relaxes the downward force on the Needle. Pressure underneath the Needle in the region of the Nozzle then forces the Needle upward. Pre-load from the Needle Spring means that pressure under the Nozzle must build to about 25 MPa before the Needle will lift from its seat. When the Needle lifts, diesel can flow from the Nozzle (11).
- When the solenoid is de-energised, the Ball seats and pressure in the Working Chamber is restored. This forces the Piston down which in turn seats the Needle and stops the injection.

- During operation of the injector, seepage past the various valves in the assembly is able to vent through the spill port at the top of the injector. This port is plumbed back to the fuel tank.

The Needle Spring ("spring") in the standard injector was strong enough such that an injection pressure of at least 25 MPa was required to lift the needle from its seat. Since this pressure was higher than that at which the NG was stored, the first modification to the injector was thus to substitute this spring for a weaker one which would allow injection of gas at approximately 16 MPa.

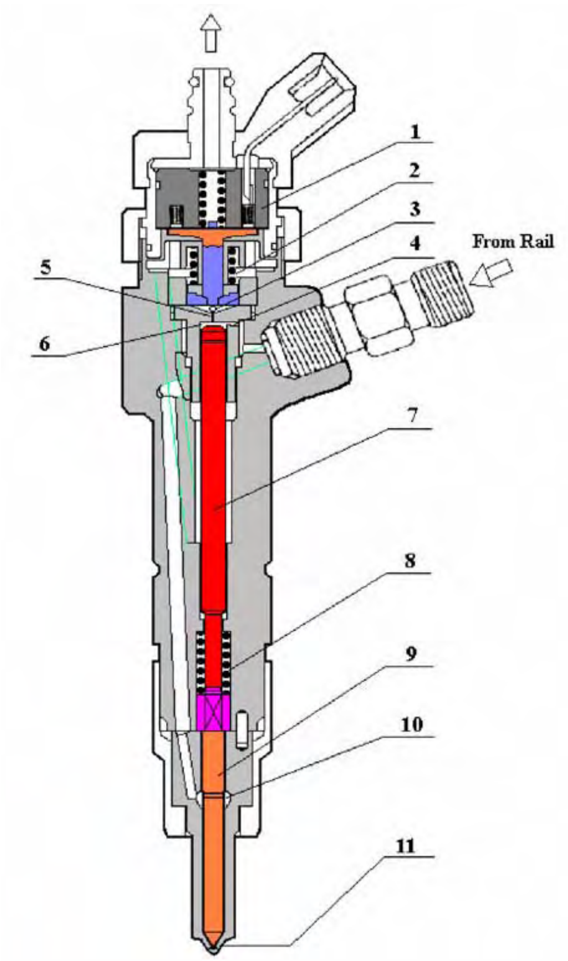

1	Solenoid
2	Plunger Spring
3	Ball
4	Inlet Orifice
5	Outlet Orifice
6	Working Chamber
7	Piston
8	Needle Spring
9	Needle
10	Needle Chamber
11	Nozzle

Figure D.1. Schematic diagram of an HPCR injector as used in the current work [150].

D.2 Modifications to the Needle Spring

Configuration 1 – Standard (Strong) Spring

As a benchmark, the standard spring was measured. It had ground and flat ends, a free-length 10.75 mm and a coil diameter of 1.10 mm. When the injector is assembled, the top face of the needle sits flush with the nozzle/nozzle body interface as shown in Figure D.1. With the nozzle body removed, this very strong spring caused the bush to protrude from the lower surface of the nozzle holder by about 1.4 mm. For the following tests, the injector was connected to a source of inert gas (Argon). Since in normal operation the internal workings of the injector are lubricated by the diesel, the injector was dismantled after every fifth injection and lubricated with penetrating oil.

When the injector fitted with the standard spring was pressurised with NG at 16 MPa, considerable leakage was noticed from the spill-port. This was assumed to be from the low-viscosity gas being able to leak through clearances in the top of the injector. These clearances would, with the more viscous diesel for which the injector was designed, not allow excessive leakage.

Configuration 2 – Intermediate Spring

Some material was ground-away from the standard spring, thus shortening it by approximately 1 mm so that the free-length became 9.75 mm. Since originally the spring had about five free coils, the effective rate of the spring would have been slightly increased because of the modification but the pre-load of the spring on the bush would be markedly decreased. With the nozzle removed, the bush now protruded only 0.4 mm from the nozzle holder.

The injector in this configuration was found, when supplied with an electrical pulse of approximately 20 ms duration, to inject well for 1 or 2 injections before the needle seemed to stick closed. The reason for this was unclear although it was suspected that even with the lower spring pre-load, the supply pressure of 16 MPa was marginal to overcome the spring force. The lower lubricity of the gas, when compared to the diesel, may have exacerbated this effect by causing "stiction" of components inside the injector. Considerable leakage was again noticed issuing from the spill port.

Configuration 3 – Weak Spring

The second substitute spring tried was a random spring found in the Laboratory. Like the standard compression spring, it had ground and flat ends. This spring was, however, much weaker. The actual rate was not measured although it is estimated that the effective rate was at most one-tenth of that of the standard spring. Whilst this spring caused the bush to protrude from the nozzle holder, the bush could easily be pushed back flush with the nozzle holder using only one finger. When the HPCR injector was pressurised with NG at 16 MPa, leakage from the spill port was perhaps a little higher than with the previous two springs. Varying pulse times were tried to gauge whether an injection could be achieved with the gas:

5.0 ms	Nothing
5.5 ms	Nothing
6.0 ms	Small puff out nozzle
6.5 ms	Weak injection
7.0 ms	Fair injection
7.5 ms	Fair injection
8.0 ms	Fair Injection
9.0 ms	Seemed acceptable

As can be seen, quite a long pulse was required for an injection of gas. As mentioned in Section 5.2, a pulse time of about 0.2 ms was all that was required for a diesel injection from this injector in its original configuration. This increase in time was attributed to the lower pneumatic forces available from the low-pressure gas to overcome inertia within the injector when compared with the high, hydraulic forces available from the diesel. Yet the delay in SOI for a given pulse timing and duration was found to be repeatable within about 1ms and so this configuration was deemed acceptable.

Configuration 4 – No Spring

In an effort to minimise the delay time between the electrical pulse and actual SOI, the injector was tested with no nozzle spring. With a feed pressure of 9 MPa, injection was achieved with a pulse of only 3.0 ms. A strong injection resulted with a pulse duration of 6.0 ms. It was decided against using this configuration, however, owing to copious amounts of gas leaking from the spill port when the injector was at rest.

From these tests, it was decided to use the injector in Configuration 3, ie. with the weak spring. Further testing again showed that the delay was repeatable to within about 1 ms. Upon selecting the new spring, the nozzle was then modified to increase the flow rate as described in Section 4.3.4.

Appendix E: Calculations

E.1 Flow Analysis of the Gas Nozzle Bodies

The first gas nozzle body was unable to produce a choked jet. Before the second nozzle was actually manufactured, simple analysis was carried-out to see whether there any chance of it actually working. Figure E.1 compare the two nozzle bodies. The long and narrow passages through which the gas must flow introduces a significant amount of friction and thus pressure loss to the flow.

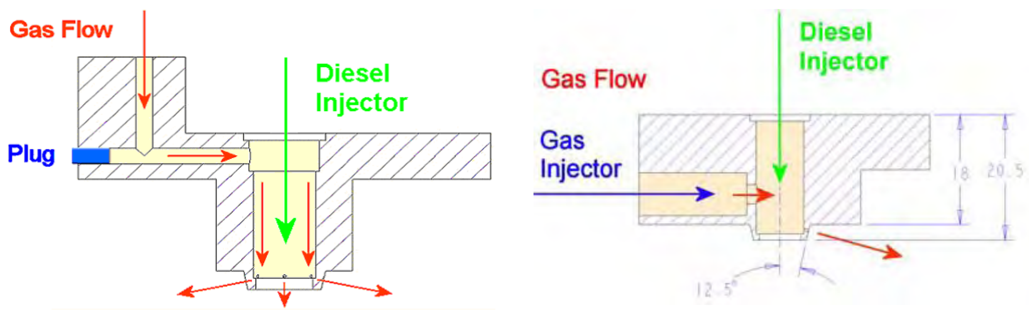

Figure E.1 Cross-sections of the first and second gas nozzle bodies built for this project. The original nozzle is shown on the left. The tortuous path between the GCV and the actual nozzle is evident when compared with the gas path in the second nozzle body.

For a compressible flow with friction, Equation E.1 determines the length of pipe that would be required to produce choked flow at the outlet for a given inlet Mach number.

$$\frac{4 \cdot f \cdot L^*}{d} = \frac{1 - M^2}{\gamma \cdot M^2} + \left(\frac{\gamma + 1}{2 \cdot \gamma}\right) \ln \left[\frac{(\gamma + 1) \cdot M^2}{2\left[1 + \left(\frac{\gamma - 1}{2}\right) M^2\right]} \right]$$

Equation E.1 [94]

Where: f = the friction factor of the walls of the pipe
d = the internal diameter of the pipe
M = the Mach number of the flow entering the pipe and
L^* = the length of pipe required to achieve choking at the exit

Rearranging Equation E.1 yields:

$$L^* = \frac{d}{4 \cdot f}\left[\frac{1-M^2}{\gamma \cdot M^2} + \left(\frac{\gamma+1}{2 \cdot \gamma}\right)\ln\left[\frac{(\gamma+1)\cdot M^2}{2\left[1+\left(\frac{\gamma-1}{2}\right)M^2\right]}\right]\right] \qquad \textbf{Equation E.2}$$

From there, the critical pipe length may be obtained using the known variables. Figure E.2 shows a schematic diagram of the flow path in the two nozzle bodies. Again, the simpler flow path of the gas from the GCV to the nozzle is evident. Also shown on the diagram is the length of each leg of the flow path in each nozzle body.

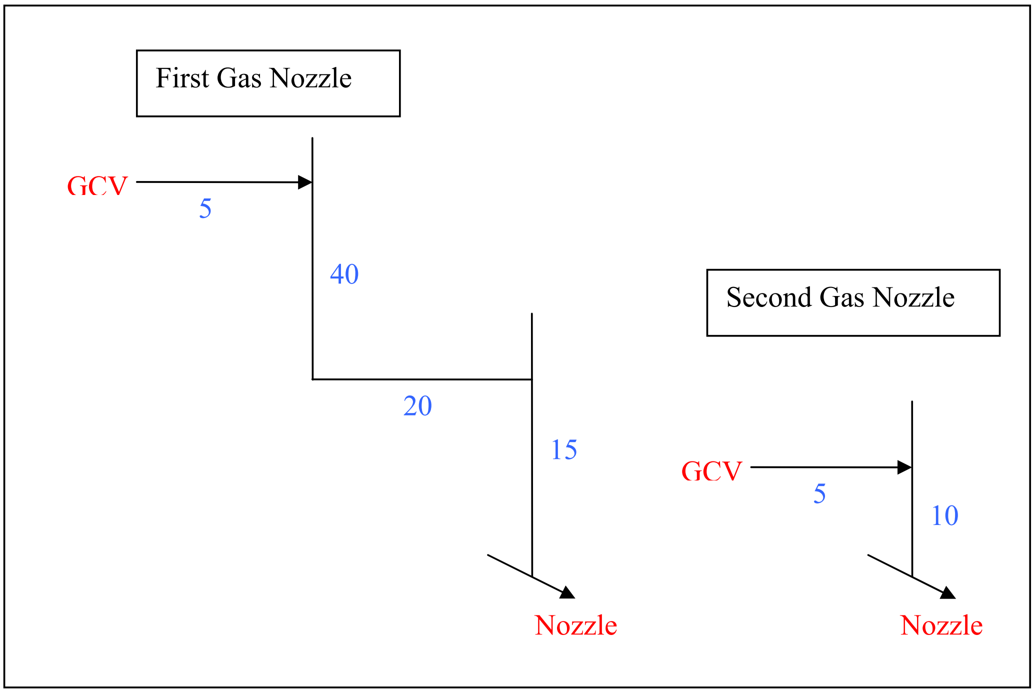

Figure E.2 Schematic diagram of the two gas nozzle bodies tried in this project. The numbers represent the approximate length of each gallery section (in millimetres).

The first nozzle included three changes in flow direction, the second nozzle one. These changes in flow direction introduced further restriction on top of the friction caused by the narrow "pipe" sections. The losses that these "corners" introduced may be expressed in terms of an additional length of pipe according to Equation E.3:

$$l_{equiv} = \frac{kd}{4f}$$ **Equation E.3 [89]**

The equivalent length, l_{equiv} is a function of the diameter of the pipe, d, the friction factor of the walls of the pipe, f and an empirical value k. Massey [89] gives a suitable friction factor for the drilled galleries as 0.003. For the particular gallery joins in the nozzle bodies, a value for k of 0.3 was found appropriate.

Table E.1 Parameters determining the flow restriction in each of the two gas nozzle bodies.

	Nozzle 1	**Nozzle 2**
Gallery diameter	1.6 mm	3.2 mm
Gallery length	80 mm	15 mm
Intersections	3	1
Bend factor, k	0.3	0.3
Friction factor, f	0.003	0.003
L_{equiv} of bends	180 mm	120 mm
Overall equivalent length	260 mm	135 mm

A spreadsheet was constructed to calculate the critical length, L^* for a range of inlet Mach numbers into each of the two gas nozzle bodies. A summary of this spreadsheet is shown in Table E.2. From this table can be seen the Mach number that could be achieved at the inlet (ie. at the GCV) for each of the nozzle bodies.

Table E.2 Spreadsheet calculations showing the critical lengths, *L, for a range of entry Mach numbers into the two gas nozzle bodies.**

			NOZZLE 1		NOZZLE 2	
M	Gamma	f	d	**L***	d	**L***
			(mm)	**(mm)**	(mm)	**(mm)**
0	1.3	0.002	1.6		3.2	
0.1	1.3	0.002	1.6	**14440.5**	3.2	**28880.9**
0.2	1.3	0.002	1.6	**3146.5**	3.2	**6293.0**
0.3	1.3	0.002	1.6	**1151.9**	3.2	**2303.8**
0.4	1.3	0.002	1.6	**504.0**	3.2	**1008.0**
0.4864	**1.3**	0.002	**1.6**	**260.0**	3.2	**519.9**
0.5	1.3	0.002	1.6	**234.5**	3.2	**469.0**
0.6	1.3	0.002	1.6	**108.2**	3.2	**216.3**
0.7	1.3	0.002	1.6	**46.1**	3.2	**92.2**
0.8	1.3	0.002	1.6	**16.1**	3.2	**32.2**
0.9	1.3	0.002	1.6	**3.2**	3.2	**6.5**
1	**1.3**	0.002	**1.6**	**0.0**	**3.2**	**0.0**
1.1	1.3	0.002	1.6	**2.2**	3.2	**4.5**
1.2	1.3	0.002	1.6	**7.6**	3.2	**15.3**
1.3	1.3	0.002	1.6	**14.8**	3.2	**29.6**
1.4	1.3	0.002	1.6	**22.8**	3.2	**45.7**
1.5	1.3	0.002	1.6	**31.3**	3.2	**62.6**
1.6	1.3	0.002	1.6	**39.8**	3.2	**79.6**
1.7	1.3	0.002	1.6	**48.2**	3.2	**96.3**
1.8	1.3	0.002	1.6	**56.3**	3.2	**112.5**
1.9	1.3	0.002	1.6	**64.1**	3.2	**128.1**
1.9457	1.3	0.002	1.6	**67.5**	**3.2**	**135.0**
2	1.3	0.002	1.6	**71.5**	3.2	**142.9**
2.1	1.3	0.002	1.6	**78.5**	3.2	**156.9**
2.2	1.3	0.002	1.6	**85.1**	3.2	**170.2**

From Table E.2:

- For the effective length of the flow path in the first nozzle body of 260 mm, the flow from the GCV is limited to a Mach number of 0.486.
- For the effective flow length in the second nozzle body of 135 mm, sonic flow is able to be achieved in the line so that the flow may be choked at the nozzle.

E.2 Analysis of the Mach Disc

Assuming that the flow may be approximated by a diverging supersonic nozzle from the throat (nozzle exit) to the Mach disc, the Mach number of the flow upstream of the shock wave may be calculated by comparing the ratio of cross-sectional areas of the Mach disc and the gas nozzle.

$$\frac{A}{A^*} = \frac{\rho^* V^*}{\rho V} = \frac{1}{M}\left(\left[\frac{2}{\gamma+1}\right]\left[1+\frac{(\gamma-1)}{2}M^2\right]\right)^{\frac{(\gamma+1)}{2(\gamma-1)}}$$ **Equation E.4 [94]**

The variables have their usual definitions and * denotes critical conditions. This equation yields the following curve for a range of area ratios:

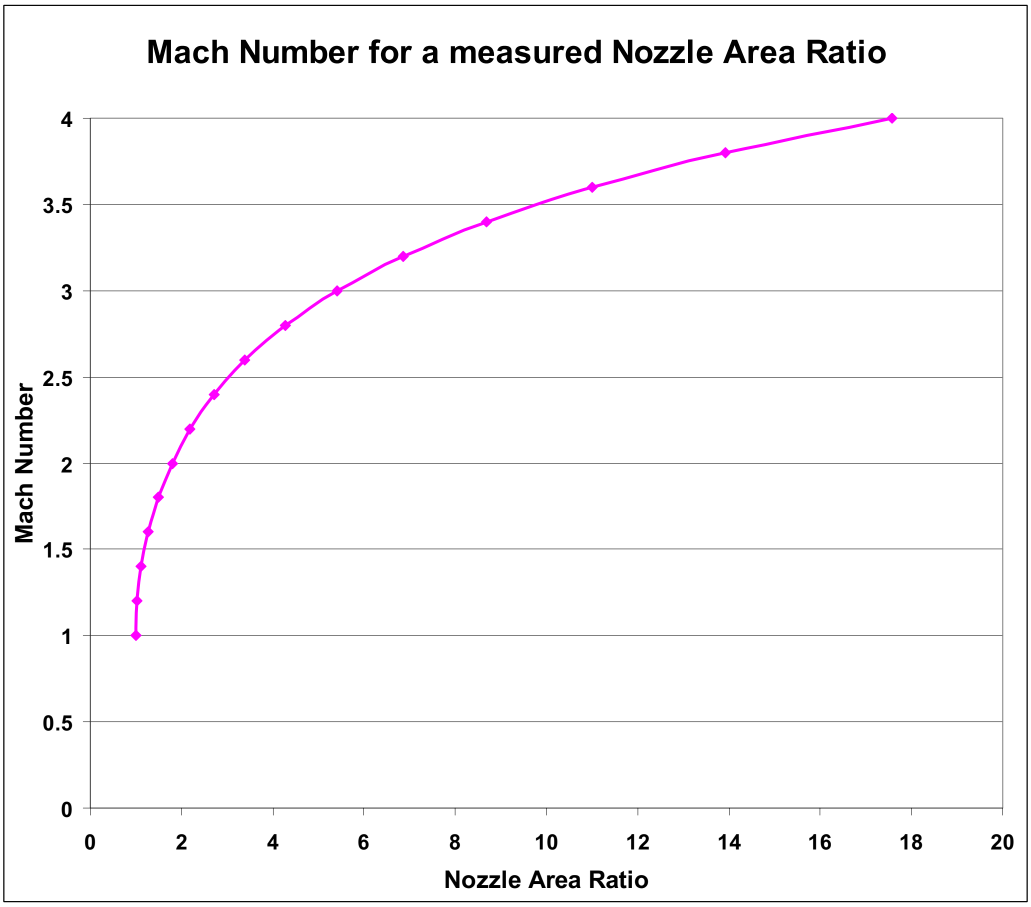

Figure E.3 Calculating the Mach number of a flow from the area ratio of the Mach disc to the nozzle.

The Mach number downstream from the shock can then be found from:

$$M_2 = \left(\frac{1 + \left(\frac{\gamma - 1}{2} \right) M_1^2}{\gamma M_1^2 - \frac{\gamma - 1}{2}} \right)^{\frac{1}{2}}$$ **Equation E.5 [94]**

For the gas nozzle used in the current work, the following curves enable determination of the Mach numbers either side of the Mach disc. The diameter of the Mach disc may be measured from photographs taken using the shadowgraph and schlieren systems.

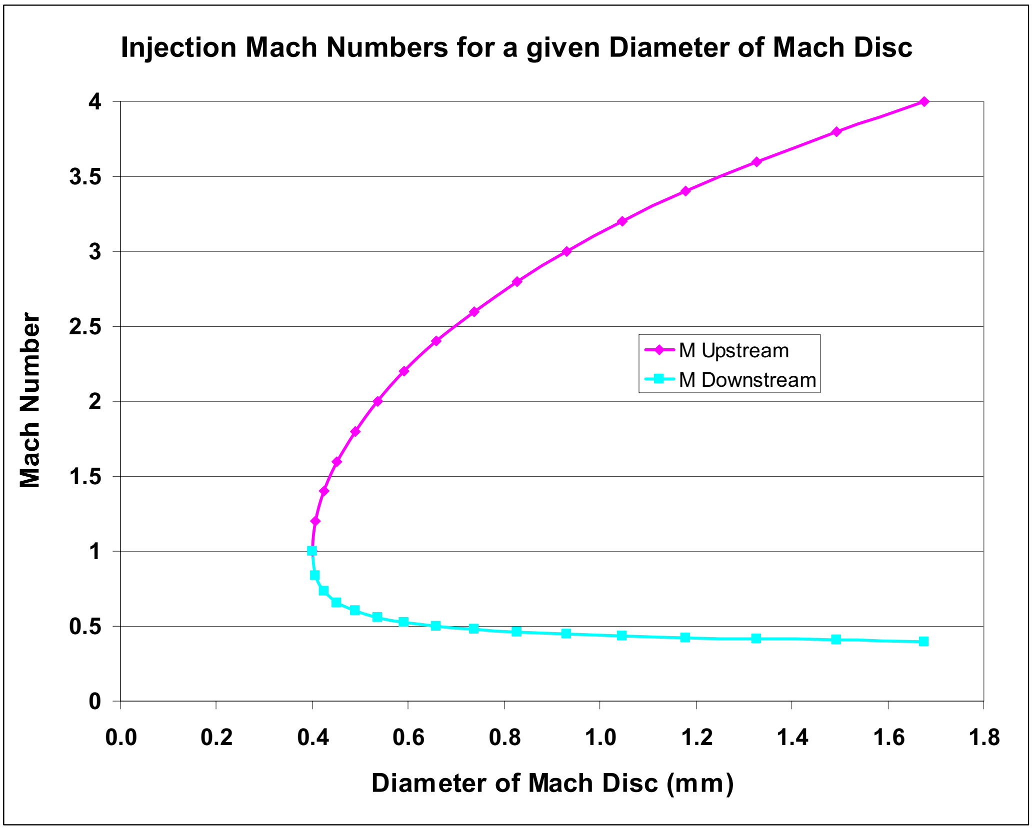

Figure E.4 Mach numbers of the flow either side of the Mach disc for a given diameter of the Mach disc.

Appendix F: Risk Assessment and Standard Operating Procedure for the Rig

F.1 Risk Assessment (RA)

Reference No.	**WHI040204 - 250505**
Laboratory	Internal Combustion Engines - L211
Activity	Spray Visualisation of Dual-Fuel Injection using the Shadowgraph/Schlieren systems and a CCD Camera.
Frequency	Weekly
Duration	Up to 6 hours at a time

Comments

The *Dual-Fuel Spray Visualisation Rig* was constructed from scratch during 2003/4. The rig enables the spray pattern of a dual-fuel injector to be photographed. The two fuels which are injected are Diesel and Compressed Natural Gas (CNG). In the case of this test rig, the injector assembly delivers the fuel jets to a transparent Perspex box rather than an actual engine which enables the spray to be photographed and then qualitatively analysed.

Prior to injection, the Diesel is pressurised (up to 180 MPa) by a pump which is connected to a three-phase electric motor. The CNG (at a pressure of up to 20 MPa) is delivered directly from a 55 L cylinder. Photographs are taken using either a CCD camera or cut film whilst the light source can be supplied either by a halogen bulb or the shadowgraph system. In any combination of the above scenarios, the camera or film is placed on one side of the Perspex box whilst the light source is placed on the other side. This results in a silhouette of the fuel jets being captured. Timing of the fuel injection, CCD camera shutter and the Shadowgraph light source are all controlled by an electronic control box which is connected to each controlled component of the system by co-axial cables.

The Diesel vapour and CNG are both flammable. The shadowgraph system creates a high-energy, short-duration spark when it is fired whilst the schlieren system relies on a high-intensity, hot halogen or Mercury-vapour bulb. Thus it is extremely important that a flammable mixture of Diesel, CNG and air does not come within close proximity of these ignition sources.

Note: If possible more than one person should carry out the assessment.
Write none for each heading if no hazard.
Add lines to the tables as required, add name/s of assessor/s and approver, print and sign.
Material Safety Data Sheets (MSDS) must be obtained and consulted for any chemical hazard.
Original to be given to Laboratory Manager, copies held by relevant persons.

A Standard Operating Procedure (SOP) must be derived from this assessment and all persons carrying out the activity must be familiar with and abide by the SOP and Risk Assessment.
Students must have signed a Student Laboratory Activity Approval form (known as RISK CONTROL) before carrying out this activity.

* C=Consequence, P=Probability, R=Rating, (AS4360 adopted by UNSW, see attached sheets for definitions and guidelines)

Hazard Type	R/C	R=Risk C=Control	C*	P*	R*
Mechanical e.g. Sharp objects Rotating equipment Hot/cold material Lifting Ergonomics Compressed gas Compressed gas storage	R1	Pump motor shaft rotates at up to 1,450 rpm. Risk of entanglement.	4	C	E
	C1	Install a guard on the rotating assembly.	4	E	H
	R2	CNG stored at up to 20 MPa. Risk of cylinder rupture and flying debris striking a person.	4	D	H
	C2	1. Place the cylinder in a secure location where it cannot fall over or be hit by other equipment. 2. Place warning signs around the area. 3. Wear eye protection when operating the rig.	4	E	H
	R3	CNG plumbing operating at up to 20 MPa. Risk of rupture and flying debris striking a person.	3	C	H
	C3	1. Place warning signs around the area. 2. Wear eye protection when operating the rig. 3. Stand clear of plumbing when operating the rig.	2	C	M
	R4	Diesel plumbing operating at up to 180 MPa. Risk of rupture and a fuel jet striking a person.	3	C	H
	C4	1. Wear eye protection and ear-muffs so that a fuel jet cannot enter the eyes or ears. 2. Wear long sleeves and trousers to avoid a jet directly hitting exposed skin.	1	C	L
	R5	Diesel injector operating at up to 400 m/s (driven by the pressure of 180 MPa). Risk of the fuel jet piercing the skin and entering the body leading to cuts, bruises, burns and infection.	4	D	H
	C5	1. Keep the operational injector within its enclosure. 2. No part of the body should enter the injector's enclosure at any time whilst the system is operational, ie. pressurised. 3. A sign must be present on the injector's enclosure stating that which appears above in (2.). 4. If for some reason the jet should happen to pierce the skin, medical attention must be sought IMMEDIATELY.	2	E	L

Hazard Type	R/C	R=Risk C=Control	C*	P*	R*
Electrical e.g. Shock Burns Overloading	R1	High Voltage (up to 600 VAC) inside the Shadowgraph box and within the pump's motor controller. Risk of electrocution if body parts or tools are inserted into the box.	4	D	H
	C1	1. Place warning signs on the outside of the boxes. 2. Keep the box closed and only allow authorized personnel to access/maintain/modify the electrical system.	4	E	H

Hazard Type	R/C	R=Risk C=Control	C*	P*	R*
Chemical e.g. Gas, Liquid, Powder, Storage and Disposal Emergency procedures	R1	Irritation from exposure to Diesel.	1	B	M
	C1	Wear gloves when re-fuelling the rig, when cleaning up spills and when cleaning the visualization box.	1	C	L
	R				
	C				

Hazard Type	R/C	R=Risk C=Control	C*	P*	R*
Environmental e.g. Vibration/noise Slipping Tripping Temperatures Gas/vapour/dust Radiation	R1	Risk of asphyxiation from the Argon used by the Shadowgraph.	3	E	M
	C1	1. Check for plumbing leaks by ensuring that the system is operating at the specified pressure of 30-40 kPa when first turning on the Argon. 2. Turn the Argon off when the Shadowgraph is not in use.	3	E	M
	R2	Risk of tripping over cables or plumbing.	3	E	M
	C2	Ensure that cables and plumbing are secured away from thoroughfares.			

Hazard Type	R/C	R=Risk C=Control	C*	P*	R*
Fire e.g. Explosion Fuels Strong oxidisers Ignition sources Housekeeping Disposal Storage Emergency procedures	R1	Accidental ignition of Diesel or CNG vapour by the Shadowgraph, schlieren bulb or by other extraneous sources.	3	D	M
	C1	1. Check audibly for leaks when first turning on the CNG. 2. Check visually for leaks when first turning on the Diesel pump. 3. Ensure that the "spill port" of the NG injector is venting to a place away from the test rig area and not in an area where there exists or can exist an ignition source. 4. Turn on the extraction fans in the laboratory before turning on the CNG. This will ensure that the vapour fraction of the flammable substance remains low and makes ignition unlikely. 5. The shadowgraph sparks only in an Argon atmosphere and so ignition by the Shadowgraph is very unlikely. 6. Purge the visualization box with fresh air or Nitrogen after every third injection.	3	E	M
	R2	Accidental ignition of stored Diesel.	2	E	L

	C2	1. Ensure that the Diesel tank's cap is always replaced after re-fuelling or checking the fuel level. 2. Place a "flammable liquid" sign on the Diesel tank. 3. Clean and ventilate the visualization box at the completion of each test session.	2	E	L
	R3	CNG plumbing operating at up to 20 MPa and Diesel at up to 180 MPa. Risk of rupture and causing a fire.	4	D	H
	C3	1. Keep ignition sources away from the test rig at all times. 2. Place warning signs to the effect of (1.).	4	E	H

Hazard Type	R/C	R=Risk C=Control	C*	P*	R*
Other	R1	Unsafe situation arising from the use of the test rig by unauthorised personnel.	4	C	E
	C1	Place warning signs outside the test rig area.	4	E	H

Assessment carried out by: T.R. White and A.G Harris

Signature/s

Approved by: A.G. Harris

Signature

Table 1 - Consequence

Level	Descriptor	Examples of Description
1	Insignificant	No injuries. Minor delays. Little financial loss. $0 - $4,999*
2	Minor	First aid required. Small spill/gas release easily contained within work area. Nil environmental impact. Financial loss $5,000 - $49,999*
3	Moderate	Medical treatment required. Large spill/gas release contained on campus with help of emergency services. Nil environmental impact. Financial loss $50,000 - $99,999*
4	Major	Extensive or multiple injuries. Hospitalisation required. Permanent severe health effects. Spill/gas release spreads outside campus area. Minimal environmental impact. Financial loss $100,000 - $250,000*
5	Catastrophic	Death of one or more people. Toxic substance or toxic gas release spreads outside campus area. Release of genetically modified organism (s) (GMO). Major environmental impact. Financial loss greater than $250,000*

* Financial loss includes direct and indirect costs, eg impact of loss of research data.

Table 2 - Probability

Level	Descriptor	Examples of Description
A	Almost certain	Task/process performed weekly or more often. The event is expected to occur in most circumstances. Common or repetitive occurrence at UNSW. Constant exposure to hazard. Very high probability of damage.
B	Likely	Task/process performed weekly to monthly. The event will probably occur in most circumstances. Known history of occurrence at UNSW. Frequent exposure to hazard. High probability of damage.
C	Possible	Task/process performed monthly to yearly. The event could occur at some time. History of single occurrence at UNSW. Regular or occasional exposure to hazard. Moderate probability of damage.
D	Unlikely	Task/process performed yearly to 5 yearly. The event is not likely to occur. Known occurrence in industry. Infrequent exposure to hazard. Low probability of damage.
E	Rare	Task/process performed 5 yearly or less often. The event may occur only in exceptional circumstances. No reported occurrence globally. Rare exposure to hazard. Very low probability of damage. Requires multiple system failures.

Table 3 – Risk Rating

Probability	Consequence				
	Insignificant 1	Minor 2	Moderate 3	Major 4	Catastrophic 5
A (Almost certain)	H	H	E	E	E
B (Likely)	M	H	H	E	E
C (Possible)	L	M	H	E	E
D (Unlikely)	L	L	M	H	E
E (Rare)	L	L	M	H	H

Recommended Action Guide:

Abbrev	Action Level	Descriptor
E	Extreme	The proposed task or process activity MUST NOT proceed. The supervisor must review the task or process design and risk controls. In the case of an existing hazard that is identified, controls must be put in place immediately.
H	High	Urgent action is required to eliminate or reduce the risk. The supervisor must be made aware of the hazard. However, the supervisor may give special permission for staff to undertake some high risk activities provided that specific training has been given and an adequate review of the task has been undertaken. This includes providing risk controls identified in Legislation, Australian Standards, Codes of Practice etc.* A detailed Safe Work Method Statement is required. *
M	Moderate	Action to eliminate or reduce the risk is required within a specified period. The supervisor should approve all moderate risk task or process activities. A Safe Work Method statement is required
L	Low	Manage by routine procedures. Action should be taken to eliminate or reduce the risk if practicable.

*Note: These regulatory documents identify specific requirements/controls that must be implemented to reduce the risk of an individual undertaking the task to a level that the regulatory body identifies as being acceptable.

F.2 Standard Operating Procedure (SOP)

Laboratory **Internal Combustion Engines - L211**

Activity Spray Visualisation of Dual-Fuel Injection using the Shadowgraph/Schlieren systems and a CCD Camera.

Risk Assessment Reference No. WHI040204-250505

Note: This SOP must be updated if the risk assessment is revised.

Date: 25 May 2005

Background

The *Dual-Fuel Spray Visualisation Rig* was constructed from scratch during 2003/4. The rig enables the spray pattern of a dual-fuel injector to be photographed. The two fuels which are injected are Diesel and Compressed Natural Gas (CNG). In the case of this test rig, the injector assembly delivers the fuel jets to a transparent Perspex box rather than an actual engine which enables the spray to be photographed and then qualitatively analysed.

Prior to injection, the Diesel is pressurised (up to 180 MPa) by a pump which is connected to a three-phase electric motor. The CNG (at a pressure of up to 20 MPa) is delivered directly from a 55 L cylinder. Photographs are taken using either a CCD camera or cut film whilst the light source can be supplied either by a halogen bulb or the shadowgraph system. In any combination of the above scenarios, the camera or film is placed on one side of the Perspex box whilst the light source is placed on the other side. This results in a silhouette of the fuel jets being captured. Timing of the fuel injection, CCD camera shutter and the Shadowgraph light source are all controlled by an electronic control box which is connected to each controlled component of the system by co-axial cables.

The Diesel vapour and CNG are both flammable whilst the shadowgraph system creates a high-energy, short-duration spark when it is fired. Thus it is extremely important that a flammable mixture of Diesel, CNG and air does not come within close proximity of the Shadowgraph's spark generator. There is a further risk of physical injury if a high-pressure fuel jet comes into contact with a part of the body. The diesel jet has the potential to pierce the skin.

Operating Procedure

1. Report to a Laboratory Staff Member and request the use of the Dual-Fuel Spray Visualisation Rig (DFSVR). If cleared to use the rig, have them instruct you on its use if you are a first-time user or if you are unsure of its use in any way. Once cleared for using the rig, proceed to the test rig area.

2. Don eye protection.

3. Visually inspect the floor around the DFSVR for Diesel or other spills. If a spill is present, mop it up so that a slip hazard does not exist. Wear gloves so that skin is not exposed to the Diesel. Dispose of the spilled Diesel in an area and manner recommended by laboratory staff.

4. Ensure that all electrical and electronic equipment is turned off and unplugged before setting up the DFSVR or commencing testing.

5. Visually inspect all Compressed Natural Gas (CNG) and Diesel lines for damage and leaks. If damage is present then have the problem fixed by a Laboratory Staff Member who is familiar with the DFSVR and authorised to work on it.

6. Position the CCD camera or film that will be used to photograph the dual-fuel spray and connect the camera to the Electronic Control Box (ECB) if applicable.

7. Position the light source or Shadowgraph and connect to the ECB if applicable.

8. Check the electrical connection between the ECB and the two injectors (CNG and Diesel). Check for positive connection so that a spark source doesn't exist.

9. If the CCD camera is being used, check the connection between the camera and its power supply and the fibre-optic connection between the camera its controlling personal computer (PC).

10. At this stage, ensure that all electrical cabling is well-stowed and doesn't present a trip hazard.

11. Check that Diesel tank on the Diesel pump rig is at least half full. If the tank is less than half-full, add Diesel (not any other liquid!) to a maximum level of 50 mm below the top of the filler neck. Ensure that the filler cap is replaced after checking/filling. Wear gloves so that skin is not exposed to the Diesel.

12. Again, visually inspect the floor around the rig for Diesel or other spills. If a spill is present, mop it up so that a slip hazard does not exist. Wear gloves so that skin is not exposed to the Diesel.

13. Check that the pressure-regulating needle-valve on the Diesel pump rig is open at least one-half of one turn.

14. Check that the fuel-rail pressure gauge is reading zero. If not, consult a Laboratory Staff Member who is familiar with the DFSVR and authorised to work on it to find out why not and rectify the problem.

15. Turn the three-phase electrical supply for the pump rig ON.

16. Select 25.00 Hz on the motor controller and press "RUN" on the controller.

17. Once the motor has reached a steady speed, slowly close the needle-valve whilst observing the pressure gauge. Stop closing the valve when the pressure reaches 50 MPa. Ensure that the pressure remains stable for at least ten (10) seconds before removing attention from the valve and gauge. If the pressure continues to rise, open the needle-valve at least one-half of one turn to release the pressure. Turn the pump rig OFF at the power-point and consult a Laboratory Staff Member who is familiar with the DFSVR and authorised to work on it. Have them inspect the plumbing system for blockages.

18. If the pressure remains stable, visually inspect all Diesel plumbing for leaks. If a leak is present, turn the pump rig OFF at the power-point consult a Laboratory Staff Member who is familiar with the DFSVR and authorised to work on it. If no leaks are visible the press "Stop" on the motor controller and proceed to the next step.

19. Ensure that the regulator on the CNG bottle frame is wound fully counter-clockwise.

20. Turn on the extraction fans at the end of the laboratory. This will diffuse any gas leaks that may occur and so reduce the likelihood of gas ignition.

21. Check that the "spill-port" of the gas injector is venting downwind of the test rig area and into a space where there does not and cannot exist an ignition source for the duration of the testing.

22. Slowly open the tap on the bottle one-half of one turn. Listen and smell for leaks during the next 10 s. If a leak is detected, close the tap and consult a Laboratory Staff Member who is familiar with the DFSVR and authorised to work on it.

23. Slowly turn the regulator clockwise until the desired injection pressure is reached. Stop regularly whilst raising the pressure and check for leaks in the plumbing between the regulator and the injector and then between the injector and the spill-port. Check also that no gas is leaking from the injection nozzles. If a leak is detected anywhere, turn off the tap on the CNG bottle and consult a Laboratory Staff Member who is familiar with the DFSVR and authorised to work on it. If no leaks are detected, close the tap on the CNG bottle and proceed.

24. If using the CCD camera, ensure that the method of its use is understood. Turn on the PC and the CCD camera: the camera needs approximately five minutes to "warm up".

25. Turn on the power to the Shadowgraph (if used).

26. Once the camera is ready, turn on the ECB and set the desired injection, Shadowgraph (if used) and camera delay and duration times. Set the camera parameters using the PC-based software and ensure that the external-trigger option is set.

27. When ready to photograph the injection, turn on the Diesel pump rig and set the desired pressure by slowly closing the needle-valve (clockwise). Ensure that the pressure remains stable for at least 10 s before removing attention from the valve and gauge.

28. IMPORTANT: Hands (and other body parts) must be kept clear of the injector whenever the diesel injection system is pressurised and especially when the injector is operating. The diesel jet has the potential to pierce the skin leading to cuts, burns, infection and even death. If for any reason the hands need to be placed within the injector's enclosure, the diesel pump should be turned OFF and the power disconnected and the gas bottle should have its valve closed and pressure bled from the gas system by backing-off the regulator.

29. Turn on the tap on the CNG cylinder and adjust the injection pressure with the regulator if necessary.

30. Turn on the Argon supply for the shadowgraph. Ensure that the operating pressure is at the specified 30-40 kPa and that the gas flow is audible. If not, turn off the Argon, Diesel pump rig and CNG bottle tap and consult a Laboratory Staff Member who is familiar with the DFSVR and authorised to work on it.

31. Activate the injection and photographing process by pressing the "Fire" button on the ECB. THE ARGON MUST BE FLOWING BEFORE FIRING THE SHADOWGRAPH. This ensures that the Shadowgraph cannot become a potential ignition source for the Diesel or CNG and is also necessary to prevent internal damage to the Shadowgraph. If any abnormal operation is observed, turn off all electrical systems and turn the tap on the CNG and Argon bottles OFF. Consult a consult a Laboratory Staff Member who is familiar with the DFSVR and authorised to work on it.

32. If normal operation occurs, proceed with testing. Remember to purge the visualisation box with fresh air or Nitrogen on every third injection to ensure that a combustible atmosphere doesn't develop in the spray box. Remain vigilant in the detection of and subsequent elimination of possible ignition sources for the duration of testing.

33. Once the testing is completed, turn off and unplug all electrical and electronic components. Turn off the Diesel Pump rig at the power-point and open the needle-valve one-half of one turn. Turn off the CNG bottle at the tap and wind the regulator fully counter-clockwise. Turn the Argon supply OFF at the tap on the bottle.

34. Inspect the test area for any Diesel spills. If a spill is present, mop it up so that a slip hazard does not exist. Wear gloves so that skin is not exposed to the Diesel. Dispose of the spilled Diesel in an area and manner recommended by laboratory staff.

35. Leave the test area in a clean and tidy state. Check that all electrical equipment, the CNG, Diesel and Argon supplies are all actually turned off.

36. Turn the extractor fans OFF. Report to a Laboratory Staff Member and advise them that you have completed your testing.

Compiled by: T. R. White

Signature:

Approved by: A.G. Harris

Signature:

Appendix G: The Rapid Compression Machine

Photo G.1. The Rapid Compression Machine installed in the laboratory.

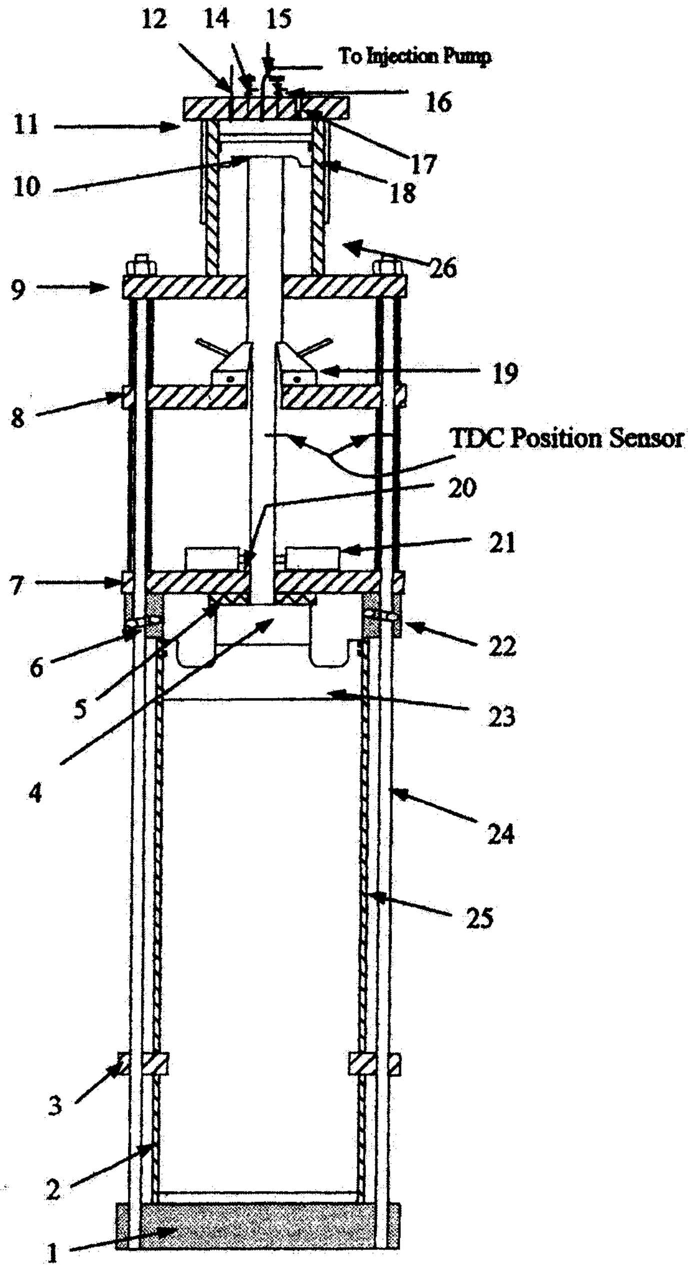

Figure 3-5 Structure of the rapid compression machine for the current research

1. Concrete base 2. Additional driving volume 3. Flange 4. Spacer 5. Rubber
6. Release holes 7. Plate I 8. Plate II 9. Plate III 10. Top piston
11. Cylinder head 12. Thermocouple 14. Inlet valve 15. Nozzle 16. Outlet valve
17. Pressure transducer 18. Heater 19. Catch 20. Pin 21. Hydraulic pump
22. Damping cylinder 23. Bottom piston (Driving cylinder) 24. Bolt
25. Driving cylinder (Bottom cylinder) 26. Combustion cylinder (Top cylinder)

Figure G.1. Schematic diagram of the Rapid Compression Machine [91].

Appendix H: Further Details of the Numerical Models used by *Fluent*

H.1 The Navier-Stokes Equations

The Navier-Stokes equations are the fundamental partial-differential equations that describe the flow of fluids. They are based on the three universal conservation laws: conservation of mass, conservation of momentum (Newton's Second Law) and conservation of energy. For all flows, *Fluent* solves conservation equations for mass and momentum. For flows involving heat transfer or compressibility, an additional equation for energy conservation is solved. For flows involving species mixing or reactions, a species conservation equation is also solved. Additional transport equations are solved when the flow is turbulent.

Mass Conservation (Continuity) Equation

$$\frac{\partial \rho}{\partial t} + \frac{\partial}{\partial x_i}(\rho u_i) = S_m$$ **Equation H.1 [39]**

where S_m is the added mass and u is a velocity vector in direction i.

Momentum Conservation Equation

$$\frac{\partial}{\partial t}(\rho u_i) + \frac{\partial}{\partial x_j}(\rho u_i u_j) = -\frac{\partial p}{\partial x_i} + \frac{\partial \tau_{ij}}{\partial x_j} + \rho g_i + F_i$$ **Equation H.2 [39]**

where p is the static pressure, τ_{ij} is the stress tensor, ρ_{gi} is the gravitational body force (buoyancy) and F_i is the external body force.

Energy Conservation Equation

$$\frac{\partial}{\partial t}(\rho E)+\frac{\partial}{\partial x_i}\left(u_1(\rho E+\rho)\right)=\frac{\partial}{\partial x_i}\left(k\frac{\partial T}{\partial x_i}-\sum_{j'}h_{j'}J_{j'}+u_j\tau_{ij}\right)+S_h$$ **Equation H.3 [39]**

where E is the total energy per unit mass, k is the conductivity, $J_{j'}$ is the diffusion flux of species j' and S_h is the source term which refers to any heat source.

These three equations can be written in vector form for a control volume V and a differential surface area dA:

$$\frac{\partial}{\partial t}\int_V W dV+\oint[F-G]\cdot dA=\int_V H dV$$ **Equation H.4 [39]**

where the vectors W, F and G are defined as:

$$W=\begin{Bmatrix}\rho\\ \rho u\\ \rho v\\ \rho w\\ \rho E\end{Bmatrix}, F=\begin{Bmatrix}\rho v\\ \rho vu+p\hat{i}\\ \rho vv+p\hat{j}\\ \rho vw+p\hat{k}\\ \rho vE+pv\end{Bmatrix}, G=\begin{Bmatrix}0\\ \tau_{xi}\\ \tau_{yi}\\ \tau_{zi}\\ \tau_{ij}v_j+q\end{Bmatrix}$$

and the total energy E is related to the total enthalpy H by:

$$E=H-\frac{p}{\rho}\quad \textbf{where}\quad H=\frac{h+|\dot{M}|^2}{2}\quad \textbf{and}\quad h=C_pT$$

H.2 Discretisation

Discretisation of the governing equations may be illustrated most easily by considering the steady-state conservation equation for transport of a scalar quantity ϕ and integrating it for an arbitrary control volume V as follows:

$$\oint \rho\phi u \cdot dA = \oint \Gamma_\phi \nabla\phi \cdot dA + \int_V S_\phi dV$$ **Equation H.5 [39]**

where:
- ρ = density
- u = velocity vector
- A = surface area
- Γ_ϕ = diffusion co-efficient for ϕ
- $\nabla\phi$ = gradient of ϕ = $\left(\frac{\partial\phi}{\partial x}\right)\hat{i} + \left(\frac{\partial\phi}{\partial y}\right)\hat{j}$
- S_ϕ = source of ϕ per unit volume

Then when Equation H.5 is applied to the control-volume or cells in the computational domain, discretisation yields:

$$\sum_f^{N_{faces}} \dot{M}_f \phi_f A_f = \sum_f^{N_{faces}} \Gamma_\phi \left(\nabla_\phi\right)_n A_f + S_\phi V$$ **Equation H.6 [39]**

where:
- N_{faces} = the number of faces enclosing the cell
- ϕ_f = the value of ϕ convected through face f
- $\dot{M}_f$ = the mass flux through the face
- A_f = the area of the face f, $|A\ | = |A_x\hat{i} + A_y\hat{j}\ |$

These equations can be applied readily to cells in the multi-dimensional computational mesh. By default, *Fluent* stores each discrete scalar value of ϕ in the centre of the cell.

The face values of the cell, ϕ_f, required for the convection terms in the equations are interpolated from the cell-centres by means of an "upwinding" scheme. Upwinding means that the face value ϕ_f is derived from quantities in the cell upstream relative to the direction of the normal velocity u_n.

Several upwinding schemes are available in *Fluent*. Editors of the Journal of Fluid Engineering [67] specify that the numerical method used must be at least formally second-order accurate in space (based on a Taylor Series expansion) for nodes in the interior of the computational grid. Second, third, and higher order methods are more computationally-expensive (per grid point) than first order schemes but the computational efficiency of these higher-order methods (accuracy per overall cost) is much greater. In the second-order scheme offered by *Fluent*, cell face values are computed using a multi-dimensional linear reconstruction approach. In this approach, higher-order accuracy is achieved at cell faces through a Taylor Series expansion of the cell-centred solution about the centroid of the cell. Thus the face value ϕ_f is computed using the following expression:

$$\phi_f = \phi + \nabla\phi \cdot \Delta s \qquad \textbf{Equation H.7 [39]}$$

where ϕ and $\nabla\phi$ are the cell-centred values and their gradient in the upstream cell respectively. Δs is the displacement vector from the centroid of the upstream cell to the centroid of the face. This formulation requires the determination of the gradient Δs in each cell. This gradient is calculated using the divergence theorem, which in discrete form is written as:

$$\nabla\phi = \frac{1}{V}\sum_{f}^{N_{faces}} \tilde{\phi}_f A \qquad \textbf{Equation H.8 [39]}$$

Here, the face values ϕ_f are computed by averaging ϕ from the two cells adjacent to the face. Finally, the gradient $\nabla\phi$ is limited so that no new maxima or minima are introduced.

H.3. Pressure-Velocity Coupling

CFD codes require an algorithm to calculate the pressure in any cell from the solution of the discretised forms of the momentum and continuity Navier-Stokes equations. The *SIMPLEC* algorithm was used for pressure-velocity coupling in the current study. It was developed by Van Doormal and Raithby in 1984 (referenced in [153]).

As described above, the momentum and continuity equations are solved sequentially in the current work using the segregated solver. In this sequential procedure, the continuity equation is used as an equation for pressure. However, pressure does not appear explicitly in Equation H.1. Also, for incompressible flows such as the liquid component of the diesel in the current work, density is not directly related to pressure. The *SIMPLE* (Semi-Implicit Method for Pressure-Linked Equations) family of algorithms is used for introducing pressure into the continuity equation. The *SIMPLE* algorithm uses a relationship between velocity and pressure corrections to enforce mass conservation and to obtain the pressure field. It is essentially a trial-and-error procedure for the calculation of pressure. It was put forward by Patankar and Spalding in 1972 (referenced in [153]).

SIMPLEC (*SIMPLE*-Consistent) is an optimised version which includes only terms that are more relevant to the case than *SIMPLE* and is more suitable to compressible flows [83]. Also, with incompressible flows, it usually allows a faster solution time [39]. Another scheme recommended for compressible flows, *PISO* (Pressure-Implicit with Splitting of Operators) was tried but was found to make the solution unstable.

H.4 Modelling Turbulence

H.4.1 Reynolds (Ensemble) Averaging

In Reynolds Averaging, the solution variables in the instantaneous (exact) Navier-Stokes equation are decomposed into the mean (ensemble-averaged or time-averaged) and fluctuating components. For example, for the velocity components:

$$u_i = \overline{u}_i + u_i'$$

$\overline{u}_i$ and u_i' are the mean and instantaneous velocity components respectively and, for a three-dimensional model, i = 1, 2 or 3. Similarly, pressure and other scalar quantities are decomposed into their mean and instantaneous quantities. Substituting expressions of this form for the flow variables into the instantaneous continuity and momentum equations and taking the time-average yields the ensemble-averaged momentum equations. These can be written in Cartesian tensor form as:

$$\frac{\partial p}{\partial t} + \frac{\partial}{\partial x_i}(\rho u_i) = 0$$

Equation H.9 [39]

$$\frac{\partial}{\partial t}(\rho u_i) + \frac{\partial}{\partial x_j}(\rho u_i u_j) = -\frac{\partial p}{\partial x_i} + \frac{\partial}{\partial x_j}\left[\mu\left(\frac{\partial u_i}{\partial x_j} + \frac{\partial u_j}{\partial x_i} - \frac{2}{3}\delta_{ij}\frac{\partial u_l}{\partial x_l}\right)\right] + \frac{\partial}{\partial x_j}(-\rho\overline{u'_i u'_j})$$

Equation H.10 [39]

The same is done for the energy equation and collectively these equations are called the Reynolds-Averaged Navier-Stokes equations. They have the same general form as the instantaneous Navier-Stokes equations but with the velocities and other solution variables now representing ensemble-averaged values. The additional term $-\rho\overline{u_i'u_j'}$ is known as the Reynolds Stress Tensor. In order to close the equation, it must be solved by the turbulence model. A common method to model the Reynolds Stresses employs the Boussinesq hypothesis to relate the Reynolds Stresses to mean velocity gradients as such:

$$-\rho\overline{u_i'u_j'} = \mu_t\left(\frac{\partial u_i}{\partial x_j}+\frac{\partial u_j}{\partial x_i}\right)-\frac{2}{3}\left(\rho k+\mu_t\frac{\partial u_i}{\partial x_i}\right)\delta_{ij}$$

Equation H.11 [39]

The Boussinesq hypothesis is used in several industry-standard turbulence models including the Spalart-Almaras model, the k-ε models and the k-ω models. The advantage of this approach is the relatively-low computational cost associated with the computation of the turbulent viscosity, μ_t.

No single turbulence model is universally accepted for all simulations and the choice of model thus depends on the physics of the individual case. *Fluent* allows the use of several different turbulence models as mentioned above. The k-ε model has been used in this study since whilst it is both versatile and robust it is also computationally inexpensive [83].

H.4.2 The "k-Epsilon" Turbulence Model

The simplest "complete" models of turbulence are two-equation models in which the solution of two separate transport equations allow the turbulent velocity and length scales to be independently determined. The standard k-ε model in *Fluent* is such a model and has become the standard for engineering flow calculations in the time since its inception because of its robustness, economy of processing-power and its reasonable accuracy for a wide range of turbulent flows.

The k-ε model was first proposed by Launder and Spalding and focuses on the mechanisms that affect the turbulent kinetic energy [39]. It is based on the presumption that there exists an analogy between the action of the viscous stresses and the Reynolds stresses on the mean flow. The model uses two transport (partial differential) equations. The first is for the turbulent kinetic energy, k, while the second one is for the rate of dissipation of turbulent kinetic energy, ε. The model transport equation for k is derived from the exact equation, while the model transport equation for ε is obtained using physical reasoning and bears little resemblance to its mathematically-exact counterpart. In deriving the k-ε model, it is assumed that the flow is fully turbulent and the effects of molecular viscosity are negligible. The standard k-ε model is therefore valid only for fully turbulent flows. The production and destruction of turbulence kinetic energy are always closely linked, ie. when k is large then ε is also large.

As the strengths and weaknesses of the standard k-ε model have become known, developments have been made to the model to improve its performance. One of these is the "Realisable" k-ε model. The term Realisable means that the model satisfies certain mathematical constraints on the normal stresses, consistent with the physics of turbulent flows. It differs from the standard k-ε model in that it contains a new formulation for the turbulent viscosity. Also, a new transport equation for the dissipation rate, ε, has been derived from an exact equation for the transport of the mean-squared vorticity fluctuation. An immediate benefit of the Realisable k-ε model applicable to this study is that it more accurately predicts the spreading rate of both planar and round jets [39]. The realisable model was chosen for the current work and its modelled transport equations are:

$$\frac{\partial}{\partial t}(\rho k)+\frac{\partial}{\partial x_i}(\rho k u_j)=\frac{\partial}{\partial xi}\left[\left(\mu+\frac{\mu_t}{\sigma_k}\right)\frac{\partial_k}{\partial x_j}\right]+G_k+G_b-\rho\varepsilon-Y_M+S_k$$

Equation H.12 [39]

and

$$\frac{\partial}{\partial t}(\rho \varepsilon)+\frac{\partial}{\partial x_j}(\rho \varepsilon u_j)=\frac{\partial}{\partial x_j}\left[\left(\mu+\frac{\mu_t}{\sigma_\varepsilon}\right)\frac{\partial \varepsilon}{\partial x_j}\right]+\rho C_1 S_\varepsilon-\rho C_2\frac{\varepsilon^2}{k+\sqrt{\upsilon\varepsilon}}+C_{1\varepsilon}\frac{\varepsilon}{k}C_{3\varepsilon}G_b+S_\varepsilon$$

Equation H.13 [39]

where

$$C_1 = \max\left[0.43, \frac{\eta}{\eta + 5}\right], \eta = S\frac{k}{\varepsilon}$$

In these equations, G_k represents the generation of turbulence kinetic energy caused by the mean velocity gradients. G_b is the generation of turbulence kinetic energy from buoyancy. Y_M represents the contribution of the fluctuating dilatation in compressible turbulence to the overall dissipation rate. C_2 and $C_{1\varepsilon}$ are constants. σ_k and σ_ε are the turbulent Prandtl numbers for k and ε respectively. S_k and S_e are user-defined source terms. *Fluent* provides the following default values for the constants which have been established to ensure that the model performs well for certain canonical flows:

$C_{1\varepsilon} = 1.44$ $C_2 = 1.92$ $\sigma_k = 1.0$ $\sigma_\varepsilon = 1.2$.

Kuo and Bracco [77] modelled transient gas jets with the standard k-ε model in 1982. Their results compared well with theory for jets with *Re* between 8,650 and 135,000. They found the penetration constant, Γ, as described in Section 3.7, to equal 2.75 although comparison with the work presented previously is not valid since they had *Re* dependency in their code.

Gaillard in 1984 [42] found the standard k-ε model to over-estimate the spread of round jets. This was attributed to the model assuming isotropy for turbulence whereas real jets have normal strains different from axial strains.

Changing coefficients for ε has been reported to help with modelling round jets. Pope in 1978 [114] changed $C_{1\varepsilon}$ from 1.44 to 1.6 but found that C_2 was best left unchanged at 1.92.

H.5. Specifying Chamber Turbulence under "Engine Conditions"

CFD simulation of the laboratory experiments in the current work was carried-out under quiescent conditions such as those found in the JVB. For some of the numerical simulation of testing under "engine conditions" (ie. approaching TDC in an actual engine), chamber turbulence was specified. The k-ε model, described in the previous section, requires initial specification of the terms for turbulence kinetic energy, k and the turbulence dissipation rate, ε.

The *Fluent* Manual [39] defines turbulence kinetic energy as:

$$k = \frac{3}{2}\left(u_{avg} I\right)^2$$ **Equation H.14 [39]**

where u_{avg} is the mean flow velocity and I is the turbulence intensity. Heywood [54] states that the flow through the intake valve of an engine is responsible for many features of the in-cylinder motion. The flow through the valve is itself proportional to the piston speed and so it can be expected that in-cylinder flow velocities at different engine speeds would scale with the mean piston speed.

Figure H.1 shows a compilation of experimentally-derived, ensemble-averaged rms fluctuation velocity (or ensemble-averaged individual cycle turbulence intensity) results at TDC at the end of the compression stroke for thirteen different flow configurations and combustion chamber geometries. Of the ensemble-averaged data, two of the data sets are for ported two-stroke engines whilst four are for four-stroke engines which have intake-generated swirl. The latter case is that which is applicable to this project. For the ported engines, a consensus emerges that the turbulence intensity at TDC has a maximum value equal to about half the mean piston speed. For the four-strokes with induced swirl, the intensity is usually a little higher than this, lying somewhere between one-half the mean piston speed and the mean piston speed itself.

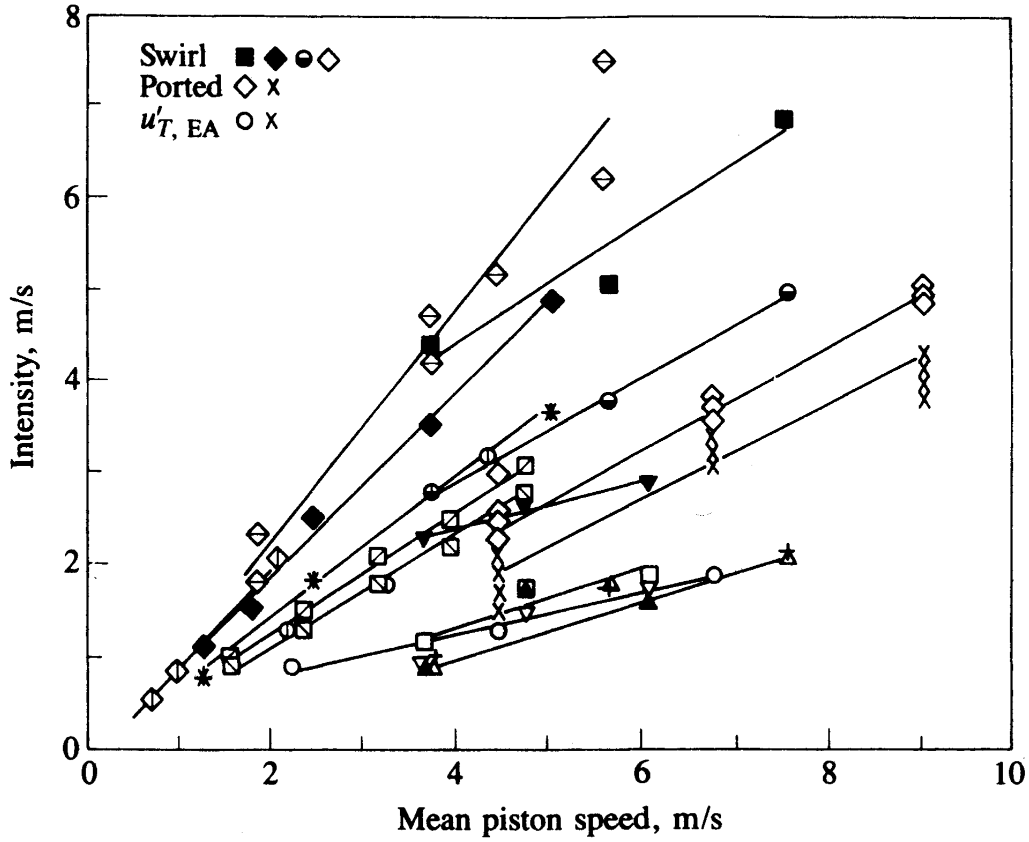

Figure H.1. Turbulence intensity as a function of Mean Piston Speed [87].

Heywood [54] summarises these results as shown in Equation H.15:

$$u'_{T,EA}(TDC) \approx 0.5\bar{S}p$$ **Equation H.15 [54]**

In the current work, an engine with cylinders of the size of that in the RCM has been considered, ie. the bore is 108 mm and the stroke is 157 mm. Such an engine would typically operate at speeds between 600 and 2,400 rpm which equates to mean piston speeds between 3.14 and 12.56 m/s. For an operating speed of 1,300 rpm the mean piston speed would be 6.8 m/s. Taking the turbulence intensity to be half of the mean piston speed, this yields a value of k for the RCM-sized engine in the current work of 17.4 m^2/s^2.

As a comparison, Hill and Ouellette in 2000 [56] used the k-ε model with the commercial CFD code *KIVA-2*. Their assumptions for turbulence at TDC were based on Heywood's statement (ie. Equation H.15) that turbulent fluctuations are of the order of half of the mean piston speed. For their models, Ouellette and Hill assumed mean piston speeds between 2 and 8 m/s. The turbulent fluctuations were then between 1 and 4 m/s which corresponded to turbulence kinetic energies between 1.5 m^2/s^2 to 20 m^2/s^2.

Since the turbulence dissipation rate in the k-ε model is closely related to the turbulent kinetic energy, the value of ε can be calculated from:

$$\varepsilon = C_\mu^{3/4}\left(k^{3/2}/l\right)$$ **Equation H.16 [39]**

Where the turbulence length scale, l, is a physical quantity related to the size of the large eddies that contain the energy in turbulent flows and C_μ is an empirical constant specified in the turbulence model with a value of approximately 0.09.

Tanner et al in 2001 [144] used a *KIVA*-based code with the k-ε model to simulate in-cylinder turbulence. As the cylinder approached TDC, the turbulent length scale was found to approach a value between 1 and 3 mm for a variety of cases. Using a value of 2mm and for k = 17.4 m^2/s^2 in the current work, a value for ε of 5,963 m^2/s^3 was chosen.

So the initial conditions for chamber turbulence in the "engine conditions" simulations are:

Turbulence Kinetic Energy, k = 17.4 m^2/s^2
Turbulence Dissipation Rate, ε = 5,963 m^2/s^3

Thus ends this thesis. I hope that reading it wasn't as big a chore as was writing it.